

Static and Dynamic Magnetization in Magnetic Antidot Lattice Arrays

By

Sougata Mallick

Enrolment No. PHYS11201204016

**National Institute Of Science Education and Research,
Bhubaneswar**

A thesis submitted to the

Board of Studies in Physical Sciences

In partial fulfillment of requirements

for the Degree of

DOCTOR OF PHILOSOPHY

of

HOMI BHABHA NATIONAL INSTITUTE



January, 2019

Homi Bhabha National Institute

Recommendations of the Viva Voce Committee

As members of the Viva Voce Committee, we certify that we have read the dissertation prepared by Mr. Sougata Mallick entitled "Static and Dynamic Magnetization in Magnetic Antidot Lattice Arrays" and recommend that it may be accepted as fulfilling the thesis requirement for the award of Degree of Doctor of Philosophy.

B. Mohanty 14/1/2019
Chairman – Prof. Bedangadas Mohanty **Date:**

S. Bedanta 14/01/2019
Guide – Dr. Subhankar Bedanta **Date:**

P. S. Anil Kumar 14.01.2019
Examiner – Prof. P. S. Anil Kumar **Date:**

V. R. Chandra 14-01-2019
Member 1 – Dr. V. Ravi Chandra **Date:**

P. K. Sahoo 14.01.2019
Member 2 – Dr. Pratap Kumar Sahoo **Date:**

D. Samal 14/01/2019
Member 3 – Dr. Debakanta Samal **Date:**

Final approval and acceptance of this thesis is contingent upon the candidate's submission of the final copies of the thesis to HBNI.

I/We hereby certify that I/we have read this thesis prepared under my/our direction and recommend that it may be accepted as fulfilling the thesis requirement.

Date: 14/01/2019

Place: SPS, NISER, Jatni

S. Bedanta
Guide 14/01/2019

Dr. Subhankar Bedanta

STATEMENT BY AUTHOR

This dissertation has been submitted in partial fulfillment of requirements for an advanced degree at Homi Bhabha National Institute (HBNI) and is deposited in the Library to be made available to borrowers under rules of the HBNI.

Brief quotations from this dissertation are allowable without special permission, provided that accurate acknowledgement of source is made. Requests for permission for extended quotation from or reproduction of this manuscript in whole or in part may be granted by the Competent Authority of HBNI when in his or her judgment the proposed use of the material is in the interests of scholarship. In all other instances, however, permission must be obtained from the author.

Sougata Mallick

(Sougata Mallick)

DECLARATION

I, hereby declare that the investigation presented in the thesis has been carried out by me. The work is original and has not been submitted earlier as a whole or in part for a degree / diploma at this or any other Institution / University.

Sougata Mallick

(Sougata Mallick)

List of Publications arising from the thesis

Journal

1. *"Magnetic domain imaging in $L1_0$ ordered FePt thin films with in-plane uniaxial magnetic anisotropy", **S. Mallick**, S. Bedanta, T. Seki, and K. Takanashi, *J. Appl. Phys.*, **2014**, *116*, 133904-1 – 133904-6.
2. *"Size and shape dependence study of magnetization reversal in magnetic antidot lattice arrays", **S. Mallick**, and S. Bedanta, *J. Magn. Magn. Mater.*, **2015**, *382*, 158 – 164.
3. *"Effect of substrate rotation on domain structure and magnetic relaxation in magnetic antidot lattice arrays", **S. Mallick**, S. Mallik, and S. Bedanta, *J. Appl. Phys.*, **2015**, *118*, 083904-1 – 083904-6.
4. *"Study of magnetization relaxation in Co thin films prepared by substrate rotation", N. Chowdhury, **S. Mallick**, S. Mallik, and S. Bedanta, *Thin Solid Films*, **2016**, *616*, 328 – 334.
5. *"Static and dynamic behavior of domain walls in high B_s soft magnetic ribbons tuned by the annealing temperature", **S. Mallick**, P. Sharma, K. Takenaka, A. Makino, and S. Bedanta, *J. Phys. D: Appl. Phys.*, **2018**, *51*, 065007-1 – 065007-6.
6. *"Tuning the anisotropy and domain structure of Co films by variable growth conditions and seed layers", **S. Mallick**, S. Mallik, B. B. Singh, N. Chowdhury, R. Gieniusz, A. Maziewski, and S. Bedanta, *J. Phys. D: Appl. Phys.*, **2018**, *51*, 275003-1 – 275003-8.
7. *"Relaxation dynamics in magnetic antidot lattice arrays of Co/Pt with perpendicular anisotropy", **S. Mallick**, S. S. Mishra, and S. Bedanta, *Sci. Rep.*, **2018**, *8*, 11648.

Manuscript in preparation

1. *"Tunability of domain structure and magnonic spectra in antidot arrays of Heusler alloy", **S. Mallick**, S. Mondal, T. Seki, S. Sahoo, T. Forrest, F. Maccherozzi, A. Barman, K. Takanashi, and S. Bedanta

* : Publications related to the thesis

Others

1. "Effect of the growth conditions on the anisotropy, domain structures and the relaxation in Co thin films", S. Mallik, **S. Mallick**, and S. Bedanta, *J. Magn. Magn. Mater.*, **2017**, *428*, 50 – 58.
2. "Effect of sputtered flux direction on damping properties in magnetic bilayers", S. Nayak, **S. Mallick**, B. B. Singh, and S. Bedanta, *J. Phys. D: Appl. Phys.*, **2018**, *51*, 055008-1 – 055008-6.
3. "Size and shape of skyrmions for variable Dzyaloshinskii-Moriya interaction and uniaxial anisotropy", A. K. Behera, S. S. Mishra, **S. Mallick**, B. B. Singh, and S. Bedanta, *J. Phys. D: Appl. Phys.*, **2018**, *51*, 285001-1 – 285001-7.

Sougata Mallick

(Sougata Mallick)

Dedicated to my parents

ACKNOWLEDGEMENTS

Firstly, I take this opportunity to express my sincere gratitude to my supervisor Prof. Subhankar Bedanta for having faith in my abilities and allowing me to work in his group at NISER, Bhubaneswar. His constant support throughout my PhD tenure has been the predominant source of motivation towards the completion of this work. I would like to thank you from the bottom of my heart for encouraging me and helping me to grow as a research scholar. Without those stimulating discussions, your sagacious scholarly inputs and immense patience, my thesis would not have been accomplished.

I would like to specially thank Prof. Bedangadas Mohanty, Chairman, Doctoral committee (DC), School of Physical Sciences (SPS), NISER, Bhubaneswar for his continuous encouragement and sincere evaluation of my work. I would also like to thank rest of my DC members Dr. Pratap Kr. Sahoo, and Dr. V. Ravi Chandra, SPS, NISER for the continuous assessment of the work. I would further thank Dr. Debakanta Samal from IOP Bhubaneswar for his kind evaluation of my work as an external DC member.

I would also thank Dr. Braj Bhusan Singh, INSPIRE faculty, NISER, Bhubaneswar for his important inputs regarding the synthesis of Co/Pt thin films. It has been always a pleasure in having scientific discussions with him.

I would be always indebted to my senior Dr. Niru Chowdhury for helping me learn the tricks of the trade and training me in different instruments. I would specially thank Dr. Thiruvengadam Vijayabaskaran for all his technical helps and sharing of research experience. I would further like to thank my juniors Swapna, Bikas, Aroop, Purbasha, Gajanan, Brindaban, Sagarika, Suaknta, Mona, Koustuv, Eshita, Purshpendra, Abhilash, Biswajit for their unfading enthusiasm and constant co-operation.

I acknowledge NISER, DAE, and DST-SERB (SB/S2/CMP-107/2013), Govt. of India for providing the research funding, and infrastructure for the entire span of my PhD.

I am grateful to our collaborator Prof. Koki Takanashi from IMR, Tohoku University, Japan

for allowing me to work in his laboratory under the fellowship from ICC-IMR for 2 months. I would like to specially thank Prof. Takeshi Seki for his extensive help in fabrication, magnetic characterization, and fruitful discussion regarding the Heusler alloy and FePt antidot arrays.

I express my sincere thank towards our collaborator Prof. Parmanand Sharma, IMR, Tohoku University, Japan for providing us with the nanocrystalline ribbon samples and scientific discussions.

I am immensely thankful to our collaborators Prof. Anjan Barman, Ms. Sucheta Mondal, and Mr. Sourav Sahoo from SNBNCBS, Kolkata, for their help in TR-MOKE measurements of the Heusler alloy antidots. I would also like to thank the Visitor, Associates and Students' Programme (VASP) in SNBNCBS for providing me the funding for short stay at SNBNCBS for the TR-MOKE experiments.

I am grateful towards Prof. Andrzej Maziewski and Dr. Ryszard Gienuisz for allowing me to perform FMR measurements in their laboratory at University of Bialystok, Poland. I would thank DST-Polish joint project (DST/INT/POL/P-01/2014) for providing the funding for my 1 month visit to University of Bialystok, Poland, to perform the FMR measurements.

I would like to thank Dr. Thomas Forrest, and Dr. Francesco Maccerozzi for their help in XPEEM measurements in I06 beamline of Diamond Light Source in UK.

I take this opportunity to specially thank my lab-mate, friend, and wife Mrs. Srijani Mallik for her continuous care. Your mere presence, understanding, cooperation, and patience was the reason I could complete this journey. Our prolonged discussions and fruitful partnership in research have significantly enriched my knowledge. Remarkably, we finished our Master's degree to join this lab and co-evolved as a scientist from strength to strength.

Last but definitely not the least, I would like to express my gratitude and love towards my parents for letting me achieve my goal. Their unconditional support, care, and encouragement has led to the culmination of this coveted dream. This degree is theirs as much as is mine.

CONTENTS

Content Details	Page No.
SYNOPSIS	i-x
LIST OF ABBREVIATIONS	xi-xii
LIST OF FIGURES	xiii-xx
LIST OF TABLES	xxi
CHAPTER 1: Introduction and Fundamentals	1-32
1.1: Introduction	1
1.2: Magnetic interactions	5
1.3: Magnetic anisotropy	6
1.3.1: Magnetocrystalline anisotropy	7
1.3.1.1: Uniaxial anisotropy	8
1.3.1.2: Cubic anisotropy	8
1.3.2: Shape anisotropy	9
1.3.3: Surface anisotropy	11
1.3.4: Magnetoelastic anisotropy	12
1.4: Zeeman energy	12
1.5: Magnetic domains and domain walls	13
1.6: Magnetization reversal	16
1.6.1: Domain wall motion	18
1.6.2: Coherent rotation	19
1.7: Magnetization dynamics	20
1.7.1: Landau-Lifshitz-Gilbert (LLG) equation	20
1.7.2: Time scales of magnetization	22
1.8: Kittel formula and macrospin model	23
1.9: Spin wave and magnon	26
1.9.1: Exchange dominated SW	27
1.9.2: Dipole dominated SW	29
1.10: Object oriented micromagnetic framework (OOMMF) simulation	32
CHAPTER 2: Experimental Techniques	33-61
2.1: Sample Fabrication	34
2.1.1: Lithography	34
2.1.1.1: Photolithography	34
2.1.1.2: E-beam lithography	36
2.1.2: Thin film deposition techniques	37
2.1.2.1: Sputtering	37

2.1.2.2: E-beam evaporation	40
2.2: Structural Characterization	42
2.2.1: Reflection high-energy electron diffraction (RHEED)	42
2.2.2: X-ray diffraction (XRD)	43
2.2.3: Scanning electron microscope (SEM)	45
2.2.4: Atomic force microscope (AFM)	46
2.3: Magnetic Characterization	49
2.3.1: Superconducting quantum interference device (SQUID)	49
2.3.2: Magneto-optic Kerr effect (MOKE) microscopy	50
2.3.3: X-ray photoemission electron microscopy (XPEEM)	54
2.3.4: Ferromagnetic resonance (FMR) spectroscopy	57
2.3.5: Time resolved MOKE magnetometer	59
CHAPTER 3: MAL arrays of Co with in-plane anisotropy	62-96
3.1: Formation of isotropic Co thin films with in-plane magnetization	63
3.2: Tuning the anisotropy, domain structure, and magnetic relaxation in MAL arrays of Co with in-plane anisotropy	78
3.3: Controlling the relaxation dynamics and magnetization switching of in-plane magnetized antidot arrays of Co by employing substrate rotation	88
CHAPTER 4: MAL arrays of Co with out-of-plane anisotropy	97-108
CHAPTER 5: MAL arrays of Heusler alloy	109-131
CHAPTER 6: FePt alloy with in-plane and out-of-plane anisotropy	132-149
6.1: Magnetization reversal and domain structure in FePt thin films with in-plane anisotropy	133
6.2: Micromagnetic simulations on effect of edge defects on domain patterns in MAL arrays of FePt with PMA using OOMMF	142
CHAPTER 7: Nanocrystalline Ribbons	150-160
CHAPTER 8: Summary and Outlook	161-163
REFERENCES	164-172

SYNOPSIS

Magnetism at nanoscale is receiving significant research interests over the last few decades because of its potential applications in ultrahigh density data storage technology, biomedical engineering, high frequency inductors, transformers, etc. [1]. In addition, the fundamental physics at nanoscale is remarkably different in comparison to its bulk counterparts. Recently, the attention has been shifted towards the patterned nanostructures due to their unique advantages of precisely controlling the shape, size, and geometry of the individual magnetic elements [2]. Magnetic antidot lattice (MAL) arrays are arrangement of well-defined periodic holes in a continuous thin film [3]. The exchange coupled MAL arrays are free from the superparamagnetic blocking [4] and hence are proposed replacement for bit patterned media [5]. The antidot edges act as domain wall traps which offers the potential for domain engineering [6]. Further, MAL arrays with feature size comparable to the wavelength of the light can be used as magnonic crystals to tune the spin wave spectra [7]. The static and dynamic features of magnetization reversal can be controlled by varying the antidot architecture [8]. In this work, we have studied the following aspects of MAL arrays in materials with different anisotropy contributions:

- Domain engineering has been performed in MAL arrays of Co with in-plane anisotropy by varying the shape, size, and inter-separation of the holes. The magnetization relaxation, domain structure, and anisotropy behavior are discussed in-terms of the grain structure in the antidot arrays due to variable speed of substrate rotation.
- The possibility of achieving faster relaxation in comparison to the parent continuous thin films has been discussed in the out-of-plane magnetized Co antidot arrays. Micromagnetic simulation shows that the experimental observations can be reproduced and extended to nano-dimension.

- The feasibility of tuning the spin wave spectra is explored in low damping half-metallic Heusler alloy antidot arrays by changing the shape of the holes. We further show that the shape anisotropy along with the intrinsic magnetocrystalline anisotropy play a major role in determining the modes of propagation for the spin waves.
- We show that the domain structure in MAL arrays of out-of-plane magnetized $L1_0$ ordered FePt can be explained in-terms of additional defect induced anisotropy in the vicinity of the periodic holes.

A major part of the thesis is devoted to study the nature of switching in MAL arrays of Co where the anisotropy is oriented along either in-plane or out-of-plane directions. In spite of several works reported in the field of antidots, to the best of our knowledge, there has been no report in quantification of domain sizes with the change in effective magnetic area. Further, the temporal evolution of domains under constant Zeeman energy has not been discussed in literature. In this context we have first studied the parent continuous thin films and then focused on antidot arrays. For in-plane magnetized Co systems, thin films of $\text{AlO}_x(2 \text{ nm})/\text{Co}(10 \text{ nm})/\text{AlO}_x(2 \text{ nm})$ have been prepared on Si (100) substrates in a high vacuum (HV) sputtering chamber (base pressure better than 5×10^{-8} mbar). Previous work, in thin films with similar heterostructure, reported formation of a growth induced uniaxial magnetic anisotropy (UMA) due to oblique angular deposition [9]. Angular variation of coercivity plot depicted decrease in UMA with substrate rotation during deposition. However, the rotation speed of 20 rpm was not sufficient to completely remove the contribution of growth induced anisotropy [9]. Often films with extremely low anisotropy are desired in transformers, microwave devices etc. The foundation for excellent soft-magnetic properties is provided by the suppressed magnetocrystalline anisotropy [10]. Further, the presence of induced UMA may hinder other anisotropy contribution arising from shape, surface of the nanostructure. Hence, sometimes it becomes necessary to eliminate the growth induced anisotropy from both applications and

fundamental research point of view. In this context, we have discussed in the present work that the growth induced anisotropy can be removed completely, in Co films on different seed layers, by incorporating substrate rotation along with high temperature deposition (200°C). We further observe that high temperature deposition leads to enhancement of grain uniformity which results in lowering of the magnetic damping [11].

The antidot arrays of Co with different shapes (triangular, circular, square) and sizes have been prepared using photolithography followed by sputtering deposition technique. During deposition, the substrate was either fixed ($\omega = 0 \text{ rpm}$) or rotated ($\omega = 20 \text{ rpm}$) to tune the strength of the in-plane UMA [12]. Surface topography imaging performed by atomic force microscopy (AFM) revealed that the growth of the grains changes from regular chain like formation to island structures due to the substrate rotation [12]. Static hysteresis measurements along with simultaneous domain imaging have been performed using magneto optic Kerr effect (MOKE) based microscopy at room temperature in longitudinal mode by varying the angle (ϕ) between the applied field and easy axis. The change in anisotropy behavior due to substrate rotation in the MAL arrays is similar to their thin film counterparts [9]. Further Kerr microscopy measurements reveal that the domain sizes strongly depend on the availability of the active area (net available magnetic area in the sample) for $\omega = 0 \text{ rpm}$ MALs. The domains nucleate from the antidot edges and move in a zigzag path hindered by the holes in the path of propagation [13]. It should be noted that the shape of the domains remains unchanged to small branched structure for both sets of the antidots ($\omega = 0$ and 20 rpm). This behavior is in contrary to their parent continuous thin film where the domain structure changes from branched to ripple and labyrinth structure with substrate rotation [9]. However, the domain size increases in the MAL arrays prepared with substrate rotation ($\omega = 20 \text{ rpm}$) [12,13].

To understand the switching mechanism, magnetic relaxation measurements were performed at sub-coercive fields. For such relaxation experiments, first the samples have been saturated

and then a reverse field is applied to relax the magnetic spins under the influence of thermal activation and constant Zeeman energy. The relaxation data can be fitted with the compressed exponential function: $I(t) = I_1 + I_2(1 - \exp(-\frac{t}{\tau}^\Gamma))$, where $I(t)$: measured Kerr intensity, I_1+I_2 : normalized Kerr intensity, τ : relaxation time constant, and Γ : exponent with a value between 1 to 3. At $\Gamma= 1$, the reversal is dominated by domain nucleation and the equation reduces to Fatuzzo-Labrune [14,15] type exponential behavior. $\Gamma= 3$ indicates that the magnetization switching is governed by domain wall (DW) motion. We have obtained Fatuzzo-Labrune type single and double exponential behavior (depending on the amplitude of the constant applied field) for both the in-plane magnetized antidot arrays prepared with $\omega = 0$ and 20 rpm . We note that the relaxation becomes faster for the antidots prepared by rotating the substrate. Strong exchange coupling between the clustered grains led to formation of bigger domains and faster relaxation in the MAL arrays with $\omega = 20 \text{ rpm}$ [12,13].

However, from our work on in-plane magnetized systems we observe that the relaxation time increases in the MAL arrays in comparison to its parent continuous thin film [13,16]. The periodic holes act as pinning centers (leading to magnetic hardening) and hinder the propagation of the domains in the lateral direction which essentially slow down the global relaxation in the antidots. This is not desirable from storage applications point of view where rapid reversal of spins is essential in reading and writing information [17]. Nevertheless, MAL arrays with perpendicular magnetic anisotropy (PMA) pose the potential to overcome these limitations. The Bloch type magnetic DWs in PMA based antidots propagate in out-of-plane direction and hence is expected to face less obstruction in the lateral path of propagation. In addition, the thermal stability of the magnetization even at ultralow dimension is ensured by the use of materials with high PMA [18]. In this context, we have prepared thin films and MAL arrays of Co with PMA on Si (100) substrates with the structure Ta(3 nm)/Pt(3.5 nm)/Co(0.8 nm)/Pt(4.5 nm). The Ta seed layer promotes the (111) growth orientation of Pt which in-turn

ensures the high out-of-plane magnetization of the system. Kerr microscopy domain imaging for the continuous thin film reveals formation of typical bubble domains of perpendicular media with high anisotropy ($K_u/K_d \gg 1$, K_u and K_d being perpendicular anisotropy and stray field energy densities, respectively) [19]. Presence of periodic holes in the MAL arrays lead to nucleation of localized smaller bubbles. However, the overall nature of the bubble domains is similar to its parent continuous thin film. This behavior is different to in-plane magnetized systems where the domain structure changes significantly for the antidots when compared to its thin film counterparts. We have performed simulations using object oriented micromagnetic framework (OOMMF) [20] which reproduced the experimental observations and has been extended to nano-dimension. Simulations with different shapes and orientations of the antidots further reveal that the nucleation and propagation of bubble domains strongly depends on the antidot architecture [21].

To study the nature of the magnetization dynamics under thermal activation energy, relaxation measurements have been performed out-of-plane magnetized MAL arrays of Co. The experimental data have been fitted with compressed exponential function as discussed earlier. The values of τ , extracted from the best fits, confirm that the reversal is dominated by DW motion and domain nucleation for the continuous thin film and MAL arrays, respectively. It should be noted that the global relaxation time in the MAL arrays of Co/Pt is faster in compared to its parent thin film. This hints that, unlike the in-plane magnetized systems, in perpendicularly magnetized Co/Pt the propagation of DWs is not restricted by the presence of the antidots [21]. We further obtain that the overall relaxation in out-of-plane magnetized system is faster than its in-plane counterparts [12,13,16,21]. The possibility of achieving faster relaxation in MAL arrays in comparison to the parent thin film may have significant impact in MRAM based devices and future spintronic applications.

We have further explored the possibility of utilizing the antidot arrays as magnonic crystals.

The propagation and detection of magnonic excitation through a medium requires extremely low magnetic damping and intrinsic anisotropy of the constituent material from experimental point of view [22,23]. However, the magnetic damping (0.07) observed in the in-plane magnetized Co film [11] is significantly high and hence the magnons will have low propagation lifetime through such film. This property makes the spin wave detection challenging in such systems. Nevertheless, presence of lower density states at E_F in Co based Heusler compounds reduces the spin flip scattering significantly which leads to extremely low magnetic damping (0.005) and high spin polarization [23-25]. Hence, such Co based half-metallic Heusler compounds with in-plane anisotropy [22,23,26] serve as ideal candidates for spin-wave detection. In this context, $\text{Co}_2\text{Fe}_{0.4}\text{Mn}_{0.6}\text{Si}$ (CFMS) thin films with thicknesses 15, 20, and 25 nm have been deposited on MgO (001) substrates in a UHV chamber with a base pressure better than 1.5×10^{-9} mbar. The thin-film heterostructure of MgO (001)/Cr (20 nm)/CFMS (t nm)/Al (3 nm), $t = 15, 20, \text{ and } 25$ nm, forms epitaxial films owing to specific growth conditions of the constituent layers. MOKE measurements, with a micro laser spot, indicates the presence of dominant cubic anisotropy (CA) aligned with a minor contribution of UMA. The strength of the anisotropy and magnetic damping have been extracted from the angle and frequency dependent ferromagnetic resonance (FMR) measurements. The MAL arrays with different shapes (square, circular, triangular, and diamond), sizes (100, 200, and 500 nm), and lattice symmetries (square, and hexagonal) were microfabricated using e-beam lithography and subsequently by Ar^+ ion milling.

Static hysteresis measurements along with simultaneous domain imaging reveal that the magnetic switching of the thin film (25 nm) is either governed by two 90° or one 180° DW motion depending on ϕ . Domain imaging using X-ray photoemission electron microscopy (XPEEM) exhibits formation of chain like domain structure in the circular antidots of CFMS thin film. However, the triangular antidot shows appearance of large domains structures rather

than narrow chain like patterns. The possible reason behind this is the availability of higher effective magnetic area in the triangular antidots in comparison to that of the circular antidots. This may also be due to the inhomogeneous anisotropy distribution and energy landscape arising from the triangular shape of the holes in the MAL array. The ultrafast magnetization dynamics, in MAL arrays of CFMS (25 nm) film with 200 nm feature size, has been measured using a time-resolved MOKE (TR-MOKE) microscope based on a two-color collinear pump-probe setup. The second harmonic ($\lambda= 400$ nm) of a Ti sapphire laser has been used to pump the samples, whereas the time-delayed fundamental ($\lambda= 800$ nm) laser beam has been used to probe the dynamics by measuring the polar Kerr rotation. The measurement of precessional dynamics demonstrates that the spin wave spectra of the square and circular shaped antidots are significantly different in comparison to the triangular and diamond shaped ones. The experimental data is qualitatively reproduced by OOMMF simulation considering the parameters extracted from VSM and FMR measurements. The band gap reduces in the triangular and diamond shaped antidots with appearance of small peaks in FFT spectra of the precession data. The nature of the spin wave spectra can be associated to the anisotropy distribution of the MAL arrays. The intrinsic four-fold anisotropy remains unaffected in circular and square shaped antidots due to their symmetric shape. However, additional effect of shape anisotropy (along with the intrinsic magnetocrystalline anisotropy) plays an important role in case of the triangular and diamond shaped antidots. In order to understand the mode profiles corresponding to the resonant peaks, the phase and power maps of the resonant modes have been calculated [27]. We obtain low frequency edge mode, Damon-Eshback type magnetostatic surface wave (MSSW) mode, and high frequency quantized modes in the circular and square antidots. On the other hand, additional high frequency quantized modes appear in the triangular and diamond shaped antidots. The modifications in the mode profile is due to the sharp corners concentrating the demagnetizing fields and thereby introducing

additional pinning regions. In conclusion, the tunability of the spin wave spectrum with the antidot shapes and anisotropy may give rise to applications magnonic based spintronic devices viz. in magnonic filters, splitters, etc. [28]

As discussed earlier, the thermal stability of magnetization at ultralow dimension is ensured by the use of materials with high anisotropy energy. FePt alloy with $L1_0$ ordering is a promising candidate of fulfilling this aspect because of having remarkably high magnetocrystalline anisotropy energy density ($7 \times 10^6 \text{ J/m}^3$) and strong corrosion resistance [29]. A small part of the present work contains simulations on MAL arrays of FePt with PMA. For complete understanding of the magnetization reversal, static hysteresis measurements along with domain imaging have been performed in the parent continuous thin films with both the in-plane and out-of-plane anisotropy. The out-of-plane magnetized FePt thin films show presence of bubble domains which changes to chain like structure in the antidot arrays [30]. However, the experimental section of this work is not a part of this thesis. The results have been qualitatively reproduced with OOMMF simulation. It has been observed that additional defects (anisotropy lower than the constituent film), present on the antidot edges, modifies the domain structure significantly from typical bubble formation to chain like domains observed in the experiment [30]. For the in-plane magnetized FePt thin films, the domain structure and hysteresis behavior changes significantly with change in the film thickness. Domains with round boundaries have been observed for films with very high value of $\mu_0 H_C / K_{in}$ ($> 0.4 \times 10^{-6} \text{ m/A}$). However, the domain structure changes to zigzag patterns when $\mu_0 H_C / K_{in} < 0.1 \times 10^{-6} \text{ m/A}$ [31].

The work presented in this thesis can be used as a guideline to precisely tune the static and dynamic nature of magnetization in MAL arrays by varying the antidot architecture. Choice of desired lattice symmetry, geometry, structure, and anisotropy of the antidots may have significant implications in future data storage and magnonic spintronics applications.

A small part of the thesis is devoted to investigate the response of DWs to static (dc) and

alternating (ac) magnetic field in soft magnetic ribbons. Along with the magnetocrystalline and shape anisotropy discussed till now, magnetostriction also plays an important role in determining the switching mechanism in few systems. The nanocrystalline ribbons can be classified in such categories where the combined effect of magnetocrystalline and magnetoelastic anisotropy determine the static and dynamic nature of the DWs. Such ribbons have several important applications in the distribution of efficient electrical power because of generation of high magnetic flux density (B_s) and low core loss. $\text{Fe}_{81.2}\text{Co}_4\text{Si}_{0.5}\text{B}_{9.5}\text{P}_4\text{Cu}_{0.8}$ alloys are prepared by high frequency induction melting of a mixture of raw materials [32]. Further the ribbons have been annealed under Ar atmosphere from $T_a= 370^\circ\text{C}$ to 460°C to tune the crystallinity. XRD measurements confirms that annealing the ribbons beyond $T_a= 400^\circ\text{C}$ crystallizes the alloy with appearance of bcc-Fe(-Co) phase. Under static dc field the as-quenched (non-annealed) ribbon shows presence of fingerprint-like ‘stress patterns’ along with 180° DWs. The optimally annealed ($T_a= 420^\circ\text{C}$) ribbon shows dense packing of bcc-Fe(-Co) grains which leads to strong exchange coupling, reduction in magnetocrystalline anisotropy, and formation of stripe domains with smooth boundary. We have further examined the response of the DWs in the ribbons to ac field with variable amplitude and frequency. The ‘stress patterns’ in as-quenched ribbons remain stable under the ac field. Ribbons annealed at very high temperature introduces high anisotropy grains which work as the pinning barrier for the DWs hindering free motion under the ac field [33]. The study of DW dynamics under such ac field will be helpful in gaining insights for further reduction of energy loss in power transformer and motor cores.

List of Conference attended:

1. Presented a **contributory oral** presentation in ‘Indo-Japan Workshop on Magnetism at Nanoscale (**IJWMN**)’ in 2016, in IMR, Tohoku University, Sendai, Japan
2. Presented a **contributory oral** presentation in ‘Current Trends in Materials Science and Engineering (**CTMSE**)’ in 2018, in SNBNCBS, Kolkata, India
3. Presented a **poster** in ‘International Conference on Magnetic Materials and Applications (**ICMAGMA**)’ in 2013, in IIT Guwahati, Guwahati, India
4. Presented two **posters** in ‘Indo-Japan Workshop on Magnetism at Nanoscale (**IJWMN**)’ in 2015, in NISER, Bhubaneswar, India
5. Presented a **poster** in ‘Current Trends in Condensed Matter Physics (**CTCMP**)’ in 2015, in NISER Bhubaneswar, India
6. Presented a **poster** in ‘International Conference on Fine Particle Magnetism (**ICFPM**)’ in 2016, in NIST, Gaithersburg, Maryland, USA
7. Presented a **poster** in ‘Emerging Trends in Advanced Functional Materials (**ETAFM**)’ in 2016, in IOP Bhubaneswar, India
8. Presented a **poster** in ‘DAE Solid State Physics Symposium (**SSPS**)’ in 2016, in KIIT Bhubaneswar, India
9. Attended ‘Conference on Emerging Materials (**CEMAT**)’ in 2016, in IISc Bangalore, India.
10. Presented a **poster** in ‘International Conference on Magnetic Materials and Applications (**ICMAGMA**)’ in 2017, in DMRL Hyderabad, India

List of Schools/Workshops attended:

1. Attended ‘Advanced School in High Resolution Transmission Electron Microscopy (**ASTEM**)’ in 2013 in IOP Bhubaneswar, India
2. Attended a school on ‘Basics of Magnetism and Investigations of Magnetic Properties of Materials’ using Synchrotron Radiation in RRCAT Indore, India
3. Attended two ‘Hands on Training Workshop’ in INUP, IIT Bombay and IISc Bangalore in 2013 and 2017, respectively.

LIST OF ABBREVIATIONS

• AC	Alternating current
• AFM	Atomic force microscopy
• BWVMS	Backward volume magnetostatic
• CA	Circular antidot
• CFMS	$\text{Co}_2\text{Fe}_{0.4}\text{Mn}_{0.6}\text{Si}$
• CMA	Cubic magnetic anisotropy
• DA	Diamond antidot
• DC	Direct current
• DE	Damon-Eshbach
• DED	Double exponential decay
• DW	Domain wall
• EA	Easy axis / axes
• FMR	Ferromagnetic resonance
• FWVMS	Forward volume magnetostatic
• H / H_{ext}	External magnetic field
• HA	Hard axis / axes
• H_C	Coercive field
• H_D	Amplitude of disorder field
• H_K	Anisotropy field
• H_M	Reverse magnetic field for relaxation measurements
• H_N	Nucleation field
• H_R	Resonance field
• H_S	Saturation field
• IMR	Institute for Materials Research
• K / K_{eff}	Total / effective anisotropy constant
• K_2	Uniaxial / two-fold anisotropy constant
• K_4	Cubic / four-fold anisotropy constant
• K_B	Boltzmann constant
• K_d	Demagnetizing energy density
• K_{out}	Perpendicular uniaxial anisotropy constant
• K_s	Surface anisotropy constant
• K_v	Volume anisotropy constant
• LLG	Landau-Lifshitz-Gilbert
• M	Magnetization
• MAL	Magnetic antidot lattice
• MFM	Magnetic force microscopy
• MOKE	Magneto optic Kerr effect
• M_R	Remanent magnetization
• MRAM	Magnetic random access memory
• M_s	Saturation magnetization
• MSSW	Magnetostatic surface spin wave
• NISER	National Institute of Science Education and Research

- NR Not rotated
- OOMMF Object oriented micromagnetic framework
- PMA Perpendicular magnetic anisotropy
- PMMA poly-methyl methacrylate
- PVD Physical vapor deposition
- QCM Quartz crystal monitor
- R Rotated
- RF Radio frequency
- RHEED Reflection high energy electron diffraction
- RT Room temperature
- SW Spin wave
- SA Square antidot
- SED Single exponential decay
- SEM Scanning electron microscopy
- SNBNCBS S. N. Bose National Centre for Basic Sciences
- SO Spin-orbit
- SQUID Superconducting quantum interference device
- SS Simulated sample
- STM Scanning tunnelling microscopy
- T_a Annealing temperature
- TA Triangular antidot
- T_{dep} Deposition temperature
- TF Thin film
- TR-MOKE Time resolved magneto optic Kerr effect
- UHV Ultrahigh vacuum
- UMA Uniaxial magnetic anisotropy
- UV Ultraviolet
- VdW Van der Walls
- XAS X-ray absorption spectroscopy
- XMCD X-ray magnetic circular dichroism
- XPEEM X-ray photoemission electron microscopy
- XRD X-ray diffraction

LIST OF FIGURES

- 1.1 Schematic diagram of MAL array showing arrangement of the periodic holes (white circles) on the continuous thin film (dark grey area).
- 1.2 Orientation of magnetization with respect to the direction cosine.
- 1.3 Schematic representation showing reduction of the magnetic stray field energy leading to domain formation.
- 1.4 Schematic representation of (a) Bloch wall and (b) Néel wall with the out-of-plane and in-plane spin rotations, respectively. The magnetization direction in perpendicular and in-plane orientation is depicted in (a) and (b), respectively.
- 1.5 Schematic representation of (a) 90° , and (b) 180° DWs. The black line in between the domains represents the DW.
- 1.6 Hysteresis loop showing the magnetization (M) vs applied field (H) behavior in a ferromagnet.
- 1.7 Schematic of the coordinate system for a single domain nanoparticle for Stoner Wohlfarth model.
- 1.8 Precession of magnetization around the applied field.
- 1.9 Time scale of magnetization showing occurrence of different physical phenomenon. Image taken from *ref.* [127].
- 1.10 Demagnetizing field and magnetization components with respect to different angles in an orthogonal coordinate system. The image is taken from *ref.* [135].
- 1.11 Spin wave propagation with precession of magnetization (\mathbf{M}) around the effective magnetic field vector (\mathbf{H}).
- 1.12 Dispersion curve for various magnetostatic spin wave modes. Image is taken from *ref.* [127].
- 2.1 Schematic of photolithography technique using positive and negative photoresist.
- 2.2 (a) Mask aligner with photolithography at NISER, Bhubaneswar, India. (b) E-beam lithography at IMR, Tohoku University, Japan.
- 2.3 Schematic for sputtering deposition technique in a vacuum chamber. The Ar^+ ions (green circles) hit the target after a voltage is applied to it. The target atoms (purple circles) are ejected upon momentum transfer and deposit on the substrate which is kept on its line of sight.
- 2.4 (a) Multipurpose deposition system from MANTIS at NISER, Bhubaneswar. (b) Schematic diagram of plume orientation relative to the EA in the substrate plane.
- 2.5 RHEED construction of the Ewald's sphere (red color) at the sample surface. The sample surface is represented by parallel infinite rods (purple color) in reciprocal lattice space.

- 2.6 Schematic of X-ray diffraction (XRD). The incident X-ray (green lines) gets diffracted (blue lines) from the atoms (orange balls) of the material and interfere constructively to form the diffraction patterns.
- 2.7 Schematic diagram of scanning electron microscope and image formation. It shows two modes of detection: backscattered electron and secondary electron mode.
- 2.8 Schematic of atomic force microscopy (AFM). The laser light deflection from the tip during sample scanning is detected by the photodetector.
- 2.9 Graph showing the different force regime between a tip and surface as a function of distance between them.
- 2.10 Schematic diagram of SQUID with the pick-up coil in a second order gradiometer geometry. The red curve shows a typical response signal of magnetic dipole as a function of scan length in the magnetometer. Concept of the image is taken from *ref.* [37].
- 2.11 (a) Schematic of MOKE interaction for longitudinal mode. (b) The orientation of normally reflected component (N), Kerr amplitude (K), with analyzer and polarizer. The figure is taken from *ref.* [176].
- 2.12 Different geometries of MOKE: (a) Longitudinal, (b) Transverse, and (c) Polar mode.
- 2.13 A conventional Kerr microscopy set-up. For simplicity the contrast formation is depicted with respect to two domain states. Concept of the image is taken from *ref.* [37].
- 2.14 (a) Electronic transitions in conventional L -edge absorption of X-rays. (b) X-ray magnetic circular dichroism (XMCD) phenomenon presented for one-electron model. (c) Schematic of X-ray photoemission electron microscopy (XPEEM) phenomenon to obtain magnetic contrast. Concept of image taken from *ref.* [179]
- 2.15 Schematic layout of the XPEEM at $I06$ beamline at Diamond Light Source, UK [182].
- 2.16 (a) A schematic diagram of an FMR set-up showing the sample position on the CPW with respect to H and h_{RF} , (b) Zeeman splitting by application of an external magnetic field (H), (c) a typical FMR signal as a function of applied field.
- 2.17 A schematic diagram of a TR-MOKE set-up with collinear pump-probe geometry. Concept of the image is taken from *ref.* [129].
- 3.1 AFM image and grain size distribution for samples S1-TF-A (a & b), S1-TF-D (c & d), S2-TF-A (e & f), and S2-TF-D (g & h), respectively. All the AFM images are in same length scale.
- 3.2 Hysteresis loops for series 1 samples S1-TF-A – S1-TF-F (a – f), and series 2 samples S2-TF-A – S2-TF-F (g – l), respectively, along the EA ($\phi = 0^\circ$) (red line with solid circle) and HA ($\phi = 90^\circ$) (black line with open circle). (g – i) are reproduced with permission from *ref.* [9]. The samples prepared at room temperature and 200°C are represented by RT and HT, respectively.
- 3.3 Coercivity (H_C) vs ϕ plot for samples S1-TF-A – S1-TF-C (a), S1-TF-D – S1-TF-F (b), S2-TF-A – S2-TF-C (c), and S2-TF-D – S2-TF-F (d). Red line with solid circle, black

- line with open circle, and green line with solid star, represents the samples prepared with $\omega = 0, 10, \text{ and } 20$ rpm, respectively. Fig. 3.3 (c) is reproduced with permission from *ref.* [9].
- 3.4 Angular dependence of coercivity plots fitted with Stoner-Wohlfarth model for (a – d) samples S1-TF-A, S1-TF-D, S2-TF-A, and S2-TF-D, respectively. The black open circles are the experimental data points whereas the red lines are the fitted curve using eqn. 3.3.
 - 3.5 ΔH_C vs ω plot for samples S1-TF-A – S1-TF-C (solid pink circles), S1-TF-D – S1-TF-F (solid blue triangles), S2-TF-A – S2-TF-C (open orange stars), and S2-TF-D – S2-TF-F (open cyan diamonds).
 - 3.6 Schematic diagram showing the orientation of \mathbf{M} and \mathbf{H} wrt the azimuthal angle (θ), polar angle (ϕ), and the easy axis in the sample plane.
 - 3.7 Resonance field (H_R) vs angle (ϕ) plot for samples (a) S1-TF-D, (b) S1-TF-E, and (c) S1-TF-F. Black solid circles and red line represent the experimentally observed data and fitted curves, respectively.
 - 3.8 Resonance field (H_R) vs angle (ϕ) plot for samples (a) S2-TF-A, and (b) S2-TF-D. Black solid circles and red line represent the experimentally observed data and fitted curve, respectively.
 - 3.9 Domain images measured using MOKE microscope at RT at $\sim H_C$ for (a – f) samples S1-TF-A – S1-TF-F, and (g – l) samples S2-TF-A – S2-TF-F, respectively. The scale bars for (a – c) are shown individually. The scale bars of (d – f) are same and shown in (d). Similarly, the scale bars of (g – l) are same and shown in (g) and (j). (g – i) are reproduced with permission from *ref.* [9].
 - 3.10 SEM images for samples (a) S3-SCA (small circular antidot): $d = 3.2 \mu\text{m}$, $D = 6 \mu\text{m}$; (b) S3-BCA (big circular antidot): $d = 5.8 \mu\text{m}$, $D = 10 \mu\text{m}$; (c) S3-SA (square antidot): $d = 3.2 \mu\text{m}$, $D = 6 \mu\text{m}$; and (d) S3-TA-NR (triangular antidot): $d = 5 \mu\text{m}$, $D_1 = 9.2 \mu\text{m}$, $D_2 = 12.1 \mu\text{m}$.
 - 3.11 Hysteresis loops measured by Kerr microscopy for (a – d) samples S3-SCA, S3-BCA, S3-SA, and S3-TA-NR, respectively. The red and black curves correspond to the hysteresis loops along $\phi = 0^\circ$ and 90° , respectively.
 - 3.12 Domain images measured using Kerr microscopy for samples S2-TF-A (a – d), S3-SCA (e – h), S3-BCA (i – l), S3-SA (m – p), and S3-TA-NR (q – t), at $-H_S$, H_N , H_C , and $\sim H_S$, respectively. The scale bar and the direction of applied field for all the samples are same and is shown in (a). The higher resolution domain images for samples S3-SCA, and S3-SA are shown in inset of (f), (g), and (n), (o), respectively. The higher resolution images are measured on the area marked by the red box as shown in (f).

- 3.13 Hysteresis loop showing the field (H_M) for relaxation measurements. The sample has been first saturated ($-H_S$) and then a reverse magnetic field H_M is set to a sub-coercive (H_C) value to relax the spins under constant Zeeman energy.
- 3.14 Relaxation measurement by longitudinal Kerr microscope for sample S3-TA-NR along easy axis. Fig. (b – i) are domain images marked by point 1 to 8 in (a) at 0, 5, 12, 20, 30, 35, 50, and 120 s, respectively, after fixing the applied magnetic field to $H_M = 0.995H_C$.
- 3.15 Relaxation measurement along easy axis for (a) sample S2-TF-A, (b) sample S3-TA-NR, at $H_M = 0.995H_C$ (red curve), $0.99H_C$ (blue curve), and $0.985H_C$ (green curve). The inset of (a) shows the zoomed-in view of the relaxation curve for sample S2-TF-A at $H_M = 0.995H_C$.
- 3.16 (a) SEM image of triangular antidot patterns of sample S3-TA-R, (b) the AFM image of the antidot structure showing four triangular holes. (c) Surface morphology of sample S3-TA-NR performed in between two successive triangular holes marked by the box in figure (b). (d) Surface morphology of sample S3-TA-R in between two successive triangular holes performed similar to (c). The insets of figure (c) and (d) are zoomed views of the corresponding images.
- 3.17 (a) H_C vs ϕ plots for sample S3-TA-NR (blue curve) and sample S3-TA-R (red curve). Angular dependence of coercivity plots fitted with Stoner-Wohlfarth model for (b) sample S3-TA-NR and (c) sample S3-TA-R, respectively. The black open circles are the experimental data points whereas the red line is the fitted curve using eqn. 3.3.
- 3.18 Resonance field (H_R) vs angle (ϕ) plot for samples (a) S3-TA-NR, and (b) S3-TA-R. Black solid circles and red line represent the experimentally observed data and fitted curve, respectively.
- 3.19 (a), (b) and (c), (d) are the domain images along easy axis ($\phi = 0^\circ$) at nucleation (H_N) and coercive field (H_C) for sample S3-TA-NR and sample S3-TA-R, respectively. Fig. (e), (f) and (g), (h) are the domain images along $\phi = 30^\circ$ at H_N and H_C for samples S3-TA-NR and S3-TA-R, respectively. The insets of fig. 5 (c), (d), (g), and (h) show the zoomed version of the domains encircled by the red line. The red arrows shown in the inset images of fig. 5 (c), (d), (g), and (h) represent the widths of the individual domains. All inset images are in the same scale and the total widths of the insets are $33 \mu\text{m}$.
- 3.20 (a) Relaxation behavior of samples S3-TA-NR (black colored solid diamonds) and S3-TA-R (pink colored solid triangles) along the EA at a constant applied magnetic field of $H_M = 0.97H_C$. (b) Relaxation behavior of sample S3-TA-R at $H_M = 0.995H_C$ (red colored solid circles), $H_M = 0.99H_C$ (blue colored solid stars) and $H_M = 0.985H_C$ (green colored solid squares), respectively.
- 4.1 Figure 4.1: SEM images of (a) triangular, (b) circular, and (c) square antidot arrays of Co/Pt.

- 4.2 Hysteresis loops measured by Kerr microscope in polar mode for samples S4-TF (black hollow square with line) and S4-TA (red solid circle with line).
- 4.3 (a – c) and (d – f) are the domain images at $-H_S$, H_N , and H_C , for samples S4-TF and S4-TA, respectively. The direction of applied magnetic field and scale bar for all the images are same and shown in (a). The insets of (e) and (f) show the high-resolution images marked by the yellow boxes in the corresponding images.
- 4.4 OOMMF simulated domain images for various MAL patterns (a – d) SS-TF, (e – h) SS-ATA, (i – l) SS-STA, (m – p) SS-CA, (q – t) SS-SA at H_S , $-H_N$, $-H_C$, and $\sim -H_S$, respectively. The scale bar and direction of applied magnetic field are same for all the samples which are shown in (a).
- 4.5 (a) Relaxation behavior for the continuous thin film sample S4-TF measured at $H_M = 0.99H_C$, where hollow black circle and red curve represent the raw data, and the fitted curve with compressed exponential function, respectively. (b – i) show the domain images measured at 0, 3, 8, 13, 18, 23, 29, and 44s, respectively, as marked in (a). The scale bar and applied field direction are same for all the images and shown in (b).
- 4.6 (a) Relaxation behavior for the triangular antidot sample S4-TA measured at $H_M = 0.99H_C$, where hollow black circle and red curve represent the raw data, and the fitted curve with compressed exponential function, respectively. (b – i) show the domain images measured at 0, 3, 5, 8, 11, 15, 19, and 27s, respectively, as marked in (a). The scale bar and applied field direction are same for all the images and shown in (b).
- 4.7 Relaxation behavior measured at $H_M = 0.99H_C$ (red circle), $0.97H_C$ (blue circle), and $0.95H_C$ (green circle) for samples S4-TF (a) and S4-TA (b). The solid lines represent the best fits with compressed exponential function.
- 5.1 (a) XRD pattern for samples S5-TF (red line), S6-TF (blue line), and S7-TF (green line) showing the CFMS, Cr, and MgO peaks. The peaks denoted by * appearing around 38° arise from the (200) diffraction of the MgO substrate with Cu-K $_{\beta}$ sources. (b) Variation of normalized CFMS (400) peak [i.e. I(400)] and ratio of CFMS (200), CFMS (400) intensity peaks as a function of thickness (t) of the CFMS layers. (c) and (d) RHEED images for sample S7-TF along CFMS [100] and CFMS [110] directions.
- 5.2 (a) M-H curve for samples S5-TF (red line), S6-TF (blue line), and S7-TF (green line) measured by VSM at room temperature along the EA i.e. MgO [100] || CFMS [110] direction. (b) Variation in coercivity (H_C) (purple curve) and relative magnetization (M_R/M_S) (orange curve) as a function of the thickness of the CFMS layers.
- 5.3 (a) Angular (ϕ) dependence of coercivity plot for sample S7-TF measured using micro-MOKE in longitudinal mode. (b) Angular dependence of resonance field (H_R) plot for sample S7-TF extracted from the FMR measurements. The black dots represent the experimental data points whereas the red line represents the best fit using Kittel equation with two anisotropy model.

- 5.4 Domain images in sample S7-TF measured by Kerr microscope for different $\phi = 0^\circ$ (a), 40° (b), 75° (c), and 80° (d), marked by numbers 1 – 4, 5 – 8, 9 – 12, and 13 – 16, respectively. The applied field values for the different images are marked in the respective images. Scale bar for all the images are equal and is shown in 1. The green arrows marked in the images depict the net magnetization direction within a particular domain contrast in the sample.
- 5.5 SEM images of (a – d) circular (sample S7-CA), square (sample S7-SA), triangular (sample S7-TA), and diamond antidots (sample S7-DA), respectively. The scale bar for all the images are same and is shown in (a).
- 5.6 Hysteresis loops measured using micro-MOKE at room temperature for (a – d) samples S7-CA (circular antidot), S7-SA (square antidot), S7-TA (triangular antidot), and S7-DA (diamond antidot), respectively. The insets show the corresponding SEM images.
- 5.7 (a) SEM image of sample S7-CA (circular antidot). (b – f) show the domain images measured at magnetic field pulses of -40.56 , 5.07 , 8.11 , 9.13 , and 40.56 mT, respectively, in sample S7-CA using XPEEM. (g) SEM image of sample S7-TA (triangular antidot). (h – l) show the domain images in sample S7-TA at field pulses of -40.56 , 4.26 , 4.46 , 5.07 , and 40.56 mT, respectively. The scale bar for the XPEEM images are same and shown in (b) and (h). The field has been applied along the EA (CFMS $[1\bar{1}0]$) and the direction is shown in (l).
- 5.8 Experimentally observed time resolved Kerr rotation data (a) and corresponding FFT spectra (b) for the continuous thin film sample S7-TF at $\mu_0H = 153$ mT. Similarly, (c) and (d) show the OOMMF simulated Kerr rotation and the corresponding FFT spectra, respectively, at the same applied field. (e) shows the extracted precessional frequency as a function of the external field for both experiment (red dots) and simulation (blue squares).
- 5.9 (a – d) Spin wave spectra obtained at $\mu_0H = 153$ mT from the experimental time-resolved Kerr rotation data for samples S7-CA (circular antidot), S7-SA (square antidot), S7-TA (triangular antidot), and S7-DA (diamond antidot), respectively. (e – h) Simulated spin wave spectra for samples S7-CA, S7-SA, S7-TA, and S7-DA, respectively. The numbers corresponding to different modes are shown in the individual images. The images in the insets of (a – d) and (e – h) show the shape of a single hole in the antidot array obtained from SEM images and bitmap images considered in the simulation, respectively.
- 5.10 Simulated power maps for different precessional modes as shown in fig. 5.9 (e – h) for circular, square, triangular, and diamond antidots (samples S7-CA, S7-SA, S7-TA, and S7-DA), respectively. The colormap for the power distribution is shown at the right top of the image. Respective mode numbers as per fig. 5.9 is shown in the right side of the image. Magnetic field $\mu_0H = 153$ mT is applied along the EA (MgO $[010] \parallel$ CFMS $[1\bar{1}0]$).

- 5.11 Simulated phase maps for different precessional modes as shown in fig. 5.9 (e – h) for circular, square, triangular, and diamond antidots (samples S7-CA, S7-SA, S7-TA, and S7-DA), respectively. The colormap for the phase distribution is shown at the right top of the image. The respective mode numbers as per fig. 5.9 is shown in the right side of the image.
- 6.1 Hysteresis loops measured by the SQUID magnetometer for samples S8-TF-A – S8-TF-I shown in (a – i), respectively. The magnetic field has been applied along the MgO [001] and MgO [1 $\bar{1}$ 0] directions represented by blue circles and red squares, respectively. The inset images in (a – i) show the zoomed-in views of the loops near the reversal.
- 6.2 Deposition temperature dependence of (a) coercivity (H_C), (b) saturation field (H_S), (c) magnetic anisotropy energy (K_{in}), for the FePt films with various thicknesses.
- 6.3 (a) Hysteresis loop measured by Kerr microscope in longitudinal mode along EA for sample S8-TF-F ($t_{FePt} = 20$ nm, $T_{dep} = 400^\circ\text{C}$). (b – f) show the domain images captured at various positions of the hysteresis loop marked by point 1–5 in (a), respectively.
- 6.4 Domain images along EA at H_N (a – c) and at H_C (d – f) for samples S8-TF-D – S8-TF-F, respectively.
- 6.5 Domain images along EA (a – c) at H_N and (d – f) at H_C for samples S8-TF-C, S8-TF-F, and S8-TF-I, respectively.
- 6.6 Deposition temperature dependence of $\mu_0 H_C / K_{in}$ for all the films prepared with varying t_{FePt} .
- 6.7 The masks used in OOMMF simulation for the triangular antidot sample S9-SS-TA with (a) no defect, (b) defects at each vertices of the triangles, (c) defects at two vertices sharing the base of the triangles. The defects are marked in red color and encircled by yellow circles for a few defects.
- 6.8 (a – l) Evolution of domains in sample S9-SS-TA under application of varying magnetic field. The applied field direction and scale bar is shown in (a). The mask used in this simulation is depicted in fig. 6.7 (a).
- 6.9 (a – l) Evolution of domains in sample S9-SS-TA under application of varying magnetic field. The applied field direction and scale bar is shown in (a). The mask used in this simulation is depicted in fig. 6.7 (b).
- 6.10 (a – l) Evolution of domains in sample S9-SS-TA under application of varying magnetic field. The applied field direction and scale bar is shown in (a). The mask used in this simulation is depicted in fig. 6.7 (c).
- 6.11 (a – l) Evolution of domains in sample S9-SS-SA under application of varying magnetic field. The applied field direction and scale bar is shown in (a). In the sample mask, the defects are present in all four vertices of the square holes.

- 6.12 (a – l) Evolution of domains in sample S9-SS-DA under application of varying magnetic field. The applied field direction and scale bar is shown in (a). In the sample mask, the defects are present in all four vertices of the diamond shaped holes.
- 7.1 XRD patterns of samples S10A–S10E annealed at different temperatures represented by black, red, blue, pink, and green curves, respectively.
- 7.2 (a) Hysteresis loops for samples S10A–S10E, represented by brown, green, pink, blue, and red curves, respectively. (b) H_C vs T_a plot for all the samples extracted from (a). The inset in (b) shows the zoomed-in image of the plot represented by the dotted orange area.
- 7.3 Domain images recorded at various magnetic fields corresponding to different points of the hysteresis loops for S10A (a – e), S10B (f – j), S10C (k – o), S10D (p – t), and S10E (u – y), respectively. The scale bar and applied field direction for all the images are same and is shown in (a). See main text for the detailed values of the magnetic field for these images.
- 7.4 (a – c) Domain structure for sample S10A at remanence measured at time (t) = 0, 6, and 11 s after applying an AC field of $\mu_0 H_{AC} = 1$ mT and $f_{AC} = 20$ Hz.
- 7.5 (a – p) Domain structure for sample S10D at remanence measured at $t = 0$ to 7.5 s after applying an AC field of $\mu_0 H_{AC} = 1$ mT and $f_{AC} = 20$ Hz.

LIST OF TABLES

- 3.1 Sample structure of in-plane magnetized Co thin films on Au and AlO_x seed layers
- 3.2 Sample structure of in-plane magnetized thin film and MAL arrays of Co
- 3.3 Structural details of the in-plane magnetized antidot arrays
- 3.4 A comparison of domain width and coercivity for different antidots
- 4.1 Details of experimental and simulated samples of Co/Pt with PMA
- 5.1 Details of the thin film and antidot samples of Heusler alloy
- 6.1 Details of FePt thin film samples with in-plane anisotropy
- 6.2 List of the simulated antidot samples of FePt with perpendicular anisotropy
- 7.1 Details of prepared nanocrystalline ribbon samples

CHAPTER 1: Introduction and Fundamentals

1.1. Introduction:

Magnetism at nanoscale is remarkably different from its bulk counterparts due to quantum size effect, and high surface to volume ratio [34,35]. Further, the static and dynamic nature of magnetization in nanostructures are quite different in comparison to their parent thin films due to their reduced dimension even in lateral direction. Such nanomagnets are of prime research interest in various spintronics applications. Patterned magnetic nanostructure has recently drawn significant research interest due to their unique advantage of precisely controlled geometry and dimensionality of the individual nano-elements [2,36]. Such nanostructures are broadly subdivided into two parts: magnetic dot and antidot lattice arrays. Magnetic dot arrays are periodic arrangement of well-defined magnetic elements distributed over a plane substrate. The ever increasing necessity of high density data storage technology demands reduction of the size of a single magnetic dot. However, lowering the dimension of the individual dots below a critical value precludes the domain wall (DW) formation. In such single domain magnetic nanodots the magnetization becomes unstable due to the thermal fluctuation (a phenomenon known as superparamagnetism) [4,37]. Hence, the size of a single magnetic dot cannot be reduced beyond a certain value, which is a drawback for storage applications. One way to ensure thermal stability at ultralow dimension is by using magnetic materials with very high anisotropy. The $L1_0$ ordered FePt, CoPt, FePd, MnAl based alloys exhibit large uniaxial anisotropy energy [38-41]. However, there are very few material which poses such remarkable large anisotropy. Further, achieving such $L1_0$ ordered structures demands high crystalline growth and involves rigorous deposition techniques.

Magnetic antidot lattice (MAL) arrays provides another simple and convenient path of avoiding this superparamagnetic blockade. MALs are periodic arrangement of holes in a continuous thin film. A schematic diagram of an antidot lattice array is shown in fig. 1.1. The white circles

represents the non-magnetic periodic holes arranged on the continuous magnetic thin film (dark grey area). Such systems are essentially exchange coupled (similar to a thin ferromagnetic film). Hence, the size of the holes can be reduced to any desired value without the concern of thermal fluctuations. Further, the holes present in the antidot arrays work as the nucleation and pinning centers for the domains. The domains nucleate from the edge of the holes and propagate in a zigzag path under the influence of external magnetic field. Therefore the magnetization reversal mechanism in such MAL arrays is better controlled compared to their parent thin films where the defects are random. In addition, the DWs can be confined in between the holes and their motion can be tuned by varying the antidot architecture. Further, MAL arrays provides the opportunity of tuning the global anisotropy of the system. The major source of anisotropy in a continuous ferromagnetic thin film is the magnetocrystalline one which arises from the spin-orbit coupling. However, the lattice symmetry and geometry of the antidots introduces an additional shape anisotropy. The shape induced anisotropy may become dominant over other anisotropy contributions depending on the size, shape, and inter-separation of the holes in the MAL arrays. The shape anisotropy can be controlled by varying the geometry and symmetry of the antidots which enables precise control of the magnetic switching and engineering of the domain structure.

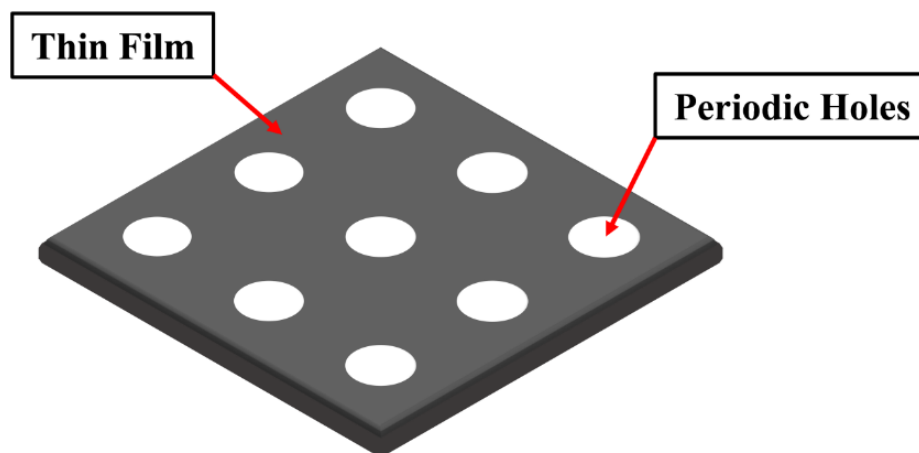


Figure 1.1: Schematic diagram of MAL array showing arrangement of the periodic holes (white circles) on the continuous thin film (dark grey area).

Due to such advantages MALs are receiving intense research interest in modern data storage applications as well as from fundamental research point of view. Domain formation in lithography patterned MAL arrays was investigated in 1997 by Cowburn *et al.* [3]. Since then there has been several reports on controlling the anisotropy, magnetization reversal and domain structure in antidot arrays by varying the shape, size, and distribution of the periodic holes [42-65]. Many other aspects related to MAL arrays viz. magnetotransport effects [66,67], dipolar induced spatially localized resonance [68], ferromagnetic resonance [69-71], geometric coercivity scaling [72-74], magnetoresistance [75-77], etc. have also been explored. Recently, a few work have focused on tuning the magnetization reversal vis-à-vis lattice symmetry and dimension in out-of-plane magnetized MAL arrays [78-87]. However, the presence of holes in the path of propagation slows down the DW velocity in the antidot arrays in comparison to its thin film counterparts [13,16]. This is not desired in storage applications where rapid reversal of spins is required for reading and writing information [17]. In this thesis we have discussed how the speed of magnetic relaxation can be enhanced by varying the deposition condition in the antidot arrays with in-plane anisotropy [12,13]. Further, the possibility of achieving faster relaxation in the out-of-plane magnetized antidot arrays compared to its parent thin film has been discussed [21].

Another important aspect of MAL arrays is its potential in confinement and tunability of spin waves (SW) as magnonic crystals. SW has several potential applications in novel wave based computing, telecommunications system, room temperature transport of spin information without Joule heating, etc. [88]. Patterned magnetic nanostructures (dot and antidot arrays) can be used to confine the SWs when the periodicity of the lattice is comparable to the wavelength of light [89]. MALs are preferred over dot arrays as magnonic crystals due to their larger propagation velocity or steeper dispersion [90,91]. The edges of the periodic holes in the antidots quantizes the SW modes by modulating the internal field profiles. Over the last decade,

many work have been reported on the control of spin wave dynamics in antidot arrays by varying the antidot architecture [7,90-101]. In this thesis we have discussed that by controlling both the magnetocrystalline as well as the shape anisotropies, the SW magnonic band gaps can be tuned.

In order to elucidate the effect of the periodic holes in the system, we have first investigated the parent continuous thin films. Based on the above discussion, we have tried to address the following open issues in this field:

- Quantification of domain size and anisotropy with the availability of the active magnetic area in antidot arrays with various shapes and sizes of the holes
- Possibility of achieving faster relaxation in the MAL arrays in comparison to its parent continuous thin film counterparts
- Determine the role of localized defects in the vicinity of the holes to control the nature of domain formation and magnetization reversal in MAL arrays
- Tuning the spin wave spectra in antidot arrays by modifying the intrinsic magnetocrystalline and induced shape anisotropies of such systems

The thesis is organized as the following:

In **Chapter 1**, the basic concepts of ferromagnetism and theoretical background related to the work has been presented. **Chapter 2** reviews all the experimental techniques that have been used for the preparation and characterization of the samples discussed in this work. In **Chapter 3**, we have discussed the domain engineering and magnetization relaxation mechanism in MAL arrays of Co thin films with in-plane anisotropy. We have discussed the nature of domain formation and relaxation mechanism in out-of-plane magnetized antidot arrays of Co/Pt in **Chapter 4**. The experimental observations have been reproduced and extended to nano-dimension using micromagnetic simulations. Here, we have further explored the possibility of achieving faster relaxation in such antidot arrays of Co in comparison to its thin film

counterparts. The feasibility of tuning the SW spectra in antidot arrays of half-metallic Heusler alloy thin films has been presented in **Chapter 5**. We report that the combined effect of shape (arising from the antidot architecture) and intrinsic magnetocrystalline anisotropies govern the domain structure and SW dynamics in such systems. We have shown in **Chapter 6** that the domain structure in $L1_0$ ordered FePt thin film depends on both thickness of the films as well as on the deposition temperature. We further report that, the domain structure in MAL arrays of out-of-plane magnetized FePt changes from typical bubble domains of perpendicular media to stripe like domains by inclusion of defects at the vicinity of the edges of the antidots. We have observed remarkable difference in the domain formation by varying the position of the defects. In **Chapter 7**, a short part of this thesis has been devoted towards the study of response of the DWs under AC and DC fields in soft magnetic ribbons. We have discussed that the static and dynamic response of the DWs can be controlled by modifying the anisotropy in such nanocrystalline ribbons. The summary, future scopes, and prospects of the works presented in this thesis have been discussed in **Chapter 8**. In the following we describe the basic theory and concepts of the results discussed in this thesis.

1.2. Magnetic interactions:

Magnetic interactions in a material are responsible for the overall ferromagnetic ordering of the system. The basic interaction occurring between two single magnetic entities (dipoles) is known as the dipole-dipole interaction. However, the strength of the dipole-dipole interaction is too small to cause ferromagnetism. The magnetic ordering in a ferromagnetic material is governed by the exchange interaction which is a pure quantum mechanical effect and is a manifestation of the Coulomb interaction and Pauli Exclusion Principle. Depending on the distance between the magnetic moments, exchange interaction can be broadly subdivided into direct and indirect exchange. In a situation where the electrons of the neighboring spins directly interacts with each other without the presence of any intermediate atom, is known as direct

exchange. Similarly, if the overlap between the wave functions of the neighboring electrons is small, the interaction is mediated by another atom/ion, and hence the interaction type is known as indirect exchange. Another important contribution of magnetic interaction in a ferromagnetic system arises from the spin-orbit (SO) coupling between the spin and orbital angular momentum of the system. The strength of the SO interaction is about 10-100 times lesser than that of the exchange interaction. However, they play a crucial role in determining the anisotropy of the magnetic system.

1.3. Magnetic anisotropy:

Anisotropy is an important parameter for ferromagnetic systems. The Heisenberg Hamiltonian for a magnetic system is isotropic in nature and in the absence of any other energy term will lead to vanishing magnetization under zero applied field. However, in reality magnetic materials are not isotropic. The total energy of the system depends on both the magnitude as well as the direction of the magnetization. In a real magnetic material, the moments cannot be rotated along any direction by application of infinitesimal energy. Requirement of the additional energy to rotate the moments arises from the anisotropy energy which is a measure of the dependence of internal energy on the direction of spontaneous magnetization. Magnetic anisotropy gives rise to preferential and non-preferential directions of magnetization known as the easy axis (EA) and hard axis (HA), respectively. The energy difference between EA and HA arises from two microscopic phenomenon: spin-orbit interaction and long-range dipolar interaction. Magnetic anisotropy are majorly classified in four types: magnetocrystalline, shape, surface, and strain (magnetostriction) anisotropies. The SO interaction is responsible for magnetocrystalline, surface, and strain induced anisotropies whereas the dipolar interaction gives rise to the shape anisotropy. The strength of the anisotropy in a magnetic system lies in the range of 10^2 – 10^7 J/m³. In bulk ferromagnetic materials magnetocrystalline and magnetoelastic anisotropy dominates. However, in thin ferromagnetic films and

nanostructures, the effect of shape and surface anisotropies also play relevant roles along with the magnetocrystalline one. In the subsequent section, we describe the origin and nature of different anisotropies in detail.

1.3.1. Magnetocrystalline anisotropy:

The most important contribution of anisotropy in a magnetic system arises from the magnetocrystalline anisotropy which is a manifestation of SO interaction of the electrons. The electron orbitals inside a material are linked with specific crystallographic axes. Interaction between the orbitals and the spins of the electrons tend to align the spins along these crystallographic axes. It should be noted that the strength of the energy associated with magnetocrystalline anisotropy is usually less in comparison to the exchange energy. However, it plays the governing role in determining the spontaneous magnetization directions since the exchange coupling tries to align the spins parallel or anti-parallel to each other irrespective of their direction. The strength of the spin-orbit interaction is evaluated phenomenologically by power series expansion of the energy with the consideration of the crystal symmetry. The magnetization direction ($\mathbf{m} = \frac{\mathbf{M}}{|\mathbf{M}|}$) relative to the coordinate axes in Cartesian system can be expressed as the following (\mathbf{M} being the magnetization of the system):

$$m_x = \sin\theta\cos\phi, m_y = \sin\theta\sin\phi, m_z = \cos\theta \quad (1.1)$$

Fig. 1.2 shows the components of magnetization with respect to the crystalline axes.

Components of magnetization along the coordinate axes satisfy the relation: $m_x^2 + m_y^2 + m_z^2 = 1$.

The magnetocrystalline energy per unit volume can be represented as power series of the component of magnetization (b being the coefficient of anisotropy energy) [102]:

$$E_{crystal} = E_a + \sum_i b_i m_i + \sum_{ij} b_{ij} m_i m_j + \sum_{ijk} b_{ijk} m_i m_j m_k + \sum_{ijkl} b_{ijkl} m_i m_j m_k m_l + T(m^5) \quad (1.2)$$

The terms from and above $T(m^5)$ are small and hence neglected. The energy associated to the

oppositely magnetized states are equal in magnitude and $E(m_i) = E(-m_i)$. Hence, all odd terms of m_i in the power series will cancel out with each other. Hence, eq. 1.2 reduces to:

$$E_{crystal} = E_a + \sum_{ij} b_{ij} m_i m_j + \sum_{ijkl} b_{ijkl} m_i m_j m_k m_l \quad (1.3)$$

Magnetocrystalline anisotropy in a ferromagnetic system can be broadly subdivided into several parts depending on the crystallographic orientation viz. uniaxial anisotropy, cubic anisotropy, six-fold anisotropy (hexagonal system), etc. However, the major types of anisotropies considered in this thesis are uniaxial and cubic in nature.

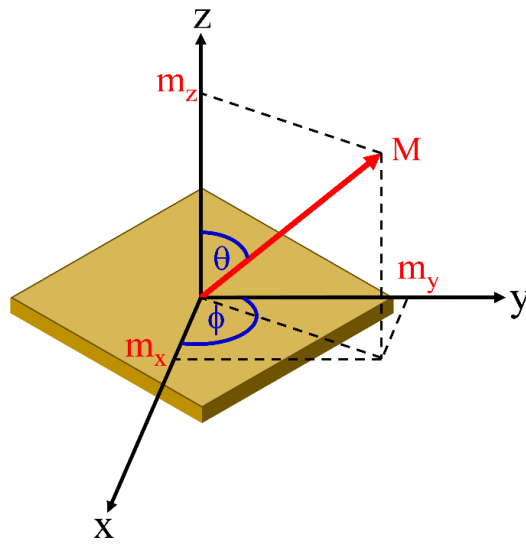


Figure 1.2: Orientation of magnetization with respect to the direction cosine.

1.3.1.1. Uniaxial anisotropy: Since $E(m_i) = E(-m_i)$, all the cross terms of $m_i m_j$ will cancel out, i.e. $b_{ij} = 0$ for $i \neq j$. For a sample with uniaxial symmetry, let us assume that the easy axis lies along the z axis. Hence the anisotropy energy can be expressed as [102]:

$$E_{crystal} = K_a + b_{xx} m_x^2 + b_{yy} m_y^2 = K_a + b_{xx} (m_x^2 + m_y^2), \text{ since } b_{xx} = b_{yy}.$$

Hence, for uniaxial anisotropy, the associated energy per unit volume can be represented as $E_{crystal} = b_{xx} \sin^2 \theta$, where b_{xx} is the uniaxial/two-fold anisotropy constant. The strength of the uniaxial anisotropy (constant) has been denoted by K_2 in this thesis due to its two-fold symmetry.

1.3.1.2. Cubic anisotropy: For a system with cubic anisotropy the indices $i = 1, 2, 3$, are

undistinguishable, hence $b_{xx} = b_{yy} = b_{zz}$. The second term of eq. 1.8 can be expressed as:

$\sum_{ij} b_{ij} m_i m_j = b_{xx} (m_x^2 + m_y^2 + m_z^2) = b_{xx}$. Similarly, the third term can be expressed as:

$$\sum_{ijkl} b_{ijkl} m_i m_j m_k m_l = b_{xxxx} (m_x^4 + m_y^4 + m_z^4) + 6b_{xxyy} (m_x^2 m_y^2 + m_x^2 m_z^2 + m_y^2 m_z^2)$$

Eq. 1.3 can be rewritten as (by considering terms up to sixth order) [102]:

$$\begin{aligned} E_{crystal}^{cubic} &= E_a + b_{xx} + b_{xxxx} (m_x^4 + m_y^4 + m_z^4) + 6b_{xxyy} (m_x^2 m_y^2 + m_x^2 m_z^2 + m_y^2 m_z^2) + \\ &b_{xxxxxx} (m_x^6 + m_y^6 + m_z^6) + 90b_{xxyyzz} m_x^2 m_y^2 m_z^2 + 15b_{xxxxyy} (m_x^2 m_y^4 + m_x^4 m_y^2 + m_x^2 m_z^4 + \\ &m_x^4 m_z^2 + m_y^2 m_z^4 + m_y^4 m_z^2) \\ \Rightarrow E_{crystal}^{cubic} &= K'_a + K_b (m_x^2 m_y^2 + m_x^2 m_z^2 + m_y^2 m_z^2) + K_c m_x^2 m_y^2 m_z^2 + \dots \end{aligned} \quad (1.4)$$

Energy associated to [100] ($m_x = 1, m_y = m_z = 0$) is given by: $E_{100} = K'_a$

Energy associated to [110] ($m_x = m_y = \frac{1}{\sqrt{2}}, m_z = 0$) is given by: $E_{110} = K'_a + \frac{1}{4} K_b$.

Energy associated to [111] ($m_x = m_y = m_z = \frac{1}{\sqrt{3}}$) is given by: $E_{110} = K'_a + \frac{1}{3} K_b + \frac{1}{27} K_c$.

Now assuming, $K_b, K_c > 0$, [100] is the easy direction whereas [111] is the hard direction. If the anisotropy is distributed purely over in-plane (xy-plane) so that there is no component of magnetization along the z-axis, then [100] is the easy direction whereas [110] is the hard direction. Similarly, [010] will also lead to another easy direction since $E_{100} = E_{010}$. The strength of the cubic anisotropy has been denoted as K_4 in this thesis due to its four-fold symmetry.

1.3.2. Shape anisotropy:

Another important source of anisotropy arises from the shape of the ferromagnetic sample. It is understood that the demagnetizing field is uniform along all possible direction for a spherical particle or dot. However, if the sample is non-spherical, then it is easier to magnetize it along one or multiple specific directions depending on its shape. Since the demagnetizing field along the long axis is lower than that compared to the short axis, the easy direction lies along the long

axis of the material. This occurs because the induced poles in the surface of the samples are further apart along the long axis of the sample. The stray field energy of a sample is given by [102]: $E_{demag} = -\frac{1}{2} \int \mu_0 \mathbf{M} \cdot \mathbf{H}_{demag} dV$, where \mathbf{H}_{demag} represents the demagnetizing field inside the sample. The following derivation of the shape anisotropy has been performed for an ellipsoid due to simplicity of the calculation. In an ellipsoid $\mathbf{H}_{demag} = -N\mathbf{M}$, where N is the demagnetization tensor. Hence the stray field energy leads to $E_{demag} = \frac{\mu_0 V}{2} \mathbf{M} \cdot N\mathbf{M}$. N is a diagonal tensor if the semiaxes of the ellipsoid represent the axes of the coordinate system. The tensor N (trace $N = 1$) is given by:

$$N = \begin{pmatrix} N_x & 0 & 0 \\ 0 & N_y & 0 \\ 0 & 0 & N_z \end{pmatrix}$$

The stray field energy related to the shape anisotropy can be rewritten as [103,104]:

$$E_{demag}^{shape} = \frac{1}{2} \mu_0 V (N_x m_x^2 + N_y m_y^2 + N_z m_z^2) \quad (1.5)$$

For an ellipsoid of revolution ($N_x = N_y$ along the equatorial axis), eq. 1.5 reduces to:

$$E_{demag}^{shape} = \frac{1}{2} \mu_0 V M_S^2 (N_x \sin^2 \theta + N_z \cos^2 \theta) \quad (1.6)$$

Eq. 1.6 can be expressed as:

$$E_{demag}^{shape} = \frac{1}{2} \mu_0 V M_S^2 (N_x - N_z) \sin^2 \theta = KV \sin^2 \theta \quad (1.7)$$

where, $K = \frac{1}{2} \mu_0 M_S^2 (N_x - N_z)$ represent the strength of the shape anisotropy of the system. For prolate ellipsoid, $K > 0$ and the effective anisotropy is easy axis type (with the easy axis lying in $\pm z$ axis). Similarly, for oblate ellipsoid, $K < 0$ and the effective anisotropy is easy plane type (x-y plane).

Shape anisotropy in arrays of magnetic dot or antidot structure depends on the lattice symmetry of the systems. The anisotropy in such arrays is determined by the nearest neighbor interaction between the constituent magnetic elements. For example, the shape anisotropy of square,

honeycomb, and octagonal arrangements of the antidots are of four, six, and eight folds, respectively [2,50]. It should be noted that the shape anisotropy becomes important in case of magnetic nanostructures. For the nano-dimensional MAL arrays discussed in this thesis, shape anisotropy plays a crucial role in determining the total anisotropy of the system. However, for the micro-dimensional MAL arrays, the contribution of shape anisotropy is significantly lower than the intrinsic magnetocrystalline anisotropy and hence the effect is suppressed.

1.3.3. Surface anisotropy:

In ferromagnetic thin film systems, the surface contribution turns significant due to broken symmetry at the interfaces. Lower order energy terms which are forbidden in thick 3D systems are allowed in such thin 2D thin films. Hence, in ultrathin magnetic systems, the surface contribution of anisotropy dominates over the conventional bulk (volume) one. The effective anisotropy of such a system can be divided into two parts (volume and surface contribution):

$$K_{eff} = K_V + 2K_S/t \quad (1.8)$$

where, K_V and K_S are the volume and surface dependent magnetocrystalline anisotropy constants, respectively. t is the thickness of the ferromagnetic system. The factor of 2 in the second term in eq. 1.8 arises because of presence of two surfaces in the film. It should be noted that, the second term becomes relevant only for the low values of t . Rewriting, eq. 1.8 by multiplying both sides with t ,

$$tK_{eff} = tK_V + 2K_S \quad (1.9)$$

At critical thickness of $t = t_c$, the surface and volume contributions become equal, where $t_c = -2K_S/K_V$. When $t > t_c$, the system exhibits in-plane magnetization whereas at $t < t_c$, the system exhibits magnetization perpendicular to the film plane. This is known as the ‘spin reorientation transition’ [105]. Hence, the volume contribution of anisotropy dominates in thick films leading to in-plane magnetization. However, the surface contribution increases with decreasing thickness of the ferromagnetic layer leading to spin reorientation transition aiding

perpendicular anisotropy.

1.3.4. Magnetoelastic anisotropy (Stress anisotropy):

The calculation of anisotropy discussed so far has been considered in a rigid solid sample with fixed lattice constant. If one introduces elasticity as an additional degree of freedom, the displacements between the atoms leads to change in behavior in magnetic crystals. This is in principle opposite to the phenomenon of magnetostriction where the sample dimension changes due to modification in the magnetization. Magnetoelastic or stress anisotropy can be induced in magnetic system via different methods, viz. stress produced in the films during deposition, difference in thermal expansion coefficients of the constituent layers, mismatch of lattice parameters between the substrate and films, etc. [106]. For a uniaxial system, the net volume Magnetoelastic energy is given by [107]:

$$E_{strain} = -\frac{3}{2}\sigma\lambda_s\cos^2\vartheta \quad (1.10)$$

where, λ_s is isotropic magnetostriction coefficient, σ is the strain value by surface unit and ϑ is the angle between magnetization and strain tensor axis. Magnetoelastic anisotropy plays a major role in determining the overall anisotropy and magnetization switching mechanism in the soft magnetic nanocrystalline ribbons [33] discussed in chapter 7 of this thesis.

1.4. Zeeman energy:

In the absence of any external magnetic field, exchange (E_{exch}), demagnetizing (E_{demag}), and anisotropy energy (E_{ani}) comprises the total magnetic energy of the system [108]. However, in the presence of an external field (\mathbf{H}_{ext}), the energy arising from the interaction between the magnetization (\mathbf{M}) and \mathbf{H}_{ext} , is given by:

$$E_{Zeeman} = -\mu_0 \int \mathbf{M} \cdot \mathbf{H}_{ext} dV \quad (1.11)$$

It is understood from eq. 1.11 that E_{Zeeman} is minimum when the magnetization of the sample is aligned with the applied field. It should be noted that this energy is independent of the shape and structure of the sample. However, the strength of E_{Zeeman} strongly depends on the

magnetization of the system. Hence, in presence of the magnetic field the total energy of a magnetic system can be defined as:

$$E_{tot} = E_{exch} + E_{demag} + E_{ani} + E_{Zeeman} \quad (1.12)$$

1.5. Magnetic domains and domain walls:

Macroscopic properties of magnetic systems are described in-terms of magnetic microstructures. In 1907, P. Weiss postulated that there are several small regions ('magnetic domains') inside a magnetic material inside which all the spins are oriented along one particular direction [109]. However, it should be noted that the magnetization direction for all the individual domains are not necessarily parallel to the EA of the material. In the absence of any magnetic field, the domains with different spontaneous magnetization direction align themselves to yield the lowest energy configuration (zero magnetization state). The individual domains are separated by finite boundaries which are known as 'domain walls' (DWs).

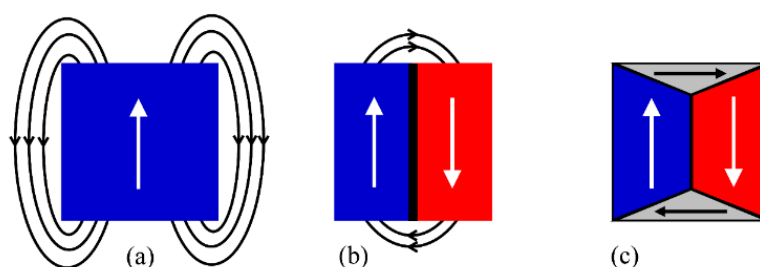


Figure 1.3: Schematic representation showing reduction of the magnetic stray field energy leading to domain formation.

If magnetic anisotropy energy solely determines the direction of magnetization in a material, then all the spins inside the sample will tend to align themselves towards the easy direction leading to a single domain state. The exchange energy of the system is minimum when all the spins are either parallel or anti-parallel to each other. However, depending on the shape of the material, orientation of all spins along a specific direction will lead to generation of demagnetizing energy in the sample (fig. 1.3 (a)). In order to decrease this stray field energy of the system, the magnetization will split into multiple domains separated by DWs (fig. 1.3

(b), (c)). It should be noted that a finite energy is required for the formation of DWs. Hence, a competition between the stray field and DW formation energy determines the ground state microstructure of the system. Landau and Lifshitz suggested that the stray field energy of a system can be reduced to zero by flux enclosure type domain (fig. 1.3 (c)) [110].

Domain wall (DW) is a region/boundary with finite thickness which separates two neighboring domains with different spontaneous magnetization directions. The idea of existence of DWs was first proposed by Sixtus and Tonks [111]. Inside a DW, the direction of the magnetic moments change continuously to maintain the energy minimization. The exchange energy between two neighboring moments (at an angle ϵ with respect to each other) is given by:

$$E_{exch} = -2JS_1 \cdot S_2 = -2JS^2 \cos\epsilon$$

Considering $\epsilon = \pi$, the energy required to flip one spin is $2JS^2$. Now extending this for an ensemble of spins, the total exchange energy distributed among each pair spins over N lattice spacing is given by [102] :

$$\Delta E_{exch}^{total} = E_{exch} - E_{exch}^{\epsilon=0} = -N \cdot JS^2 \left(\cos \frac{\epsilon}{N} - 1 \right) = -N \cdot JS^2 \left(1 - \frac{\epsilon^2}{N^2} - 1 \right) = \frac{JS^2 \pi^2}{N}$$

If the lattice constant for the magnetic material is a , then the number of spin rotation inside a Bloch wall (defined subsequently) is $1/a^2$, which leads to reduction of the exchange energy to:

$$E_{exch}^{Bloch} = \frac{JS^2 \pi^2}{Na^2} \quad (1.13)$$

From eq. 1.13, it is seen that the exchange energy of the walls decreases with increasing N . This in turn leads to gradual rotation of the spins inside the DW leading to increasing width of the wall. However, this increases the anisotropy energy of the system which tends to align the spins along the EA. The anisotropy energy inside a Bloch wall is represented as [102]:

$$E_{ani}^{Bloch} = \sum_{i=1}^N K \sin^2 \epsilon_i \cong \frac{NKa}{2} \quad (1.14)$$

A competition between the anisotropy and exchange energy (shown in eq. 1.13 and 1.14) leads to stabilization of the width of the DW.

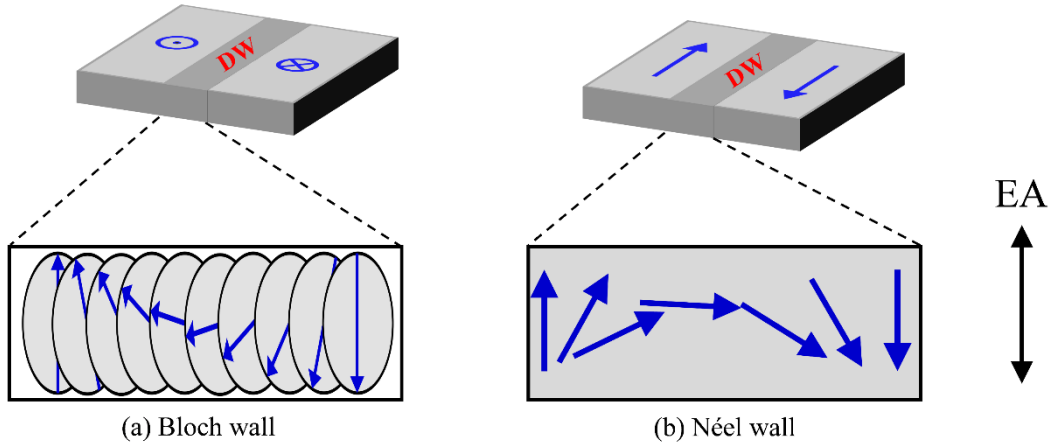


Figure 1.4: Schematic representation of (a) Bloch wall and (b) Néel wall with the out-of-plane and in-plane spin rotations, respectively. The magnetization direction in perpendicular and in-plane orientation is depicted in (a) and (b), respectively.

The two important types of magnetic DWs are depicted in fig. 1.4 (a) and (b). In both cases the spins of two oppositely oriented magnetizations are separated by a transition region as shown by DW. In a Bloch wall [112] (fig. 1.4 (a)) the spin rotation inside the DW occurs in out-of-plane direction (i.e. moments inside the wall oriented parallel to the wall). Inside a Bloch wall the total magnetic charge is zero due to normal components of magnetization in both side of the wall being same. However, magnetic charges will accumulate on the surface leading to strong demagnetizing field across the sample surface. Hence, the Bloch walls are usually obtained in ferromagnetic thick films/bulk materials. However, formation of the Bloch walls becomes energetically unfavored in ultrathin films where the thickness of the film becomes comparable to the width of the wall. In such cases Néel wall [113] (fig. 1.4 (b)) is formed where the spin rotates in the in-plane direction (i.e. the magnetization inside the wall rotates perpendicular to the wall). Here the demagnetization energy caused by the surface magnetic charges is less in comparison to that in the Bloch walls [114]. Width of the Bloch and Néel walls are represented as:

$$\delta_{Bloch} = \pi \sqrt{A/K}, \text{ and } \delta_{Néel} = \pi \sqrt{\frac{2A}{\mu_0 M_s^2}}, \text{ where } A = \frac{2JS^2}{a}.$$

Further, depending on the orientation of magnetization between two neighboring domains, the DWs described in this thesis can be broadly classified into two parts: 90° and 180° DWs.

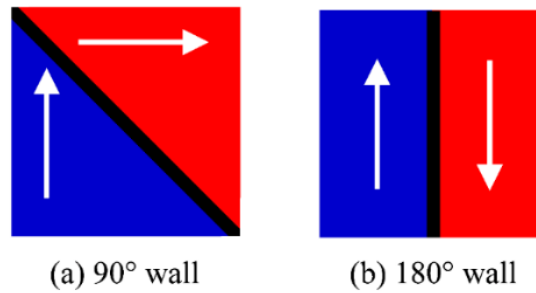


Figure 1.5: Schematic representation of (a) 90°, and (b) 180° DWs. The black line in between the domains represents the DW.

The schematic representation of such DWs is depicted in fig. 1.5 (a) and (b). In systems with cubic anisotropy, 90° DWs (fig. 1.5 (a)) are obtained since the easy direction of magnetizations are 90° away from each other. Hence, under the application of external magnetic field, the magnetization switching happens either via two simultaneous or successive 90° DW motion [115]. Details about such 90° DWs are described in detail in chapter 5 of the thesis. Systems with uniaxial anisotropy usually leads to formation of 180° DW motion (fig. 1.5 (b)) during the magnetization reversal [9,11]. We have obtained 180° DW motion in different thin films and nanostructures governed by uniaxial anisotropy. Apart from the abovementioned two types, there are a few other types of DWs viz. 360°, 109°, 71° walls which are observed in very few materials [116-118].

1.6. Magnetization reversal:

Magnetization reversal (switching) is a phenomenon where the spontaneous magnetization of a ferromagnet switches/reverses from one stable state to another under the presence of an external magnetic field. When an external field is applied a torque ($\boldsymbol{\tau} = \mathbf{M} \times \mathbf{H}$) acts on the spins and the magnetic microstructure changes to minimize the energy of the system. The reversal of the spins can happen majorly via two methods: coherent rotation (all the spins

rotating coherently from one stable state to another) and domain wall motion (aligning of magnetization from one state to another by movement of the DWs). The reversal process depends on the initial distribution of magnetization (the history) in the sample. Further, it should be noted that the reversal phenomenon strongly depends on the speed of reversal field. For example, if magnetic pulses shorter than 10^{-9} s is applied, the precessional motion of magnetization becomes dominant. The following discussion will be based on the assumption that the reversal field is varied quasistatically.

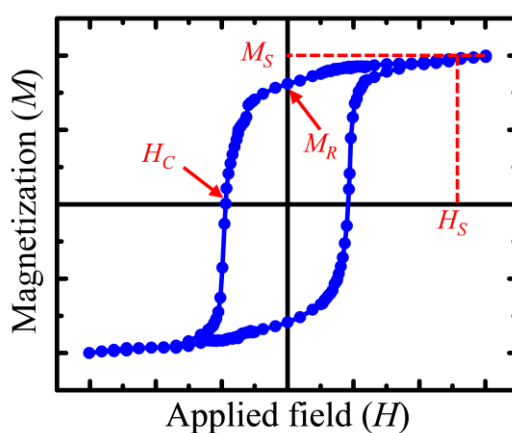


Figure 1.6: Hysteresis loop showing the magnetization (M) vs applied field (H) behavior in a ferromagnet.

The magnetization of a ferromagnetic sample does not follow the change in applied field linearly, giving rise to the hysteresis loop. Hysteresis is a nonlinear, non-equilibrium, complex first order phase transition [119]. Further complexity in the loop arises due to the effect of local microstructure, structural, and morphological defects, etc. in the system [120]. A typical hysteresis loop in a ferromagnetic sample is depicted in fig. 1.6. When a sufficiently large external magnetic field is applied, all the spins inside a system align towards the applied field direction. This state is called magnetic saturation state. Magnetization of the system in this state is called the saturation magnetization (M_S) and the required field is called saturation field (H_S). After saturating the system, if the applied field is reduced to zero, the ferromagnetic sample

still retains a finite magnetization, which is known as the remanent magnetization (M_R). A finite magnetic field in the reverse direction is required to reach a state with zero magnetization, which is known as the coercive field (H_C). The position of M_R , M_S , H_C , and H_S are shown in fig. 1.6. The hardness of a magnetic material is measured by the coercive field of that system. The smaller (larger) shape of the hysteresis loop is a manifestation of smaller (larger) value of H_C which in-turn is the signature of magnetically softer (harder) material. The squareness of the hysteresis loop is defined as $S = \frac{M_R}{M_S}$. In an ideal ferromagnet, S should be 1 and 0 along the EA and HA, respectively. In the following we discuss the mechanism of DW motion and coherent rotation phenomenon.

1.6.1. Domain wall motion:

As discussed previously, in large ferromagnetic particles or thin films, domain formation occurs to reduce the magnetic stray field energy of the system. Domain nucleation can occur from the defects or imperfections present in the system [121]. In such systems, the magnetization reversal takes place via propagation of the DWs, known as DW motion. When magnetic field is applied to a demagnetized sample, the domains nearest to the EA grow in expense of the other domains which are unfavorably aligned. At small applied external field, the DWs can move a small distance and come back to its initial position upon removal of the field. This is known as reversible displacement which corresponds to the initial curved part of the hysteresis loop. In this region the DW remains pinned by the structural defects present in the sample. This expansion of the DWs like elastic membrane is known as the DW relaxation [37]. The reversible bending of the DWs can often become irreversible if the wall is deformed sufficiently under the high applied field or if the DWs get pinned by the defects. At higher fields, the anisotropy can be overcome where the magnetization rotate away from its EA to the next crystallographic easy orientation nearest to the field direction. At further high magnetic field the process is collective rotation of the domains towards the applied field direction,

irrespective of that being the EA or HA of the system. In the steep part of the hysteresis close to the H_C , often the magnetization change in a discontinuous way (yielding small steps) which is known as the Barkhausen effect. The Barkhausen jumps in the loop occurs when the DW proceeds from one local minima to the other of the potential [122,123].

1.6.2. Coherent rotation:

The coherent rotation of the single domain nanoparticles can be explained in terms of Stoner-Wohlfarth model [124]. However, this can be also extended to understand the magnetization reversal of the thin films where the spins rotate coherently to complete the reversal. When the dimension of a ferromagnetic particle/entity is reduced to low value, the energy required for DW formation becomes significantly high leading to alignment of all the atomic moments in one specific direction. In such a scenario, the exchange energy of the system will be minimum due to the parallel orientation of the atomic spins. Hence, the magnetic free energy under application of magnetic field can be written as the sum of Zeeman and anisotropy energy [125]:

$$E = K \sin^2 \theta - \mu_0 H M_S \cos(\phi - \theta) \quad (1.15)$$

where, the orientations of θ and ϕ with respect to H , M , the EA are depicted in fig. 1.7. The equilibrium of magnetization can be derived by minimizing eq. 1.15 with respect to θ . By minimizing E (eq. 1.15) with respect to θ , one can obtain the saturation field along the HA ($\phi = 90^\circ$). This is known as the anisotropy field (H_K), given by:

$$H_K = \frac{2K}{\mu_0 M_S} \quad (1.16)$$

Hence, for the EA ($\phi = 0^\circ$), when a field is applied along the reverse direction, the orientation of magnetization remains unaffected until the magnitude of the field equals H_K . Along the EA, if the field is further applied along $\phi = 180^\circ$, there is essentially no torque on M_S . However, the magnetization will become unstable at $\phi = 0^\circ$ and flip over to $\phi = 180^\circ$. Further, when the applied field is at an angle away from the EA ($0^\circ < \phi < 90^\circ$), the magnetization reversal initially occurs by reversible rotation of the spins. This aligns the spins away from the applied

field direction by aligning them towards the EA. Along the HA ($\phi = 90^\circ$), when the field is applied in the reverse direction, all the atomic spins rotate coherently which leads to the formation of ‘S’ shaped hysteresis loop. There is no jump in the hysteresis loop along the HA since the magnetization rotates from one energetically unstable direction towards the other forced by an applied field $H > H_K$.

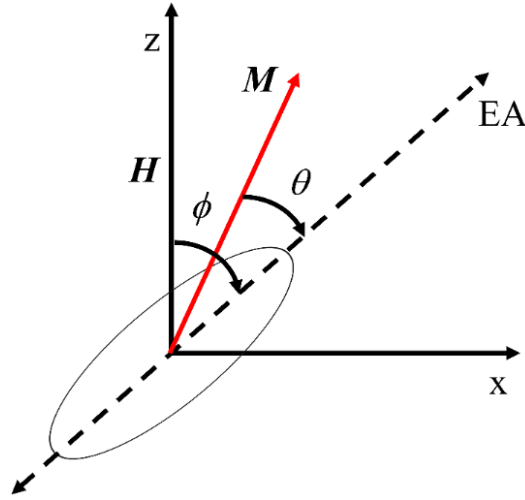


Figure 1.7: Schematic of the coordinate system for a single domain nanoparticle for Stoner Wohlfarth model.

From the above discussion, it should be noted that in thin films the magnetization reversal occurs both via coherent rotation of the spins as well as DW motion. In a few cases, the magnetic switching occurs via partial rotation of spins followed by the DW motion.

1.7. Magnetization dynamics:

1.7.1. Landau-Lifshitz-Gilbert (LLG) equation:

The dynamic properties of a magnetic system can be explained in-terms of Landau-Lifshitz-Gilbert (LLG) equation. To understand the mechanism behind LLG equation, let us consider the case of an electron moving in a circular loop with radius r . The motion of the electron generates a current i (in the opposite direction) in the loop. The magnetic moment of a single electron in such condition is defined as: $\mu = iA$, A being the area of the circular loop. The

angular momentum of the electron is $\mathbf{L} = m_e \mathbf{v} \times \mathbf{r}$, where m_e is the mass of an electron.

Hence, the magnetic moment of the electron can be expressed as:

$$\boldsymbol{\mu} = i\mathbf{A} = -\frac{e}{t}\mathbf{A} = -\frac{e\mathbf{v}}{2\pi r} \times \pi r^2 = -\frac{e\mathbf{v} \times \mathbf{r}}{2} = -\frac{e}{2m_e}\mathbf{L} = -\gamma\mathbf{L} \quad (1.17)$$

where, $\gamma = \frac{e}{2m_e}$ is the Gyromagnetic ratio. Differentiating eq. 1.17, we can obtain,

$$-\frac{1}{\gamma} \frac{d\boldsymbol{\mu}}{dt} = \frac{d\mathbf{L}}{dt} = \boldsymbol{\tau}$$

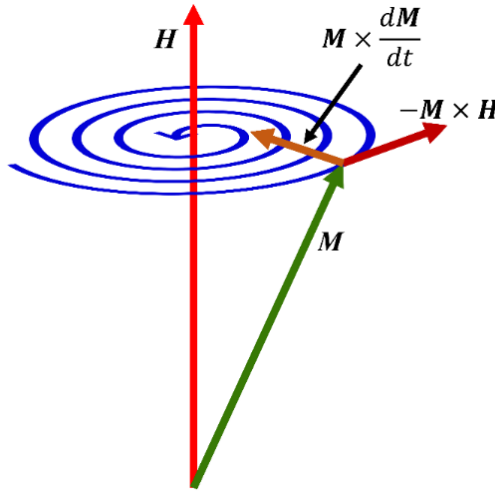


Figure 1.8: Precession of magnetization around the applied field.

When an electron is placed under an applied magnetic field (\mathbf{H}), the torque ($\boldsymbol{\tau}$) experienced by the electron can be expressed as: $-\frac{1}{\gamma} \frac{d\boldsymbol{\mu}}{dt} = \boldsymbol{\mu} \times \mathbf{H}$. This is the equation of motion for an electron flowing through a loop. In this scenario, the magnetic moment ($\boldsymbol{\mu}$) starts precessing around \mathbf{H} by forming a cone. Total magnetic moment of a ferromagnetic material comprising of N atomic spins can be written as: $\mathbf{M} = N\boldsymbol{\mu}$. Hence, the equation of motion for a ferromagnetic material is represented as:

$$\frac{d\mathbf{M}}{dt} = -\gamma(\mathbf{M} \times \mathbf{H}) \quad (1.18)$$

It should be noted that the precessional motion of eq. 1.18 does not depend on the angle between \mathbf{M} and \mathbf{H} , which further indicates infinite motion of the moment. This term was introduced by Landau and Lifshitz, which represents damp free motion of the electrons [110].

However, this is not true in real system where the magnetic moment eventually moves towards the field direction or damps. Gilbert introduced the damping term in the system which is represented by $\tau_D = \frac{\alpha}{M_S} (\mathbf{M} \times \frac{d\mathbf{M}}{dt})$, where α is a positive damping parameter [126]. Hence the final form of the LLG equation is the following:

$$\frac{d\mathbf{M}}{dt} = -\gamma(\mathbf{M} \times \mathbf{H}) + \frac{\alpha}{M_S} (\mathbf{M} \times \frac{d\mathbf{M}}{dt}) \quad (1.19)$$

Fig. 1.8 shows the precession of magnetization around an applied field.

1.7.2. Time scales of magnetization:

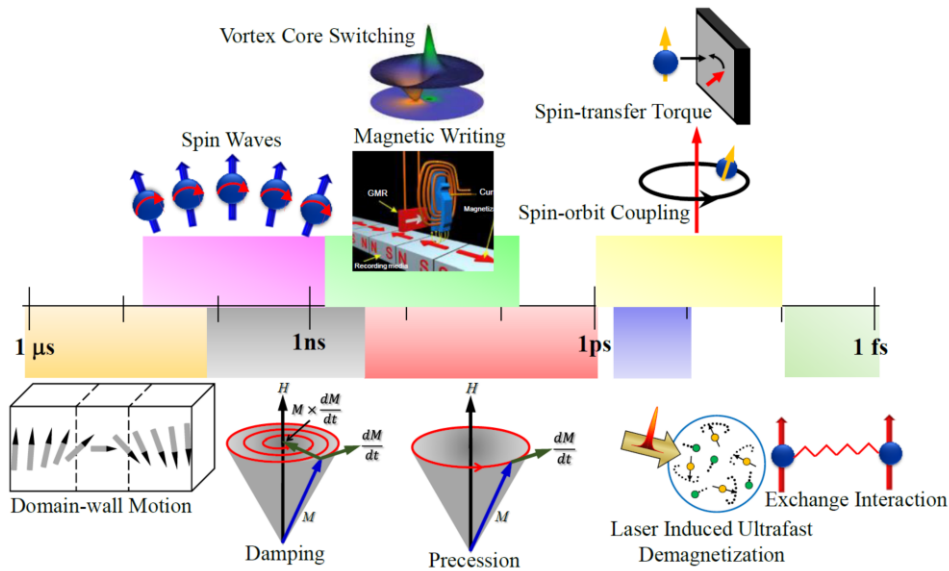


Figure 1.9: Time scale of magnetization showing occurrence of different physical phenomenon. Image taken from *ref.* [127].

Magnetization dynamics can occur over a broad range of time starting from μs to fs [127-129]. The whole range of time scale for the magnetization dynamics and different physical phenomenon associated with such time scale is depicted in fig. 1.9. The time scale of magnetization is determined from the relation $\tau = \frac{\hbar}{E}$, where E is the Heisenberg interaction energy. The slowest form of dynamics is DW motion whereas the fastest is the fundamental exchange interaction of the spins. DW motion occurs in the regime of few ns to μs . The

fundamental exchange interaction occurs within the time scale of ~ 10 fs - 1 ps [130]. Precession of magnetization is relatively faster in comparison to the DW motion which occurs within 10-100 ps and further gets damped in sub-ns to tens of ns [131]. It should be noted that the magnetic writing is done at around 10-100 ps range. The vortex core switching occurs in few tens of ps to several ns time scale [130]. The laser induced ultrafast demagnetization occurs within the range of few hundred fs. The demagnetization process is followed by very fast partial remagnetization of spins within 1-10 ps. Further, a slow recovery of magnetization follows due to the diffusion of electrons and lattice heat to the surroundings. The spin-orbit coupling and spin-transfer torque happens in the wide time range of 10 fs - 1 ps [130].

1.8. Kittel formula and macrospin model:

Collective excitation of electron spins under the influence of an external field in a magnetic material is known as the ferromagnetic resonance (FMR). The detailed theory regarding the experimental FMR technique is described later in section 2.3.4. The precessional frequency (Larmor precession) of an electron kept under a static magnetic field can be represented as $\omega_L = \gamma H$. Resonance occurs when the precessional frequency of the electrons matches with the frequency of the applied alternating (RF) field. The resonance frequency for a ferromagnetic material is defined as $\omega_0 = \gamma(BH)^{1/2}$, where B is the magnetic induction. FMR was first experimentally observed by Griffiths and surprisingly the resonance frequency was significantly higher than the Larmor frequency [132]. The anomaly was resolved by C. Kittel by considering the dynamical coupling arising due to the demagnetizing field [133,134]. For simplicity, the calculations were done in macrospin model with the assumption that all the magnetic moment in the sample can be replaced by a macrospin.

The equation of motion for the magnetization in a ferromagnetic material can be written in the form of LLG eq. 1.19:

$$\frac{d\mathbf{M}}{dt} = -\gamma(\mathbf{M} \times \mathbf{H}_{eff}) + \frac{\alpha}{M_S} (\mathbf{M} \times \frac{d\mathbf{M}}{dt}).$$

If uniform precessional motion is considered (zero damping), the LLG equation reduces to Landau-Lifshitz form (eq. 1.18):

$$\frac{d\mathbf{M}}{dt} = -\gamma(\mathbf{M} \times \mathbf{H}_{eff})$$

The equation can be expressed in Cartesian coordinate system:

$$\frac{dM_x}{dt} = \gamma(M_y H_z^{eff} - H_y^{eff} M_z), \frac{dM_y}{dt} = \gamma(M_z H_x^{eff} - H_z^{eff} M_x), \frac{dM_z}{dt} = \gamma(M_x H_y^{eff} - H_x^{eff} M_y) \quad (1.20)$$

In case of a general ellipsoid, the demagnetizing factors along the coordinate axes are N_x , N_y , and N_z , respectively. Let us assume that H_z and H_x are the static field applied along the z axis and RF field applied along the x axis, respectively. Under this scenario, the effective magnetic fields can be written as [134]:

$$H_x^{eff} = H_x - N_x M_x, H_y^{eff} = -N_y M_y, H_z^{eff} = H_z - N_z M_z \quad (1.21)$$

Substituting the values of effective magnetic fields from eq. 1.21 to eq. 1.20, we obtain:

$$\frac{dM_x}{dt} = \gamma[H_z + (N_y - N_z)M_z]M_y \quad (1.22)$$

$$\frac{dM_y}{dt} = \gamma[M_z H_x - (N_x - N_z)M_z M_x - M_x H_z] \quad (1.23)$$

$$\frac{dM_z}{dt} = 0 \quad (1.24)$$

Eq. 1.22 – 1.24 is solved by considering plane wave solution for magnetization i.e. $M = m e^{i\omega t}$,

which leads to the susceptibility $\chi_x = \frac{M_x}{H_x} = \frac{\chi_0}{[1 - (\frac{\omega}{\omega_0})^2]}$ where,

$$\omega_0 = \gamma \sqrt{[H_z + (N_y - N_z)M_z] \times [H_z + (N_x - N_z)M_z]} \quad (1.25)$$

ω_0 represents the resonance frequency of the system [134]. For an infinite thin film system ($H_z \perp$ film plane), the demagnetizing factors can be reduced to $N_x = N_y = 0, N_z = 4\pi$. Hence, eq. 1.25 for a thin film can be expressed as:

$$\omega_0 = \gamma[H_z - 4\pi M_z] \quad (1.26)$$

Whereas, for $H_z \parallel$ film plane, $N_x = N_z = 0, N_y = 4\pi$, which leads to:

$$\omega_0 = \gamma \sqrt{H_z(H_z + 4\pi M_z)} \quad (1.27)$$

Resonance equation for uniaxial and cubic anisotropies:

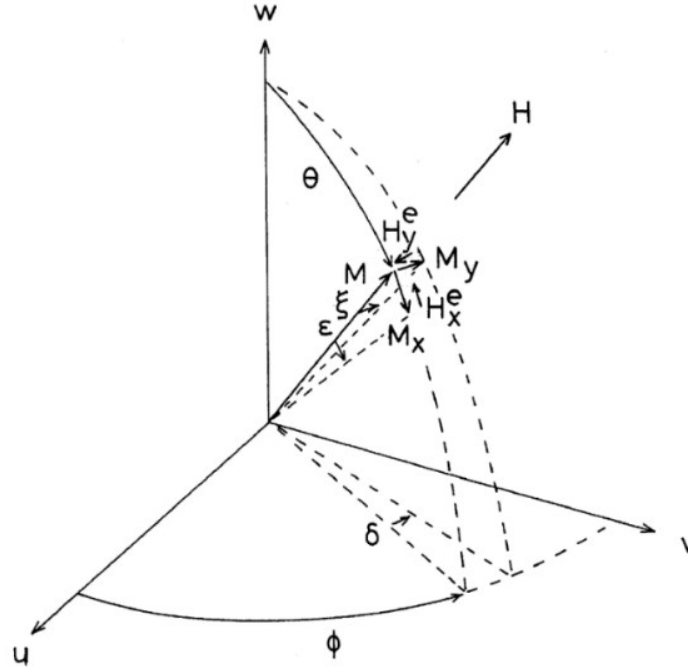


Figure 1.10: Demagnetizing field and magnetization components with respect to different angles in an orthogonal coordinate system. The image is taken from *ref.* [135].

The General expression of the demagnetizing energy in an orthogonal coordinate system can be expressed as [135]:

$$N_x^e M_S^2 \sin \varepsilon = \left[\left(\frac{\partial E}{\partial \theta} \right)_{\phi+\varepsilon} - \left(\frac{\partial E}{\partial \theta} \right)_{\theta} \right] \phi \quad (1.28)$$

$$N_y^e M_S^2 \sin \delta = \frac{\left[\left(\frac{\partial E}{\partial \theta} \right)_{\phi+\delta} - \left(\frac{\partial E}{\partial \phi} \right)_{\phi} \right]_{\theta}}{\sin^2 \theta} + \frac{\sin \delta \cos \theta}{\sin \theta} \frac{\partial E}{\partial \theta} \quad (1.29)$$

where, E is the magnetocrystalline anisotropy energy of the system, and N^e is the effective demagnetizing energy. The angles are defined in terms of the coordinate axes in fig. 1.10. The

general expression for uniaxial anisotropy is given by $E = K_2 \sin^2 \theta$. Replacing $\frac{\partial E}{\partial \theta}$ and $\frac{\partial E}{\partial \phi}$ in

eq. 1.28 and 1.29 (at $\phi = 0$ under small angle approximation), one can obtain the expressions

for the demagnetizing energies:

$$N_x^e = \frac{2K_2}{M_S^2} \cos 2\theta, N_y^e = \frac{2K_2}{M_S^2} \cos^2 \theta \quad (1.30)$$

Eq. 1.25 for an infinite cylinder can be expressed as [136]:

$$\omega_0 = \gamma \sqrt{[H_z + (N_y + N_y^e - N_z)M_z] \times [H_z + (N_x + N_x^e - N_z)M_z]} \quad (1.31)$$

Substituting, the values of demagnetizing energy from eq. 1.30 to eq. 1.31,

$$\omega_0 = \gamma \sqrt{[H_z + \left(N_y - N_z + \frac{2K_2}{M_S^2} \cos 2\theta\right) M_z] \times [H_z + \left(N_x - N_z + \frac{2K_2}{M_S^2} \cos^2 \theta\right) M_z]} \quad (1.32)$$

For an infinite thin film ($N_x = N_z = 0, N_y = 4\pi$), the resonance frequency of a system with uniaxial anisotropy can be expressed as:

$$\omega_0 = \gamma \sqrt{[H_z + \frac{2K_2}{M_S} \cos 2\theta] \times [H_z + \frac{2K_2}{M_S} \cos^2 \theta + 4\pi M_S]} \quad (1.33)$$

Similarly, the resonance frequency for a system with cubic anisotropy can be expressed as [136]:

$$\omega_0 = \gamma \sqrt{[H_z + \left(N_y - N_z - \frac{4K_4}{M_S^2} \cos 4\theta\right) M_z] \times [H_z + \left(N_x - N_z + \frac{2K_4}{M_S^2} (3 + 4\cos 4\theta)\right) M_z]} \quad (1.34)$$

1.9. Spin wave and magnon:

Spin waves (SW) are defined as the propagating disturbance in any ordered ferromagnetic material [137]. In an exchange or dipolar coupled spin system, a local perturbation (formed by any external force) transfers the disturbance to its nearest neighbor and propagates in the form of a wave. The concept of such low-lying collective excitations (spin waves) was first introduced by Bloch in 1930 [138]. Fig. 1.11 shows a schematic diagram of a SW with precession of magnetization around the effective magnetic field. The orientation of the spins in a ferromagnetic material can be disturbed by application of different external perturbation

viz. temperature, pressure, magnetic field, spin polarized current, electromagnetic waves, etc. Similar to other physical waves, SW can exhibit dispersion, resonance, reflection, Doppler effect, interference, diffraction, etc. [132,139-142]. The smallest quanta of a SW, known as magnons, are spin 1 quasiparticles (bosons) and hence follow Bose-Einstein statistics. In the subsequent section we will discuss about the exchange and the dipole dominated SW dispersion phenomenon.

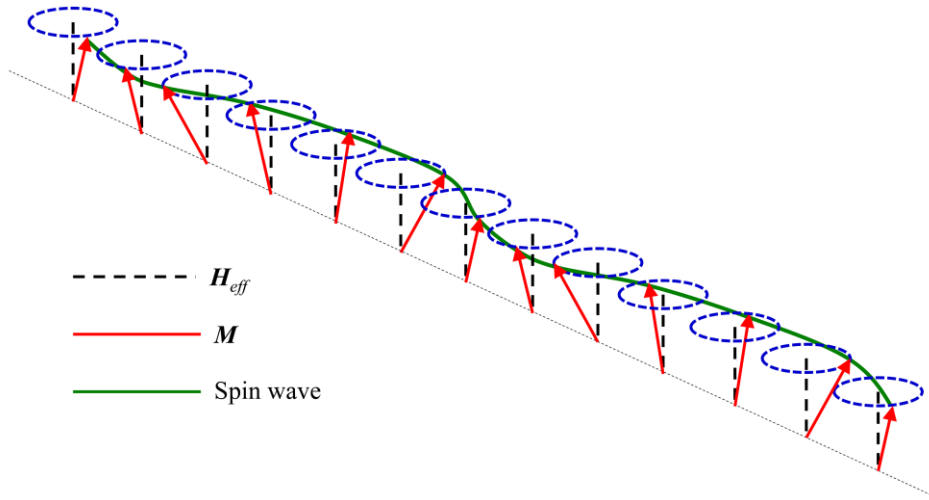


Figure 1.11: Spin wave propagation with precession of magnetization (M) around the effective magnetic field vector (H).

1.9.1. Exchange dominated SW:

In large wave vector (k) limit (i.e. short wavelength of SW), the interaction is primarily exchange dominated. Due to such strong exchange interaction, the atomic spins remain parallel to each other in the ground state. Let us consider chain of N spins (each with magnitude S) in the presence of strong exchange coupling. The Heisenberg exchange of such a system can be expressed as [143]:

$$E_{exch} = -2J \sum_{p=1}^N \mathbf{S}_p \cdot \mathbf{S}_{p+1} \quad (1.35)$$

Hence, the exchange energy of the p^{th} spin is:

$$E_{exch} = -2J \mathbf{S}_p \cdot (\mathbf{S}_{p-1} + \mathbf{S}_{p+1}) \quad (1.36)$$

Substituting the value of magnetic moment ($\mu_p = -g\mu_B \mathbf{S}_p$) of p^{th} spin in eq. 1.36, the

exchange energy is modified to:

$$E_{exch} = -\boldsymbol{\mu}_p \left[\left(-\frac{2J}{g\mu_B} \right) (\mathbf{S}_{p-1} + \mathbf{S}_{p+1}) \right] = -\boldsymbol{\mu}_p \cdot \mathbf{B}_p \quad (1.37)$$

Where, $\mathbf{B}_p = \left(-\frac{2J}{g\mu_B} \right) (\mathbf{S}_{p-1} + \mathbf{S}_{p+1})$ is the exchange field corresponding to the p^{th} spin. The torque acting on the spin is equal to the rate of change of angular momentum $\hbar S_p$.

$$\begin{aligned} \hbar \frac{d\mathbf{S}_p}{dt} &= \boldsymbol{\mu}_p \times \mathbf{B}_p \\ \Rightarrow \frac{d\mathbf{S}_p}{dt} &= -\frac{g\mu_B}{\hbar} \mathbf{S}_p \times \left[\left(-\frac{2J}{g\mu_B} \right) (\mathbf{S}_{p-1} + \mathbf{S}_{p+1}) \right] \\ \Rightarrow \frac{d\mathbf{S}_p}{dt} &= \left(\frac{2J}{\hbar} \right) (\mathbf{S}_p \times \mathbf{S}_{p-1} + \mathbf{S}_p \times \mathbf{S}_{p+1}) \end{aligned} \quad (1.38)$$

For small amplitude of excitation, in Cartesian coordinate, eq. 1.38 can be approximated to:

$$\begin{aligned} \frac{dS_p^x}{dt} &= \left(\frac{2JS}{\hbar} \right) (2S_p^y - S_{p-1}^y - S_{p+1}^y) \\ \frac{dS_p^y}{dt} &= -\left(\frac{2JS}{\hbar} \right) (2S_p^x - S_{p-1}^x - S_{p+1}^x) \\ \frac{dS_p^z}{dt} &= 0 \end{aligned} \quad (1.39)$$

where, $S_p^x, S_p^y \ll S$ and $S_p^z \cong S$. Let us assume that the solutions are sinusoidal in nature,

$$S_p^x = m e^{i(pka - \omega t)}, \quad S_p^y = n e^{i(pka - \omega t)}$$

where, m, n are the amplitude of the exponents, a is the lattice constant, and ω is the angular frequency. Substituting S_p^x and S_p^y in eq. 1.39,

$$-i\omega m = \left(\frac{2JS}{\hbar} \right) (2 - e^{ika} - e^{-ika}) n = \left(\frac{4JS}{\hbar} \right) (1 - \cos ka) n \quad (1.40)$$

Similarly,

$$i\omega n = \left(\frac{2JS}{\hbar} \right) (2 - e^{ika} - e^{-ika}) m = \left(\frac{4JS}{\hbar} \right) (1 - \cos ka) m \quad (1.41)$$

To obtain a finite solution for eq. 1.40, and 1.41, the determinant of the coefficients should be zero:

$$\begin{vmatrix} i\omega & \left(\frac{4JS}{\hbar} \right) (1 - \cos ka) \\ -\left(\frac{4JS}{\hbar} \right) (1 - \cos ka) & i\omega \end{vmatrix} = 0 \quad (1.42)$$

The solution for eq. 1.42 yields:

$$\hbar\omega = 4JS(1 - \cos ka) \quad (1.43)$$

At long wavelength limit, $ka \ll 1$, hence eq. 1.43 reduces to:

$$\hbar\omega = 2JSa^2k^2 \quad (1.44)$$

Hence at long wavelength limit, the dispersion relation of magnons is quadratic in nature. This is in contrary with the phonon dispersion relation which follows a linear behavior. Further, it can be shown that the exchange energy of a SW varies with Dk^2 , where $D = \frac{2A}{M_S}$. The dispersion equation takes the following form [144,145]:

$$\frac{\omega_k}{\gamma} = H - 4\pi M_S + Dk^2 \quad (1.45)$$

1.9.2. Dipole dominated SW (magnetostatic SW modes in thin films):

Let us consider the case of an infinite ferromagnetic thin film. Here, if an in-plane field is applied, the moments will align themselves in the film plane. Such modes travelling in the plane of the film usually have wavelength in the range of hundreds of nm to several μm . Hence, it is evident that the wavelength is significantly larger than the interatomic distance. The exchange interaction is usually weak in such system and the dipolar interaction dominates. However, for relatively higher values of the wave vector, the exchange interaction becomes non-negligible and the SWs in such regime are known as dipole-exchange SWs [136]. To obtain the dispersion relation for the dipolar-exchange SWs, one needs to solve the Landau-Lifshitz equation (eq. 1.18). The total magnetization for a system can be expressed as [146]:

$$\mathbf{M}(\mathbf{r}, t) = M_S + \mathbf{m}(\mathbf{r}, t)$$

where, M_S is the saturation magnetization and $\mathbf{m}(\mathbf{r}, t)$ is infinitesimal variation of magnetization due to the precession. It is expected that for small angle of precession, $m \ll M_S$. Under such approximation, $\mathbf{m}(\mathbf{r}, t)$ can be expressed as summation of a series of plane waves:

$$\mathbf{m}(\mathbf{r}, t) = \sum_k \mathbf{m}_k e^{i(\omega t - \mathbf{k} \cdot \mathbf{r})}$$

The non-linear Landau-Lifshitz equation can be linearized and solved with such

approximation. The dispersion relation for a dipole-exchange SW in an infinite ferromagnetic system can be expressed by Herrings-Kittel formula [147]:

$$\omega = \gamma \sqrt{\left[\left(H + \frac{2A}{M_S} k^2 \right) \left(H + \frac{2A}{M_S} k^2 + 4\pi M_S \sin^2 \theta_k \right) \right]} \quad (1.46)$$

where, θ_k is the angle between k and M_S .

In a thin film of thickness d , the broken translational symmetry modifies the dispersion relation. Damon and Eshbach (DE) calculated the dispersion relation in a magnetic thin film system [148]. They considered a thin ferromagnetic film with thickness d oriented in the y-z plane where the external magnetic field has been applied along the z axis. The dispersion relations yield two distinct types of modes: namely the surface or the DE mode and the volume mode. The surface mode is distributed at the vicinity of the plane of the film which decays exponentially away from it. Surface modes exist up to a critical angle (ζ_c) with respect to the perpendicular magnetization direction [148]:

$$\zeta_c = \tan^{-1} \sqrt{\frac{4\pi M_S}{H}} \quad (1.47)$$

The penetration depth (δ) is inversely proportional to the wave vector and becomes zero at $\zeta = \zeta_c$. Hence it should be noted that at the critical angle the surface mode is completely confined at the surface of the material. The DE mode is unidirectional in nature i.e. for the range of ζ where the mode exists, it propagates only in one particular direction. The DE mode propagates in the opposite direction at the other side of the surface of the sample. Further, we note that when the wave vector equals to zero, $\delta \sim \infty$ and hence DE mode turns into Kittel mode. The surface mode is converted to bulk mode when the penetration depth becomes comparable to the thickness of the film. When the propagation vector and magnetization lies in the same plane however perpendicular to each other, the mode is called as magnetostatic surface spin wave (MSSW) mode. The dispersion relation for such MSSW mode is:

$$\omega_{DE} = \gamma \sqrt{H(H + 4\pi M_S) + (2\pi M_S)^2 (1 - e^{-2kd})} \quad (1.48)$$

As discussed, at $k = 0$, the DE mode turns into Kittel mode, with

$$(\omega_{DE})_{k=0} = \gamma\sqrt{H(H + 4\pi M_s)} \quad (1.49)$$

At $k \rightarrow \infty$,

$$(\omega_{DE})_{k=\infty} = \gamma(H + 2\pi M_s) \quad (1.50)$$

If the propagation vector and magnetization are collinear and coplanar, a mode with negative dispersion is observed. This is known as backward volume magnetostatic (BWVMS) mode. In such modes the group and phase velocity point towards the opposite directions. The dispersion relation for the BWVMS mode is the following [146]:

$$\omega_{BWVMS} = \gamma\sqrt{H[H + 4\pi M_s \left(\frac{1-e^{-2kd}}{kd}\right)]} \quad (1.51)$$

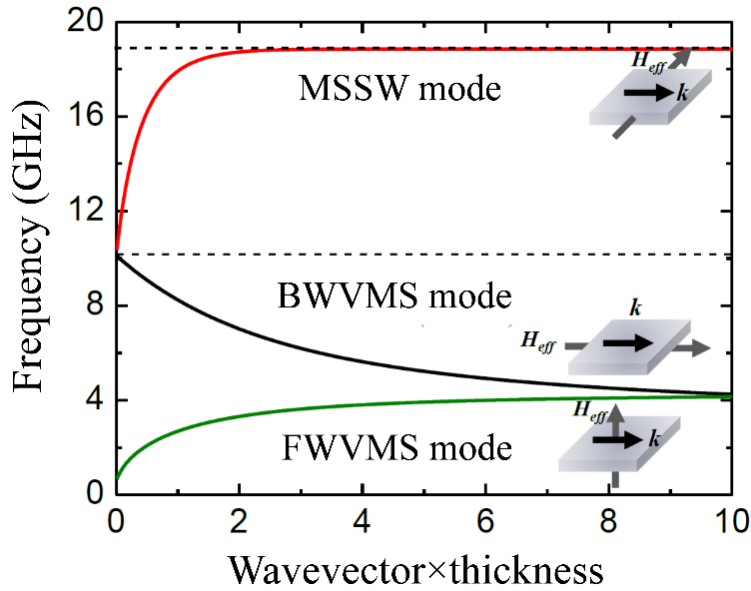


Figure 1.12: Dispersion curve for various magnetostatic spin wave modes. Image is taken from *ref.* [127].

Similar to DE mode at $k = 0$, the frequency of BWVMS mode becomes equal to that of the Kittel mode. The mode is called forward volume magnetostatic (FWVMS) mode, when the magnetization and propagation direction lies in planes perpendicular to each other. This occurs when the magnetization lies perpendicular to the film plane whereas the propagation direction lies in the plane of the film. The dispersion relation for FWVMS mode is [146]:

$$\omega_{FWVMS} = \gamma \sqrt{(H - 4\pi M_s) \left[H - 4\pi M_s \left(\frac{1 - e^{-2kd}}{kd} \right) \right]} \quad (1.52)$$

The dispersion curves for different magnetostatic SW modes are shown in fig. 1.12.

1.10. Object Oriented Micro-Magnetic Framework (OOMMF) simulation:

Object oriented micromagnetic framework (OOMMF) is a free code aimed to develop a portable, extensible public domain micromagnetic program. OOMMF has been developed by Dr. Mike Donahue and Dr. Don Porter at Information Technology Laboratory (ITL) at the National Institute of Science and Technology (NIST), USA . The code for the software is written on C++ and Tcl/Tk. OOMMF deals with functional micromagnetics package and provides the additional feasibility of developing new codes based on its foundation. Different extension models to the OOMMF are also available which can be added to explore further details of a micromagnetic problem. OOMMF solves LLG equation (eq. 1.19) at each cell of the simulation area.

To begin with the simulation, a ‘MIF file’ is written in Tcl script. In the script all the parameters viz. saturation magnetization, exchange stiffness constant, magnetocrystalline anisotropy, external magnetic field, sample dimension as well as structure, cell size, damping, stopping criteria, etc. can be defined for a particular system. There are two major evolvers used in OOMMF: (i) time-evolver, and (ii) minimization evolver. In this thesis, all the simulations are performed using the time-evolver which implements first order Euler method to solve the LLG equation. It should be noted that OOMMF runs at $T = 0K$, and hence the effect of temperature is not considered in the simulation.

CHAPTER 2: Experimental Techniques

In this chapter we have described the experimental techniques employed to prepare the samples as well as the techniques used for structural and magnetic characterization. We have prepared the thin films of Co with either in-plane or out-of-plane anisotropy using sputtering technique. Further, the in-plane magnetized Heusler alloy and FePt alloy thin films have been prepared using sputtering via a collaboration with Prof. Koki Takanashi, in IMR, Tohoku University, Sendai, Japan. Patterning for the antidot arrays of Co, Heusler alloy, and FePt alloy, has been performed by either photolithography (in our lab at NISER) or e-beam lithography (in IMR) depending on the dimension of the desired microstructure. The nanocrystalline ribbons have been prepared via a collaboration with Prof. Parmanand Sharma, in IMR, Tohoku University, Sendai, Japan. The microstructure as well as the layer quality of the thin films have been probed using reflection high energy electron diffraction (RHEED), X-ray diffraction (XRD), and atomic force microscopy (AFM). The shape, size, and distribution of the antidots have been imaged using scanning electron microscopy (SEM). Magnetic characterization of the samples has been performed using magneto optic Kerr effect (MOKE) and superconducting quantum interference device (SQUID) magnetometry. Nature of anisotropy, and magnetic damping have been studied by using ferromagnetic resonance (FMR) spectroscopy. The domain imaging has been performed using Kerr microscopy in our lab or via X-ray photoemission electron microscopy (XPEEM) at Diamond Light Source, UK. The nature of SW spectra in the nano-dimensional Heusler alloy MAL arrays has been studied with time resolved MOKE (TR-MOKE) magnetometry in the lab of Prof. Anjan Barman, SNBNCBS, Kolkata. The detailed sample structure of different systems will be discussed in tabular form in the respective chapters.

2.1. Sample Fabrication:

2.1.1. Lithography:

Lithography is a process of printing on a solid flat surface. Initially during 1796, the printing surface was a flat piece of stone which was etched using acid to form a pattern to transfer ink to the paper kept below. Advancement of technology over the years has significantly improved the modern lithography process where individual patterns down to ~ 20 nm can be transferred with accuracy. Depending on the desired resolution, patterning area, and cost, modern lithography process is divided into several categories. Followings are the most commonly used lithography techniques:

1. Scanning technique: (scanning e-beam lithography, scanning optical beam lithography, scanning ion-beam lithography, scanning-probe lithography, etc.)
2. Pattern replication technique:
 - a. Photolithography
 - b. Nano-imprint lithography
 - c. E-beam lithography

In this thesis, the samples are mostly fabricated using photolithography and e-beam lithography techniques. E-beam lithography is used to create patterns down to ultralow dimension (< 100 nm). However, for large area patterning with low cost and time, optical lithography is used. The resolution of patterns ($\sim 1 \mu\text{m}$) created by photolithography is limited by the diffraction limit of the visible light.

2.1.1.1. Photolithography: Optical lithography (photolithography/ UV lithography) is a process which is used in microfabrication to transfer patterns of desired designs over a large area. This is achieved by passing UV light through a mask to project the design on top of a resist coated substrate. Fig. 2.1 shows the photolithography process in a step by step manner. In a typical experiment, a substrate is first cleaned in acetone and isopropanol using ultrasonication. A

properly cleaned substrate is the most important pre-requisite condition for any lithography process. Then the substrate is spin coated with uniform layer of photoresist. The resist coated substrates are further soft-baked to remove the solvent and promote adhesion to the substrate. The polymer chains in the photoresist either gets broken (positive photoresist) or becomes cross-linked (negative photoresist) upon exposure to UV light. Next, the exposed resist coated substrates are developed in proper chemical to obtain 3D structure of the desired design transferred from the physical mask. The developer dissolves the exposed and unexposed parts of the resist coated substrates in case of the use of positive and negative photoresist, respectively. The thin film heterostructure is deposited on the patterned substrates inside vacuum chamber. Finally, lift-off is performed on the sample to end up with the desired structures with the thin film stacking.

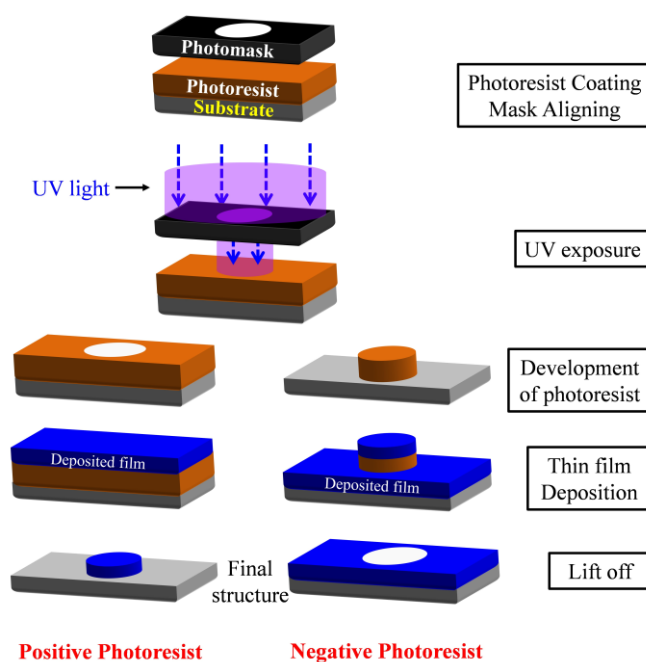


Figure 2.1: Schematic of photolithography technique using positive and negative photoresist.

We have used the mask aligner (MDA-400M) with UV lithography from MIDAS systems, Korea [149] to pattern the samples. Fig. 2.2 (a) shows the photolithography setup from MIDAS available at NISER, Bhubaneswar, India. The beam wavelength is $\sim 350-450$ nm and the

resolution is $\sim 1 \mu\text{m}$ with vacuum contact. The beam uniformity is $\sim 110 \times 110 \text{ mm}^2$, which is well above the sample size of $\sim 10 \times 10 \text{ mm}^2$. The samples used in the thesis are all prepared using hard contact option. We have used ma-P 1205 and ma-D 533S from Microresist Technology GmbH [150], as the photoresist and developer, respectively.

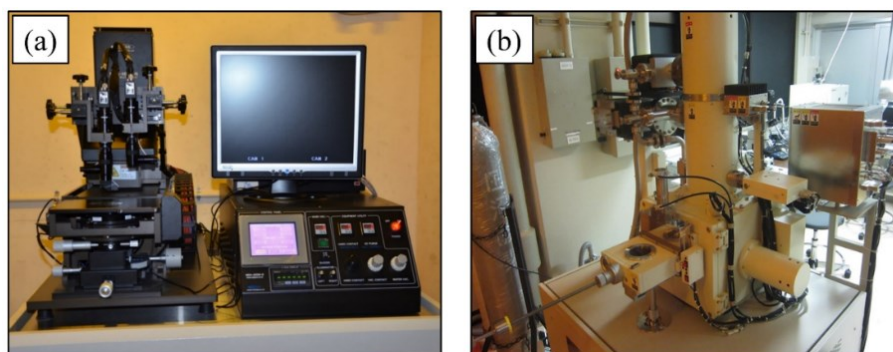


Figure 2.2: (a) Mask aligner with photolithography at NISER, Bhubaneswar, India. (b) E-beam lithography at IMR, Tohoku University, Japan.

2.1.1.2. E-beam lithography: In electron beam (e-beam) lithography, a focused beam of electrons are scanned over a substrate coated with an electron sensitive film (e-beam resist). The e-beam modifies the solubility of the resist which enables selective removal of either the exposed or the non-exposed parts of the resist by developing it in desired solvent. The process is very similar to the flowchart of photolithography shown in fig. 2.1 with the differences in the use of the materials as well as the source of the beam. However, the operation of e-beam lithography does not require the use of a physical mask, rather the electron beam is focused on desired areas by computer generated mask. E-beam lithography has been performed to prepare magnetic nanostructures down to 100 nm feature size in the laboratory of Prof. Koki Takanashi, IMR, Tohoku University, Sendai, Japan. Fig. 2.2 (b) shows the e-beam lithography setup at IMR, Japan. We have used poly-methyl methacrylate (PMMA) and pyrrolidone as the resist and developer, respectively. The electron beam is controlled by a pattern generator (non-physical mask designed in software) to expose the desired portion of the resist coated substrate

[151]. The dose and exposure time of the electron beam plays the most crucial role in proper patterning using e-beam lithography. Similar steps as mentioned for the photolithography technique are followed to obtain the final microstructure after the lift-off.

2.1.2. Thin film deposition techniques:

Various methods of thin film deposition techniques can be broadly subdivided into two parts: chemical vapor deposition (CVD) and physical vapor deposition (PVD). In CVD the substrate is exposed to volatile precursors which reacts or decomposes on the substrate surface to produce the thin films of the desired materials [152]. There are various popular methods of CVD viz. thermal-assisted, photo-assisted, plasma-enhanced CVD, etc. On the other hand, in PVD, the atoms or molecules from a material are vaporized from the source (solid/liquid form) which are then transported through a vacuum (low-pressure environment) and deposited on a substrate [153]. One major advantage of PVD over CVD is the working temperature. CVD usually operates between 300°C to 900°C, which makes them unsuitable for substrates which cannot withstand such high temperature. Further, the bi-products of the precursors used in CVD are often toxic, pyrophoric, or corrosive. The PVD technique can be broadly subdivided into three parts: vacuum evaporation, ion plating, and sputtering. The samples in this thesis are majorly prepared using sputtering technique. However, we have used e-beam evaporation to prepare Au seed and buffer layers in few thin films.

2.1.2.1 Sputtering: Sputtering is ejection of atoms by bombarding a solid target using highly energetic ions via energy transfer [154,155]. There are several advantages of sputtering over other deposition techniques viz. deposition capability of wide range of material irrespective of its conductivity, deposition over large area, etc. The total yield of the process is defined by the ratio of the number of sputtered ejected atoms and incident projectiles. This can be achieved in a straight forward way by aiming an ion source towards the target. However, due to high cost and low yield, ion beam sputtering is not commonly implemented in laboratory as well as large

scale applications. The other way is by creating a gaseous plasma and then accelerating the ions from the plasma towards the source material (target). Fig. 2.3 shows the schematic diagram of a typical sputtering deposition technique/system. In our deposition chamber, we have used Ar gas to create the plasma by applying a high negative voltage to the target (cathode). A typical image of Ar gas plasma can be seen in left bottom side of fig. 2.3. The free electrons are driven away from the negatively charged target and approach the outer shell of the Ar atoms. The free electrons remove electrons from the outermost shell of the neutral Ar atoms upon collision, leaving them as positively charged ions (Ar^+). These Ar^+ ions are attracted towards the negatively charged target (cathode) and upon hitting they remove neutral target materials due to momentum transfer. The additional free electrons generated in this process leads to generation of additional Ar^+ ions and hence continue the plasma. The ejected neutral particles (in the form of individual atoms, and/or molecule) travel in a solid cone and sit on the substrate kept in the path of propagation (line-of-sight). However, since the free electrons can bombard the substrate extensively, the process (diode sputtering) may cause overheating of the substrate and lead to structural damage. In order to avoid such scenario, magnets are put behind the cathode to trap the free electrons in the vicinity of the target surface. This process is known as ‘magnetron sputtering’ and is employed in our deposition system. This restricts the rapid bombardment of the free electrons to the substrates. Further, the formation of free electron cloud around the target significantly enhances the rate of sputtering. In a conventional set-up, one pole of the magnet is positioned at the central axis of the target whereas the other pole is at the outer ring of the target. If the strength of the magnetic poles at the central axis and outer rings are equal, they cancel out each other [156]. This is a major drawback as the plasma remains confined in the vicinity of the target in such scenario. An unbalanced magnetron is utilized to get rid of this issue which results in uncompensated flux directed towards the substrate.

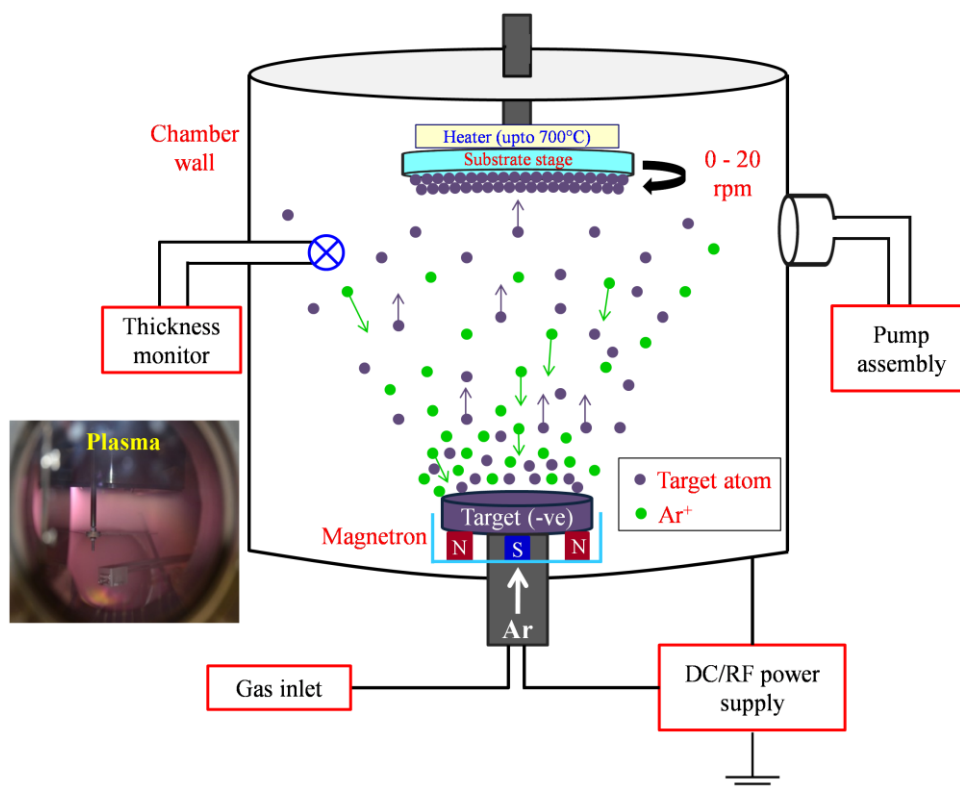


Figure 2.3: Schematic for sputtering deposition technique in a vacuum chamber. The Ar^+ ions (green circles) hit the target after a voltage is applied to it. The target atoms (purple circles) are ejected upon momentum transfer and deposit on the substrate which is kept on its line of sight.

Magnetron sputtering can be classified in to two different types: DC (direct current) and RF (radio frequency) [157]. DC sputtering is the most basic and inexpensive type of physical vapor deposition method which is used for conductive metallic materials. A negative DC voltage is applied to the target which leads to formation of the plasma. However, DC sputtering cannot be used for insulators as positive charge will accumulate on the target surface resulting in plasma extinguishment. In case of such insulating materials an alternating RF power is applied. During the negative half of the RF power, Ar^+ ions get attracted to the target leading to charge accumulation. However, during the positive half, the electrons from the plasma gets attracted towards the target surface which leads to charge neutralization. RF sputtering can be used for

both conducting and non-conducting materials. However, since the sputtering occurs only during one (negative) half of the cycle, the rate of deposition here is significantly low in compared to DC sputtering [158].

2.1.2.2. E-beam evaporation: Electron beam evaporation is a PVD technique where the target material is bombarded with an electron beam emerging from a charged tungsten filament. Due to energy transfer between the incident electron beam and the source material, at a certain point the source material gathers sufficient energy (work function) to leave the surface of the target. These target materials further travel in the vacuum chamber and gets deposited on the substrate surface to form a uniform layer of thin film. It should be noted that the thermal energy of the source material is extremely low (< 1 eV) and hence high vacuum is desired so that the mean free path is larger than the distance between the electron beam source and the substrate. E-beam evaporation allows the direct transfer of the energy from the electrons which makes them suitable for deposition of metals with high melting point. In addition, this can yield significantly high rate of deposition (starting from 0.1 nm to 100 nm per minute). It also concentrates the energy on the target rather than the whole deposition chamber, helping the possibility of reducing the heat damage of the substrate [159].

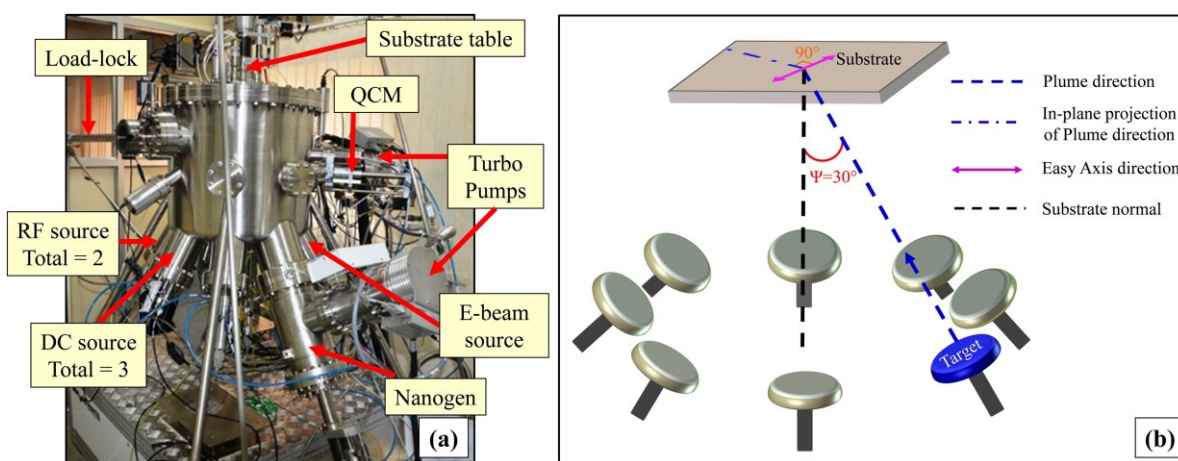


Figure 2.4: (a) Multipurpose deposition system from MANTIS at NISER, Bhubaneswar.

(b) Schematic diagram of plume orientation relative to the EA in the substrate plane.

We have used a multi-deposition unit (QPrep series) from Mantis Deposition Ltd., UK [160] for deposition of thin films and MAL arrays of Co with both in-plane as well as out-of-plane anisotropy. A load-lock is attached to the deposition unit to transfer the samples without breaking the vacuum of the main chamber. The best achievable working pressure in the deposition chamber is 5×10^{-10} mbar. The substrate table can be rotated and heated upto 20 rpm 800°C, respectively, during deposition. The thickness of the deposited films are controlled using a quartz crystal monitor (QCM) attached to the system. A picture of the UHV deposition chamber is shown in fig. 2.4 (a). The deposition unit contains the following growth possibilities:

- 5 unbalanced magnetron sputtering (DC and RF) guns,
- 2 thermal evaporation sources
- A 4-pocket e-beam evaporator
- A dedicated nanoparticle generator (Nanogen)
- A Mat60 unit for producing atomic oxygen from molecular oxygen to maintain proper stoichiometry of oxide-based materials.

The thermal source is kept at the bottom centre of the chamber whereas 8 sources are positioned at equal angles away from each other over the circumference i.e. over 360° (fig. 2.4 (b)). The substrate table is positioned at the centre on top of the main chamber. Due to the geometric constriction of the deposition chamber, all the targets are at an angle of 45° wrt to the substrate plane. However, the targets are at an angle of $\psi = 30^\circ$ wrt to the substrate normal. Therefore, the easy axis of the uniaxial anisotropy is induced along the perpendicular direction to the in-plane projection of the plume. The columnar growth of the grains perpendicular to the plume direction is discussed in detail in *ref.* [161]. The long axis of the crystallites, due to such columnar growth, forms a chain like structure leading to a uniaxial anisotropy along that direction. A schematic diagram to understand the growth configuration is shown in fig. 2.4 (b).

2.2. Structural Characterization:

2.2.1. Reflection High-Energy Electron Diffraction (RHEED):

Reflection high-energy electron diffraction (RHEED) employs collimated high energy (10-100 keV) electron beam to characterize the surface of crystalline materials [162,163]. A typical RHEED set up consists of an electron gun, a photoluminescent detector screen, and a clean surface. Due to glancing angle of the incident electrons, only the atoms at the surface of the sample contribute to the RHEED patterns. The surface atoms diffract the incident electrons due to the wavelike nature. The diffracted electrons interfere constructively at specific angles and collides with the detector to leave certain diffraction patterns according to the feature of the sample surface. One can characterize the crystallography and flatness of the sample surface by analyzing the diffraction patterns. The reciprocal lattice of the sample can be directly calculated by relating the Ewald's spheres geometry to the diffraction pattern at the screen.

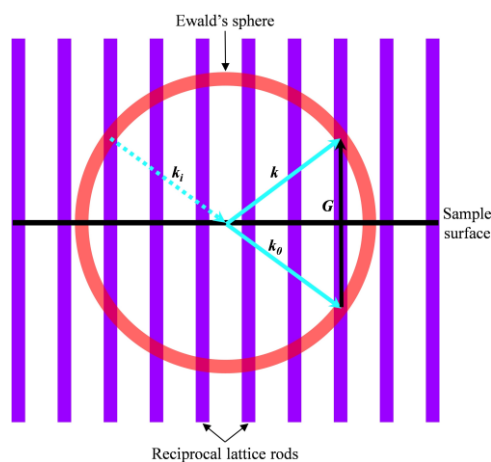


Figure 2.5: RHEED construction of the Ewald's sphere (red color) at the sample surface.

The sample surface is represented by parallel infinite rods (purple color) in reciprocal lattice space.

Fig. 2.5 shows schematic of the RHEED construction of the Ewald's sphere at the surface of the sample. Since only the first few layers of the sample contribute to the pattern, the third diffraction condition is not present. Hence, the reciprocal lattice of the crystal surface will be a

series of parallel infinite rods (purple lines) oriented perpendicularly to the sample surface (black line). The Ewald's sphere (red circle) can be drawn at the centre of the sample surface with the radius equal to the reciprocal of the wavelength of the incident electrons. The radius of the Ewald's sphere is given by, $k_0 = \frac{2\pi}{\lambda}$, where λ is the wavelength of the incident electrons in real space. The vector \mathbf{k} is defined as the electron wave vector at any intersection of the reciprocal lattice and Ewald's sphere, where the constructive interferences occur. The vector \mathbf{G} is defined as: $\mathbf{G} = \mathbf{k} - \mathbf{k}_0$. The orientation and position of \mathbf{k} , \mathbf{k}_0 , and \mathbf{G} in a typical Ewald's sphere construction is shown in fig. 2.5. It should be noted that at several places, the reciprocal lattice rods meet the Ewald's sphere. However, the RHEED design allows only the low order diffractions which are within the angular range of the detector.

In real scenario, the incident electron beam diverges. Further the electrons in the beam have a range of energies. This leads to a finite width in the Ewald's sphere. Additionally, the reciprocal lattice rods have finite thickness depending on the quality of the sample surface. Hence, the intersection between the rods and the Ewald's sphere are not perfect points rather elongated points or 'streaks' (fig. 2.5). This leads to the formation of 'streaks' along the vertical axis of the RHEED patterns. In such cases, streaky RHEED patterns indicate flat surface whereas the broadening of the streaks hints at small coherent area in the surface. In-situ RHEED spectroscopy has been performed on the CFMS thin films in the laboratory of Prof. Koki Takashi, IMR, Tohoku University, Sendai, Japan.

2.2.2 X-ray Diffraction (XRD):

X-ray diffraction (XRD) is one of the most powerful, non-destructive tool to analyse the microstructural properties of thin films because the wavelength of the X-ray is comparable to the lattice spacing of the material. In 1912, Max von Laue discovered the XRD with the idea of sending a beam of X-rays through a copper sulphate crystal and record the results on photographic plates. Fig. 2.6 shows schematic diagram of the operational principle of an XRD.

The periodic arrangement of atoms (orange balls) inside a crystalline material elastically scatter the incident X-ray. The incident angle of the X-rays (θ) can be varied over a wide range and the corresponding reflected X-rays are measured at the detector. The reflected X-rays interfere constructively when the Bragg's condition [164] $2d\sin\theta = n\lambda$ is satisfied, where λ is the wavelength of the incident beam, d is the distance between adjacent atomic planes, and n is an integer giving the order of interference. The intensity of the reflected X-rays is measured as a function of the angle (2θ) between the reflected and the incident beam. The X-rays can be also used in reflectivity mode (XRR) to study the thickness and roughness of the samples.

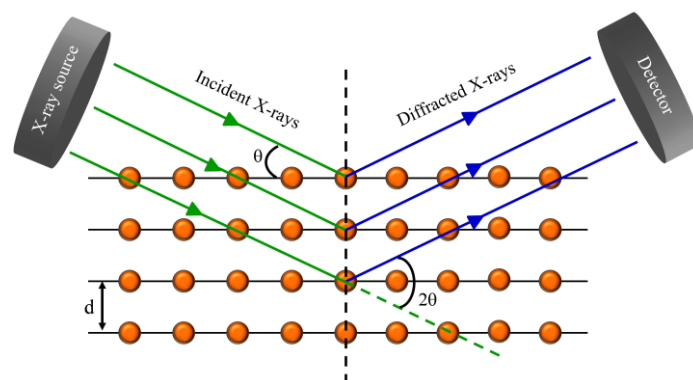


Figure 2.6: Schematic of X-ray diffraction (XRD). The incident X-ray (green lines) gets diffracted (blue lines) from the atoms (orange balls) of the material and interfere constructively to form the diffraction patterns.

We have performed XRD measurements of Heusler alloy thin film (CFMS) samples using the X-ray diffractometer from Smart Lab Rigaku [165] with the K_{α} radiation of Cu with an average wavelength of $\lambda \sim 0.15$ nm. The measurements have been performed at IMR, Tohoku University, Japan. During the measurements, the source and detector arm move in a fashion to maintain the θ - 2θ geometry. Each material has unique set of d -spacing associated to the different $(h k l)$ indices. Hence the conversion of the diffraction peaks to d -spacing leads to identification of the elements present in the sample. This is performed by comparing the d -spacing with standard reference data (inorganic crystal structure database: ICSD).

2.2.3. Scanning Electron Microscope (SEM):

The scanning electron microscope (SEM) is the most popular tool for high resolution surface imaging in nanotechnology. In a typical SEM, the electrons are generated either via thermionic emission or by applying an electric field. We have used the field emission based SEM (FESEM) process which results in better spatial resolution in comparison to thermionic emission of electrons. The energy of the emitted electrons can be varied from few eV to tens of keV. A schematic diagram of image formation using an SEM is depicted in fig. 2.7. The Anode attracts the electrons to form a uniform beam. The beam of electron then passes through two electromagnetic condenser lens which focuses the spot size to $\sim 0.4 - 5$ nm diameter [166]. The beam then goes through the scanning coils or pairs of deflector plates in the electron column. These coils deflect the electron beam in the x and y axes so that the scanning is enabled in raster fashion over the rectangular sample area.

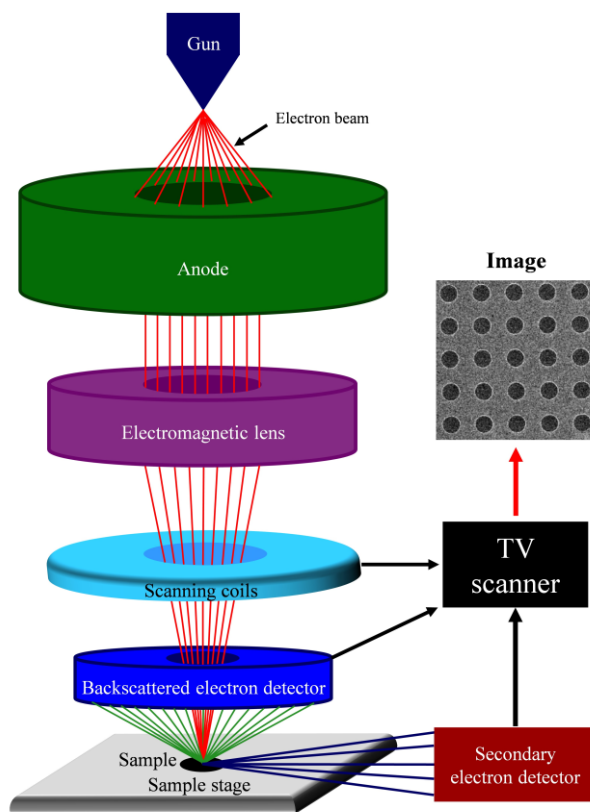


Figure 2.7: Schematic diagram of scanning electron microscope and image formation. It shows two modes of detection: backscattered electron and secondary electron mode.

Depending on the interaction between the sample and the highly energetic electron beam, different types of electrons viz. secondary electrons, backscattered electrons, Auger electrons, etc. emit from the sample surface due to elastic and inelastic scattering. The most common mode of operation for SEM is the detection of secondary electrons which are emitted due to inelastic scattering. In this mode, the electrons are emitted from very close to the sample surface. This gives information regarding the sample topography with high lateral resolution (~ 1 nm). On the other hand, backscattered electrons emerge from deeper position of the sample which provides information about the specimen/elements in the sample. However, the lateral resolution in backscattered electron mode is less in comparison to that of the secondary electron mode. In this thesis the antidot samples are measured in secondary electron mode with the electron energy ranging from 5-10 keV using the field effect SEM by Zeiss (model-Sigma) [167]. During imaging the column chamber pressure was mentioned at $\sim 1 \times 10^{-5}$ mbar whereas the gun pressure was better than 3×10^{-9} mbar.

2.2.4. Atomic Force Microscope (AFM):

Atomic force microscopy (AFM) is a powerful surface scanning technique for extracting topography related information down to atomic scale resolution. Initially, the scanning probe microscopy (SPM) was introduced which relies on proximal probing to investigate the local properties of a conducting surface. Scanning tunneling microscope (STM) was the first type of SPM introduced in 1892. STM has unique advantages over electron microscopy because they can provide 3D information about the topography as well as the physical properties of the samples. However, STM is fundamentally limited by the use of conducting substrates to guide a tunnel current. In order to overcome this deficiency, atomic force microscope (AFM) was introduced in 1986 by Binnig, Quate, and Gerber [168].

Fig. 2.8 shows schematic diagram of the working principle of a conventional AFM. The basic operation of an AFM relies on the surface force acting on the tip (which is in close proximity

to the sample surface). The probe is typically made of Si and is supported by a cantilever. The sharp tip is raster scanned over the surface using a feedback loop by adjusting the parameters required to image the surface. The feedback further helps in maintaining a constant force of interaction using a piezoelectric (PZT) scanner so that the tip does not collide with the sample. The interaction between the tip and the surface can either be long range attractive or short range repulsive type. Any change in surface height will change the force associated with it leading to deflection in the cantilever. The laser beam is focused on the cantilever and the deflection during scanning is recorded in the photodetector. The change in intensity pattern in the photodetector gives information regarding the exact topography of the sample surface.

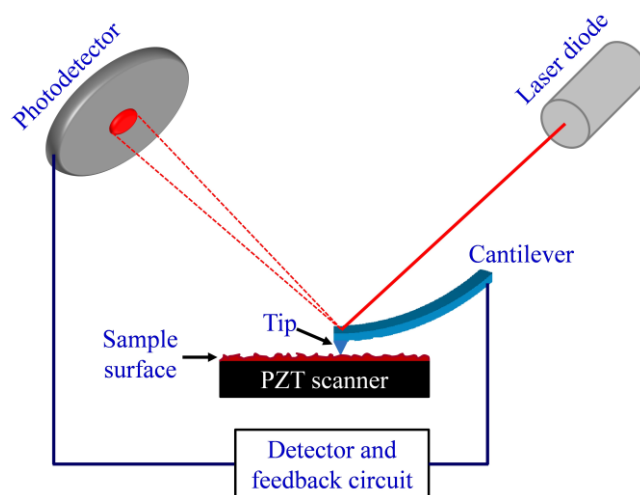


Figure 2.8: Schematic of atomic force microscopy (AFM). The laser light deflection from the tip during sample scanning is detected by the photodetector.

Fig. 2.9 shows the different regimes of interaction of forces between the tip and the surface as a function of the distance between them. The dominant form of interactions in the AFM are of Van der Waals (VdW) type. The other long-range interactions (electrostatic, magnetic, etc.) are significant further away from the sample surface. There are three primary modes of imaging in AFM:

- Contact mode (probe-surface separation < 1 nm)
- Tapping/intermittent mode (probe-surface separation $\sim 1.0 - 2.0$ nm)

- Non-contact mode (probe-surface separation $\sim 2.0 - 20.0$ nm)

In the contact mode, the probe (tip) experiences majorly repulsive VdW forces. The feedback loops are used to keep a constant cantilever deflection. This method of operation provides the advantages of fast scanning. However, often the sample surface can be damaged by this technique. For the tapping mode, the cantilever is oscillated at its resonant frequency in the vicinity of the sample surface. Here the tip gently taps the sample touching the surface at the bottom of its swing. This process results in high resolution imaging of the surface without damaging the sample. In non-contact mode, the probe does not come in contact with the sample surface. It oscillates under the attractive force during scanning. Although the probe lifetime is enhanced in this operational mode, the measurements should be performed in UHV condition for best resolution (due to requirement of fine tip-force control and absence of surface contamination).

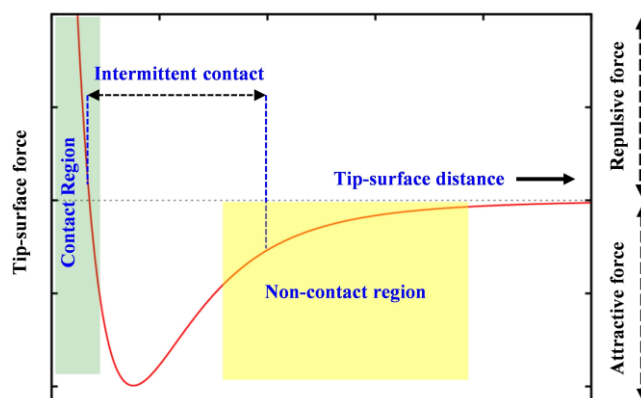


Figure 2.9: Graph showing the different force regime between a tip and surface as a function of distance between them.

We have used the AFM Nano-observer from Concept Scientific Instrument, France [169] to investigate the surface topography of the in-plane magnetized Co thin films and MAL arrays in tapping mode. The probes with tip radius < 10 nm from AppNano have been used for the scanning. The force constant and resonant frequency of the cantilever was $0.6 - 3.7$ N/m and $43 - 83$ kHz, respectively. Grain size analysis has been performed using Gwyddion software.

2.3. Magnetic Characterization:

2.3.1. Superconducting Quantum Interference Device (SQUID):

The superconducting quantum interference device (SQUID) is made of two superconductors separated by a thin insulating layer to form two parallel Josephson junctions [170-172]. SQUID magnetometers can measure the magnetic sensitivity in the order of 10^{-11} Am². The electrical current density between two superconductors through an insulator depends on the phase difference ($\Delta\phi$) between the wave functions of the superconductors. However, in a superconducting ring with two (DC SQUID) weak contacts, the additional $\Delta\phi$ is influenced by the magnetic flux (Φ) within the ring. This additional magnetic flux is representation of the magnetization of the sample. In a typical setup the sample is located within a superconducting detection coil (fig. 2.10). The coil is made of a superconducting wire wound in a three-coil configuration in a second order gradiometer geometry. The upper coil is a single turn wound clockwise, the center coil consists of two turns wound counter-clockwise, and the bottom coil single turn wound clockwise like the upper coil. In such configuration, the pick-up coil only senses the stray field contributions coming from the sample, whereas any component coming from the external fields are cancelled out. The pick-up coil is centrally placed within a superconducting electromagnet which is capable of producing uniform magnetic field in the entire coil region (fig. 2.10).

A sample is suspended from a rod mounted inside the pick-up coil. The sample vibration (up-down through the pick-up coil) leads to production of an alternating magnetic flux in the pick-up coil which in turn induces an electric current in the detection coil. Any modification in the detection coil gives rise to generation of persistent current in the detection circuit which is proportional to the magnetic flux. The device then converts the detected magnetic flux into voltage which is proportional to the magnetic moment of the sample. Finally, the output signal (V) is recorded as a function of scan position as shown in fig. 2.10. The magnetization of the

Co thin films (with both in-plane and out-of-plane anisotropies) has been measured at room temperature using the magnetic property measurement system (MPMS 3 SQUID) from Quantum Design, USA [173].

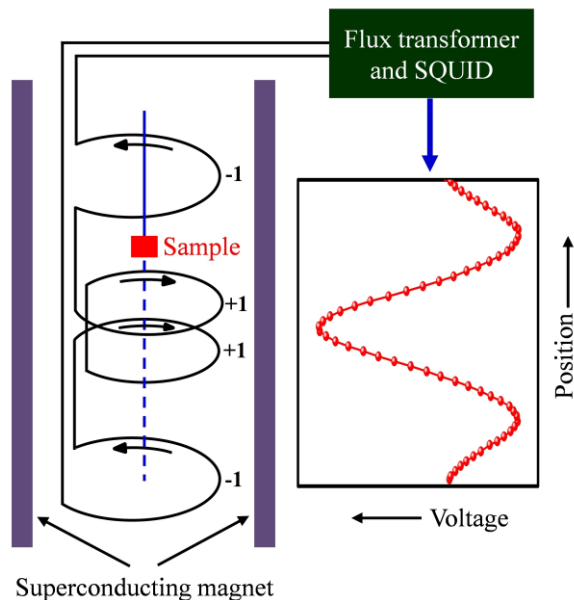


Figure 2.10: Schematic diagram of SQUID with the pick-up coil in a second order gradiometer geometry. The red curve shows a typical response signal of magnetic dipole as a function of scan length in the magnetometer. Concept of the image is taken from *ref.* [37].

2.3.2. Magneto-optic Kerr effect (MOKE) microscopy:

Magneto-optic Kerr effect is the change in polarization of the incident light after being reflected from the surface of a magnetic sample. There are different types of magneto-optic effects viz. Kerr, Faraday, Voigt, Cotton-Mouton effect, etc. [174,175]. Among various magneto-optic effects Kerr and Faraday effects are linearly proportional to the magnetization (or to the applied magnetic field) of the material. Both of these are rotational effect, with Kerr effect occurring on reflection of light from a non-transparent sample whereas in Faraday effect the plane-polarized light is rotated on transmission through optically transparent sample. Depending on the type of detector MOKE can be used in magnetometry as well as in microscopy. Kerr

microscopy is a local probing technique where domain images can be recorded at each point of the hysteresis loop. The resolution of the Kerr microscope is spatially limited by the diffraction criterion of the visible light. However, it is faster in-comparison to other domain imaging techniques viz. magnetic force microscopy (MFM), X-ray photoemission electron microscopy (XPEEM), scanning electron microscopy with polarization analysis (SEMPA), Lorentz transmission electron microscopy (LTEM), etc. Further, it provides the unique advantage of real time domain imaging over a comparatively larger area.

Kerr effect can be phenomenologically explained in terms of the dielectric law: $\mathbf{D} = \boldsymbol{\varepsilon}\mathbf{E}$, where $\boldsymbol{\varepsilon}$ is an asymmetric tensor containing the magnetization, \mathbf{E} is the electric field vector associated to the incident light, and \mathbf{D} is the induced displacement vector. Upon interaction with a magnetic medium, the relation is modified to:

$$\mathbf{D} = \varepsilon(\mathbf{E} + iQ\mathbf{m} \times \mathbf{E}) \quad (2.1)$$

where, ε is regular dielectric constant, Q is a material parameter proportional to the saturation magnetization of the medium. The dielectric tensor for a magnetic material can be expressed in matrix form as:

$$\boldsymbol{\varepsilon}' = \varepsilon \begin{pmatrix} 1 & iQ_z & -iQ_y \\ iQ_z & 1 & iQ_x \\ iQ_y & -iQ_x & 1 \end{pmatrix}$$

where, Q_x , Q_y , and Q_z are components of magnetization vector along x, y, and z-axis, respectively. \mathbf{D} can be interpreted as a reflected light amplitude generating from the interaction between the electric field of the light and magnetization vector of the medium.

The second term of equation 2.1 is similar to the Lorentz force. It is observed in fig. 2.11 that, if the Lorentz movement V_{Lor} is projected to the plane perpendicular to the propagation direction of the reflected light wave, then Kerr amplitude (\mathbf{K}) is obtained. \mathbf{K} is perpendicular to \mathbf{N} , where \mathbf{N} is the amplitude of regularly reflected light which is in the same plane as of the incident light. By applying small angle approximation, one can obtain the angle of Kerr rotation

(ϕ_K) of the polarization vector of light as $\phi_K = \frac{K}{N}$ (see fig. 2.11 (b)). The Kerr rotation amplitude K is opposite for domains with opposite magnetization direction. A domain contrast is obtained in the image plane if the reflected light from one of the domain type is blocked by the analyzer. The relative signal between the dark and bright domains can be expressed as $S \approx 4\beta KN$, where β is the angle between the analyzer and N [176].

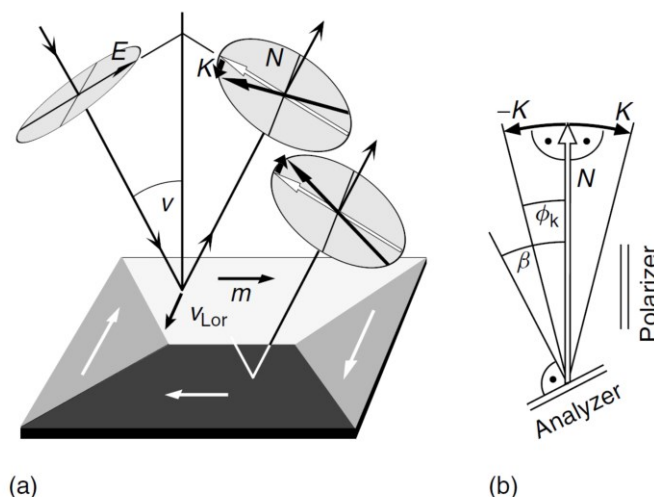


Figure 2.11: (a) Schematic of MOKE interaction for longitudinal mode. (b) The orientation of normally reflected component (N), Kerr amplitude (K), with analyzer and polarizer. The figure is taken from *ref.* [176].

Microscopically, the MOKE principle can be understood as circular birefringence. Linearly polarized light can be treated as superposition of left and right circularly polarized light with equal magnitude, angular momentum, and opposite helicity. The light drives the electrons in left and right circular motion upon interacting with a non-magnetic sample. The radius of the circular motion is equal to the electric dipole moment. However, in a magnetic sample the Lorentz force points either toward or away from the circle's centre for the left or right circularly polarized light, resulting in an unequal radius for both. This difference in the radii between the right and left circularly polarized light results in rotation of plane polarized light with Kerr rotation and ellipticity.

Fig. 2.12 shows the three possible geometries for the MOKE depending on the direction of magnetization and plane of incident light beam:

- Longitudinal Mode: In this configuration, the spontaneous magnetization direction is parallel to both the plane of incidence and sample plane.
- Transverse Mode: In this configuration, the spontaneous magnetization direction is parallel to the film surface but perpendicular to the plane of incidence.
- Polar Mode: In this configuration, the spontaneous magnetization is perpendicular (out-of-plane) to the sample surface and parallel to plane of incidence.

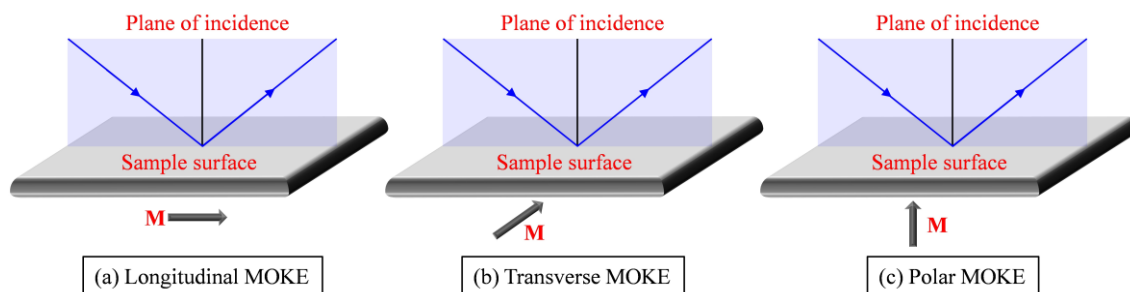


Figure 2.12: Different geometries of MOKE: (a) Longitudinal, (b) Transverse, and (c) Polar mode.

A schematic of a Kerr microscope set-up is shown in fig. 2.13. The light from a LED source passes through a polarizer and turns into plane polarized light. For simplicity, let us assume the simple two domain state of the magnetic sample which are anti-parallel to each other as indicated by the arrows in fig. 2.13. The plane of polarization of the light for beam 1 and 2 will be rotated in equal (θ) and opposite direction after reflecting from the sample surface. Now, if the analyzer is rotated crossed to one of the beams, the contrast will appear dark in the image plane for that beam. Similarly, the contrast will appear bright for the other beam. By this method, contrast between different domains are achieved in a conventional Kerr microscope.

The Kerr microscope used for domain imaging in this thesis is manufactured by Evico Magnetic Ltd., Germany [177]. The highest resolution of the microscope is obtained by oil-immersion ($n = 1.5$) based 100X objective lens. The in-plane and out-of-plane magnetized

systems have been studied in longitudinal and polar mode, respectively. The contrast of the domain images can be manually enhanced using an open software (Image J). By considering the image at saturation as the reference image, the contrast of images taken at each point of the hysteresis loop is recorded. For the relaxation measurements, first the samples were saturated and then reverse magnetic field was set to a sub-coercive value to relax the spins under constant Zeeman energy.

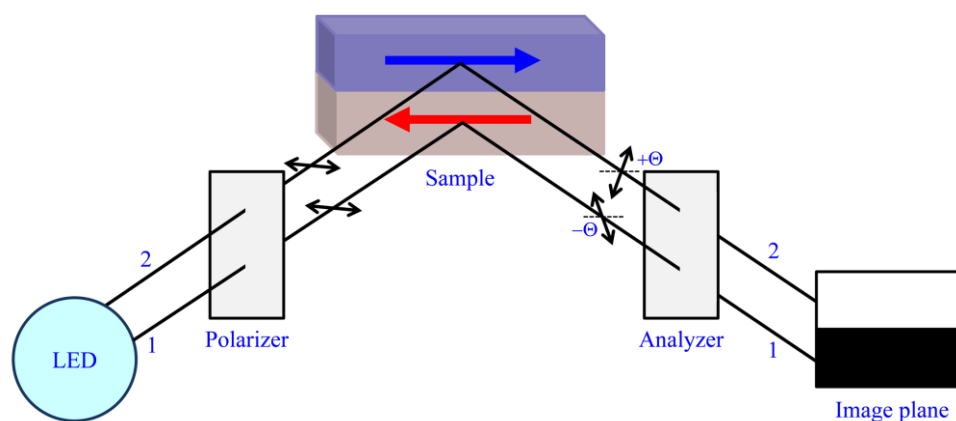


Figure 2.13: A conventional Kerr microscopy set-up. For simplicity the contrast formation is depicted with respect to two domain states. Concept of the image is taken from *ref.* [37].

2.3.3. X-ray Photoemission Electron Microscopy (XPEEM):

Due to diffraction limit of the visible light, domain imaging in magnetic nanostructures is challenging using Kerr microscopy. Intensive research work has been devoted over last few decades to discover several powerful imaging techniques viz. SEMPA, LTEM, MFM, SPLEEM, XPEEM etc. XPEEM can yield ultrafine spatial resolution (~ 20 nm) even with low numerical aperture optics. Further, it does not require any special sample treatment prior to the measurements. One of the most unique feature of XPEEM is its ability to provide element specific magnetic signal of a material. By using the concept of X-ray magnetic circular dichroism and X-ray absorption spectroscopy, XPEEM was first introduced in 1993 by Stöhr et al. [178].

The X-ray absorption spectroscopy (XAS) is a popularly used technique to determine the geometric and electronic structure of matter. The properties of the $3d$ electrons can be probed by exciting the $2p$ core electrons in the unfilled $3d$ states as shown in fig. 2. 14 (a). Due to spin-orbit coupling, the p orbital is divided in $p_{3/2}$ and $p_{1/2}$ levels (obtained from $l+s$ and $l-s$, respectively). When an X-ray radiation (with energy higher than the work function) is incident on the material, the electrons from p orbital excites to the unoccupied d orbital. The electrons which transit from $p_{3/2}$ to d states are known as the L_3 edge electrons. Similarly, the electron movement from $p_{1/2}$ to d orbital is known as the L_2 edge transition. Because of the intensity sum and selection rules, the intensity from the L_3 edge is significantly higher than the L_2 edge transition (fig. 2.14 (a)). The line intensities $I(L_3)$ and $I(L_2)$ depend on the number of unfilled electrons of d orbital [179].

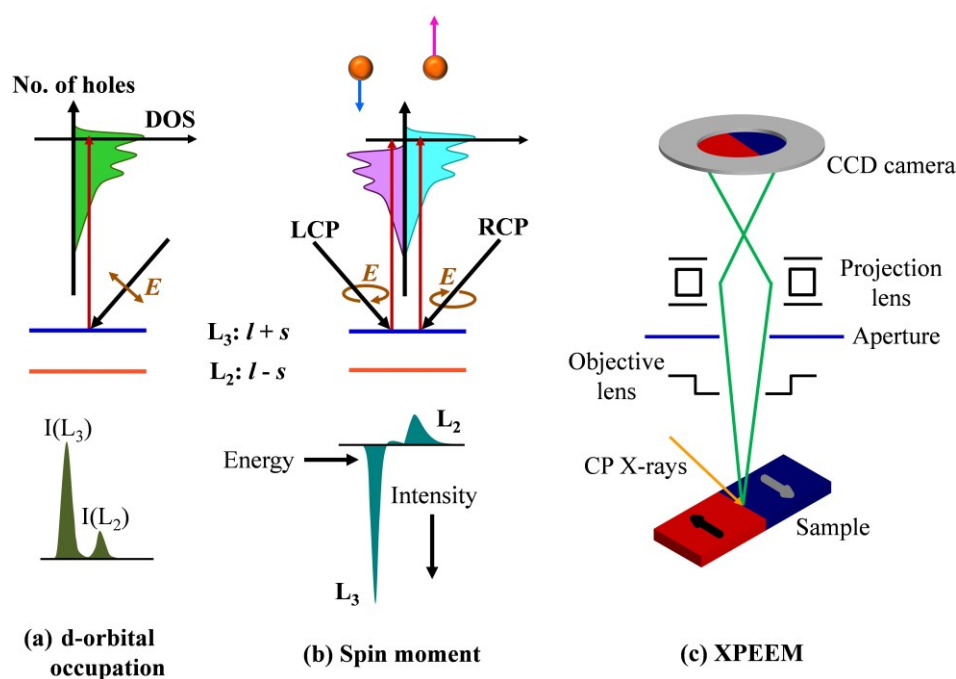


Figure 2.14: (a) Electronic transitions in conventional L -edge absorption of X-rays. (b) X-ray magnetic circular dichroism (XMCD) phenomenon presented for one-electron model. (c) Schematic of X-ray photoemission electron microscopy (XPEEM) phenomenon to obtain magnetic contrast. Concept of image taken from *ref.* [179]

The information regarding magnetism of the material can be extracted by the use of circularly polarized X-rays. The right and left circularly polarized (RCP and LCP) photons transfer their angular momentum (\hbar and $-\hbar$, respectively) to the photoelectrons. Hence, photoelectrons with opposite spins are created for RCP and LCP photons. Let us define the XMCD contrast as the difference between the intensities obtained from the RCP and LCP photons. Expectedly, the XMCD intensity at L_3 edge is higher than that at the L_2 edge as shown in fig. 2.14 (b). Again, due to the opposite spin-orbit coupling of $p_{3/2}$ and $p_{1/2}$ levels, the XMCD intensity for L_3 and L_2 edge are opposite to each other [179]. In case of absorption, ‘spin-up’ and ‘spin-down’ states are defined in terms of photon helicity or spin which in turn is parallel (RCP) or antiparallel (LCP) to the direction of X-ray propagation. Since ‘spin-flip’ is forbidden in electric dipole transition, the spin-up (or down) photoelectrons from the p orbital can only be excited to the spin-up (or down) unfilled d orbital. Hence, the transition intensity is directly proportional to the number of unfilled d orbital. Hence, typically the XMCD signal at L edge of Fe is higher than that of Co and Ni.

XPEEM is a surface sensitive X-ray absorption technique since the contrast is generated by lateral variation of the X-ray absorption cross section [180]. XPEEM is performed by imaging the secondary electrons and hence the signal is generated from the top 2-5 nm [181]. The XMCD intensity of the L edges is used to create the magnetic domain contrast. Since the energy of the incident X-ray can be tuned to generate photoelectrons from different materials, XPEEM provides the unique opportunity to image the magnetic contrast coming from individual element of a sample. In a typical set-up, a monochromatic X-ray beam is focussed on a sample to create excited electrons (fig. 2.14 (c)). The electrons are accelerated by electric field between the sample and outer electrode of the objective lens. Successively, the electrons are guided through a series of projection lenses for image magnification and ultimately the final image is captured by a CCD camera. The spatial resolution in PEEM is determined by the resolution of

the electron optics and the intensity is proportional to the flux-density of the X-rays. X-rays are produced by ejecting the electrons inside three particle accelerators: linear accelerator, booster synchrotron, and the storage ring. We have used the *I06: Nanoscience* beamline of Diamond Light Source, UK, [182] to perform the XPEEM measurements on the Heusler alloy antidots. A schematic diagram of the XPEEM facility at *I06* beamline is shown in fig. 2.15. The working energy range of X-ray in this beamline is 106-1300 eV whereas the spot size of the X-ray is 200 μm . The spatial resolution of this system is better than 20 nm. The samples must be conductive to avoid charging effects during the measurement. The measurements for our samples are performed by tuning the X-ray to the L_3 edge of Fe and by keeping the direction of X-ray aligned to the easy axis.

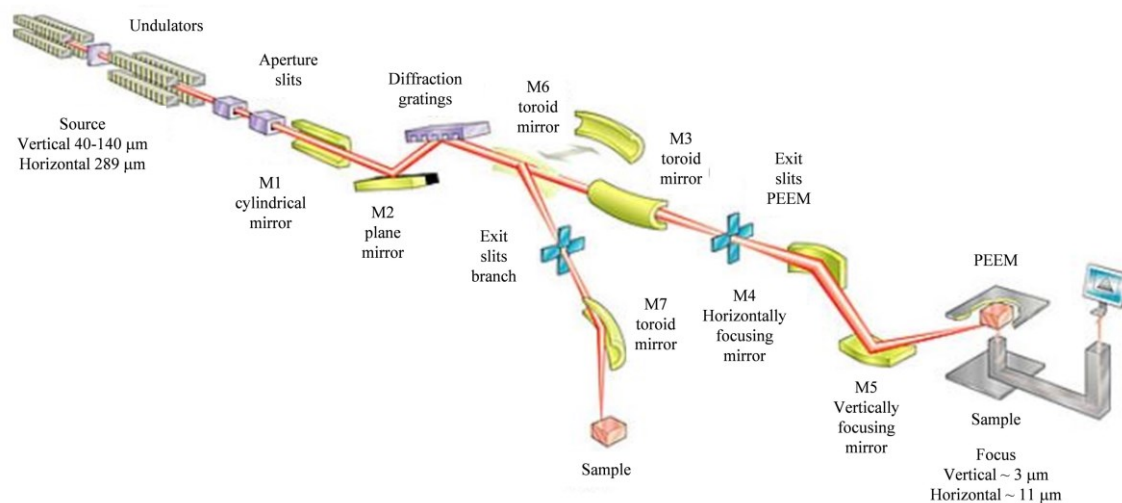


Figure 2.15: Schematic layout of the XPEEM at *I06* beamline at Diamond Light Source, UK [182].

2.3.4. Ferromagnetic Resonance (FMR) spectroscopy:

Ferromagnetic resonance (FMR) is a technique to measure the dynamic magnetization by detecting the precessional motion of the spins in a ferromagnetic sample. The working principle of FMR is very similar to electron paramagnetic resonance technique [183]. First experimental demonstration of FMR was provided by D. J. Griffiths in a measurement along to the Purcell-

Torrey-Pound nuclear resonance experiment [184]. However, it was observed that the resonant frequency was substantially larger than the Larmor frequency. Kittel provided the explanation for this anomaly by considering macrospin formalism where it was assumed that the magnetization is uniform throughout the sample [133,134]. From the macroscopic point of view the phenomenon can be explained by the spins of a magnetic material precessing around the applied magnetic field (H). The precession continues until the relaxation process damps it. Now, let's assume that the sample is put under a transverse ac field (h_{RF}), where the frequency of the RF field matches with the precessional frequency of the magnetic material. In this scenario the resonance condition is satisfied and the microwave power gets absorbed by the material. This leads to formation of a peak in the absorption spectra. The magnitude of the external magnetic field for which the precessional frequency matches with the frequency of the RF signal is known as the resonance field H_R .

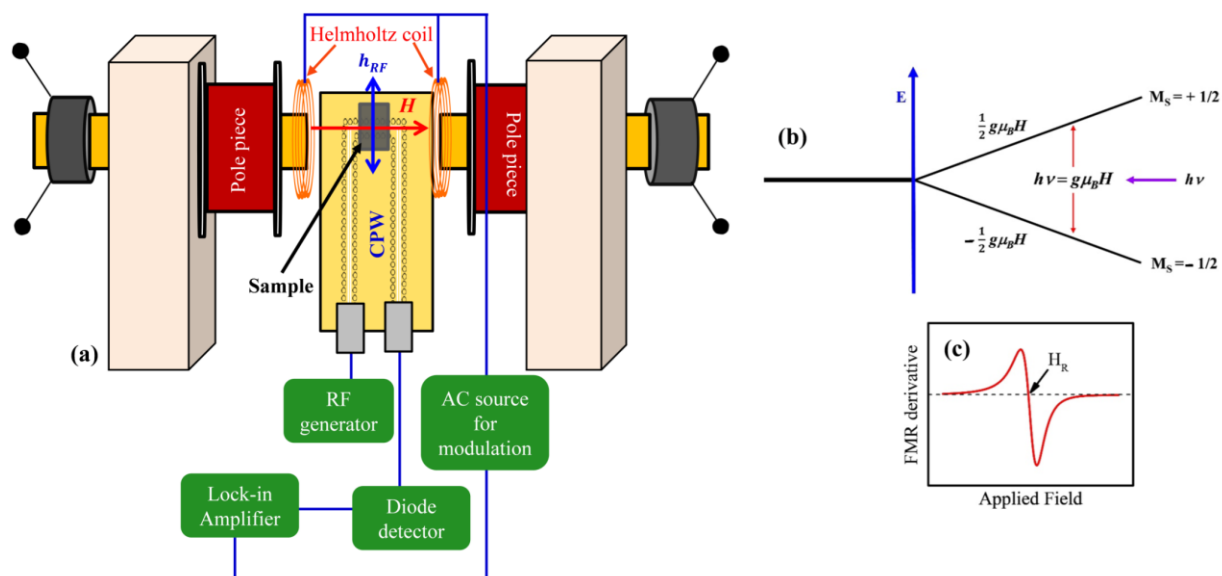


Fig. 2.16: (a) A schematic diagram of an FMR set-up showing the sample position on the CPW with respect to H and h_{RF} , (b) Zeeman splitting by application of an external magnetic field (H), (c) a typical FMR signal as a function of applied field.

From microscopic point of view, the mechanism can be understood in terms of Zeeman splitting between the energy levels under the application of an external magnetic field. Energy

separation due to Zeeman splitting between two energy levels is $g\mu_B H$, where g is the Landé g factor, and μ_B is Bohr magneton. The energy levels of the free electrons are splitted at $\pm \frac{1}{2}g\mu_B H$. Now, if an electromagnetic radiation (RF field) with frequency ν is applied where $h\nu = g\mu_B H$, the material absorbs the energy to reach the excited state. Since the resonance frequency of the magnetization depends on the local field, sweeping the external magnetic field by maintaining a constant frequency of the RF field will lead to an absorption spectrum corresponding to the FMR response at that particular frequency.

Fig. 2.16 (a) shows schematic of our set-up based on coplanar waveguide based ferromagnetic resonance (CPW-FMR). Fig. 2.16 (b) shows the Zeeman splitting of electron energy levels with application of an external H , whereas (c) shows a typical FMR spectra showing the presence of resonance field (H_R). We have used a CPW-FMR manufactured by NanoOsc Instruments, Sweden [185]. The FMR Bandwidth is 2-18 GHz and the maximum applied field is ~ 0.42 T. We have performed angle dependent FMR measurements to study the anisotropy nature of the Heusler alloy and in-plane magnetized Co thin films. Further, we have performed frequency dependent FMR measurements to extract information regarding the damping of the systems.

2.3.5. Time Resolved MOKE (TR-MOKE) magnetometer:

The precessional dynamics of the Heusler alloy antidots and their thin film counterpart have been measured using the all-optical TR-MOKE setup in the lab of Prof. Anjan Barman, at S. N. Bose National Centre for Basic Sciences (SNBNCBS), Kolkata. Fig. 2.17 shows the schematic of the TR-MOKE setup with collinear pump-probe geometry. The diode pumped solid state (DPSS) laser is pumped by an array of diode lasers to produce laser with the wavelength of 532 nm and a maximum power of 10 W. Further, the output of the DPSS laser pumps the Ti-Sapphire laser. Regenerative mode locking leads to production of laser pulses with ~ 70 fs width and maximum average power of 2W with ~ 2 mm spot size at a repetition

rate of 80 MHz. The output of the laser is fixed at 800 nm for obtaining better spectral response of Si based detectors.

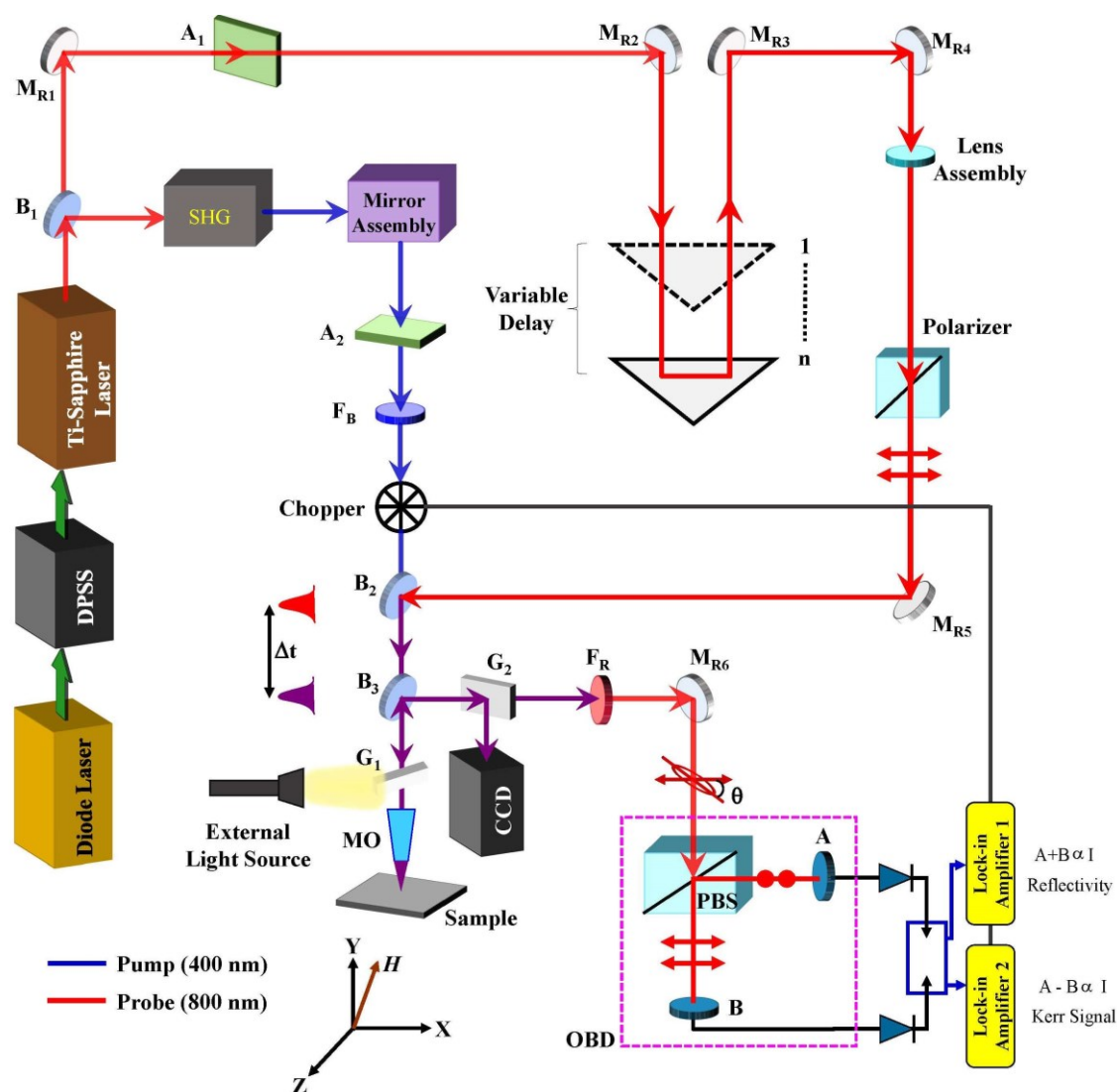


Fig. 2.17: A schematic diagram of a TR-MOKE set-up with collinear pump-probe geometry. Concept of the image is taken from *ref.* [129].

The beam splitter (B_1) splits the laser beam into two parts (70:30). The maximum power beam goes through a second harmonic generator (SHG) to produce laser pulses with wavelength of 400 nm, which will be further used to pump the samples. The beam passes through a mirror assembly, which comprises of broadband mirror in the wavelength region of 400-750 nm to eliminate the residual fundamental beam. The beam power is attenuated using a variable natural density filter (A_2) and further passed through a filter (F_B) to reduce remaining residual

fundamental beam. The pump is modulated by a mechanical chopper oscillating at 2 kHz, which is used as the reference signal of the lock-in amplifier during the phase sensitive detection. The relatively low power probe beam is passed through an optical path using a set of highly reflecting mirror assembly (M_{R1} , M_{R2} , M_{R3} , M_{R4}). The beam is passed through a variable delay circuit to manually tune the delay (Δt) between the pump and the probe beam. The probe beam is then passed through a lens assembly (kept in telescopic arrangement) to increase the beam diameter to fill the back-aperture of the microscope objective. Next, the beam is polarized by passing through a Glan-Thompson polarizer.

The modulated pump beam and linearly polarized probe beam are combined using a 50:50 non-polarized beam splitter (B_2). The combined beam enters the microscope objective (MO) at normal incidence. The sample is mounted on a stage, which is controlled via piezo-electric scanner. The probe beam is focused at the center of the pump beam. The back reflected beams are collimated by the beam splitter B_3 towards the detector. The beams further pass through the spectral filter (F_R) which blocks the pump beam and sends the probe beam to the optical bridge detector (OBD). A polarized beam splitter (PBS) present inside the OBD separates the beam into two orthogonally polarized components. OBD measures the Kerr rotation and further separates from the reflectivity signal. Hence, by this method the spin (Kerr rotation) and phonon dynamics (reflectivity) can be separated from each other [129].

In a typical measurement, samples are kept under an external magnetic field higher than the saturation field of the samples. When the high-power pump beam hits the samples, due to thermal energy, the sample loses its magnetization. However, the heat is quickly dissipated, and the sample starts remagnetizing slowly. Under the application of strong magnetic field, the spins start precessing around the applied magnetic field direction. The probe beam falls on the samples with a certain delay (Δt) controlled by the variable delay circuit. The beam interacts with the magnetic spins and the Kerr signal is analyzed at the detector circuit.

CHAPTER 3: MAL arrays of Co with in-plane anisotropy

In this chapter the structural and magnetic properties of thin films and MAL arrays of Co with in-plane anisotropy have been discussed. It has been reported in our previous works that in-plane uniaxial magnetic anisotropy (UMA) gets introduced in the samples due to oblique angular deposition arising from the geometry of the sputtering chamber [9,16,186]. Such growth induced magnetocrystalline anisotropy hinders other anisotropy contributions which are desired to tune the effective anisotropy of the system from application as well as fundamental research point of view [12,13]. It is also noted that substrate rotation of 20 rpm (which is the maximum possible substrate rotation speed in our sputtering chamber), is not sufficient to completely remove the growth induced UMA [9,16,186]. In this thesis we have explored the possibility of growing isotropic Co film by varying the deposition conditions [11]. We have further prepared magnetic antidot lattice (MAL) arrays of Co with in-plane anisotropy by choosing proper combination of seed layer and deposition temperature to obtain films with rich structural and magnetic properties viz., homogeneous distribution of grains, low magnetic damping, etc. We have tuned the domain structure, anisotropy, and magnetic relaxation of the antidot arrays by varying the deposition conditions. Formation of smaller domains and precise control over domain size by changing the antidot architecture paves a path for future magnetic data storage technology [13]. By employing substrate rotation during deposition, the relaxation speed in the in-plane magnetized antidots can be increased in comparison to the antidots prepared without any substrate rotation [12]. However, the magnetic relaxation mechanism for the antidots is slower in comparison to the parent continuous thin film of Co with in-plane anisotropy [12,13,16]. Such slow relaxation is not desired from application point of view due to requirement of fast reading and writing of information in modern data storage technology. We will show in the next chapter that such slow relaxation in the antidots can be avoided by preparing MAL arrays of Co with out-of-plane anisotropy [21].

The content of this chapter can be broadly subdivided into three parts:

3.1. Formation of isotropic Co thin films with in-plane magnetization.

3.2. Tuning the anisotropy, domain structure, and magnetic relaxation in MAL arrays of Co with in-plane anisotropy.

3.3. Controlling the relaxation dynamics and magnetization switching of in-plane magnetized antidot arrays of Co by employing substrate rotation.

3.1. Formation of isotropic Co thin films with in-plane magnetization:

Understanding the anisotropy in magnetic thin films has direct implications in various aspects viz. ultrahigh density storage technology, biomedical applications etc. [187,188]. High UMA is desired in magnetic recording media, high frequency magnetic and magnetostrictive random access memory devices. There are various methods to induce UMA in a system such as oblique angular deposition, application of magnetic field during deposition, magnetic annealing, growth of films in stepped substrate, etc. [161,189-191]. Among different mechanisms, formation of UMA owing to oblique angular deposition is common due to occurrence of columnar structure or formation of elongated adatoms during the growth [192,193]. On the other hand, films with extremely low anisotropy is often desired in transformers, microwave devices, etc. [10,194]. Further, the dominant contribution of the growth induced anisotropy may suppress other anisotropy contributions (viz. shape anisotropy arising from the antidot architecture) which are desired to control the effective anisotropy of the systems [12,13]. Hence, often it becomes necessary to tune the total anisotropy of the system from both applications and fundamental research point of view [194-196]. It has been observed in our previous studies that substrate rotation speed of 20 rpm reduces the anisotropy, however, cannot completely remove it [9,16,186]. Another way of decreasing the anisotropy is by growing the films at high temperature or post annealing [193,197]. Therefore, a combination of both growth temperature and substrate rotation may lead to a well-controlled recipe for

tuning the anisotropy in such films. In this section, we show the combined effect of substrate rotation (ω), and deposition temperature (T_{dep}) on the anisotropy and damping properties of Co thin films. We show that by using both ω and T_{dep} , it is possible to synthesize isotropic films. To check the wide applicability of the proposed growth conditions, we have explored the possibility of forming isotropic films on two different combinations of the seed layers (Au as well as AlO_x).

Table 3.1: Sample structure of in-plane magnetized Co thin films on Au and AlO_x seed layers

Sample Name	Sample Structure	Sample Type	Deposition condition	
			Deposition temperature (T_{dep})	Substrate rotation (ω)
S1-TF-A	Series 1: Si(100)/Au(2 nm)/Co(10 nm)/Au(3 nm)	Thin film	RT	0 rpm
S1-TF-B			RT	10 rpm
S1-TF-C			RT	20 rpm
S1-TF-D			200°C	0 rpm
S1-TF-E			200°C	10 rpm
S1-TF-F			200°C	20 rpm
S2-TF-A	Series 2: Si(100)/AlO _x (2 nm)/Co(10 nm)/AlO _x (2 nm)	Thin film	RT	0 rpm
S2-TF-B			RT	10 rpm
S2-TF-C			RT	20 rpm
S2-TF-D			200°C	0 rpm
S2-TF-E			200°C	10 rpm
S2-TF-F			200°C	20 rpm

Table 3.1 shows the detailed sample structure for all the in-plane magnetized thin film samples prepared with Au or AlO_x seed layers on Si (100) substrates in a vacuum chamber with the base pressure better than 7×10^{-8} mbar. The acronym TF has been used in the sample naming to denote the thin film samples. The thin film heterostructure of Si (100)/Au (2 nm)/Co (10 nm)/Au (3 nm) and Si (100)/AlO_x (2 nm)/Co (10 nm)/AlO_x (2 nm) have been grown at Ar pressure of 5×10^{-3} mbar. Prior to the deposition, the Si substrates have been cleaned in acetone

and isopropanol each for 10 minutes and were blow dried using N₂ gas (5N purity). The bottom Au/AlO_x works as a seed layer reducing the strain due to lattice mismatch between Si and Co whereas the top Au/AlO_x works as a capping layer protecting the films from oxidation. Au has been deposited by e-beam evaporation with the rate of ~0.01 nm/s. The insulating AlO_x layers have been deposited using RF sputtering from an Al₂O₃ target with the rate of ~ 0.005-0.006 nm/s. Due to the deficiency of O₂ during deposition inside the vacuum chamber, the stoichiometry of Al₂O₃ was not proper and hence we have denoted it as AlO_x throughout the thesis. Co has been deposited using DC sputtering technique at a rate of ~0.02 nm/s. Due to the geometry of the deposition chamber, the plume direction leads to oblique angular deposition which in turn introduces uniaxial anisotropy in the samples. The substrate has been rotated upto 20 rpm to control the strength of the induced uniaxial anisotropy. The films have been prepared for both AlO_x and Au as seed layers at room temperature as well as at 200°C to investigate the possibility of complete removal of the growth induced anisotropy.

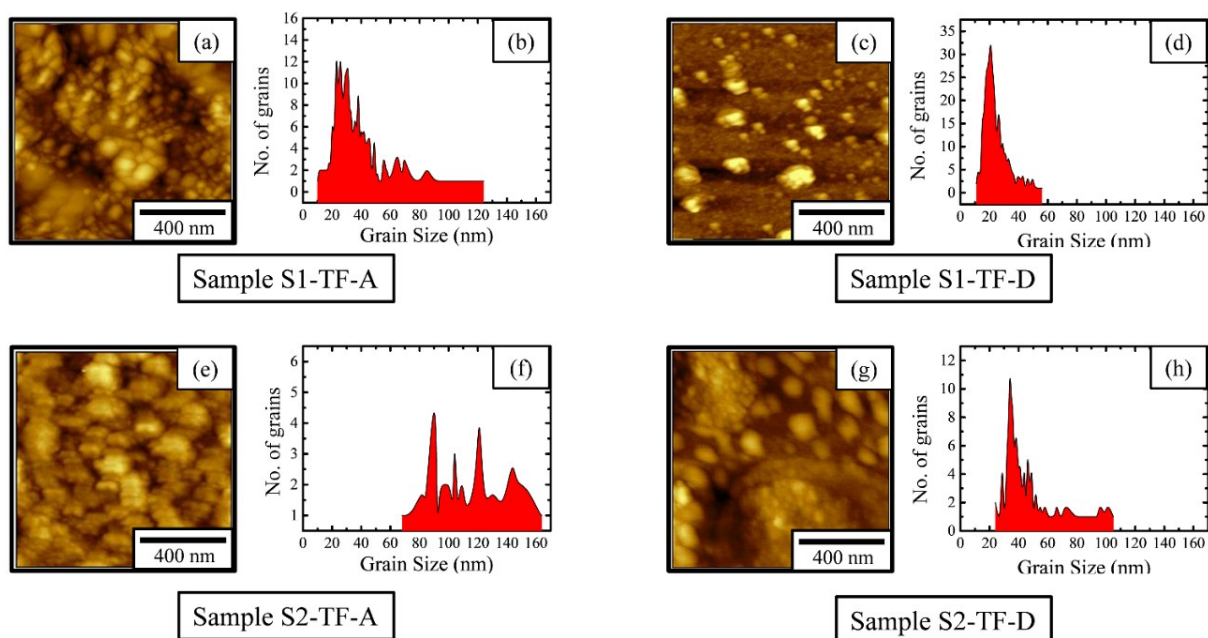


Figure 3.1: AFM image and grain size distribution for samples S1-TF-A (a & b), S1-TF-D (c & d), S2-TF-A (e & f), and S2-TF-D (g & h), respectively. All the AFM images are in same length scale.

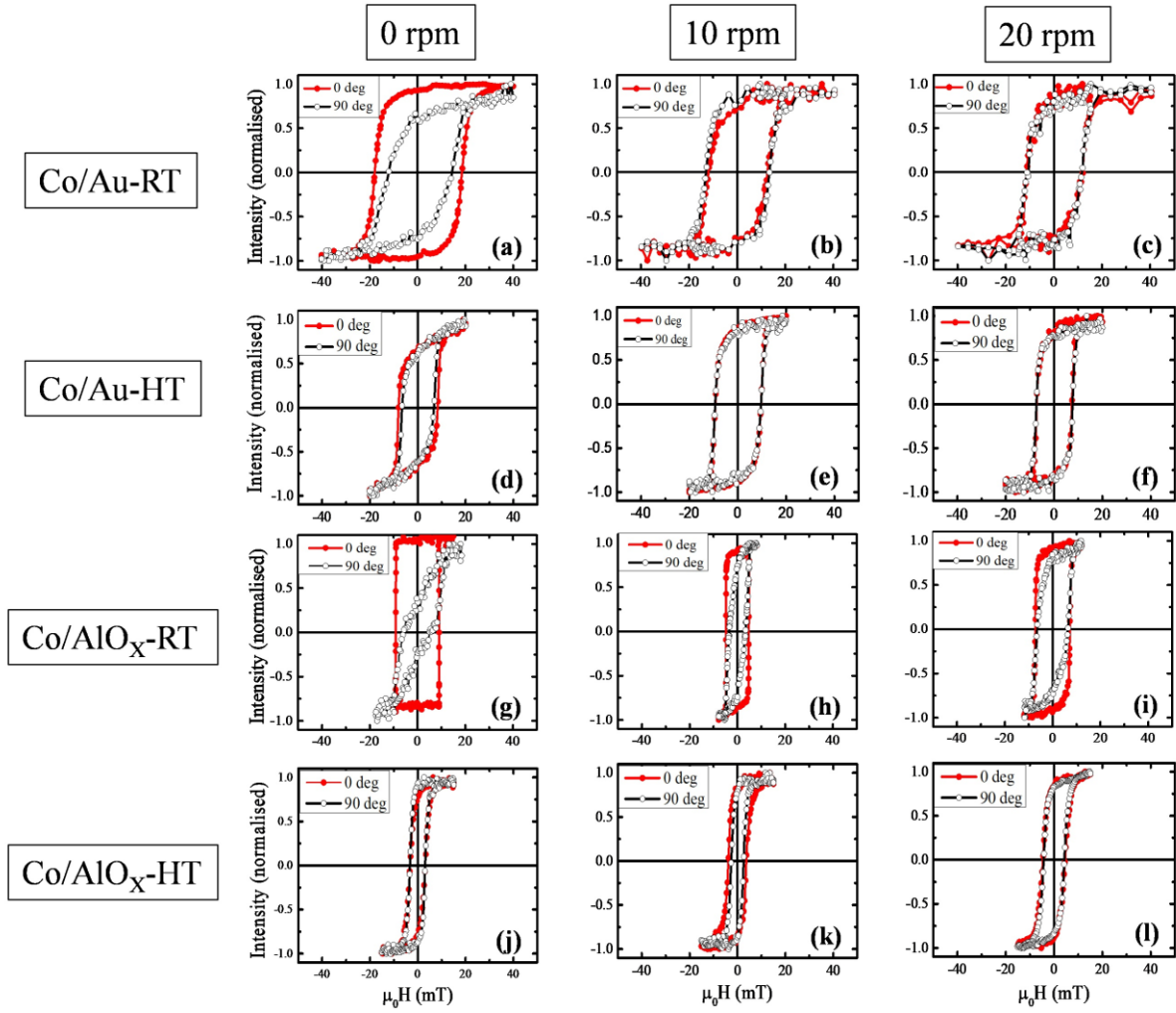


Figure 3.2: Hysteresis loops for series 1 samples S1-TF-A – S1-TF-F (a – f), and series 2 samples S2-TF-A – S2-TF-F (g – l), respectively, along the EA ($\phi = 0^\circ$) (red line with solid circle) and HA ($\phi = 90^\circ$) (black line with open circle). (g – l) are reproduced with permission from *ref.* [9]. The samples prepared at room temperature and 200°C are represented by RT and HT, respectively.

Fig. 3.1 shows the AFM images and corresponding grain size distribution for samples S1-TF-A (a), (b); S1-TF-D (c), (d); S2-TF-A (e), (f), and S2-TF-D (g), (h), respectively. From fig. 3.1(b) and (d), it has been observed that the grain size distribution becomes narrower for the Co/Au film (sample S1-TF-D) prepared at high temperature when compared to the Co/Au film deposited at RT (sample S1-TF-A). Similarly, the grain size distribution is narrow for sample

S2-TF-D in comparison to that of sample S2-TF-A (fig. 3.1(f), (h)). Hence, we note that the growth uniformity increases with increase in T_{dep} for Co films with both kind of seed layers. Further, the average size of the grains decreases for the samples deposited at high temperatures. However, it should be noted that, in comparison to Co/Au films the average grain size is relatively higher in Co/AlO_x films.

Fig. 3.2 shows the hysteresis loops measured by Kerr microscope at RT along the EA ($\phi = 0^\circ$) (red line with solid circles) and HA ($\phi = 90^\circ$) (black line with open circles) for samples S1-TF-A – S1-TF-F (a – f), and samples S2-TF-A – S2-TF-F (g – l), respectively. From the loops it has been observed that the squareness (M_R/M_S) of the loops along the HA increases with increase in substrate rotation for samples with both types of seed layers. The nature of the loops along EA and HA follow similar trend for samples S1-TF-A (fig. 3.2(a)), and S2-TF-A (fig. 3.2(g)). However, a ferromagnetic sample with profound UMA is expected to yield perfect square loop along the EA and s-shaped (closed) loop along the HA. Equivalent shape of the hysteresis loops along EA and HA indicates reduction in UMA with increase in T_{dep} and ω for films with both kind of seed layers. The reduction in anisotropy due to increase in T_{dep} can be attributed to the reduction in aspect ratio of the adatoms [193]. By comparing the saturation magnetic field (H_S) for series 1 (Co films with Au seed layer) with that of series 2 (Co films with AlO_x seed layer) we conclude that samples in series 2 is magnetically softer in comparison to series 1.

Fig. 3.3 shows the H_C vs ϕ plot for samples S1-TF-A – S1-TF-C (a), samples S1-TF-D – S1-TF-F (b), samples S2-TF-A – S2-TF-C (c), and samples S2-TF-D – S2-TF-F (d), respectively. For both the series we have found that the samples prepared without any substrate rotation ($\omega = 0$ rpm) (red curves with solid circular dots), exhibit uniaxial anisotropy symmetry with the EA along $\phi = 0^\circ$ and 180° , respectively. The uniaxial anisotropy is induced due to the oblique angular deposition owing to the geometry of the sputtering target with respect to the substrate

position. As discussed in section 2.1.2, due to the geometry of the deposition chamber, all the targets are at $\psi = 30^\circ$ angle with respect to the substrate normal (fig. 2.4). Hence, the easy axis of the uniaxial anisotropy is induced along the perpendicular to the in-plane projection of the plume direction in the samples. The columnar growth of grains perpendicular to the plume direction is discussed in *ref.* [161]. The long axis of the crystallites, due to such columnar growth forms chain like structure leading to the induced UMA.

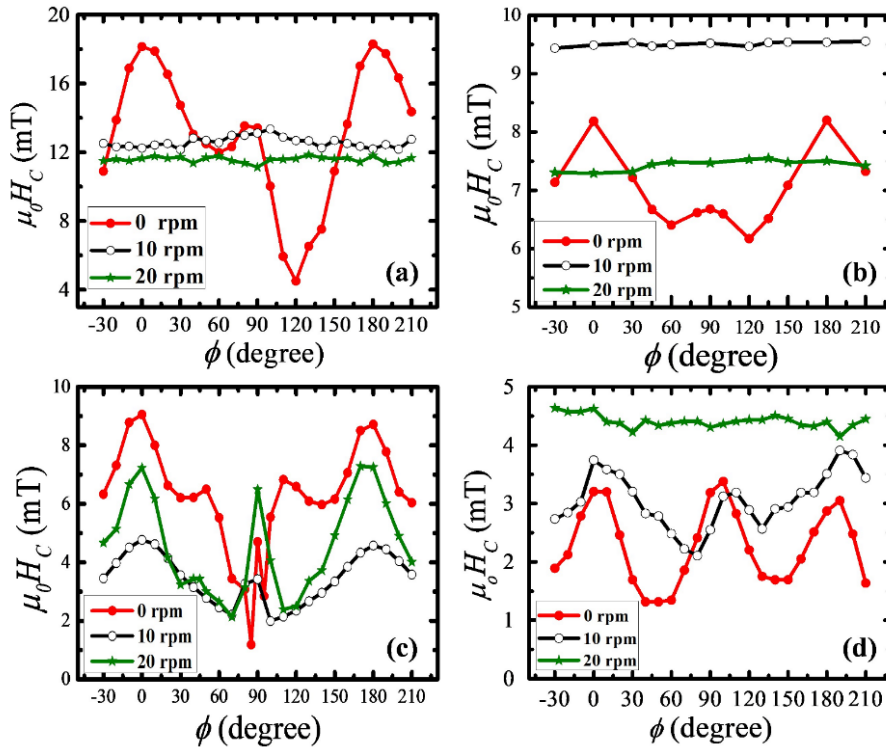


Figure 3.3: Coercivity (H_C) vs ϕ plot for samples S1-TF-A – S1-TF-C (a), S1-TF-D – S1-TF-F (b), S2-TF-A – S2-TF-C (c), and S2-TF-D – S2-TF-F (d). Red line with solid circle, black line with open circle, and green line with solid star, represents the samples prepared with $\omega = 0, 10,$ and 20 rpm, respectively. Fig. 3.3 (c) is reproduced with permission from *ref.* [9].

However, in fig. 3.3 it is seen that for all the samples prepared with $\omega = 0$ rpm, there is a peak along the HA ($\phi = 90^\circ$). This peak arises due to the misalignment of the local grain anisotropy [9,198]. Considering two-grain Stoner-Wohlfarth model with inter-granular exchange coupling

and grain misalignment, the energy equation can be written as [124,198]:

$$E = -J\mathbf{m}_1 \cdot \mathbf{m}_2 - \mathbf{H} \cdot (\mathbf{m}_1 + \mathbf{m}_2) - \frac{1}{2}K_1(\mathbf{m}_1 \cdot \mathbf{n}_1)^2 - \frac{1}{2}K_2(\mathbf{m}_2 \cdot \mathbf{n}_2)^2 \quad (3.1)$$

where, J is the intergranular exchange coupling constant between the two neighboring grains with magnetization vectors \mathbf{m}_1 and \mathbf{m}_2 . The respective magnetocrystalline anisotropy axes are represented by unit vectors \mathbf{n}_1 and \mathbf{n}_2 . Since, the neighboring grains are made up of same material Co, hence the respective magnetocrystalline anisotropy constants K_1 and K_2 are equal in magnitude. Since, the films studied here are having in-plane magnetic anisotropy, the magnetization vectors (\mathbf{m}_1 and \mathbf{m}_2) can be assumed to be restricted in the x-y plane. Hence, eqn. 3.1 can be reduced to:

$$E = -J\cos(\theta_1 - \theta_2) - H[\cos(\theta_1 - \phi) + \cos(\theta_2 - \phi)] - \frac{1}{2}K_1[\cos^2\left(\theta_1 - \frac{\Omega}{2}\right) + \cos^2\left(\theta_2 - \frac{\Omega}{2}\right)] \quad (3.2)$$

where, θ_1 , θ_2 , and ϕ are the in-plane orientation angles of \mathbf{m}_1 , \mathbf{m}_2 , and \mathbf{H} , respectively, wrt to the average anisotropy axis. Ω is defined as the angle of misalignment between the two grains. It has been reported that upto a critical value Ω_C , the system follows single grain Stoner-Wohlfarth behavior (nearly full M_R along the EA and vanishing M_R along the HA) [198]. However, above Ω_C , there exist a finite range of ϕ near the HA, where \mathbf{m}_1 and \mathbf{m}_2 exhibit opposite rotational direction. This results in increase of M_R and H_C in the hysteresis loops which leads to the formation of disorder peaks in the coercivity plots around the HA [198]. The peak width and height increases with increasing disorder between the neighboring grains in the system. It should be noted that the Co films on Si (100) grow in polycrystalline structure. This is the reason behind formation of such large (wide) disorder peaks around the HA in the samples. Further, it is observed in fig. 3.3 that, the strength of the anisotropy decreases with increase in T_{dep} . However, the strength of the peak along the HA does not vary significantly with change in T_{dep} . Hence, the contribution of the disorder peak along the HA becomes further prominent for the films prepared with $T_{\text{dep}} = 200^\circ\text{C}$.

The strength of the anisotropy energy associated to the disorder peaks at the HA has been calculated by fitting the angular dependence of coercivity data with one grain Stoner-Wohlfarth model. The fitting equation is:

$$H_C = (H_C)_{HA} + (H_C)_{EA} \cos\phi \quad (3.3)$$

Where, $(H_C)_{EA}$ and $(H_C)_{HA}$ are the coercive fields along the EA and HA, respectively. Fig. 3.4 shows the angular dependent coercivity plots fitted with Stoner-Wohlfarth model for (a – d) samples S1-TF-A, S1-TF-D, S2-TF-A, and S2-TF-D, respectively. The amplitude of disorder (H_D) is calculated by subtracting the fitted $(H_C)_{HA}$ value from the experimental H_C value at the HA ($\phi = 90^\circ$). This is shown by the blue line in fig. 3.4.

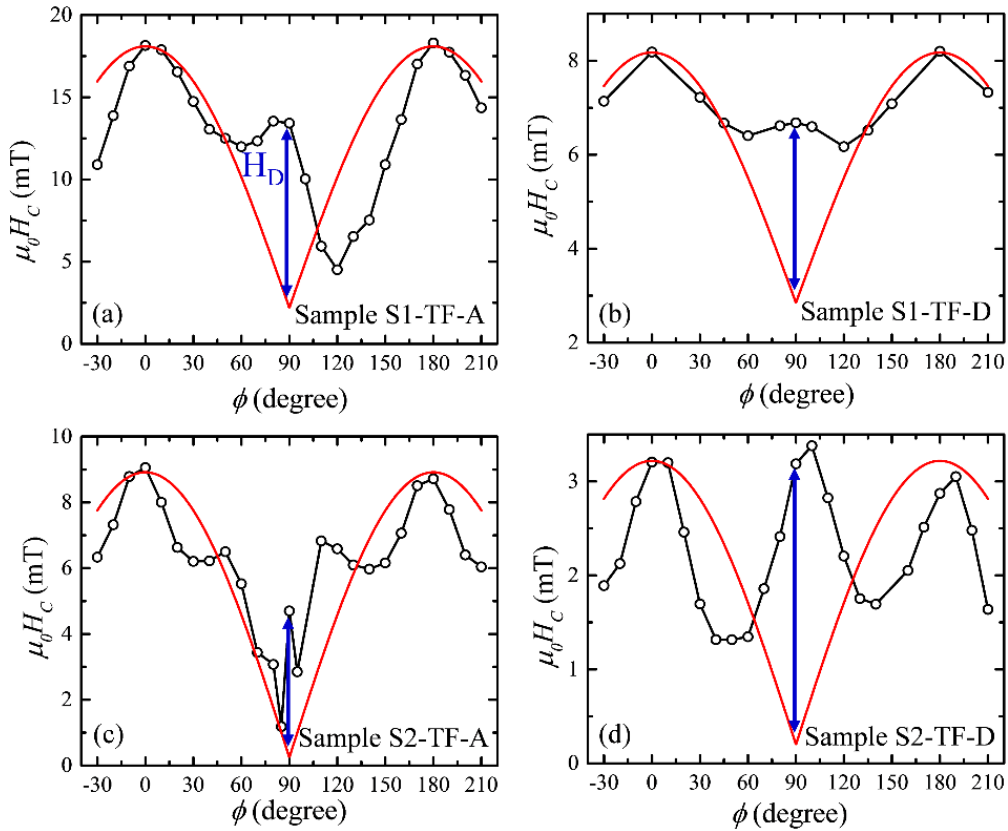


Figure 3.4: Angular dependence of coercivity plots fitted with Stoner-Wohlfarth model for (a – d) samples S1-TF-A, S1-TF-D, S2-TF-A, and S2-TF-D, respectively. The black open circles are the experimental data points whereas the red lines are the fitted curve using eqn. 3.3.

The value of H_D are 11.22, 3.85, 4.45, and 2.98 mT, for samples S1-TF-A, S1-TF-D, S2-TF-A, and S2-TF-D, respectively. The value of M_S obtained from the room temperature SQUID measurements are 8.56×10^5 , 9.84×10^5 , 13.85×10^5 , and 7.95×10^5 A/m, for samples S1-TF-A, S1-TF-D, S2-TF-A, and S2-TF-D, respectively. The anisotropy energies corresponding to the disorder peaks are calculated using the formula:

$$K_{disorder} = \frac{\mu_0 H_D M_S}{2} \quad (3.4)$$

The calculated disorder anisotropy energies along the hard axis are 4.80×10^3 , 1.89×10^3 , 3.08×10^3 , and 1.18×10^3 J/m³, for samples S1-TF-A, S1-TF-D, S2-TF-A, and S2-TF-D, respectively. A comparison between the local anisotropy energy associated to disorder and the global anisotropy energy for the samples has been discussed later.

It is observed from the nature of H_C vs ϕ plots in fig. 3.3 (a) and (b) that for series 1 (films with Au seed layer), $\omega = 10$ rpm (black curve with open circular dots) leads to formation of isotropic film. Further, in series 1 with the increase in ω to 20 rpm (green curve with solid stars), the samples sustain the isotropic nature. On the other hand, fig. 3.3 (c) reveals that in series 2 (films with AlO_x seed layer) for the films prepared at RT (samples S2-TF-A – S2-TF-C), $\omega = 20$ rpm reduces the anisotropy of the system, however the anisotropy still persists. Nevertheless for samples S2-TF-D – S2-TF-F (i.e. Co films prepared at 200°C with AlO_x seed layer), $\omega = 20$ rpm leads to the formation of isotropic film. Hence, it can be concluded that, for series 1, only rotation of substrate during deposition may lead to formation of isotropic film. Whereas, for series 2 a combination of ω and T_{dep} need to be varied to obtain isotropic film.

Fig. 3.5 shows the variation of ΔH_C ($H_{C_{max}} - H_{C_{min}}$) as a function of ω for samples S1-TF-A – S1-TF-C (solid circles in pink color), samples S1-TF-D – S1-TF-F (solid triangles in blue color), samples S2-TF-A – S2-TF-C (open stars in orange color), and samples S2-TF-D – S2-TF-F (open diamonds in cyan color), respectively. $H_{C_{max}}$ and $H_{C_{min}}$ are maximum (along EA)

and minimum values of coercivity, respectively. We note that $H_{C_{min}}$ does not necessarily correspond to the value of H_C at HA ($\phi = 90^\circ$) because of the presence of peak around the HA. Fig. 3.5 further confirms that the strength of anisotropy decreases significantly for both the series 1 and 2 when deposited at $T_{dep} = 200^\circ\text{C}$ in comparison to RT ones.

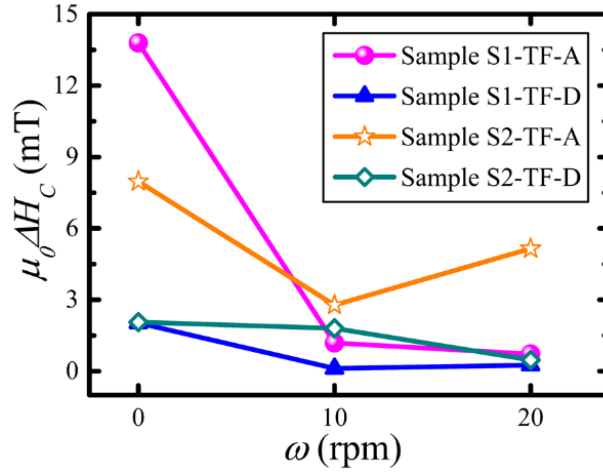


Figure 3.5: ΔH_C vs ω plot for samples S1-TF-A – S1-TF-C (solid pink circles), S1-TF-D – S1-TF-F (solid blue triangles), S2-TF-A – S2-TF-C (open orange stars), and S2-TF-D – S2-TF-F (open cyan diamonds).

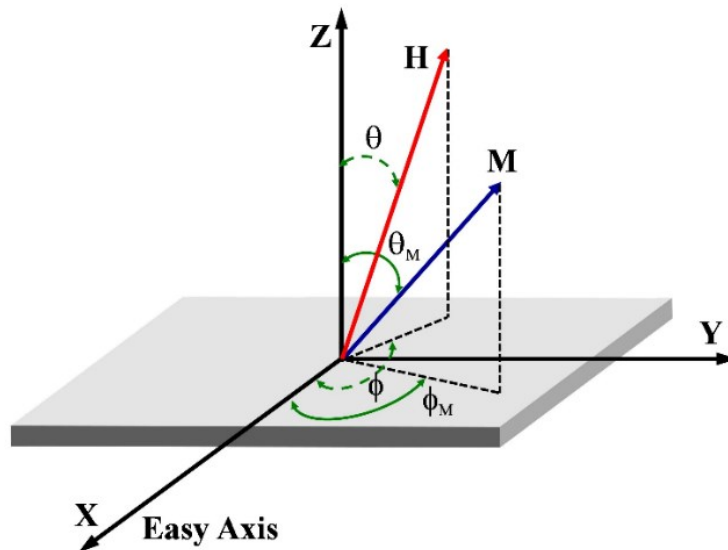


Figure 3.6: Schematic diagram showing the orientation of M and H wrt the azimuthal angle (θ), polar angle (ϕ), and the easy axis in the sample plane.

To quantify the magnetic anisotropy, angle dependent FMR measurements have been performed at room temperature. We have measured the resonance field $H_R(\theta, \phi)$ by varying the orientation of applied magnetic field defined by the polar and azimuthal angles θ , and ϕ , respectively. Since the thin films are in-plane magnetized, the magnetic field has been applied along the sample plane (i.e. $\theta = 90^\circ$). The total magnetic free energy density can be written as [199]:

$$E = -HM_S[\sin\theta\sin\theta_M\cos\phi + \cos\theta\cos\theta_M] - 2\pi M_S^2\sin^2\theta_M + K_{out}\sin^2\theta_M + K_2\sin^2\theta_M\sin^2\phi \quad (3.5)$$

where, K_{out} is the perpendicular uniaxial anisotropy constant, and K_2 is the in-plane two-fold (UMA) anisotropy constant. M_S is the saturation magnetization defined by an angle θ_M with respect to the normal (z-axis) and by an angle ϕ_M between the vector projection of \mathbf{M} in the x-y plane and the easy axis of the film. The direction of \mathbf{M} and \mathbf{H} wrt the polar, azimuthal angles and the EA is given in fig. 3.6 for clarity.

We note that since $H_R > H_S$, $\phi = \phi_M$. The first two terms of equation 3.5 represent the in-plane and out-of-plane component of Zeeman energy, respectively. The third term represents the demagnetizing energy of the system. The last two terms represent the perpendicular and in-plane contribution of the uniaxial anisotropy energy, respectively. The dispersion relation is obtained by [199,200]:

$$\left(\frac{\omega}{\gamma}\right)^2 = \frac{1}{M_S^2\sin^2\theta} \left[\frac{\partial^2 E}{\partial \theta^2} \frac{\partial^2 E}{\partial \phi^2} - \left(\frac{\partial^2 E}{\partial \theta \partial \phi} \right)^2 \right] \quad (3.6)$$

where, E is given by eqn. 3.5. The dispersion equation reduces to:

$$\left(\frac{\omega}{\gamma}\right)^2 = [H_R \cos(\phi_M - \phi) - h_{out} - h_{in}\sin^2\phi_M] [H_R \cos(\phi_M - \phi) + h_{in} + 2h_{in}\sin^2\phi_M] \quad (3.7)$$

where, $h_{out} = \frac{2K_{out}}{M_S} - 4\pi M_S$ and $h_{in} = \frac{2K_2}{M_S}$ are the anisotropy fields in perpendicular and in-plane directions, respectively. The values of h_{in} for the samples are determined by fitting

equation 3.7 to the angular dependence of the resonance field $H_R(\phi)$.

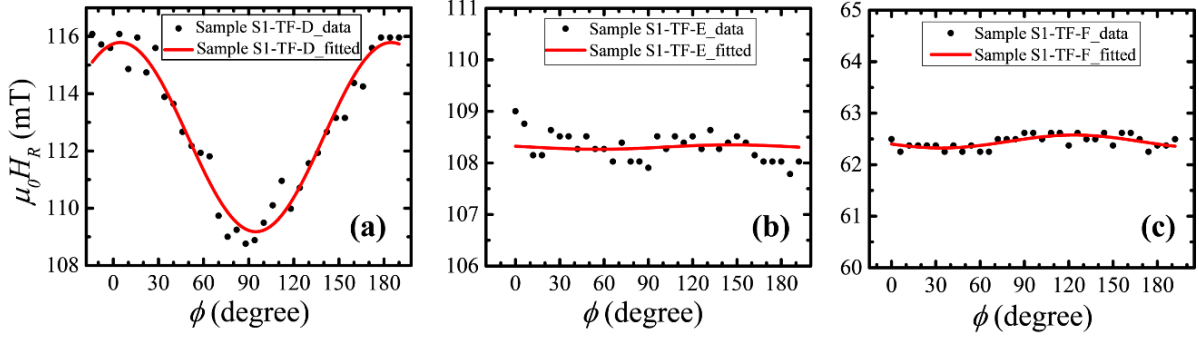


Figure 3.7: Resonance field (H_R) vs angle (ϕ) plot for samples (a) S1-TF-D, (b) S1-TF-E, and (c) S1-TF-F. Black solid circles and red line represent the experimentally observed data and fitted curves, respectively.

Fig. 3.7 shows H_R vs ϕ plot for samples S1-TF-D – S1-TF-F (a – c), respectively. The black circular points represent the experimentally observed data and the red lines represent the fitted curves with eqn. 3.7. It should be noted that the experimentally observed nature of the anisotropy in sample S1-TF-D is purely uniaxial. Hence, only one in-plane two-fold anisotropy component has been considered in the fitting equation. Here, no peak along the hard axis (similar to fig. 3.3(b)) is observed since the $H_R \gg H_S$. The best fits of the FMR data yield h_{in} to be 6.12 ± 0.23 mT, 0.08 ± 0.13 mT, and 0.23 ± 0.04 mT, for samples S1-TF-D, S1-TF-E, and S1-TF-F, respectively. The total anisotropy energy (K_2) for sample S1-TF-D (calculated using $h_{in} = \frac{2K_2}{M_S}$) is 3.01×10^3 J/m³. It should be noted that, the quality of fits for samples 1E, and 1F is poor in comparison to that of sample S1-TF-D. However, the flatness of H_R plot in fig. 3.7(b) indicates formation of isotropic film at $\omega = 10$ rpm. We did not obtain any FMR spectra for the RT deposited films with Au seed layer (samples S1-TF-A – S1-TF-C) probably due to the poor crystalline quality. The anisotropy energy (4.80×10^3 J/m³) associated with disorder due to local grain orientation is highest for sample S1-TF-A, which may also be a possible reason behind such noisy FMR spectra.

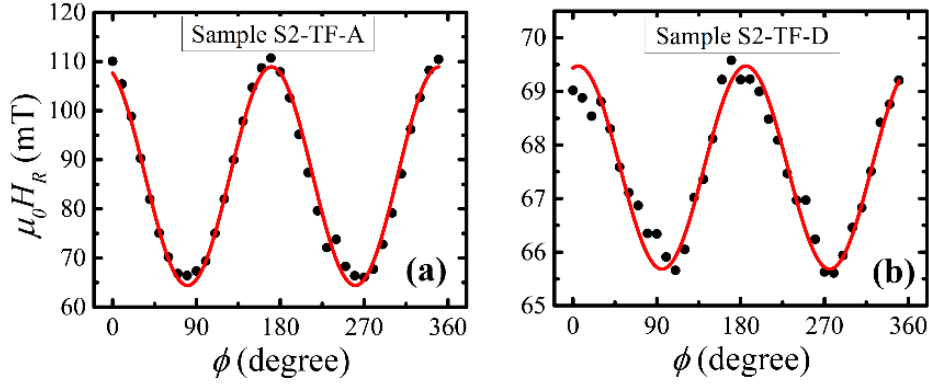


Figure 3.8: Resonance field (H_R) vs angle (ϕ) plot for samples (a) S2-TF-A, and (b) S2-TF-D. Black solid circles and red line represent the experimentally observed data and fitted curve, respectively.

Fig. 3.8 (a) and (b) show similar H_R vs ϕ plots for samples S2-TF-A, and S2-TF-D, respectively. The values of h_{in} for samples S2-TF-A and S2-TF-D are 42.52 ± 0.52 mT and 3.30 ± 0.14 mT, respectively. The total anisotropy energy for samples S2-TF-A, and S2-TF-D are 2.94×10^4 and 1.31×10^3 J/m³, respectively. This confirms significant decrease in anisotropy due to increase in T_{dep} . By comparing the anisotropy energy due to disorder with the total anisotropy of the system, we obtain that the strength of the disorder are $\sim 63\%$, 10% , and 90% for samples S1-TF-D, S2-TF-A, and S2-TF-D, respectively.

From the frequency dependent FMR measurements, we have further extracted the values of Gilbert's damping constant (α) for the samples. α for samples S1-TF-D – S1-TF-F are 0.0998, 0.0962, and 0.1527, respectively. Further, α for samples S2-TF-A – S2-TF-F are 0.0679, 0.0377, 0.0752, 0.0245, 0.0231, and 0.0315, respectively. By comparing the α values between the samples prepared at room temperature to the ones prepared at high temperature, it is found that high temperature deposition leads to the lowering of the damping in both the series. This can be corroborated to the uniform growth of the films while deposited at high temperature as discussed before. It is also observed that the damping in films of series 2 is lower than that of series 1. This behavior can be explained in terms of bigger grain size with uniform distribution

in series 2 as observed by AFM (see fig. 3.1).

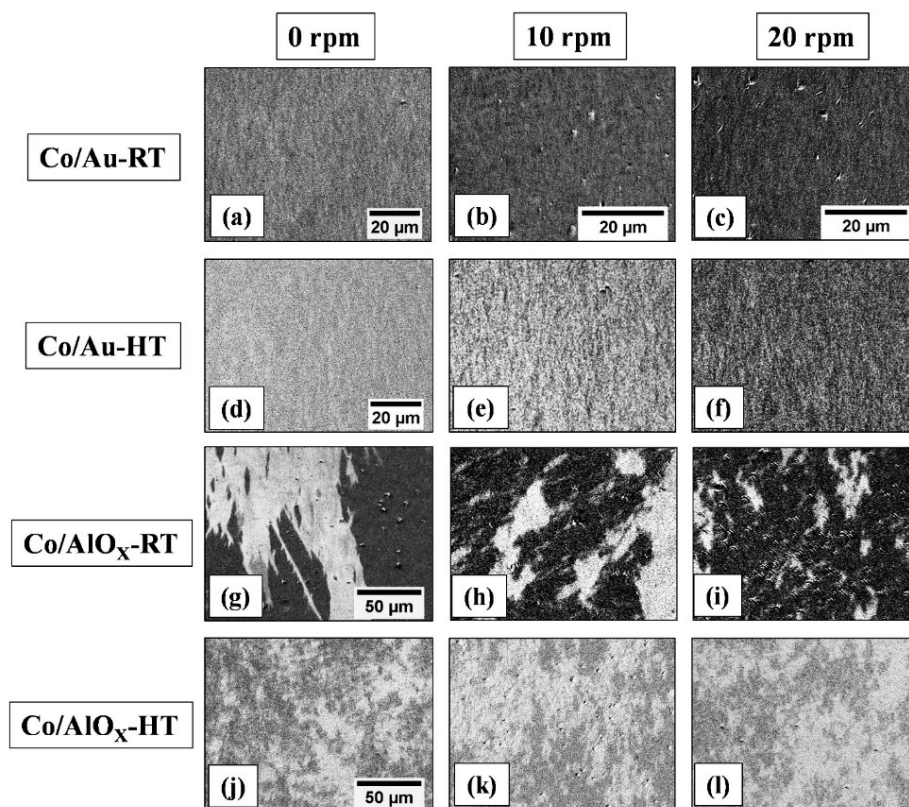


Figure 3.9: Domain images measured using MOKE microscope at RT at $\sim H_C$ for (a – f) samples S1-TF-A – S1-TF-F, and (g – l) samples S2-TF-A – S2-TF-F, respectively. The scale bars for (a – c) are shown individually. The scale bars of (d – f) are same and shown in (d). Similarly, the scale bars of (g – l) are same and shown in (g) and (j). (g – i) are reproduced with permission from *ref.* [9].

In order to understand the magnetization reversal for these thin films prepared at different growth conditions, we have performed domain imaging via Kerr microscopy. Fig. 3.9 depicts the domain images at H_C along EA for samples S1-TF-A – S1-TF-F (a – f), and samples S2-TF-A – S2-TF-F (g – l), respectively. The domain structures shown in fig. 3.9 (a – f) for samples S1-TF-A – S1-TF-F are known as ‘ripple domains’ which is a signature of polycrystalline thin films [201]. Ripple in thin films are mostly induced by irregular anisotropies connected with the polycrystalline microstructure of the films. It should be noted that the ripple structure

remains unchanged with substrate rotation for the Co (10 nm) thin films prepared on Au seed layer. However, the size of the ripples increases in samples S1-TF-D – S1-TF-F in comparison to that of samples S1-TF-A – S1-TF-C. The grain distribution (fig. 3.1) in sample S1-TF-D is more homogeneous in comparison to sample S1-TF-A, which leads to a minor elevation of size of the ripples. For sample S2-TF-A, large branch domains have been observed. This behavior is corroborated to the bigger grain sizes in sample 2A. It was observed that the grain size decreases significantly with substrate rotation for samples S2-TF-B, and S2-TF-C [9]. Hence, we obtain smaller domains in samples S2-TF-B and S2-TF-C in comparison to sample S2-TF-A. However, the grains are more closely packed in sample S2-TF-B in comparison to sample S2-TF-C. This leads to further decrease in domain size in sample S2-TF-C. It should be also noted that the UMA is most dominant in sample S2-TF-A. With substrate rotation the anisotropy decreases leading to strong modifications in the domain structure in samples S2-TF-B and S2-TF-C. Further, high temperature deposition of Co on AlO_x seed layer leads to decrease in anisotropy. In addition, the strength of disorder is significantly high for sample S2-TF-D. Therefore, characteristic irregular demagnetized domain patterns are formed in patches which are usually observed in coarse grain materials [19]. Hence, it can be concluded from series 1 (Co films with Au seed layer) and 2 (Co films with AlO_x seed layer) that the films deposited at $T_{\text{dep}} = 200^{\circ}\text{C}$ retain the domain structure irrespective of the ω . However, in series 2 there is a significant change in domain structure in the films prepared at $T_{\text{dep}} = \text{RT}$ but with change in ω .

To summarize the above results we have studied systematically the effect of growth condition on the anisotropy and the domain structure in Co thin films with different seed layers. The nature of anisotropy, damping, and domain structure in such systems has been explained in terms of their grain distribution and disorder present in the films. It has been shown that it is possible to prepare isotropic films (with Au or AlO_x as seed layer) by the combined effect of

substrate rotation and deposition temperature. High temperature deposition along with substrate rotation ensures formation of isotropic films for both Au and AlO_x seed layer. However, 20 rpm of substrate rotation during deposition was not enough to get rid of the anisotropy completely for the films with AlO_x seed layer deposited at RT. Further, high temperature deposition leads to lowering of the damping. This is corroborated to the surface topography observed by AFM, where the uniformity of grains increases when grown at high temperature. The shape and size of the domains change with substrate rotation for the films with AlO_x seed layer prepared at RT. On the contrary, the domain structure remains unchanged for both series of samples for variable ω when prepared at $T_{\text{dep}} = 200^\circ\text{C}$.

From the above discussion we further conclude that, among all, the samples prepared with AlO_x seed layer at RT shows the lowest disorder. This is reflected in the good FMR and Kerr microscopy (domain images) signal in these samples (samples S2-TF-A – S2-TF-C). Hence, we choose to fabricate the antidots on Co thin films deposited on AlO_x seed layer at room temperature to probe the role of architecture of the holes in determining the magnetization reversal mechanism.

3.2. Tuning the anisotropy, domain structure, and magnetic relaxation in MAL arrays of Co with in-plane anisotropy:

Magnetic antidot lattice (MAL) arrays are periodic defects in a continuous thin film [3]. The well-defined defects strongly pin the magnetic domains forcing the DWs to move in a zig-zag path avoiding the holes [3,12,13]. Hence, the magnetization reversal in MAL arrays is better controlled in comparison to continuous thin films where the location and structure of the defects are random. Further, the exchange coupled MAL arrays are free from the superparamagnetic blocking [4]. Hence, they are ideal candidates to replace the present bit patterned media storage technology [86]. In spite of several works reported in the field of in-plane magnetized antidots [43,44,46,47,49,51,66,68,72,77,202], reports on the quantification

of domain size depending on the availability of the active area is missing. Further, the response of domains to the thermal activation energy in such MAL arrays and their thin film counterparts are relatively unexplored. Here we show how the domain structure, anisotropy, and the magnetic relaxation can be tuned in antidot arrays of Co films with in-plane magnetization, by varying the deposition condition and antidot architecture.

Table 3.2: Sample structure of in-plane magnetized thin film and MAL arrays of Co

Sample Name	Sample structure	Sample type	Substrate rotation (ω)	
S2-TF-A	Si(100)/AlO _x (2 nm)/Co(10 nm)/AlO _x (2 nm)	Thin film	0 rpm	
S3-SCA		Circular antidot (small)	0 rpm	
S3-BCA		Circular antidot (big)	0 rpm	
S3-SA		Square antidot	0 rpm	
S3-TA-NR		Triangular antidot	0 rpm	
S3-TA-R		Triangular antidot	Triangular antidot	20 rpm

The patterning for the antidot structures prior to deposition has been performed on Si (100) substrate using UV lithography supplied by Midas System Co. Ltd., South Korea. The deposition of the thin film with the structure Si(100)/AlO_x(2 nm)/Co(10 nm)/AlO_x(2 nm) has been performed in the same way as mentioned in section 3.1. The MAL arrays are obtained by removing the residual photoresist from the surface of the films by developing in acetone. The list of all the in-plane magnetized MAL arrays and the thin film counterparts are shown in table 3.2. In the sample nomenclature, the acronyms SCA, BCA, SA, and TA have been used to denote small circular, big circular, square, and triangular antidots, respectively. Further, the acronyms NR and R have been used to designate the samples prepared without any substrate rotation (NR: not rotated) and with substrate rotation (R: rotated), respectively.

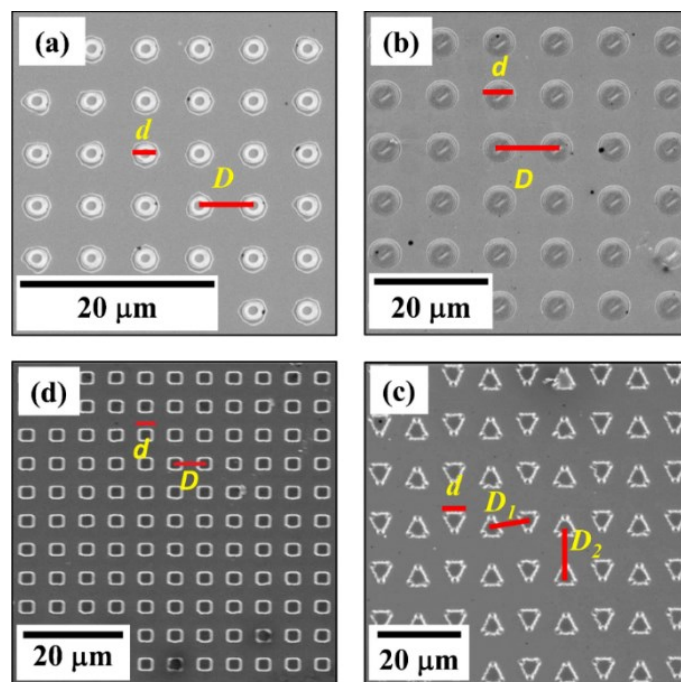


Figure 3.10: SEM images for samples (a) S3-SCA (small circular antidot): $d = 3.2 \mu\text{m}$, $D = 6 \mu\text{m}$; (b) S3-BCA (big circular antidot): $d = 5.8 \mu\text{m}$, $D = 10 \mu\text{m}$; (c) S3-SA (square antidot): $d = 3.2 \mu\text{m}$, $D = 6 \mu\text{m}$; and (d) S3-TA-NR (triangular antidot): $d = 5 \mu\text{m}$, $D_1 = 9.2 \mu\text{m}$, $D_2 = 12.1 \mu\text{m}$.

Table 3.3: Structural details of the in-plane magnetized antidot arrays

Sample Name	Shape of antidots	Diameter or Side length d (μm)	Center-to-Center distance D (μm)
S3-SCA	Circular (smaller)	3.2	6.0
S3-BCA	Circular (bigger)	5.8	10.0
S3-SA	Square	3.2	6.0
S3-TA-NR	Triangular	5.0	Horizontal (D_1) = 9.2, Vertical (D_2) = 12.1

Fig. 3.10 (a – d) show the SEM images of samples S3-SCA, S3-BCA, S3-SA, and S3-TA-NR, respectively. As seen from the figure, the edges of the patterns for the samples are not smooth and sharp. This may be due to underexposure, extra scattering, diffraction from the edges, improper lift-off, etc. [203]. The shape of the patterns improved with increase in dimension of

circular holes as seen from fig. 3.10 (b) for sample S3-BCA in comparison to fig. 3.10 (a) for sample S3-SCA. The structural details of the in-plane magnetized antidot samples of different shapes are provided in table 3.3.

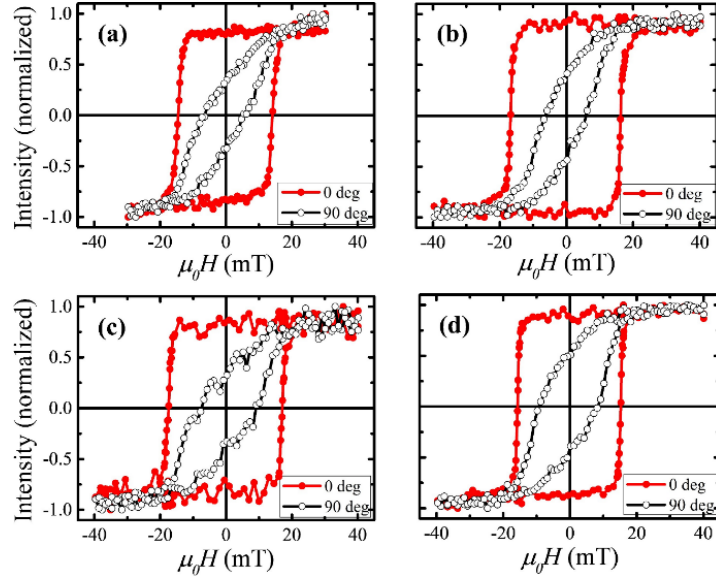


Figure 3.11: Hysteresis loops measured by Kerr microscopy for (a – d) samples S3-SCA, S3-BCA, S3-SA, and S3-TA-NR, respectively. The red and black curves correspond to the hysteresis loops along $\phi = 0^\circ$ and 90° , respectively.

Fig. 3.11 (a – d) show the room temperature hysteresis loops for samples S3-SCA, S3-BCA, S3-SA, and S3-TA-NR, respectively, measured using Kerr microscopy in longitudinal mode. For all the samples square shaped hysteresis loops (high $\frac{M_R}{M_S}$) have been observed along the EA ($\phi = 0^\circ$). However, along the HA ($\phi = 90^\circ$) the loops sustain a non-vanishing M_R which is a signature of the local grain misalignment as discussed in section 3.1. The antidots require higher saturation field in comparison to its parent thin film (fig. 3.2 (g)). This is expected since the periodic holes present in the antidot arrays act as pinning barrier for the magnetic domains [50]. Hence, the domains face hindrance in the path of their propagation during the magnetization switching. Therefore, higher saturation field (H_S) is required for the magnetization reversal in the MAL arrays. Further, it has been observed that the coercive field

(H_C) is lowest (15.45 mT) for the triangular antidot (sample S3-TA-NR) whereas the same is highest (17.25 mT) for the square antidot (sample S3-SA). This is explained in-terms of availability of active area (total magnetic area in a sample) in different antidots. The comparison between the available active areas with H_C in different shaped antidots is tabulated in table 3.4. To calculate the active area, first the total area of the field of view in the Kerr microscope has been measured. Then the area covered by the holes has been subtracted from the total area of the sample.

Fig. 3.12 shows the domain images measured simultaneously during the hysteresis cycles using Kerr microscope in longitudinal mode for samples S2-TF-A (a – d), S3-SCA (e – h), S3-BCA (i – l), S3-SA (m – p), and S3-TA-NR (q – t), at $-H_S$, H_N , H_C , and $\sim H_S$, respectively. As discussed in section 3.1 (fig. 3.9 (g)), the parent continuous thin film (sample S2-TF-A) shows formation of branch domains which expands in transverse direction with increase in the applied magnetic field to complete the reversal. However, presence of periodic holes in the antidots leads to formation of smaller fractal domains. The holes in the MAL arrays work as the nucleation and pinning centers for the domains. In addition, the lateral movement of the DWs is restricted by the holes (absence of magnetic element). Hence, the domains are forced to nucleate from the edges of the holes and propagate in a zigzag path through the magnetic channels in-between them. It is also observed that the size of the domains in big circular antidot (sample S3-BCA), and triangular antidot (sample S3-TA-NR) is larger than that in small circular antidot (sample S3-SCA), and square antidot (sample S3-SA). This can be explained in-terms of the availability of the active area in the films. The inter-separation between the holes in sample S3-TA-NR defined by D_1 , and D_2 , is higher than the rest of the antidot samples. This leads to formation of largest domains in triangular antidot sample S3-TA-NR among the other antidots. Similarly, the active area is minimum for square antidot sample S3-SA, which leads to formation of smallest domains in comparison to others.

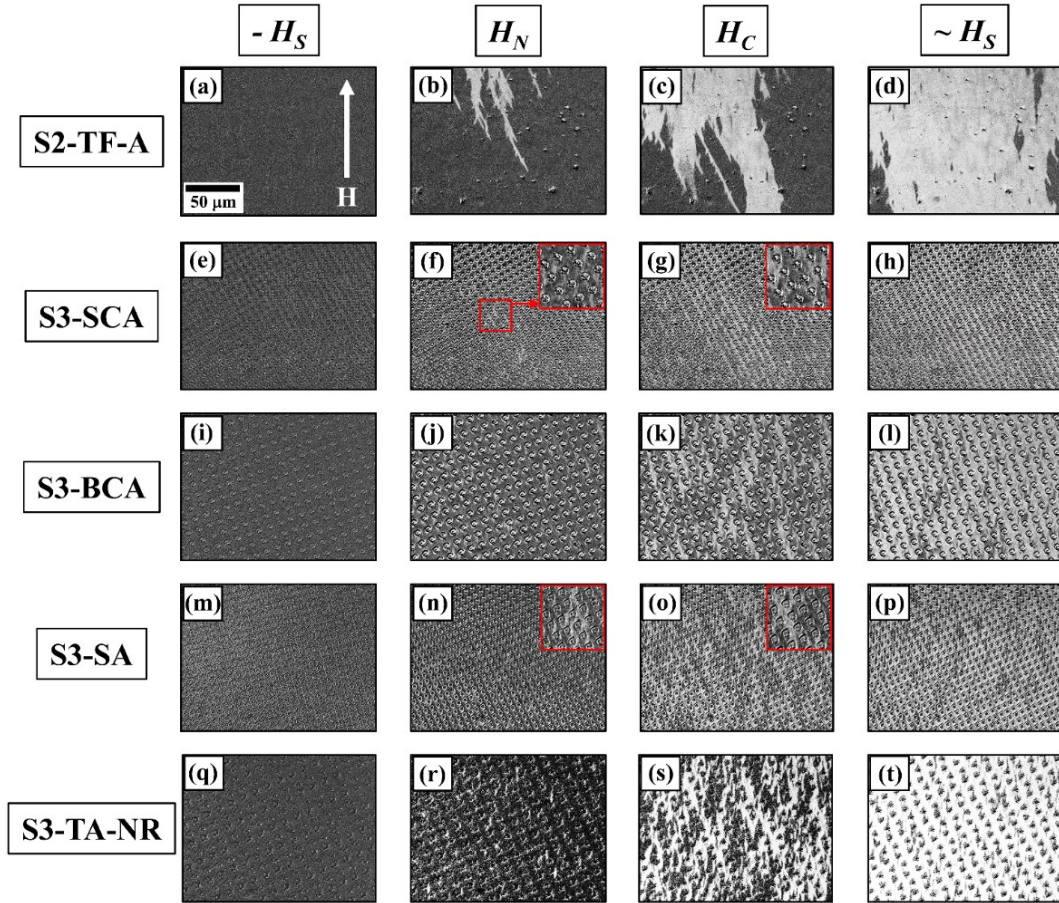


Figure 3.12: Domain images measured using Kerr microscopy for samples S2-TF-A (a – d), S3-SCA (e – h), S3-BCA (i – l), S3-SA (m – p), and S3-TA-NR (q – t), at $-H_S$, H_N , H_C , and $\sim H_S$, respectively. The scale bar and the direction of applied field for all the samples are same and is shown in (a). The higher resolution domain images for samples S3-SCA, and S3-SA are shown in inset of (f), (g), and (n), (o), respectively. The higher resolution images are measured on the area marked by the red box as shown in (f).

The domain widths for all the samples have been calculated at $\sim H_C$. The domain widths are 2.53, 2.89, 2.37, and 3.42 μm for samples S3-SCA – S3-TA-NR, respectively. The calculated domain width per active area are 0.00014, 0.00015, 0.00014, and 0.00015 μm^{-1} for samples S3-SCA – S3-TA-NR, respectively. The values are very close (same up to four decimal places) to each other which indicates that the domain size is determined by the active area of the sample. A detailed comparison between the active area and the domain size is shown in table

3.4. The calculated domain width and domain width per active area for the continuous thin film (sample S2-TF-A) are $6.84 \mu\text{m}$, and $0.000289 \mu\text{m}^{-1}$, respectively. Therefore from the above discussion, we conclude that the domain size as well as the coercivity can be engineered in the MAL arrays by varying the antidot architecture and inter-separation between the holes.

Table 3.4: A comparison of domain width and coercivity for different antidots

Sample	Active area (μm^2)	Coercivity (mT)	Domain width (μm)	Domain width per active area (μm^{-1})
S2-TF-A	23663 ± 157	7.97	6.84 ± 0.13	0.000289
S3-SCA	18436 ± 157	16.73	2.53 ± 0.13	0.00014
S3-BCA	18684 ± 157	16.45	2.89 ± 0.13	0.000155
S3-SA	16833 ± 157	17.25	2.37 ± 0.13	0.00014
S3-TA-NR	21869 ± 157	15.45	3.42 ± 0.13	0.000156

The shape of the domains as well as the general anisotropy behavior is similar for all the antidots due to their large size. However, relatively bigger size of the domains in triangular antidot sample S3-TA-NR makes them easier for Kerr microscopy imaging. Further, the sharp edges of the triangular patterns (sample S3-TA-NR) are most appropriate to observe the pinning of domains in-between successive holes. Hence, the relaxation measurements are performed in sample S3-TA-NR. Fig. 3.13 shows the position in the hysteresis loop where a typical relaxation measurement is performed. During the relaxation measurements, the sample has been first saturated and then a reverse magnetic field H_M is set to a sub-coercive value to relax the spins under constant Zeeman energy. The value of H_M has been chosen close to H_C to ensure domain nucleation. Further, it should be noted that if $H_M > H_C$, then the relaxation becomes very fast (due to the presence of significantly high Zeeman energy) and the sample relaxes rapidly. Such rapid reversal makes it hard to detect the relaxation process experimentally. Hence $H_N > H_M > H_C$ should be maintained while fixing the applied magnetic

field during the relaxation measurements. It can be also observed from fig. 3.13 that the position of H_M at the hysteresis loop depends on the sharpness of the magnetization reversal.

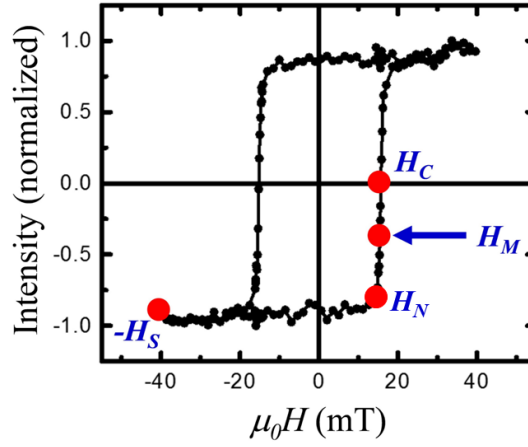


Figure 3.13: Hysteresis loop showing the field (H_M) for relaxation measurements. The sample has been first saturated ($-H_S$) and then a reverse magnetic field H_M is set to a sub-coercive (H_C) value to relax the spins under constant Zeeman energy.

Fig. 3.14 shows relaxation measurement of sample S3-TA-NR (triangular antidots) performed at $H_M = 0.995H_C$. The mean grey scale intensity of the domain images is plotted with the corresponding time to obtain the relaxation curve (a). In presence of constant applied field, the reversal occurs under the influence of thermal activation energy. Fig. 3.14 (b – i) show the domain images at 0, 5, 12, 20, 30, 35, 50, and 120 s, respectively, as marked by 1-8 in (a). It can be observed from fig. 3.14 (b) that the domain nucleation starts prior to fixing the field at H_M . Initially the domain nucleation and propagation is rapid, which further slows down and essentially becomes constant as the sample reaches the saturation. The relaxation data points are fitted (red line in fig. 3.14 (a)) with the Fatuzzo-Labrune [14,15] type single exponential decay (SED) behavior:

$$I(t) = I_F + I_I \exp(-t/\tau) \quad (3.8)$$

where, $I(t)$, I_F , I_I are measured, final, and initial Kerr intensities, respectively. τ is the relaxation time constant. Under the framework of Fatuzzo-Labrune model [14,15], the SED

type relaxation behavior indicates nucleation dominated aftereffects followed by DW motion.

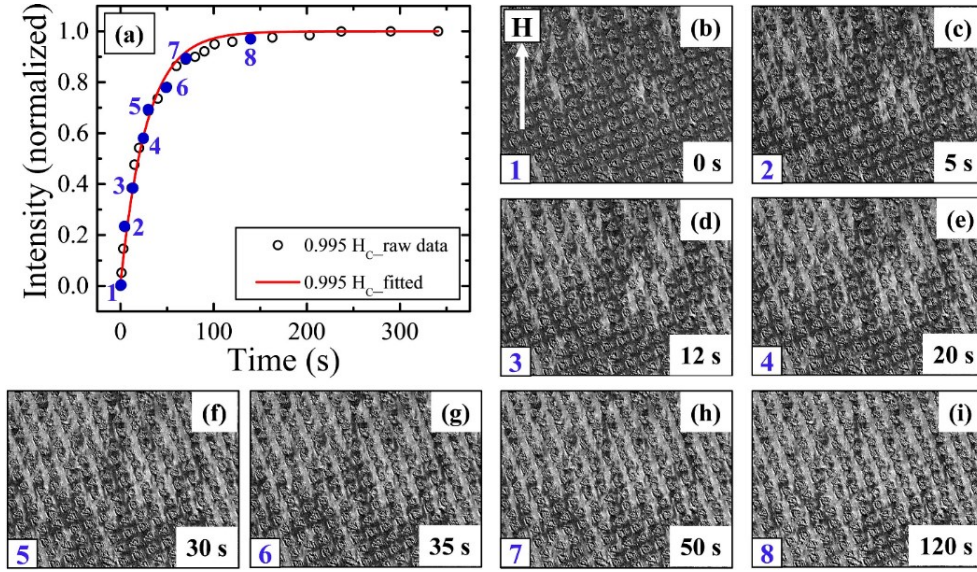


Figure 3.14: Relaxation measurement by longitudinal Kerr microscope for sample S3-TA-NR along easy axis. Fig. (b – i) are domain images marked by point 1 to 8 in (a) at 0, 5, 12, 20, 30, 35, 50, and 120 s, respectively, after fixing the applied magnetic field to $H_M = 0.995H_C$.

To compare the relaxation mechanism between the triangular antidot and its thin film counterpart, the measurements have been performed at different fields. Fig. 3.15 (a) shows the relaxation behavior in triangular antidot sample S2-TF-A at $H_M = 0.995H_C$ (red curve), $0.99H_C$ (blue curve), and $0.985H_C$ (green curve). The relaxation data of sample S2-TF-A at $H_M = 0.995H_C$ is fitted with SED function. The inset of fig. 3.15 (a) shows the zoomed-in view of the relaxation curve at $H_M = 0.995H_C$. However, the relaxation at $H_M = 0.99H_C$ and $H_M = 0.985H_C$, is best fitted with Boltzmann function [16]:

$$I(t) = I_F + (I_I - I_F)/[1 + \exp((t - t_0)/\tau)] \quad (3.9)$$

where, t_0 is the time corresponding to the mean intensity. The initial slow nature of the Boltzmann type relaxation in sample S2-TF-A is attributed to the fact that the domains start nucleating after a few seconds of keeping the field fixed at H_M . However, the speed of

relaxation sharply increases after domain nucleation, due to the fast domain wall motion.

The fitted values of τ for sample S2-TF-A are 3.33 ± 0.08 , 4.00 ± 0.09 , and 5.85 ± 0.25 s, for $H_M = 0.995$, 0.99 , and $0.985H_C$, respectively.

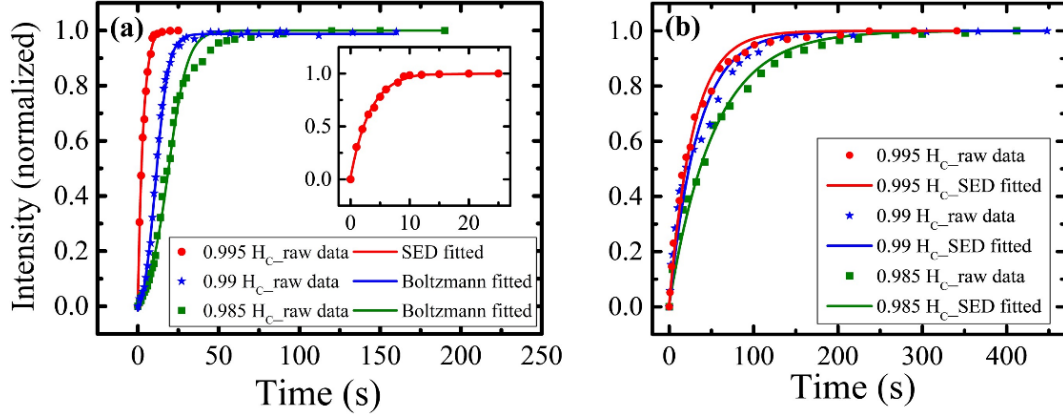


Figure 3.15: Relaxation measurement along easy axis for (a) sample S2-TF-A, (b) sample S3-TA-NR, at $H_M = 0.995H_C$ (red curve), $0.99H_C$ (blue curve), and $0.985H_C$ (green curve). The inset of (a) shows the zoomed-in view of the relaxation curve for sample S2-TF-A at $H_M = 0.995H_C$.

Fig. 3.15 (b) shows relaxation measurements in sample S3-TA-NR at $H_M = 0.995H_C$ (red curve), $0.99 H_C$ (blue curve), and $0.985 H_C$ (green curve). Here, all the data are best fitted with SED type behavior. The holes present in the triangular antidot (sample S3-TA-NR) works as the nucleation centers for the domains leading to early nucleation of domains in comparison to its thin film counterparts (sample S2-TF-A). Hence, the initial slow relaxation is absent in case of triangular antidot sample S3-TA-NR yielding such SED type behavior. Nevertheless, we note that the SED function can be derived from the Boltzmann function [16], by rewriting eqn. 3.9:

$$\begin{aligned}
 I(t) &= I_F + \frac{I_I - I_F}{1 + \exp\left(\frac{t - t_0}{\tau}\right)} \\
 &= I_F + \frac{I_x}{\exp\left(\frac{t - t_0}{\tau}\right)}, \text{ assuming } t - t_0 \gg \tau \text{ and } I_x = I_I - I_F
 \end{aligned}$$

$$\begin{aligned}
 &= I_F + I_x \exp\left(\frac{t_0-t}{\tau}\right) \\
 &= I_F + I_x \exp\left(\frac{t_0}{\tau}\right) \exp\left(-\frac{t}{\tau}\right) \\
 &= I_F + I'_x \exp\left(-\frac{t}{\tau}\right), \text{ where } I'_x = I_x \exp\left(\frac{t_0}{\tau}\right)
 \end{aligned}$$

The best fits yield τ values for sample S3-TA-NR to be 28.08 ± 1.14 , 34.05 ± 2.73 , and 52.99 ± 2.59 s, respectively, at $H_M = 0.995H_C$, $0.99H_C$, and $0.985H_C$. By comparing the τ values, it has been noted that the relaxation becomes sharp with increase in the strength of the externally applied magnetic field. However, by comparing the values of τ between samples S2-TF-A (continuous thin film) and S3-TA-NR (antidot), we conclude that the relaxation turns slower in the in-plane magnetized MAL arrays in comparison to its thin film counterpart. Such slow relaxation in the antidots occurs because the periodic holes hinders the propagation of the DWs in the lateral direction which leads to lowering of DW velocity. This is not desired for storage applications where rapid reversal of spins is essential in reading and writing information [17,204].

3.3. Controlling the relaxation dynamics and magnetization switching of in-plane magnetized antidot arrays of Co by employing substrate rotation:

In order to get rid of the aforementioned drawback of slow relaxation, we have prepared another triangular antidot sample (sample S3-TA-R) by employing substrate rotation (ω) of 20 rpm and keeping the structure similar to the non-rotated triangular antidot sample S3-TA-NR. We have further examined the possibility of engineering the anisotropy, domain size and the magnetization relaxation mechanisms by varying ω . The SEM image of the MAL patterns for sample S3-TA-R (triangular antidot: 20 rpm) is shown in fig. 3.16 (a). The image shows well-ordered triangular holes distributed uniformly across the film area. Fig. 3.16 (b) is the AFM image of the antidot structure with four triangular holes. Fig. 3.16 (c) depicts the surface morphology of sample S3-TA-NR (triangular antidot: $\omega = 0$ rpm) measured by AFM in

between two successive holes marked by the box in (b). Fig. 3.16 (d) shows AFM measurement performed on a similar area in sample S3-TA-R (triangular antidot: $\omega = 20$ rpm).

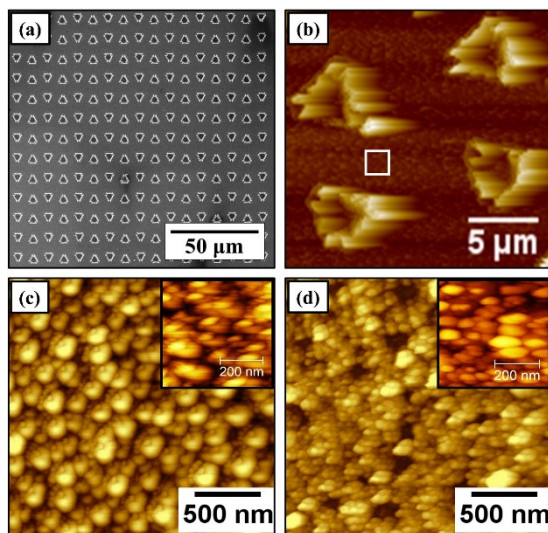


Figure 3.16: (a) SEM image of triangular antidot patterns of sample S3-TA-R, (b) the AFM image of the antidot structure showing four triangular holes. (c) Surface morphology of sample S3-TA-NR performed in between two successive triangular holes marked by the box in figure (b). (d) Surface morphology of sample S3-TA-R in between two successive triangular holes performed similar to (c). The insets of figure (c) and (d) are zoomed views of the corresponding images.

The average grain diameter (extracted from the AFM images) of samples S3-TA-NR and S3-TA-R are 127.0 ± 7.8 nm and 52.9 ± 7.8 nm, respectively. The decrease in grain size for sample S3-TA-R is expected due to the rotation of the substrate during the growth of the film. For the triangular antidot prepared without any substrate rotation (sample S3-TA-NR), the grains are regularly distributed and arranged in chain like structures due to the oblique angle of deposition (fig. 3.16 (c)). However, for the rotated triangular antidot sample S3-TA-R, the grains agglomerate and form bigger island structures. It is a well-established fact that Co follows a Volmer-Weber growth mechanism on Al_2O_3 [189]. It has been reported that in thin films with Co thickness > 1.8 nm, the islands physically percolate which leads to continuous thin films

[205]. In this present work, the Co thickness is 10 nm, so the possibility of nanoparticle nature is excluded. Therefore, it is expected that the grains will grow in an island structure and essentially form a smooth surface. This is in good agreement with the growth mechanism of non-rotated triangular antidot sample S3-TA-NR (fig. 3.16 (c)). However, for sample S3-TA-R, due to the high speed of the substrate rotation (20 rpm) during growth the grains did not get sufficient time to relax to form a smooth surface (fig. 3.16 (d)). This leads to smaller grain size in sample S3-TA-R as compared to sample S3-TA-NR. Further, from insets of fig. 3.16 (c) and (d), we note that the grains are more densely packed in the triangular antidot sample prepared with substrate rotation (sample S3-TA-R) in comparison to that in the non-rotated one (sample S3-TA-NR).

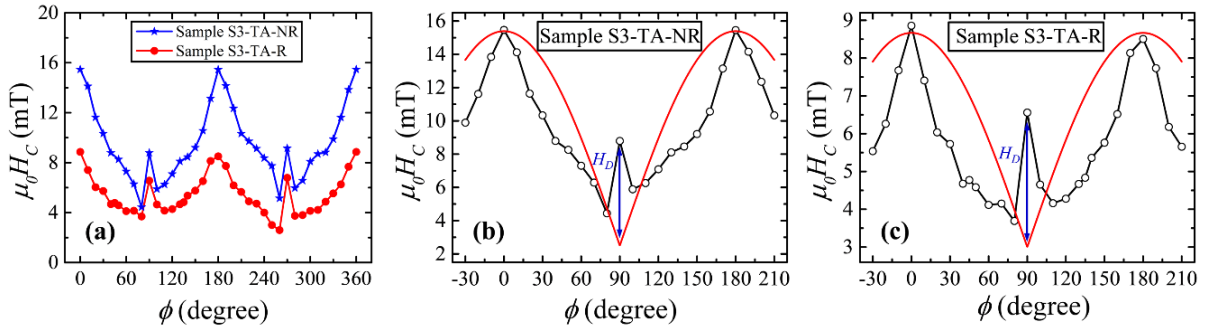


Figure 3.17: (a) H_c vs ϕ plots for sample S3-TA-NR (blue curve) and sample S3-TA-R (red curve). Angular dependence of coercivity plots fitted with Stoner-Wohlfarth model for (b) sample S3-TA-NR and (c) sample S3-TA-R, respectively. The black open circles are the experimental data points whereas the red line is the fitted curve using eqn. 3.3.

Fig. 3.17 (a) shows the angular dependence of coercivity plots for samples S3-TA-NR (blue curve) and S3-TA-R (red curve). It clearly demonstrates the presence of uniaxial anisotropy in both samples which is induced due to the oblique angle of deposition. The peak along the hard axes ($\phi = 90^\circ$ and $\phi = 270^\circ$) for both samples is attributed to the misalignment of local grain anisotropy termed as grain disorder in non-epitaxial films [11,198]. It is observed from fig. 3.17 (a) that the anisotropy (difference in H_c between $\phi = 0^\circ$ and $\phi = 90^\circ$) decreases with

increase in the substrate rotation. However, it should be noted that the rotation speed of $\omega = 20$ rpm is not sufficient to make the film isotropic. The angular dependence of coercivity data is fitted with the single grain Stoner-Wohlfarth model (eqn. 3.3) [124,198]. Fig. 3.17 (b) and (c) shows the H_C vs ϕ plots fitted with eqn. 3.3 for the triangular antidot samples prepared without (sample S3-TA-NR) and with (sample S3-TA-R) substrate rotation, respectively. The calculated values of disorder fields (H_D) from the fittings are 6.29 mT, and 3.56 mT, for samples S3-TA-NR, and S3-TA-R, respectively. Hence, the strength of the disorder between the neighboring grains decreases with substrate rotation in sample S3-TA-R in comparison to the non-rotated sample S3-TA-NR. The reason behind this can be corroborated to formation of smaller and denser grains in sample S3-TA-R (due to substrate rotation during deposition) which leads to enhancement of inter-granular exchange coupling.

In order to quantify the change in anisotropy, angle dependent FMR measurement has been performed on the triangular antidots at room temperature. Fig. 3.18 shows the angle dependent FMR measurements for samples (a) S3-TA-NR (triangular antidot: $\omega = 0$ rpm) and (b) S3-TA-R (triangular antidot: $\omega = 20$ rpm), respectively. The black circles are experimental data points whereas the red lines represent the best fit with UMA model (eqn. 3.7). The fitted values of h_{in} for samples S3-TA-NR and S3-TA-R are 49.01 ± 0.57 mT, and 32.97 ± 0.53 mT, respectively. By comparing the disorder fields (H_D) with the in-plane anisotropy fields (h_{in}), we obtain that the strength of disorder are 12.8%, and 10.8% for samples S3-TA-NR, and S3-TA-R, respectively. This further confirms that the disorder in the triangular antidot sample prepared with substrate rotation (sample S3-TA-R) is reduced in comparison to the non-rotated one (sample S3-TA-NR) because of enhanced exchange coupling between the neighboring grains.

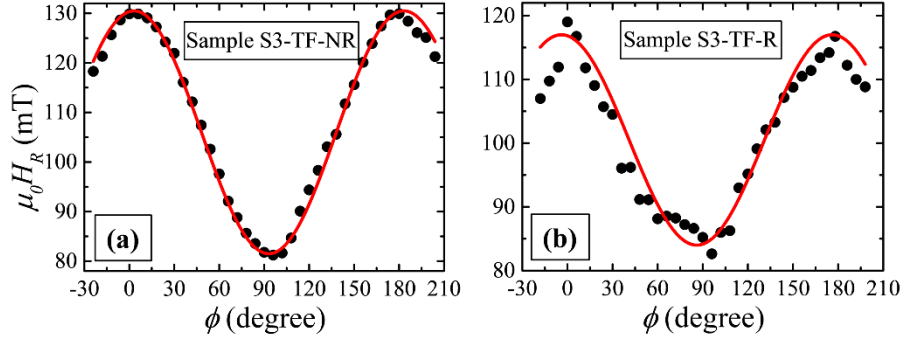


Figure 3.18: Resonance field (H_R) vs angle (ϕ) plot for samples (a) S3-TA-NR, and (b) S3-TA-R. Black solid circles and red line represent the experimentally observed data and fitted curve, respectively.

Fig. 3.19 shows the domain images at H_N and H_C along $\phi = 0^\circ$ and $\phi = 30^\circ$ for samples S3-TA-NR (triangular antidot: $\omega = 0$ rpm) and S3-TA-R (triangular antidot: $\omega = 20$ rpm), respectively. The scale bars of all images and the direction of applied magnetic field is shown in (a). The images clearly reveal collective switching of domains which are bigger for sample S3-TA-R in comparison to sample S3-TA-NR. The bigger size of domains in sample S3-TA-R (in comparison to sample S3-TA-NR) is also visible from the images at H_C along $\phi = 30^\circ$ [inset images of fig. 3.19 (g), (h)]. The nature of the domain images are in good agreement with the distribution of the grains obtained from the AFM images. As the grains are arranged in islands for the triangular antidot sample prepared with substrate rotation (sample S3-TA-R), the grains present in each island behave collectively. Further, the grains in sample S3-TA-R are more densely packed in comparison to that in the triangular antidot sample prepared without substrate rotation (sample S3-TA-NR). This results in higher exchange interaction between neighboring grains in sample S3-TA-R. However, the exchange interaction is weaker in sample S3-TA-NR since the grains are more scattered. Stronger exchange interaction in sample S3-TA-R leads to the enhancement in domain size. With the increase of the applied magnetic field, the domains expand along the transverse direction, being forced by the antidots not to propagate

through them.

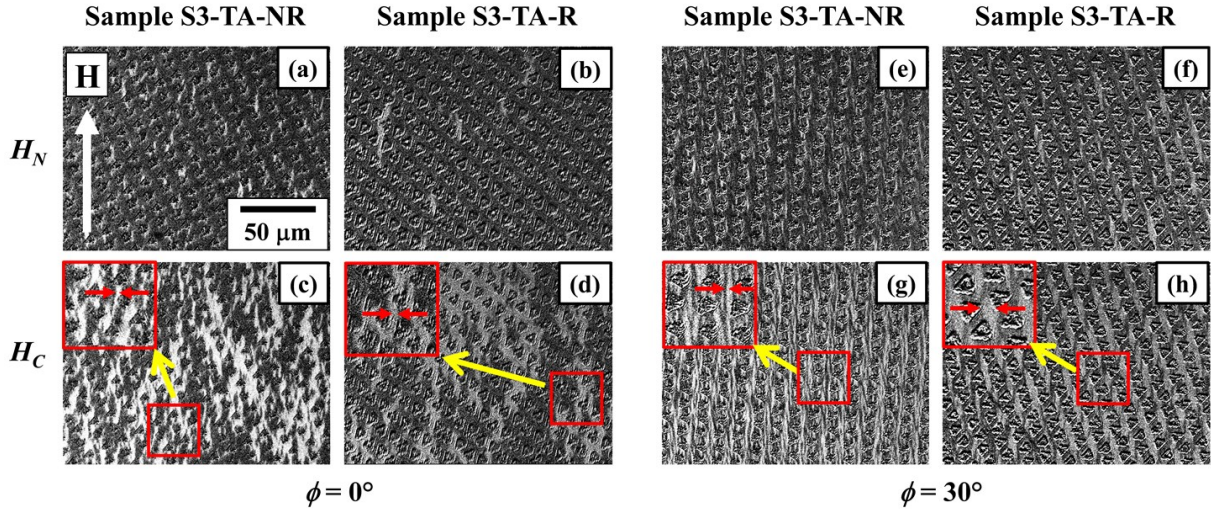


Figure 3.19: (a), (b) and (c), (d) are the domain images along easy axis ($\phi = 0^\circ$) at nucleation (H_N) and coercive field (H_C) for sample S3-TA-NR and sample S3-TA-R, respectively. Fig. (e), (f) and (g), (h) are the domain images along $\phi = 30^\circ$ at H_N and H_C for samples S3-TA-NR and S3-TA-R, respectively. The insets of fig. 5 (c), (d), (g), and (h) show the zoomed version of the domains encircled by the red line. The red arrows shown in the inset images of fig. 5 (c), (d), (g), and (h) represent the widths of the individual domains. All inset images are in the same scale and the total widths of the insets are $33 \mu\text{m}$.

We have reported in section 3.1 that in the continuous Co film the domain structure changes to ripple and labyrinth domains with substrate rotation ($\omega = 10, 20 \text{ rpm}$) which are smaller than the branch domains in the $\omega = 0 \text{ rpm}$ film. However, the antidots force the shape of the domains (branched structure) to remain unchanged. The average domain width has been calculated for both the samples at $\sim H_C$. The average domain widths along EA are $3.42 \pm 0.52 \mu\text{m}$, $7.89 \pm 0.52 \mu\text{m}$ and along an intermediate axis (30° away from EA) are $2.10 \pm 0.52 \mu\text{m}$ and $6.05 \pm 0.52 \mu\text{m}$ for the triangular antidot samples prepared without (sample S3-TA-NR) and with (sample S3-TA-R) substrate rotation, respectively. The width of these individual domains is marked with

red arrows in the inset of fig. 3.19 (c), (d), (g), and (h). Hence, it is concluded that the domains switch collectively and are bigger for the triangular antidot sample prepared with substrate rotation as compared to the non-rotated one.

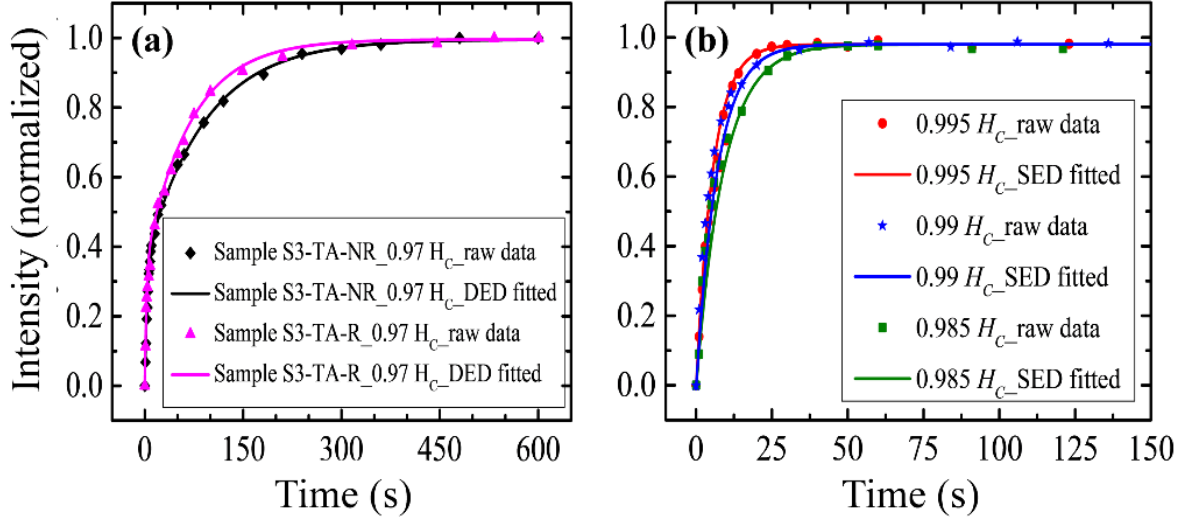


Figure 3.20: (a) Relaxation behavior of samples S3-TA-NR (black colored solid diamonds) and S3-TA-R (pink colored solid triangles) along the EA at a constant applied magnetic field of $H_M = 0.97 H_C$. (b) Relaxation behavior of sample S3-TA-R at $H_M = 0.995 H_C$ (red colored solid circles), $H_M = 0.99 H_C$ (blue colored solid stars) and $H_M = 0.985 H_C$ (green colored solid squares), respectively.

Fig. 3.20 (a) shows the relaxation behavior for samples S3-TA-NR (black colored solid diamonds) and S3-TA-R (pink colored solid triangles) at a constant applied magnetic field of $H_M = 0.97 H_C$. The relaxation data has been fitted with a double exponential decay (DED) formula:

$$I(t) = I_F + I_1 \exp\left(\frac{-t}{\tau_1}\right) + I_2 \exp\left(\frac{-t}{\tau_2}\right) \quad (3.10)$$

where, I_1 and I_2 are the amplitudes of the exponent with relaxation time constants of τ_1 and τ_2 , respectively. The DED function is a manifestation of Boltzmann function (eqn. 3.9) [186].

Rewriting eqn. 3.9:

$$\begin{aligned}
 I(t) &= I_F + (I_I - I_F)/[1 + \exp((t - t_0)/\tau)] \\
 &= I_F + \frac{I_I}{1 + \exp(\frac{t-t_0}{\tau})} - \frac{I_F}{1 + \exp(\frac{t-t_0}{\tau})} \\
 &= \frac{I_F}{\exp(\frac{t_0-t}{\tau})+1} + \frac{I_I}{1 + \exp(\frac{t-t_0}{\tau})} \\
 &= I_F \left[1 - \exp\left(\frac{t_0-t}{\tau_2}\right) \right] + I_I \exp\left(\frac{-t}{\tau_1}\right) \exp\left(\frac{t_0}{\tau_1}\right); \text{where, } \tau = \tau_1 \ll t - t_0 \text{ and } \tau = \tau_2 > t - t_0 \\
 &= I_F - I_F \exp\left(\frac{-t}{\tau_2}\right) \exp\left(\frac{t_0}{\tau_2}\right) + I_I \exp\left(\frac{-t}{\tau_1}\right) \exp\left(\frac{t_0}{\tau_1}\right) \\
 &= I_F + I_1 \exp\left(\frac{-t}{\tau_1}\right) + I_2 \exp\left(\frac{-t}{\tau_2}\right) ; \text{where, } I_I \exp\left(\frac{t_0}{\tau_1}\right) = I_1 \text{ and } -I_F \exp\left(\frac{t_0}{\tau_2}\right) = I_2
 \end{aligned}$$

The periodic holes in the MAL act as the nucleation and pinning centers for domains. Hence, even at very low applied magnetic field the domains nucleate. However, when the applied field is kept constant at such low field, the system does not get sufficient thermal energy to drive the DWs throughout the sample as the domains are pinned between the successive holes. Hence, the slope of the relaxation curve during nucleation is steeper in comparison to the same during DW motion. This particular behavior is explained by the double exponential decay (DED) nature of the relaxation curves shown in fig. 3.20 (a). For sample S3-TA-NR (triangular antidot: $\omega = 0$ rpm), the values of τ_1 and τ_2 are 4.46 ± 0.25 s and 91.20 ± 3.71 s, respectively. For sample S3-TA-R (triangular antidot: $\omega = 20$ rpm) the fit yields τ_1 and τ_2 to be 2.86 ± 0.37 s and 70.00 ± 3.61 s, respectively. By comparing the τ values between the two samples, we conclude that the relaxation is faster for sample S3-TA-R in comparison to sample S3-TA-NR. This might be due to the fact that the dense cluster of grains in sample S3-TA-R leads to higher inter-granular exchange interaction, as discussed earlier. However, in the presence of high external magnetic field, the DWs get sufficient energy to overcome the pinning barrier and the relaxation follows the faster SED type relaxation behavior (eqn. 3.8). Fig. 3.20 (b) shows the nature of relaxation in sample S3-TA-R (triangular antidot: $\omega = 20$ rpm) at $H_M = 0.995H_C$ (red colored solid circles), $H_M = 0.99H_C$ (blue colored solid stars) and $H_M = 0.985H_C$ (green

colored solid squares), respectively. The relaxation times extracted by fitting the data with equation 3.8 are 5.50 ± 0.30 s, 7.04 ± 0.27 s, and 9.10 ± 0.41 s, at $H_M = 0.995H_C$, $0.99H_C$, and $0.985H_C$, respectively. It should be noted that the speed of relaxation in sample S3-TA-R (triangular antidot: $\omega = 20$ rpm) is significantly faster than that of sample S3-TA-NR (triangular antidot: $\omega = 0$ rpm) (see fig. 3.15 (b) and related discussion). Hence, we conclude that for in-plane anisotropic Co MAL arrays the substrate rotation during deposition leads to higher exchange coupling between the neighboring grains which in turn increases the speed of relaxation in sample S3-TA-R. However, the relaxation in the triangular antidot sample prepared with substrate rotation (sample S3-TA-R) is still slower in comparison to the continuous thin film sample S2-TF-A (see fig. 3.15 (a) and related discussion).

CHAPTER 4: MAL arrays of Co with out-of-plane anisotropy

Most of the work on the MALs so far have been focused on the in-plane magnetized systems where the lateral movement of the DWs are engineered by incorporating the periodic holes [2,12,48-50]. The presence of these periodic holes in such in-plane magnetized MAL arrays hinders the path of propagation of the domains in lateral direction which essentially slows down the magnetic relaxation mechanism [12,13]. The antidot edges pin the magnetic domains and hence more energy is required to complete the reversal. Further, lowering the dimension of the holes as well as the inter-separation leads to magnetic hardening [72]. This magnetic hardening is usually accompanied by slower relaxation time in case of the MAL arrays [13]. In this context, magnetic thin films with perpendicular magnetic anisotropy (PMA) pose the potential to overcome these limitations. In PMA based MAL systems the magnetic domain walls (Bloch walls) propagate in out-of-plane direction and hence is expected to face less hindrance in the path of propagation. In addition, the thermal stability of the magnetization even at very low dimension is ensured by use of such materials with high PMA [18]. However, there are a very few literature available on the study of different magnetic phenomena in the antidot arrays with PMA [78-83,85-87,206,207]. Here, we show the investigation of magnetic domains and relaxation by state-of-art Kerr microscopy in micro-dimensional MAL arrays of Co/Pt with PMA. We demonstrate by simulation using OOMMF [208] that the experimental observations can be reproduced and extended for MAL arrays consisting of holes with dimensions of few tens of nanometer.

The SO interaction plays the pivotal role for the origin of magnetic anisotropy in a system. Orbital angular moment usually makes a minor contribution to the magnetism in 3d transition metals in a combination of magnetic and metallic nonmagnetic system. However, this plays a major role in determining the PMA of such systems when the thickness of the magnetic layer is kept below the critical thickness to aid to ‘spin reorientation transition’. It has been observed

that when ultrathin Co films are grown on Pt (111) layer, the hybridization between Co 3d and Pt 5d becomes dominant at the Pt/Co interface. This strong hybridization pushes the Pt 5d bands (with spins parallel to majority spins of Co) down with respect to the Pt 5d bands with opposite spins. This essentially leads to production of spin moment in Pt parallel to that of Co [209]. Similar phenomenon occurs at the Co/Pd interface. However, the SO interaction is higher in Pt in comparison to that in Pd. Hence, Co/Pt interface leads to formation of larger PMA. In the present work for the out-of-plane magnetized systems, Co films with 0.8 nm thickness have been prepared with the sample structure: Si (100)/Ta (3 nm)/Pt (3.5 nm)/Co (0.8 nm)/Pt (4.5 nm). To maintain the uniformity of the ultrathin Co layer, the substrate has been rotated at 20 rpm during deposition. The base pressure of the chamber has been better than 5×10^{-8} mbar. The films have been prepared using DC (for Co, and Ta) and RF (for Pt) magnetron sputtering at an Ar pressure of 5×10^{-3} mbar. The rate of deposition for Ta, Pt, and Co are ~ 0.018 , 0.020, and 0.010 nm/s, respectively. Ta layer is used to promote the (111) orientation of Pt to obtain high perpendicular magnetic anisotropy (PMA) [210]. The top Pt layer has been deposited to maintain the symmetry and avoid oxidation of the Co layer. Low deposition rate of Co has been employed to ensure the uniformity of the film over the whole sample area. To prepare the MAL arrays first the Si (100) substrates have been patterned using UV lithography technique prior to deposition via sputtering technique. The MAL patterns are prepared with different shapes (circular, square, triangular), sizes, and inter-separations.

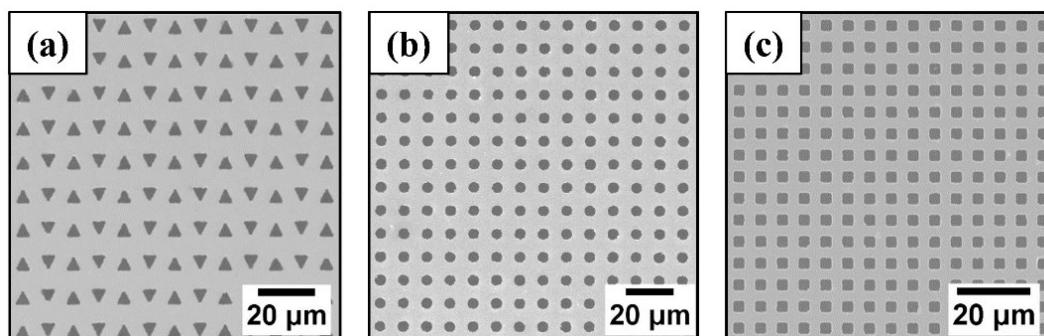


Figure 4.1: SEM images of (a) triangular, (b) circular, and (c) square antidot arrays of Co/Pt.

Fig. 4.1 (a – c) show the SEM images of the triangular, circular, and square antidot arrays of Co/Pt, respectively. It can be observed that the antidot patterns are uniform over the entire sample area. As described before, triangular antidots are ideal to investigate the effect of domain wall pinning due to their sharp edges. Further, the higher inter-separation between the holes (in comparison to circular and square antidots) helps in Kerr microscopy imaging because of elevated domain size. Hence, the experimental observation in the present section will be discussed for the triangular antidot (sample S4-TA) and these results will be compared to its parent continuous thin film (sample S4-TF) sample. The feature sizes and inter-separations between the holes of the simulated and experimental samples are given in table 4.1.

Table 4.1: Details of experimental and simulated samples of Co/Pt with PMA

Sample name	Sample class	Sample type	Side length /diameter	Center to center distance
S4-TF	experimental	Continuous thin film	–	–
S4-TA	experimental	Triangular antidot (asymmetric arrangement)	~ 4.8 μm	horizontal ~9.5 μm , vertical ~11.9 μm
SS-TF	simulated	Continuous thin film	–	–
SS-ATA	simulated	Triangular antidot (asymmetric arrangement)	50 nm	100 nm
SS-STA	simulated	Triangular antidot (symmetric arrangement)	50 nm	100 nm
SS-CA	simulated	Circular antidot	50 nm	100 nm
SS-SA	simulated	Square antidot	50 nm	100 nm

Fig. 4.2 shows the hysteresis loops measured by Kerr microscope in polar mode for the continuous thin film sample S4-TF (black hollow square) and the triangular antidot sample S4-TA (red solid circle). The extracted values of the H_C are 24.23 and 40.79 mT for samples S4-TF and S4-TA, respectively. The periodic holes work as the nucleation centers and act as pinning barriers for the magnetic domains. To overcome the additional pinning, the reversal field increases for the MAL arrays. This in principle is a general behavior for MAL arrays irrespective of their anisotropy and architecture [12,13,72,211]. However the shape of the loops

indicate that the nature of magnetization reversal is similar in both the cases.

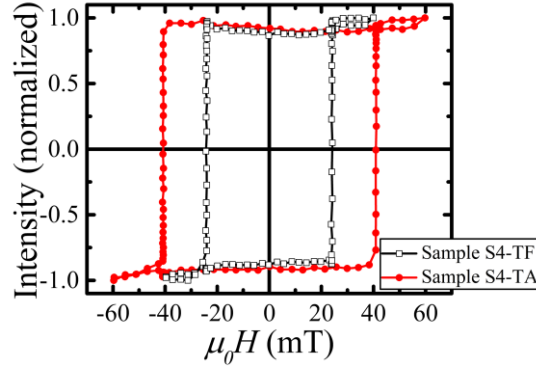


Figure 4.2: Hysteresis loops measured by Kerr microscope in polar mode for samples S4-TF (black hollow square with line) and S4-TA (red solid circle with line).

Fig. 4.3 (a – c) show the domain images observed by Kerr microscopy for samples S4-TF at $-H_S$, H_N , and H_C , respectively. It is observed that at $H_N = 24.1$ mT, bubble domains start nucleating (fig. 4.3 (b)). With increase of magnetic field the bubbles expand (fig. 4.3 (c)) before coalescing with each other to complete the reversal. It is known that uniform bubble domains are observed in thin films with $Q(=K_{out}/K_d) \gg 1$, where K_{out} and K_d are the perpendicular anisotropy and stray field energy densities, respectively [19]. The individual bubble domains remain stable between the bubble collapse field (h_{bc}) and the bubble strip out field (h_{bs}) as discussed in [19]. Fig. 4.3 (d – f) show the domain images for sample S4-TA at $-H_S$, H_N , and H_C , respectively. The sharp edges of the triangular holes act as pinning and nucleation centers for the bubble domains. This leads to nucleation of small localized bubbles in the antidot sample S4-TA (inset of fig. 4.3 (e)). The domains are irregular in shape due to the distribution of energy landscapes in the antidot array. Increase of applied magnetic field leads to further nucleation of domains along with enhancement of size (fig. 4.3 (f)). It is observed that although in case of the Co/Pt MAL arrays with PMA the reversal is nucleation dominated, however, the overall nature of the bubble domains is similar to its parent continuous thin film. It should be noted that, this behavior is different when comparing the domains of MAL arrays

having in-plane anisotropy to their parent thin films [12,13].

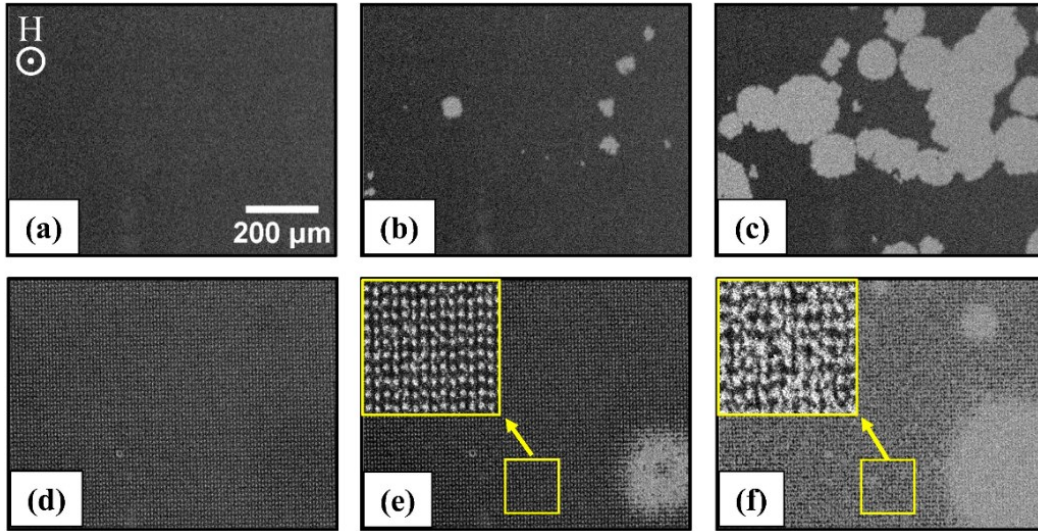


Figure 4.3: (a – c) and (d – f) are the domain images at $-H_S$, H_N , and H_C , for samples S4-TF and S4-TA, respectively. The direction of applied magnetic field and scale bar for all the images are same and shown in (a). The insets of (e) and (f) show the high-resolution images marked by the yellow boxes in the corresponding images.

In order to understand the domain formation and growth mechanism OOMMF simulations [208] have been performed. The parameters considered in the simulations are as follows: saturation magnetization $M_S = 1.1 \times 10^6$ A/m, exchange stiffness constant $A = 1 \times 10^{-11}$ J/m, and anisotropy energy density $K_{out} = 3 \times 10^6$ J/m³. The simulation parameters are taken from literature and corresponds to Co/Pt system. The anisotropy direction has been set along the z-axis i.e. perpendicular to the sample plane along with a slight misalignment in x and y-axis (5%) to aid the simulation to reach its stopping criterion. Fig. 4.4 shows the simulated domain images using OOMMF at H_S , $-H_N$, $-H_C$, and $\sim -H_S$, for the continuous thin film (sample SS-TF): (a – d); and asymmetric triangular antidot (sample SS-ATA): (e – h). It can be observed from fig. 4.4 (a – d) that a bubble nucleates and propagates uniformly under the influence of external magnetic field for sample SS-TF. Since the simulation sample is defect free, only a single bubble nucleates. However, in the experiment multiple nucleation take place

(see fig. 4.3 (b) and (c)) due to inherent magnetic inhomogeneity in the thin film which act as nucleation centers for the domains. The tilt in the bubble from a perfect circle to a slightly elliptical shape occurs due to the misalignment introduced to reach the stopping criterion for simulation. This is consistent with the previous reports on such systems where the bubbles are distorted elliptically due to the orientation dependence of domain wall energy in presence of the horizontal field [19].

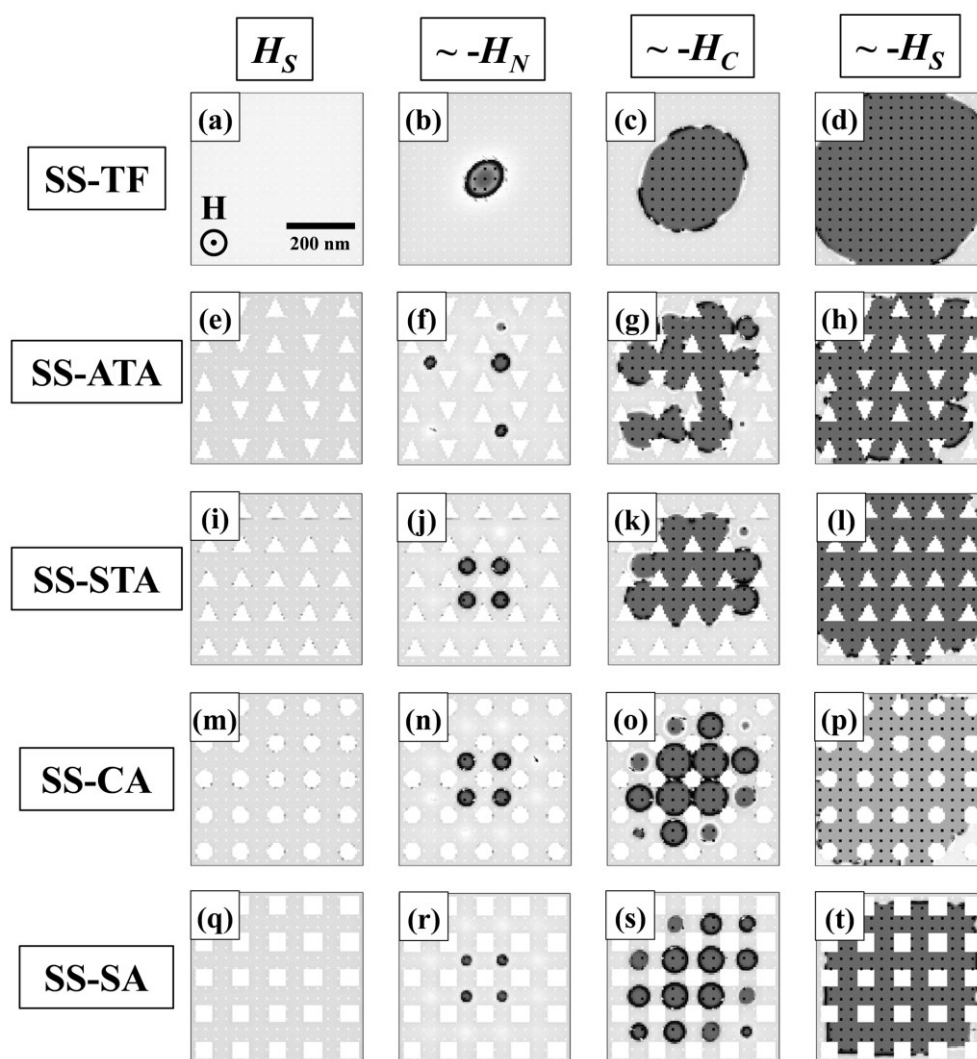


Figure 4.4: OOMMF simulated domain images for various MAL patterns (a – d) SS-TF, (e – h) SS-ATA, (i – l) SS-STA, (m – p) SS-CA, (q – t) SS-SA at H_S , $-H_N$, $-H_C$, and $\sim -H_S$, respectively. The scale bar and direction of applied magnetic field are same for all the samples which are shown in (a).

Similar OOMMF simulations have been performed for the MAL arrays to elucidate the effect of periodic defects on the domain structure. However, here we have considered the dimension of the antidots at the nanoscale (due to the limitation of the simulation capacity of the computer) which are much smaller compared to the MAL array studied experimentally in this work. Further, the symmetric shape of holes in square, circular, diamond shaped antidots do not allow the possibility of arranging them in asymmetric form. Nevertheless, the triangular holes can be arranged in asymmetric form to explore its role in determining the magnetization reversal of the system. We observe that, introduction of triangular holes (sample SS-ATA) lead to formation of multiple localized bubbles as shown in fig. 4.4 (f). Under the influence of the magnetic field, the bubbles expand asymmetrically and coalesce with each other to complete the reversal (fig. 4.4 (g – h)). The arrangement of the triangular holes (alternating pairs of straight and inverted triangles similar to the design of sample S4-TA) in the lattice leads to asymmetry which force the bubbles to nucleate from the edges, remain pinned between two successive triangular holes and propagate asymmetrically. This behavior is similar to the Kerr microscopy observation for the triangular antidot sample S4-TA (fig. 4.3 (d – f)). Hence, it should be noted that although the local nucleation is different at nano-dimension, the overall domain formation and propagation is similar for MAL arrays at both micro as well as in nano-dimension.

Further, we have tried to understand the domain formation and magnetization reversal by considering a few other shapes and distribution of antidot patterns with PMA. In this regard we have performed OOMMF simulation for three more designs which are symmetric triangular antidot (sample SS-STA), circular antidot (sample SS-CA), and square antidot (sample SS-SA). When symmetric arrangement of the triangular holes are considered in sample SS-STA, the bubbles nucleate symmetrically but propagate asymmetrically as shown in fig. 4.4 (i – l). This indicates that the orientation of the triangular holes also play a role in determining the

nucleation and propagation of the bubbles (fig. 4.4 (e – h) and (i – l)). We note that the bubble formation and propagation is symmetric in samples SS-CA, and SS-SA due to the symmetric shape and arrangements of circular and square antidot arrays, respectively, as shown in fig. 4.4 (m – t). Hence, it is concluded that by varying the MAL architecture, the bubble shape, nucleation, and propagation can be engineered. From above discussion we note that the experimental results on the continuous and MAL based thin films are very well reproduced by the OOMMF simulations (fig. 4.4 (a – h)) and can be extended to nano-dimensions. Further our OOMMF results on other MAL designs of various shape and symmetry reveal the nature of domain nucleation and propagation in nano-dimensional antidot arrays of Co/Pt.

To study the response of magnetic domains to the thermal activation energy, magnetic relaxation measurements have been performed by Kerr microscopy at room temperature. Fig. 4.5 (a) shows the relaxation behavior of the continuous thin film (sample S4-TF) at $H_M = 0.99H_C$ whereas (b – i) show the domain images measured at 0, 3, 8, 13, 18, 23, 29, and 44s, respectively as marked in (a). The image (fig. 4.5 (b)) at $t = 0$ s, represents the initial domain configuration for the sample just after setting the magnetic field to a fixed value. Observation of such domains with irregular and fractal boundaries in sample S4-TF is associated to the domain wall response to the wide spectrum of the thermal activation energy [19]. The experimental data is fitted with the compressed exponential function [212,213]:

$$I(t) = I_1 + I_2(1 - \exp\left(-\left(\frac{t}{\tau}\right)^\Gamma\right)) \quad (4.1)$$

where, $I(t)$ is the measured Kerr intensity corresponding to time t , $I_1 + I_2$ is the normalised Kerr intensity at saturation, τ is the relaxation time constant, and Γ is an exponent having a value between 1 to 3. The compressed exponential function is a generalized representation of the Fatuzzo-Labrune [14,15] type single exponential behavior (eqn. 3.8) and the former has been used to describe the relaxation in continuous thin films with PMA [213]. The exponent Γ characterizes the magnetic switching mechanism, where the low and high values of it determine

whether the reversal mechanism is dominated by domain nucleation or DW motion, respectively. The value of Γ obtained from the best fit for the Co/Pt thin film (sample S4-TF) at $H_M = 0.99H_C$ is 3.00 ± 0.05 , which reveals that the magnetization reversal in the continuous thin film is governed by DW motion.

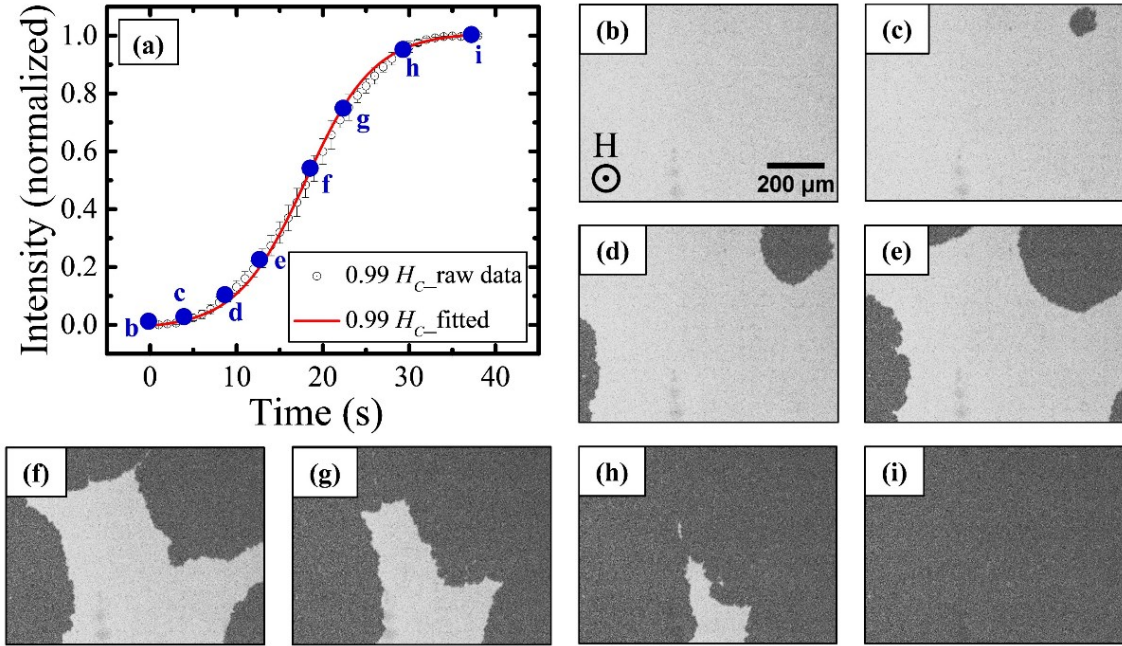


Figure 4.5: (a) Relaxation behavior for the continuous thin film sample S4-TF measured at $H_M = 0.99H_C$, where hollow black circle and red curve represent the raw data, and the fitted curve with compressed exponential function, respectively. (b – i) show the domain images measured at 0, 3, 8, 13, 18, 23, 29, and 44s, respectively, as marked in (a). The scale bar and applied field direction are same for all the images and shown in (b).

Similarly, fig. 4.6 (a) shows the relaxation behavior for the triangular antidot sample S4-TA fitted with compressed exponential function. Fig. 4.6 (b – i) show the domain images at 0, 3, 5, 8, 11, 15, 19, and 27s, respectively, as marked in (a). The value of $\Gamma(1.46 \pm 0.02)$ obtained from the best fit indicates that the switching in the antidot array is dominated by domain nucleation followed by DW motion. It has been observed from fig. 4.6 (b) that the domain nucleation has already taken place at $t = 0$ s. This is different in comparison to the behavior in

the parent continuous thin film sample S4-TF because the presence of triangular holes in sample S4-TA act as nucleation centers for the domains. The insets of fig. 4.6 (c – h) show the high-resolution images of the area marked by the red box in (c). It has been observed that several bubbles (domains) nucleated adjacent to the antidots (holes). Then they expand and coalesce with the neighboring bubbles to complete the reversal process under the influence of thermal activation and constant Zeeman energy.

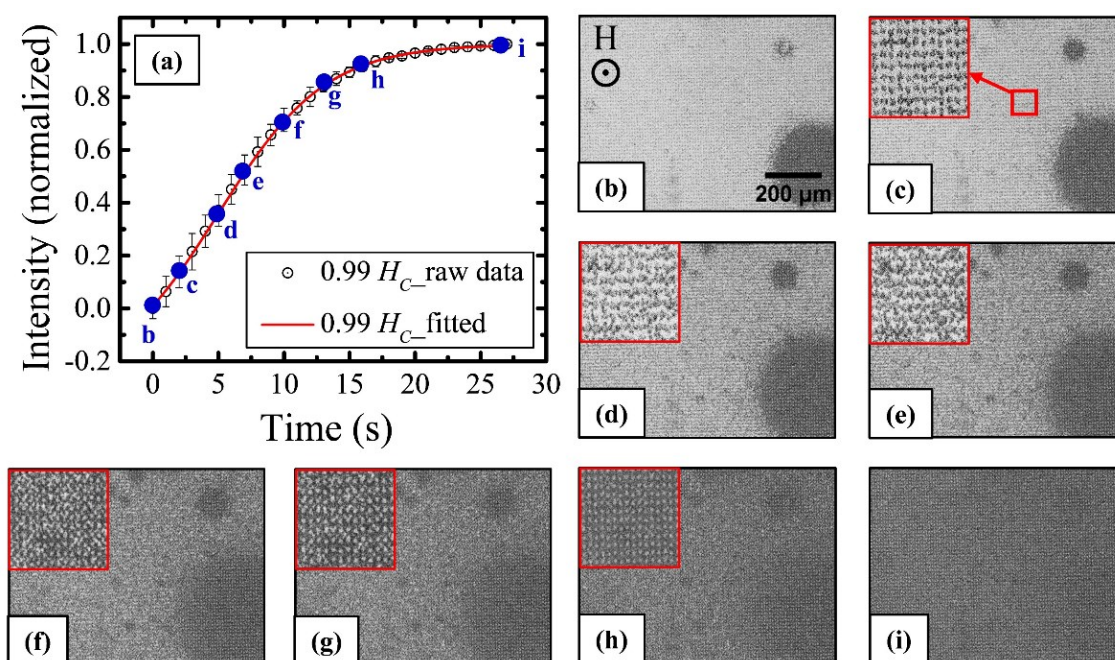


Figure 4.6: (a) Relaxation behavior for the triangular antidot sample S4-TA measured at $H_M = 0.99H_C$, where hollow black circle and red curve represent the raw data, and the fitted curve with compressed exponential function, respectively. (b – i) show the domain images measured at 0, 3, 5, 8, 11, 15, 19, and 27s, respectively, as marked in (a). The scale bar and applied field direction are same for all the images and shown in (b).

In order to compare the nature and speed of relaxation for variable Zeeman energy, relaxation measurements have been performed for both the continuous thin film (sample S4-TF) and triangular antidots (sample S4-TA) at different sub-coercive fields. Fig. 4.7 shows the relaxation behavior at $H_M = 0.99H_C$ (red hollow circle), $0.97H_C$ (blue hollow circle), and

$0.95H_C$ (green hollow circle), for samples (a) S4-TF, and (b) S4-TA. The solid lines (red, blue, and green) represent the corresponding best fits with the compressed exponential function (eqn. 4.1). The values of Γ from the best fits for sample S4-TF are 3.00 ± 0.05 (at $0.99H_C$), 3.00 ± 0.11 (at $0.97H_C$), and 3.00 ± 0.03 (at $0.95H_C$). For sample S4-TA, Γ values obtained from the best fits are 1.46 ± 0.02 , 1.46 ± 0.01 , and 1.44 ± 0.01 , at $0.99H_C$, $0.97H_C$, and $0.95H_C$, respectively. The relaxation time constant τ for sample S4-TF are 20.16 ± 0.13 , 29.94 ± 0.54 , 42.64 ± 0.14 s, for $0.99H_C$, $0.97H_C$, and $0.95H_C$, respectively. Similarly, τ for sample S4-TA are 8.59 ± 0.08 , 12.40 ± 0.10 , 15.81 ± 0.10 s for the above mentioned fields. As expected, the relaxation becomes slow as the amplitude of the applied magnetic field is reduced.

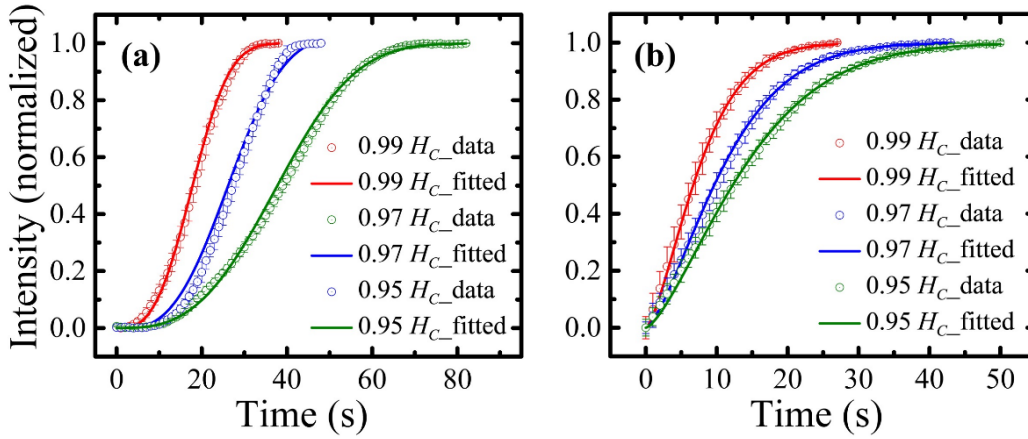


Figure 4.7: Relaxation behavior measured at $H_M = 0.99H_C$ (red circle), $0.97H_C$ (blue circle), and $0.95H_C$ (green circle) for samples S4-TF (a) and S4-TA (b). The solid lines represent the best fits with compressed exponential function.

However, it should be noted that τ in the antidot sample S4-TF is less as compared to its parent continuous thin film sample S4-TA. The magnetization reversal for the thin film is dominated by DW motion. Whereas, the reversal for the antidot sample occurs simultaneously via domain nucleation and DW motion. Further, the out-of-plane motion of the Bloch walls in MAL arrays with PMA face less obstruction from the periodic holes in the path of propagation. It should be noted that, the global relaxation time for saturation is less in the out-of-plane magnetized Co

(both thin film and antidot) in comparison to the in-plane magnetized Co.

In summary, the magnetization reversal and relaxation in perpendicular magnetic anisotropic thin films and antidots of Co/Pt have been discussed. We have observed typical bubble domains for the continuous thin film with high PMA. However, by introducing periodic holes in the form of MAL arrays, it leads to the formation of multiple localized small bubbles. OOMMF simulation supports the experimental observations which is further extended to nano-dimension. In addition, the simulations reveal that the bubble nucleation and propagation are significantly affected by the structure and arrangements of the antidots. The nature of the domain structure and the magnetization reversal observed in the experiments (for micro-dimensional MAL arrays) qualitatively matches with the simulation (at nano-scale). Hence, it is noted that the domain nucleation may differ at nano-scale, however the overall domain structure remains similar for MAL arrays with PMA for both micro as well as nano-dimensional feature sizes of the holes. The speed of magnetic relaxation turns faster in the MAL arrays in comparison to its thin film counterpart. This is in contrary to the in-plane magnetized MALs where the relaxation dynamics turns slower in the antidots in comparison to its parent thin films. The possibility of achieving faster relaxation in comparison to the parent thin film in MAL arrays may have significant impact in MRAM based devices and spintronic applications where reading and writing with rapid speed is desired.

CHAPTER 5: MAL arrays of Heusler alloy

Magnon spintronics has emerged as a future potential candidates for novel computing and data storage technology due to several advantages viz. highly efficient wave-based computing, applicability in devices of sizes down to ~ 10 nm, operation frequency varying from sub-GHz to THz range, room temperature transport of spin information without generating Joule heating, etc. [88]. Further, the spin waves (SW) also find their applications in on-chip communication systems due to their wavelength being one order shorter than that of the electromagnetic waves, which enables them to minimize the data processing bits [88]. In recent years, magnonic crystals have been rigorously studied for the propagation and confinement of the SWs. There are two kinds of interactions present in magnonic crystals such as short ranged exchange and long ranged dipolar interactions. In large wave vector (\mathbf{k}) limit (i.e. short wavelength of SW), the interaction is primarily exchange dominated. Due to such strong exchange interaction (nearest neighbor Heisenberg exchange interaction), the atomic spins remain parallel to each other in the ground state. However, in case of a ferromagnetic thin film, the moments will align themselves in the film plane under an in-plane bias magnetic field. Such modes travelling in the film plane usually possess long wavelength (hundreds of nm to several μm) which is significantly larger than the interatomic distance. In such low \mathbf{k} limit, the exchange interaction is weak and dipolar interactions dominate. Further, for SWs with relatively higher \mathbf{k} values both interaction become non-negligible which is known as the dipole-exchange SW modes [214]. The interactions can be controlled to tune the dispersion relation in such systems.

The two-dimensional magnonic crystals can be broadly subdivided into two parts: dot and MAL arrays. The MALs are superior to the dot arrays as magnonic crystals because of their larger SW propagation velocity (viz. steeper dispersion) [90,94]. The edges of the holes in the antidot arrays quantize the SW modes and modulate internal magnetic field periodically due to the demagnetizing effect [90]. Over the last decade several work have been reported on the

control of SW dynamics in the MAL arrays by controlling the shape anisotropy of the systems via antidot architecture [50,93,96-100].

On the other hand, the most desired characteristics of a material for magnonic based applications are low magnetic damping, high saturation magnetization, high curie temperature, long spin wave propagation distance, etc. [88]. Among various materials reported till date, YIG possesses remarkably low magnetic damping of ~ 0.0002 and high SW propagation distance of $\sim 22.5 \mu\text{m}$ [88]. However the thickness of good quality YIG thin films is in the range of microns which restricts the possibility of device miniaturization. The growth process of YIG is not suitable for CMOS based applications [215]. Further, the saturation magnetization of such YIG films is significantly low ($\sim 0.14 \times 10^6 \text{ A/m}$) [88]. The aforementioned drawbacks make YIG a model system with restrictions in real life technical applications. Over the years Permalloy (NiFe) has been used for SW detection due to their low damping (~ 0.008) and relatively high saturation magnetization ($\sim 0.80 \times 10^6 \text{ A/m}$). However, the SW propagation distance is rather short ($\sim 3.9 \mu\text{m}$) in Permalloy thin films [88]. Intensive research over potential candidates for real life magnonic applications has revealed Co based Heusler compounds as ideal because of their high saturation magnetization ($\sim 1.00 \times 10^6 \text{ A/m}$), low magnetic damping (~ 0.003), and moderately high SW propagation distance ($\sim 10.1 \mu\text{m}$) [22,88,215-217]. Because of lower density of states at the Fermi level in one spin channel, the spin flip scattering gets reduced leading to such remarkable low damping in Co based Heusler compounds [25]. Recently it has been observed that low magnetic damping down to ~ 0.0045 can be achieved from epitaxial Co based Heusler alloy thin films deposited on Cr buffer layer [23]. Conventional Permalloy thin films usually poses very low anisotropy and hence anisotropy field $H_K = 0$ is considered while calculating the precessional frequency using the Kittel equation [7,101]. Hence, only the shape anisotropy introduced from the antidot architecture governs the overall anisotropy of the system. However, it has been reported that the Co based Heusler compounds comprise of

growth induced uniaxial magnetic anisotropy (UMA) and cubic anisotropy (CMA) which can be tuned by varying the thickness as well as the choice of seed layers [22,23]. By controlling the orientations of both magnetocrystalline and shape anisotropies, the global symmetry of the system can be tuned. The anisotropy symmetry of the system can further control the tunability of the SW spectra. Hence, antidot arrays of Heusler alloy thin films may provide additional degrees of freedom to control the spin waves and might be useful for future applications. The combination of magnetocrystalline and shape anisotropies to tune the SW spectra is unexplored. In addition, there are very few reports on antidot arrays with the anisotropic structures like triangular and diamond shaped holes which may significantly modify the internal field distribution in the vicinity of the holes leading to further modifications of the SW spectra of such systems [7,90,101].

In this chapter we have chosen $\text{Co}_2\text{Fe}_{0.4}\text{Mn}_{0.6}\text{Si}$ (CFMS) thin films and their antidot arrays for the investigation of SW dynamics. We show that under the influence of both magnetocrystalline and shape anisotropies, the magnonic band gaps can be tuned with formation of various modes by varying the shape of the antidots. We have also explored the possibility of tuning the domain structure in such antidot arrays depending on the available magnetic area and anisotropy distribution.

Epitaxial CFMS thin films with the thickness (t) = 15, 20, and 25 nm have been deposited at room temperature on MgO (100) substrates in a ultrahigh vacuum compatible magnetron sputtering chamber with a base pressure of $\sim 1.5 \times 10^{-9}$ mbar. The thin film heterostructure of Cr (20 nm)/CFMS (t nm)/Al (3 nm), has been deposited using a sputtering technique. Prior to deposition, the MgO (100) substrate has been annealed at 600°C for 15 minutes for surface reconstruction and removal of impurity from the surface. The-20-nm thick Cr seed layer has been deposited on MgO (100) at a rate of ~ 0.03 nm/s at 1.2×10^{-3} mbar. After the deposition of Cr, it has been annealed in-situ at 700°C for 1 hour to form a flat surface. The Cr layer has been

placed between MgO and CFMS to reduce the magnetic damping of the system [23] as well as to eliminate the possibility of inter-diffusion between MgO and CFMS. Further, the CFMS layer has been deposited at a rate of ~ 0.018 nm/s at 1.2×10^{-3} mbar. Next, the thin film heterostructure has been post annealed in-situ at 500°C for 15 minutes to promote the $B2$ (random position of Fe, Mn, and Si, with respect to Co) and $L2_1$ (completely ordered state) ordering of CFMS. Finally, a 3-nm-thick capping layer of Al has been deposited at ~ 0.039 nm/s at 1.2×10^{-3} mbar to avoid oxidation of the magnetic layer. The CFMS layer shares the following epitaxial relationship with MgO: $\text{CFMS}(001)[110] \parallel \text{MgO}(001)[100]$ [218]. The thin films are denoted as samples S5-TF (CFMS: 15 nm), S6-TF (CFMS: 20 nm), and S7-TF (CFMS: 25 nm). Deposition of the thin films has been performed in the laboratory of Prof. Koki Takanashi at IMR, Tohoku University, Japan.

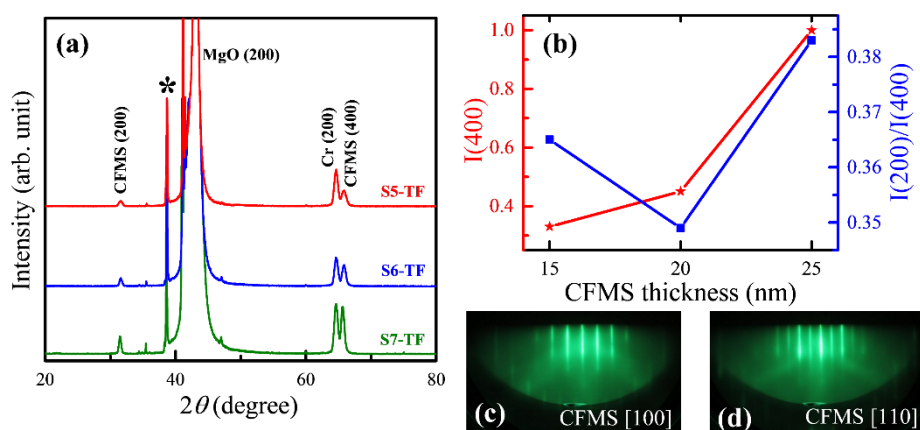


Figure 5.1: (a) XRD pattern for samples S5-TF (red line), S6-TF (blue line), and S7-TF (green line) showing the CFMS, Cr, and MgO peaks. The peaks denoted by * appearing around 38° arise from the (200) diffraction of the MgO substrate with $\text{Cu-K}\beta$ sources. (b) Variation of normalized CFMS (400) peak [i.e. $I(400)$] and ratio of CFMS (200), CFMS (400) intensity peaks as a function of thickness (t) of the CFMS layers. (c) and (d) RHEED images for sample S7-TF along CFMS [100] and CFMS [110] directions.

Fig. 5.1 (a) shows the XRD patterns obtained for samples S5-TF (red line), S6-TF (blue line),

and S7-TF (green line) in the θ - 2θ geometry. MgO (200) corresponds to the most intense peak whereas the peak marked by * appears from (200) diffraction of MgO substrate arising from the Cu-K β source. Both CFMS (200) superlattice and CFMS (400) fundamental diffractions have been observed for all the samples. There are existence of three distinct phases in the phase diagram of CFMS namely $L2_1$, $B2$, and $A2$ phases [219]. $L2_1$ phase shows the perfect chemical structure with well-defined position of the constituent atoms (Co, Fe, Mn, and Si). In $B2$ phase, the Co atoms show regular site ordering with Fe, Mn, Si atoms are located randomly. In the disordered $A2$ phase all the constituent atoms are located randomly. The CFMS (200) superlattice peak corresponds to the formation of $B2$ or $L2_1$ structure [220]. However, it is difficult to quantitatively determine the strength of the $B2$ or $L2_1$ ordering individually from the θ - 2θ geometry.

Further, CFMS (400) corresponds to the overall crystallinity of the film. The ratio of intensities of CFMS (200) and CFMS (400) i.e. $I(200)/I(400)$ yields information about the atomic site ordering of Co in the system [22]. The relative intensity of CFMS (400) peak as well as the ratio of $I(200)/I(400)$ is depicted in fig. 5.1 (b). It is observed that both the intensity of (400) peak as well as the ratios of two intensities are highest for sample S7-TF (CFMS thin film with $t = 25$ nm). This implies that better crystalline structure is formed in the 25 nm thick CFMS film (sample S7-TF) in comparison to samples S5-TF and S6-TF. Fig. 5.1 (c) and (d) show the in-situ RHEED patterns for sample S7-TF with electron beam incidence parallel to MgO [110] (CFMS [100]) and MgO [100] (CFMS [110]) directions, respectively. The well-defined reflected spots in the RHEED patterns ensures the formation of epitaxial CFMS film on MgO with the relation: CFMS [110] || Cr [110] || MgO [100]. The formation of streak lines in the RHEED pattern indicates the flat film surface. Superlattice streaks are also observed in sample S7-TF indicating the chemical ordering of CFMS into either $B2$ or $L2_1$ structure which is coherent to the observation from the XRD measurements.

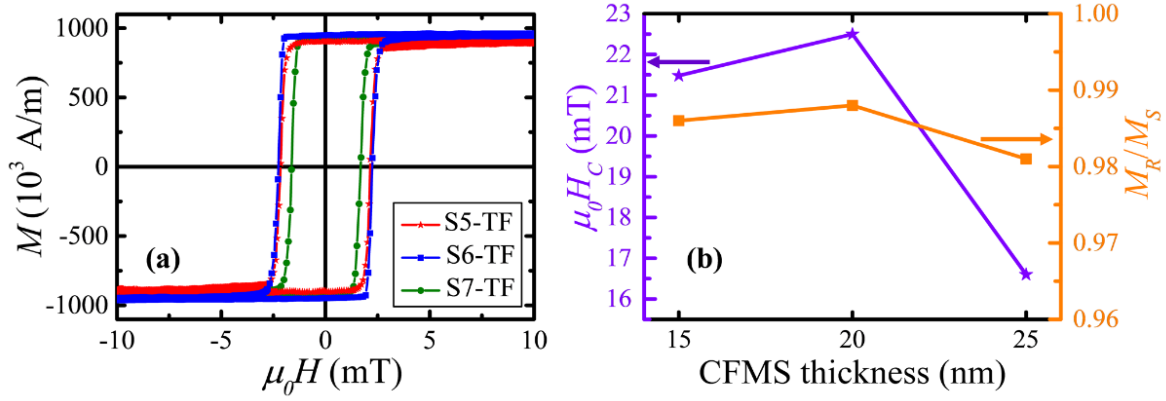


Figure 5.2: (a) M-H curve for samples S5-TF (red line), S6-TF (blue line), and S7-TF (green line) measured by VSM at room temperature along the EA i.e. MgO [100] || CFMS [110] direction. (b) Variation in coercivity (H_C) (purple curve) and relative magnetization (M_R/M_S) (orange curve) as a function of the thickness of the CFMS layers.

Fig. 5.2 (a) shows the M-H loop measured using VSM at room temperature for samples S5-TF (red line), S6-TF (blue line), and S7-TF (green line) while the external magnetic field is applied along the EA (CFMS [110] direction). Fig. 5.2 (b) shows the variation in coercivity (H_C) (purple curve) and relative magnetization (M_R/M_S) (orange curve) as a function of the thickness of the CFMS layers. The relative magnetization provides information regarding the squareness of the films. It is observed that the hysteresis loop shape remain almost unaffected with the change in the thickness of the CFMS layers. For all the samples, square hysteresis loop with $\sim 100\%$ remanence has been observed. The values of H_C along the EA (i.e. CFMS [110]) direction are 2.15, 2.25, and 1.66 mT for samples S5-TF, S6-TF, and S7-TF, respectively. This significant decrease in H_C value implies that sample S7-TF (CFMS thin film with $t = 25$ nm) is the softest among all the samples. Soft magnetic thin film with high saturation magnetization is essential for the study of spin wave. Hence, by comparing both structural as well as magnetic properties, we conclude that sample S7-TF is the best choice of thin film for the work presented in this thesis.

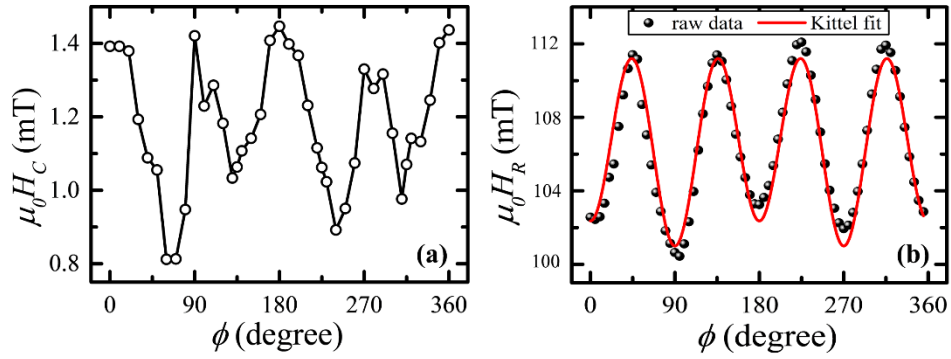


Figure 5.3: (a) Angular (ϕ) dependence of coercivity plot for sample S7-TF measured using micro-MOKE in longitudinal mode. (b) Angular dependence of resonance field (H_R) plot for sample S7-TF extracted from the FMR measurements. The black dots represent the experimental data points whereas the red line represents the best fit using Kittel equation with two anisotropy model.

Fig. 5.3 (a) shows the angular dependence of coercive field plot for sample S7-TF (CFMS thin film with $t = 25$ nm). The values of H_C have been extracted from the angle dependent hysteresis measurements performed using micro-MOKE. Here the magnetic field has been applied at various angles (ϕ) to the EA (CFMS [110]). The easy axes (maximum H_C) at 0° , 90° , 180° , and 270° reveal that the film exhibits anisotropy with cubic symmetry. However, it should be noted that the position of all the hard axes (HA) are not well defined. There are two minima at 135° , and 315° which are the ideal positions for the HA with cubic symmetry. Nevertheless, minima along 60° and 240° are shifted from the original HA position of 45° , and 225° . Further, the strengths of H_C along all the easy axes are unequal. This indicates presence of another type of anisotropy (uniaxial), superimposed on the cubic one. The uniaxial anisotropy has its EA along 0° , and 180° , separated by the HA along 90° , and 270° . This leads to shift of the minima in the coercivity plot to 60° , and 240° , respectively. In order to quantify the strength of the UMA and CMA, we have performed angle dependent FMR measurements on sample S7-TF at the frequency of 10 GHz. We have plotted the resonance field (H_R) as a function of the angle (ϕ)

to obtain the anisotropy behavior. The experimental data points have been fitted with the two anisotropy model Kittel formula, which under small angle approximation can be represented as:

$$f = \frac{\gamma}{2\pi} \sqrt{\left[H + \frac{2K_2}{M_S} \cos 2\phi - \frac{4K_4}{M_S} \cos 4\phi \right] \times \left[H + 4\pi M_S + \frac{2K_2}{M_S} \cos^2 \phi - \frac{K_4}{M_S} (3 + \cos 4\phi) \right]} \quad (5.1)$$

where, γ is the gyromagnetic ratio, K_2 is the UMA constant, K_4 is the CMA constant. The value of M_S was obtained from the VSM measurement and used here to calculate K_2 and K_4 . Fig. 5.3 (b) shows the angular dependent resonance field data fitted with eq. 5.1 for sample S7-TF (CFMS thin film with $t = 25$ nm). The fitted values of K_2 and K_4 are 0.34×10^3 , and 1.17×10^3 J/m³, respectively. Hence, it can be concluded that a noticeable contribution of UMA is present in sample S7-TF, which is $\sim 29\%$ of the dominant CMA. The UMA in the CFMS film can be introduced due to several reasons viz. oblique angular deposition, anisotropic strain relaxation, miscut in the substrate, interfacial roughness, interfacial alloy formation, growth on a stepped substrate, etc. [11,221-223]. The presence of such strong UMA leads to the shift in the position of the hard axes as observed in fig. 5.3 (a). We have further extracted the damping constant (α) = 0.0056 from the frequency dependent FMR measurements. The parameters extracted from the FMR measurements have been used in OOMMF simulation which is discussed in the later part of this chapter.

In order to understand the magnetization reversal mechanism, we have performed domain imaging in the continuous thin film sample S7-TF (CFMS with $t = 25$ nm) using Kerr microscopy in longitudinal mode. Fig. 5.4 shows the domain images in sample S7-TF measured at different $\phi = 0^\circ$ (a), 40° (b), 75° (c), and 80° (d), marked by numbers 1 – 4, 5 – 8, 9 – 12, and 13 – 16, respectively. Along the EA for cubic anisotropy i.e. at $\phi = 0^\circ$ (fig. 5.4.a), the reversal occurs via two simultaneous 90° DW motion. Formation of such 90° domain walls in

Fe films with cubic anisotropy is reported in *ref.* [115,224,225]. For a magnetic system with cubic anisotropy symmetry, the easy axes are aligned along both MgO [100] ($[\bar{1}00]$), and [010] ($[0\bar{1}0]$) directions. All the domain directions are explained wrt the MgO coordinate system. Hence, under the application of reverse magnetic field, the spins prefer to align themselves along either $[\bar{1}00]$ or $[0\bar{1}0]$ direction, leading to formation of two 90° DWs. At an applied field (μ_0H) of -5.00 mT (fig. 5.4.a.1), the spins are saturated along $[\bar{1}00]$ direction. The domain contrast in this state is represented by dark black contrast. The green arrows marked in the images depict the net magnetization direction within a particular domain contrast in the sample.

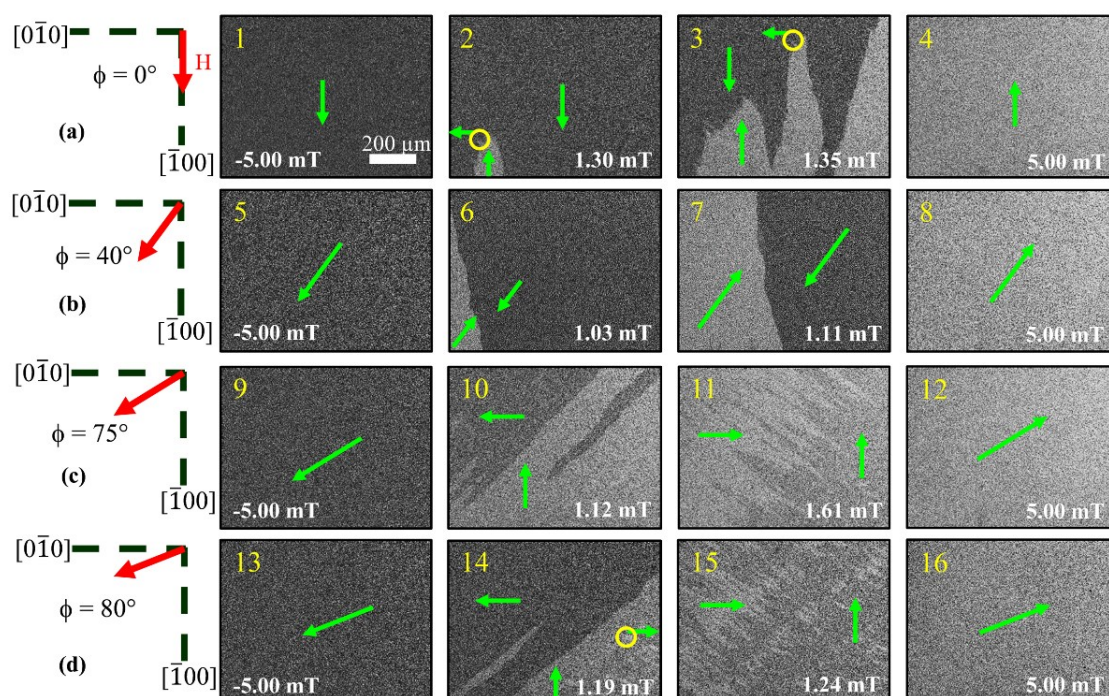


Figure 5.4: Domain images in sample S7-TF measured by Kerr microscope for different $\phi = 0^\circ$ (a), 40° (b), 75° (c), and 80° (d), marked by numbers 1 – 4, 5 – 8, 9 – 12, and 13 – 16, respectively. The applied field values for the different images are marked in the respective images. Scale bar for all the images are equal and is shown in 1. The green arrows marked in the images depict the net magnetization direction within a particular domain contrast in the sample.

During the hysteresis cycle, when a reverse field $\mu_0 H = 1.30$ mT is applied, two domain contrasts (white and grey) appears simultaneously on the black contrast (fig. 5.4.a.2). The two domains with white and grey contrast are mutually 90° wrt each other. It should be noted that the black and white domains are 180° wrt each other. This implies that the small grey color domains are aligned at 90° wrt both the white and black contrast domains. However, around the hard axis for CMA, at $\phi = 40^\circ$, the reversal occurs via one 180° DW motion. Here, at saturation, the spins are aligned towards $[\bar{1}\bar{1}0]$ direction. The magnetization switching occurs from $[\bar{1}\bar{1}0]$ to $[110]$ direction via one 180° DW (fig. 5.4.a.5 – 8) under the application of the magnetic field. Further, near another cubic easy axis ($[0\bar{1}0]$), at $\phi = 75^\circ$, the reversal occurs via two successive 90° DW motion (fig. 5.4.a.9 – 12). Similarly, at $\phi = 80^\circ$, the reversal occurs via two successive 90° DW motion (fig. 5.4.a.13 – 16). During the reversal, the system cannot generate sufficient energy for the occurrence of two simultaneous 90° DW motion along $\phi = 75^\circ$ and $\phi = 80^\circ$, as observed at $\phi = 0^\circ$.

Table 5.1: Details of the thin film and antidot samples of Heusler alloy

Sample name	Sample structure	Sample Type	Feature Size
S5-TF	MgO(100)/Cr(20 nm)/CFMS(15 nm)/Al(3 nm)	Continuous thin film	–
S6-TF	MgO(100)/Cr(20 nm)/CFMS(20 nm)/Al(3 nm)	Continuous thin film	–
S7-TF	MgO(100)/Cr(20 nm)/CFMS(25 nm)/Al(3 nm)	Continuous thin film	–
S7-CA		Circular antidot	200 nm
S7-SA		Square antidot	200 nm
S7-TA		Triangular antidot	200 nm
S7-DA		Diamond antidot	200 nm

In the following we have discussed the results obtained on the antidot arrays of various shapes and sizes. Microfabrication of the MAL arrays with different shapes (circular, square, triangular, and diamond) and feature sizes of 100, 200, and 500 nm have been performed using e-beam lithography and Ar ion milling. Patterning on the thin film has been performed using e-beam lithography followed by development in isopropanol and distilled water for 7 and 20 seconds, successively. Ar ion milling has been performed at 6×10^{-7} mbar to etch out the residual films. Finally, the MAL arrays have been obtained by developing the films in pyrrolidone for 4 hours. For this thesis we have focused on the antidot samples having feature size of 200 nm, microfabricated on 25 nm thick CFMS films. The list of all the samples are provided in table 5.1. We note that the acronyms CA, SA, TA, and DA have been used to denote the circular, square, triangular, and diamond shaped antidot samples, respectively. Fig. 5.5 shows the SEM images for (a – d) circular (sample S7-CA), square (sample S7-SA), triangular (sample S7-TA), diamond antidots (sample S7-DA), respectively. It can be observed that the antidot patterns are uniform over the entire sample area.

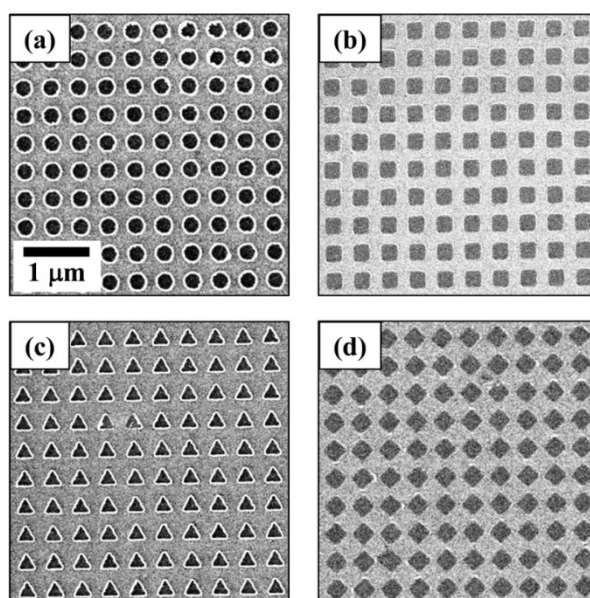


Figure 5.5: SEM images of (a – d) circular (sample S7-CA), square (sample S7-SA), triangular (sample S7-TA), and diamond antidots (sample S7-DA), respectively. The scale bar for all the images are same and is shown in (a).

Fig. 5.6 shows the hysteresis loops measured using micro-MOKE for (a – d) circular (sample S7-CA), square (sample S7-SA), triangular (sample S7-TA), and diamond (sample S7-DA) antidot arrays, respectively. The insets of fig. 5.6 (a) – (d) show the SEM images of the corresponding antidot samples. The values of H_C are 7.27, 9.53, 5.47, and 9.42 mT, for samples S7-CA, S7-SA, S7-TA, and S7-DA, respectively. The values of H_S for the samples are 8.97, 10.10, 6.25, 10.32 mT, respectively.

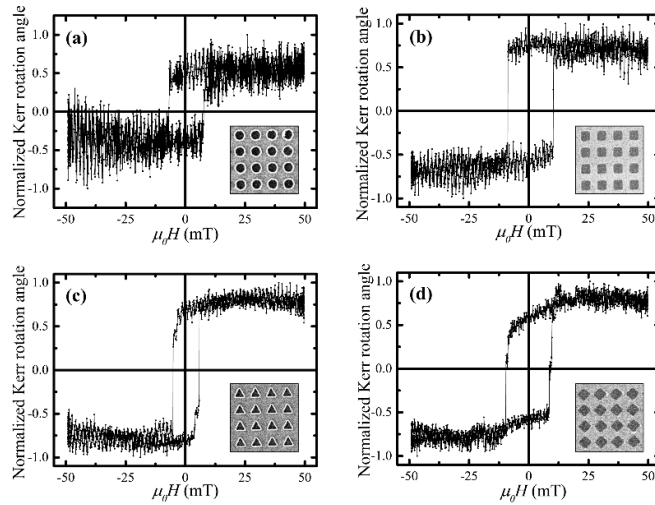


Figure 5.6: Hysteresis loops measured using micro-MOKE at room temperature for (a – d) samples S7-CA (circular antidot), S7-SA (square antidot), S7-TA (triangular antidot), and S7-DA (diamond antidot), respectively. The insets show the corresponding SEM images.

The values of H_S are significantly higher in the antidot samples in comparison to their thin film counterpart (sample S7-TF). This is natural since introduction of periodic holes pin the magnetic domains and do not allow the DWs to propagate through them leading to magnetic hardening. The variation in the strength of H_C and H_S among the antidot samples can be explained by the active area in the samples. The active area (total magnetic area) in the MAL arrays is calculated by subtracting the total area covered by all the holes from the total area of the sample. The available active area in the triangular antidot (sample S7-TA) is always higher than that in the diamond shaped antidot (sample S7-DA) with same feature size and lattice

geometry. Hence, the DWs require higher energy to avoid the holes and propagate in a zigzag path for sample S7-TA in comparison to that in sample S7-DA. A similar and detailed description for the dependence of H_C and H_S on the available active area in the antidots is discussed in section 3.2 of Chapter 3 [13].

High resolution domain imaging on the MAL arrays has been performed along the EA via X-ray photoemission electron microscopy (XPEEM) by employing X-ray magnetic circular dichroism (XMCD) at the L_3 edge of Fe. Fig. 5.7 (a) shows the SEM image of the circular antidot (sample S7-CA). Fig. 5.7 (b – f) show the domain images for sample S7-CA measured using XPEEM at field pulses of -40.56 , 5.07 , 8.11 , 9.13 , and 40.56 mT, respectively. The direction of applied magnetic field as well as the sensitivity direction of XPEEM is set along the EA [i.e. MgO [010] (CFMS [$1\bar{1}0$]) direction]. To saturate the sample, initially a high magnetic field pulse (-40.56 mT) has been applied and subsequently set to zero to observe the remanent magnetic state (fig. 5.7 (b)). Further, gradually field pulses in the reverse direction have been applied followed by removing the field and taking the images at remanence states. The values of the reverse field pulses have been mentioned above for fig. 5.7 (b – f). Presence of the periodic holes in the film act as nucleation centers and the domains remain pinned in between two successive holes. The domains propagate in a zigzag path avoiding these holes. This leads to formation of a chain like domain structure [48,49]. Further, the DWs propagate in the transverse direction with the enhancement of applied field pulses to complete the reversal. The domain sizes in the circular antidot sample S7-CA near nucleation (fig. 5.7 (c)) and coercive fields (fig. 5.7 (d)) are 0.37 , and 1.07 μm , respectively. The circular holes are symmetric in nature and hence do not possess any contribution of the shape anisotropy. Further, the holes in the array are aligned in square lattice geometry. This leads to alignment of the easy axes (due to shape anisotropy) along MgO [100] and MgO [010] direction. It should be noted that the EA of the parent thin film (sample S1) is also aligned along MgO [100] and MgO [010]

directions because of the presence of cubic anisotropy. Hence, the alignment of magnetocrystalline and the shape anisotropy in sample S7-CA coincide with each other. Since during the XPEEM measurements, the external magnetic field is applied along $[010]$, the domains align them in a chain like structure along the same (fig. 5.7 (b – e)). Nevertheless, with enhancement of the Zeeman energy (external magnetic field), the DWs are forced to move in the transverse direction before coalescing with the neighboring domains to complete the reversal.

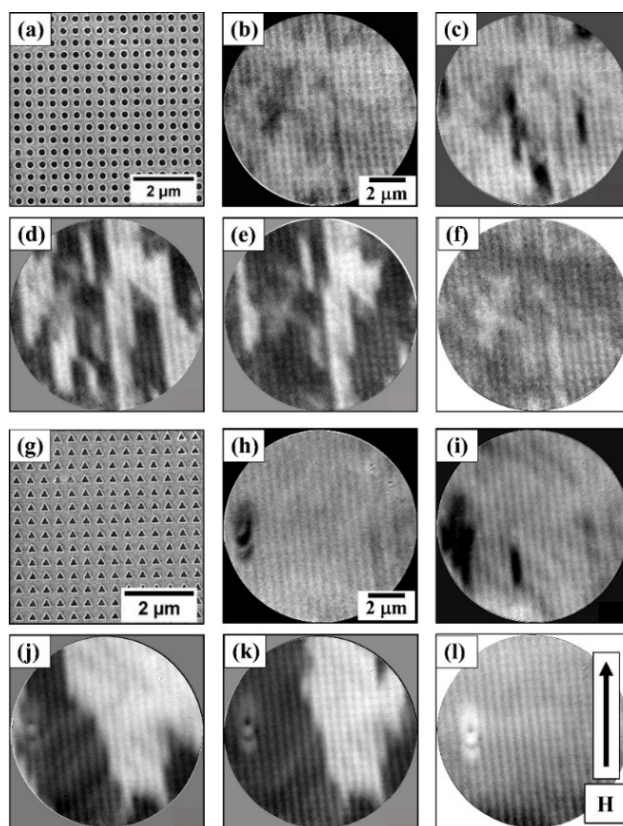


Figure 5.7: (a) SEM image of sample S7-CA (circular antidot). (b – f) show the domain images measured at magnetic field pulses of -40.56 , 5.07 , 8.11 , 9.13 , and 40.56 mT, respectively, in sample S7-CA using XPEEM. (g) SEM image of sample S7-TA (triangular antidot). (h – l) show the domain images in sample S7-TA at field pulses of -40.56 , 4.26 , 4.46 , 5.07 , and 40.56 mT, respectively. The scale bar for the XPEEM images are same and shown in (b) and (h). The field has been applied along the EA (CFMS $[1\bar{1}0]$) and the direction is shown in (l).

Fig. 5.7 (g) shows the SEM image of the triangular antidot array (sample S7-TA) whereas (h – l) show the domain images measured at -40.56 , 4.26 , 4.46 , 5.07 , and 40.56 mT, respectively. In contrary to the chain like domain formation in the circular antidot sample, the domains are correlated and bigger in the triangular antidot sample. The domain size in the triangular antidot sample S7-TA near nucleation (fig. 5.7 (i)) and coercive fields (fig. 5.7 (j)) are 0.44 , and 3.65 μm , respectively. The triangular holes in sample S7-TA are not isotropic in nature like the circular ones in sample S7-CA. Hence, the local field distribution as well as the anisotropy is different in the vicinity of the holes in the triangular antidot sample S7-TA. This modifies the overall cubic anisotropic nature of the parent film. Hence the DWs propagate along both the field as well as transverse direction leading to elevation in size of the domains. The enhancement of the domain size can be further explained by comparing the availability of the active area in samples S7-CA, and S7-TA. The available active area in the circular antidot (sample S7-CA) is 71.7% of the total sample area, whereas the same for the triangular antidot (sample S7-TA) is 84.4% . Hence, due to the availability of larger magnetic area in the triangular antidot sample, the DWs have more freedom to expand laterally during the reversal. The enhancement in domain size in the antidots depending on the availability of the active area is explained in detail in Chapter 3 [13].

The spin wave (SW) spectra of the samples is obtained by taking fast Fourier transform (FFT) of the background subtracted time-resolved Kerr rotation data [7,101]. It should be noted that the applied field needs to be significantly higher than the saturation field to employ precession of the spins. The experimental precessional data (background subtracted) of the time-resolved magneto-optical Kerr rotation for the continuous thin film sample S7-TF at $\mu_0H = 153$ mT along MgO [010] (CFMS [$\bar{1}\bar{1}0$]) is shown in fig. 5.8 (a). Fig. 5.8 (b) shows the corresponding FFT power spectrum which yields a precessional frequency of 12.51 GHz at $\mu_0H = 153$ mT. The experimentally observed spin-wave spectra have been qualitatively reproduced using

micromagnetic simulation (OOMMF) [208]. The simulation area is taken as $1600 \times 1600 \times 25$ nm³ in coherence for an antidot array of 4×4 holes (this ensures the feature size of 200 nm). The cell size for the simulations are considered to be $4 \times 4 \times 25$ nm³. This ensures presence of only one shell along the thickness of the sample. We have used the following material parameters: $\gamma = 2.14 \times 10^5$ m/As, $M_S = 9.2 \times 10^5$ A/m, $K_2 = 3.4 \times 10^2$ J/m³, $K_4 = 1.17 \times 10^3$ J/m³, $\alpha = 0.006$, and exchange stiffness (A) = 1.75×10^{-11} J/m. The values of γ , α , K_2 , and K_4 are extracted from the FMR fitting, whereas A is taken from *ref.* [23]. Two-dimensional periodic boundary condition (2D-PBC) has been used for approximating the large sample area by choosing a small part as the unit cell.

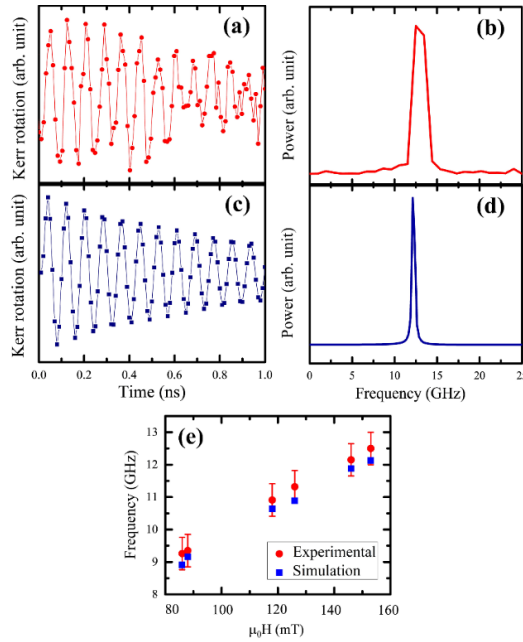


Figure 5.8: Experimentally observed time resolved Kerr rotation data (a) and corresponding FFT spectra (b) for the continuous thin film sample S7-TF at $\mu_0 H = 153$ mT. Similarly, (c) and (d) show the OOMMF simulated Kerr rotation and the corresponding FFT spectra, respectively, at the same applied field. (e) shows the extracted precessional frequency as a function of the external field for both experiment (red dots) and simulation (blue squares).

Fig. 5.8 (c – d) show the Kerr rotation and corresponding FFT spectrum at $\mu_0 H = 153$ mT

obtained by OOMMF simulation. From fig. 5.8 (b) and (d), it can be concluded that the simulated precessional frequency matches (within the error bar) with the experimental observation. Fig. 5.8 (e) shows the experimental and simulated precessional frequency plot as a function of various amplitude of applied magnetic field. This further confirms that the experimental and simulated frequency matches well within the experimental field range. The values of the parameters for simulation of the MAL arrays are chosen same as that of the continuous thin film counterpart.

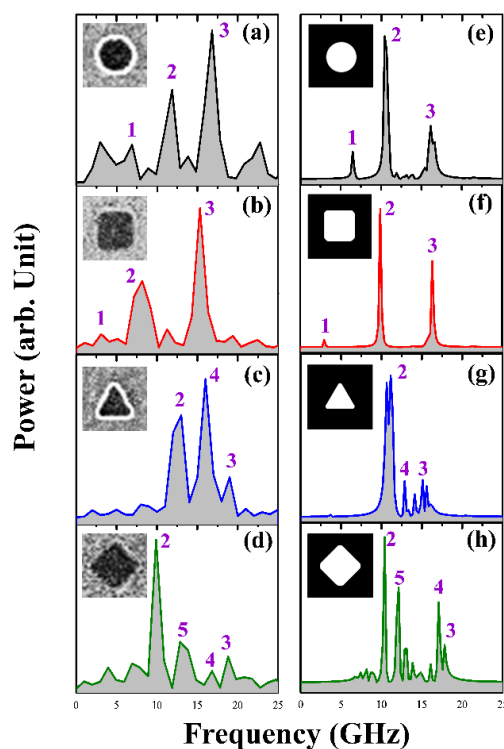


Figure 5.9: (a – d) Spin wave spectra obtained at $\mu_0H = 153$ mT from the experimental time-resolved Kerr rotation data for samples S7-CA (circular antidot), S7-SA (square antidot), S7-TA (triangular antidot), and S7-DA (diamond antidot), respectively. (e – h) Simulated spin wave spectra for samples S7-CA, S7-SA, S7-TA, and S7-DA, respectively. The numbers corresponding to different modes are shown in the individual images. The images in the insets of (a – d) and (e – h) show the shape of a single hole in the antidot array obtained from SEM images and bitmap images considered in the simulation, respectively.

Fig. 5.9 (a – d) show the SW spectra for samples S7-CA (circular antidot), S7-SA (square antidot), S7-TA (triangular antidot), S7-DA (diamond antidot) respectively, at $\mu_0 H = 153$ mT along MgO [010] (CFMS [$1\bar{1}0$]). It can be observed from fig. 5.9 (a) and (b) that there are total three modes in case of circular (sample S7-CA) and square antidot arrays (sample S7-SA). The gaps between the 1st to 2nd (mode no. 1 to 2) and 2nd to 3rd (mode no. 2 to 3) modes are 4.93, and 4.97 GHz, respectively, for sample S7-CA. Similarly the gap between the consecutive modes for sample S7-SA are 5.10, and 7.15 GHz, respectively. The bandwidths (gaps between mode no. 1 to 3) are 9.90 GHz, and 12.25 GHz, for samples S7-CA and S7-SA, respectively. The low frequency 1st mode is absent in triangular antidot (sample S7-TA) (fig. 5.9 (c)). Further, in case of sample S7-TA, an additional mode (mode no. 4) appears in the gap between mode no. 2 and 3. The bandwidth (gap between mode no. 2 to 3) in the triangular antidot sample S7-TA reduces to 5.94 GHz. The gaps among mode no. 2 to 4, and 4 to 3, are 3.02, and 2.92 GHz, respectively. Similar to sample S7-TA, the low frequency mode 1 is absent in the diamond antidot (sample S7-DA). However, in sample S7-DA, four modes occur with narrow gaps of ~ 2.97 , 3.96, and 1.98 GHz, respectively. The new mode (mode no. 5) appears between mode no. 2 and 4. The bandwidth in the diamond antidot sample S7-DA is 8.91 GHz.

We have simulated the SW spectra in the antidot samples using OOMMF. It should be noted that the simulation qualitatively reproduces the experimental observation with the quantitative disagreement appearing due to the limitations in the simulation viz., edge roughness of the holes, statistical difference in the hole structures, etc. [226]. It should be noted that, the experiments are performed at ambient temperature whereas the simulations do not consider any effect arising from the temperature. Fig. 5 (e – h) show the simulated spin wave spectra for samples S7-CA (circular antidot), S7-SA (square antidot), S7-TA (triangular antidot), and S7-DA (diamond antidot), respectively. Similar to the experimental case, no low frequency mode has been observed in samples S7-TA, and S7-DA. In the simulated spectra, the bandwidth (gap

between mode no. 2 to 3) for samples S7-CA, S7-SA, S7-TA, and S7-DA are 9.65, 13.36, 3.96, and 7.43 GHz, respectively. Hence, we conclude that the frequency gap between the successive bands decreases significantly for triangular and diamond antidots (samples S7-TA and S7-DA), in comparison to that in circular and square antidots (samples S7-CA and S7-SA). There are a few low power modes present in the simulation for samples S7-TA and S7-DA which are not resolved properly in the experiment. For all the antidot samples, mode 2 is the highest power mode with its frequency close to 10 GHz at $\mu_0 H = 153$ mT. This frequency is slightly lesser than the fundamental mode (~ 12.5 GHz) in the parent thin film sample for the same value of H , which is also known as the Kittel mode. This can be corroborated to the relative increase in the demagnetized regions between the holes which gives rise to lower effective fields in comparison to that of the parent thin film. The remarkable difference in the mode profile between the different antidots arises from the difference in their internal field distribution which leads to formation of extended and localised modes [101]. Previously Mandal *et al.*, has discussed that the symmetry of the demagnetized regions is similar for the circular and square antidots [101]. However, it changes significantly for the triangular and diamond shaped antidots. Additionally, asymmetry introduced from the fabrication process imposes further differences in the internal field profiles in the antidot arrays. Nevertheless, we have tried to address this issue by considering roundish edges during simulations (see insets of fig. 5.9 (f – h)) for square, triangular, and diamond antidot samples. Indeed, the simulation results are closer to the experimental findings when round corners are considered in comparison to the sharp corners of the holes. Previous literature on such structures have been reported by considering zero magnetocrystalline anisotropy for the constituent films [7,101]. However, in our study both cubic and uniaxial anisotropies along with the shape anisotropy play important roles in determining the total anisotropy in the antidot samples. In circular and square antidots (samples S7-CA and S7-SA), the symmetric structure of the holes does not perturb the anisotropy of the

parent thin film. However, the anisotropy is modified in case of the triangular and diamond shaped antidots (samples S7-TA and S7-DA). This leads to formation of additional high frequency modes. Similar reasons can be corroborated to the absence of low frequency mode (mode no. 1) in samples S7-TA and S7-DA.

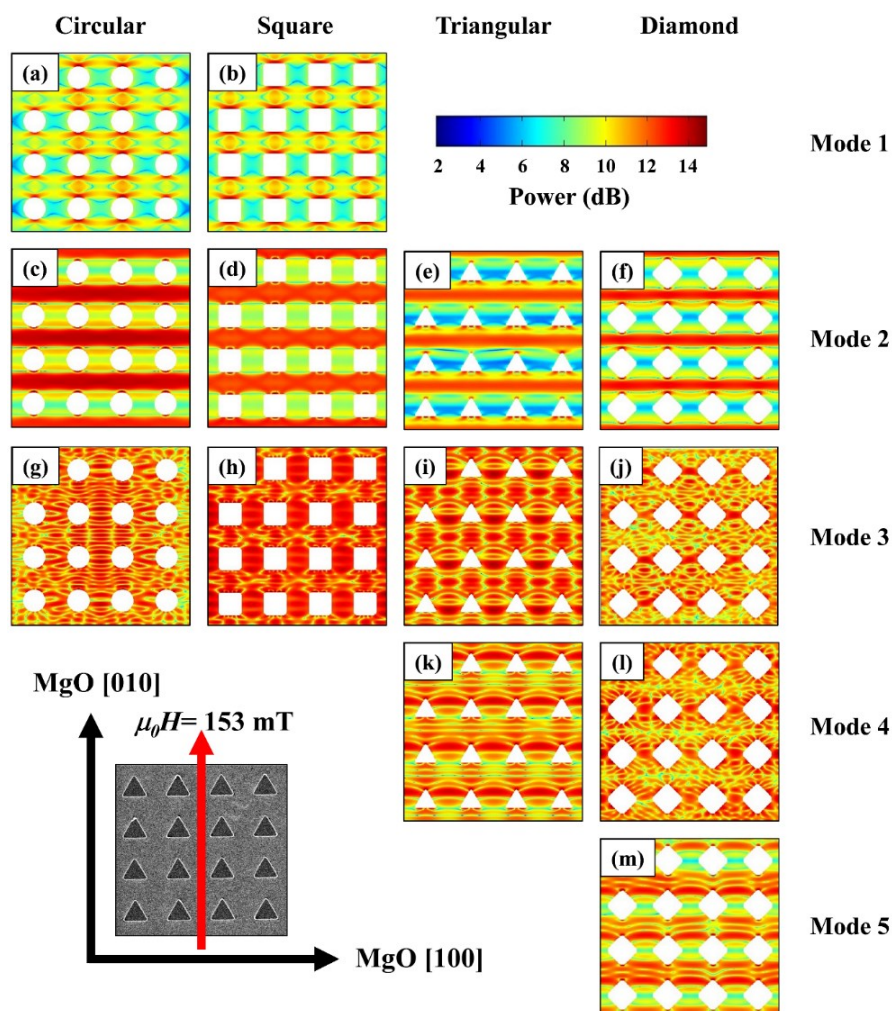


Figure 5.10: Simulated power maps for different precessional modes as shown in fig. 5.9 (e – h) for circular, square, triangular, and diamond antidots (samples S7-CA, S7-SA, S7-TA, and S7-DA), respectively. The colormap for the power distribution is shown at the right top of the image. Respective mode numbers as per fig. 5.9 is shown in the right side of the image. Magnetic field $\mu_0 H = 153$ mT is applied along the EA (MgO [010] || CFMS $[1\bar{1}0]$).

To understand the nature of the precessional modes, we have further simulated the power and

phase map profiles of the modes using a code described in *ref.* [27]. Fig. 5.10 shows the simulated power maps for the precessional modes for circular, square, triangular, and diamond antidots (samples S7-CA, S7-SA, S7-TA, and S7-DA). Fig. 5.10 (a), (b) show very low frequency edge modes (mode no. 1) in circular (sample S7-CA) and square (sample S7-SA) antidot samples, respectively. From the mode profile, it can be observed that mode 1 is a symmetric mode where the maximum power is stored at the vicinity of the circular and square holes in samples S7-CA, and S7-SA, respectively. This low frequency symmetric edge mode is absent in triangular and diamond antidots (samples S7-TA and S7-DA). The reason behind this can be corroborated to the asymmetric internal field profiles in samples S7-TA and S7-DA. Mode 2 is an extended mode which flows in Damon-Eshbach (DE) geometry through the channels between the neighboring holes (fig. 5.10 (c – f)). These modes are also known as magnetostatic surface wave (MSSW) mode where the propagation wave-vector is perpendicular to the applied field direction [7]. Mode 2 in case of triangular and diamond antidot samples are also MSSW modes however with reduced intensity. The frequency of Mode 2 is slightly reduced in comparison to the continuous thin film counterpart (sample S7-TF) because of modulation by the antidots and varying demagnetized regions in the vicinity of the holes. Mode 3 (fig. 5.10 (g – j)) is the highest frequency mode observed for all the samples. This is a quantized mode (mode number $q = 5$) in the backward volume magnetostatic (BWVMS) wave geometry between the neighboring holes. In case of the triangular and diamond shaped antidots (samples S7-TA and S7-DA), another quantized mode (Mode 4) with $q = 3$ appears in BWVMS geometry (fig. 5.10 (k), (l)). The power maps of the diamond antidots (sample S7-DA) is similar to triangular antidots (sample S7-TA) with small changes which occurs due to the different internal field profiles. Appearance of the $q = 3$ modes leads to reduction in the gap in the frequency spectra of samples S7-TA and S7-DA. The reason behind such observation is probably due to the corners of triangular and diamond shaped holes, which

provides additional pinning centre. Further, in the diamond antidot sample S7-DA, another additional mode (mode no. 5) appears having a modulated MSSW-like profile (fig. 5.10 (m)). The frequency of Mode 5 is very close to that of Mode 2 leading to formation of such a modulated mode in DE geometry. Appearance of this extra mode in sample S5 leads to further reduction in the gap of the frequency spectra. This is attributed to the effect of the shape of the diamond antidots in modifying the anisotropy, internal field profiles, and pinning energy landscapes in the system. Fig. 5.11 shows the simulated phase map profiles of all the antidot samples which conveys information similar to that of fig. 5.10.

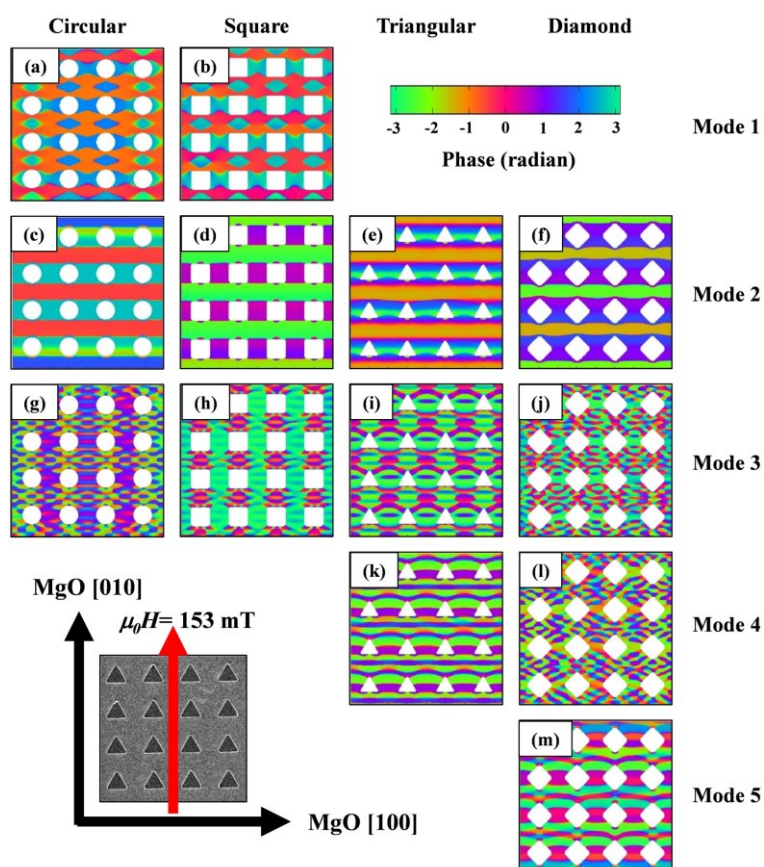


Figure 5.11: Simulated phase maps for different precessional modes as shown in fig. 5.9 (e – h) for circular, square, triangular, and diamond antidots (samples S7-CA, S7-SA, S7-TA, and S7-DA), respectively. The colormap for the phase distribution is shown at the right top of the image. The respective mode numbers as per fig. 5.9 is shown in the right side of the image.

In summary we have systematically studied the possibility of tuning the domain structure as well as the spin-wave spectra in antidot arrays of Heusler alloy thin film by varying the shape of the holes. Epitaxial Heusler alloy thin films were grown on MgO substrates with highly ordered B_2 or $L2_1$ phase. MOKE and FMR measurements confirmed the formation of cubic anisotropy due to epitaxial growth of the film along with a moderate uniaxial anisotropy. The quantification of the anisotropy has been performed using angle dependent FMR measurements which shows that the UMA is almost $\sim 29\%$ of the CMA. We have shown that the domain structure changes from chain like features to wide correlated domains by changing the shape of the holes from circular to triangular. This behaviour is explained in terms of availability of the active area and the anisotropy distribution in the vicinity of the holes in different antidot structures. The continuous thin film shows presence of a uniform precessional mode in the FFT spectra of the time-resolved Kerr rotation data. However, introduction of periodic holes leads to formation of additional quantized modes in the antidots. The isotropic circular and square antidots show presence of two dominant modes along with a low frequency mode having relatively low power. Appearance of extra modes reduces the frequency gaps in the triangular and diamond shaped antidots. The extended DE mode along with $q = 5$ quantized modes are present in all the arrays. However, the sharp corners of the holes modify the demagnetizing field in the vicinity of the antidots in triangular and diamond shaped antidots. Further, the intrinsic magnetocrystalline and the shape anisotropies are not aligned in case of triangular and diamond antidots. This leads to formation of additional $q = 3$ quantized modes. Due to its complicated structure and local field distribution another modified DE mode appears in the diamond shaped antidot which further reduces the frequency band gap. The later is promising for applications. This observed tunability of the SW spectra by varying the shape of the antidots might have significant impact in future applications based on magnonic filters, splitters, other magnonic devices, etc.

CHAPTER 6: FePt alloy with in-plane and out-of-plane anisotropy

FePt thin films having an $L1_0$ ordered structure, *i.e.* a face-centered-tetragonal (*fcc*) phase, have drawn intense research interest since the last decade due to their potential for ultrahigh density recording applications [227,228]. The possibility of smallest particle size in magnetic recording is limited by thermal fluctuation of spin or superparamagnetic limit [4]. Hence materials with very high magnetic anisotropy energy are desired for thermal stability of magnetization even at nano-dimensions [229]. In this context $L1_0$ ordered FePt alloy is very promising to fulfill this aspect because of its large uniaxial anisotropy energy of $7 \times 10^6 \text{ J/m}^3$ [29]. Further, their huge corrosion resistance makes them an ideal candidate for next generation recording media [230]. The magnetization reversal process in out-of-plane magnetized FePt thin films with different morphologies has been previously reported [39,231-235]. The magnetic domain observation revealed the occurrence of typical bubble, stripe or maze like domains for perpendicularly magnetized films [236-242]. For a highly anisotropic film with out-of-plane magnetization, parallel and isolated band domains are mostly preferred for low relative magnetization ($\frac{M}{M_S}$) and high perpendicular field. However, beyond a critical value of $\frac{M}{M_S}$ and below a perpendicular field, the bubble domain becomes energetically favorable [243]. Further, the inclusion of nonmagnetic layer inside FePt layers has changed the typical DW motion behavior into a nucleation mode [244]. A systematic analysis of the domain structure and the role of structural defects in controlling the magnetization reversal is relatively unexplored in MALs of such FePt alloys.

On the other hand, in-plane magnetized FePt films with large uniaxial anisotropy is also very useful for applications such as bias magnets in monolithic microwave integrated circuits, exchange spring magnets with large energy product and so on. The preparation of FePt film with in-plane magnetization has been performed by Farrow *et al.* using molecular beam epitaxy (MBE) method [245]. Following that, Seki *et al.* [214] fabricated in-plane magnetized FePt

thin films with large uniaxial anisotropy energy using sputter deposition technique. Since then, there have only been a few reports on the magnetization reversal mechanism for in-plane magnetized FePt thin film having high uniaxial anisotropy [246-248]. In addition, among the very few available literature on this field, none of experimental studies has focused on the domain imaging in such in-plane magnetized FePt epitaxial thin films. The growth condition and thickness of the thin film heterostructure should have significant impact in domain formation and tuning the magnetization switching mechanism. These information are useful to understand the general magnetization process for a hard magnetic material since in-plane magnetized FePt with uniaxial anisotropy is suitable as a model system for magnetization reversal compared to polycrystalline ones without uniaxial anisotropy.

In this chapter, we have discussed the variation in domain shape and size as functions of thickness and deposition temperature for in-plane magnetized FePt epitaxial thin film. The sample fabrication and measurements of the M-H loops have been performed at the laboratory of Prof. Koki Takanashi, IMR, Tohoku University, Japan. The domain imaging using Kerr microscope has been performed at NISER, Bhubaneswar, India. We have also investigated the domain structure in perpendicularly magnetized antidot arrays of highly anisotropic FePt thin films using OOMMF simulation [208]. We confirm that the position of magnetic defects in the vicinity of the holes plays a major role in determining the shape of the domains in the MAL arrays of FePt films with out-of-plane anisotropy. This chapter is divided into two major parts:

- 6.1. Magnetization reversal and domain structure in FePt thin films with in-plane anisotropy.
- 6.2. Micromagnetic simulations on effect of edge defects on domain patterns in MAL arrays of FePt with PMA using OOMMF.

6.1: Magnetization reversal and domain structure in FePt thin films with in-plane anisotropy:

In-plane magnetized FePt thin films have been deposited on an MgO (110) single crystal substrate in an ultrahigh vacuum compatible magnetron sputtering system, with the base

pressure typically below 2×10^{-9} mbar. The FePt samples have been prepared in the laboratory of Prof. Koki Takanashi at IMR, Tohoku University, Japan. First, a 2 nm-thick Fe and a 40 nm-thick Au under-layers have been deposited at ambient temperature. Then, the substrate has been heated up to a deposition temperature, followed by the preparation of the FePt layer using co-sputtering of Fe and Pt. The alloy composition of Fe₅₃Pt₄₇ has been determined by electron probe microanalysis. The epitaxial relation of the whole film stacking is the following: MgO [001] (110) || Fe [001] (100) || Au [001] (110) || FePt [001] (110). The lattice constants of the constituent layers are 0.421, 0.287, 0.408, 0.385-0.395 nm, for MgO, Fe, Au, and FePt, respectively. This allows the growth of Fe (100) along the diagonal of MgO (110). If Au is deposited directly on MgO (110) substrate, Au (111) phase appears since (111) plane is most energetically stable for Au. The ultrathin 2 nm layer of Fe promotes the growth of Au (110). Au works as the buffer layer relaxing the relatively larger lattice mismatch between MgO and FePt. Further, Au (110) promotes the growth of FePt (110). Without the presence of the Au buffer layer, FePt (101) phase appears when the deposition temperature (T_{dep}) is increased to promote the $L1_0$ ordering. Hence, Au buffer layer aids to obtain $L1_0$ ordered FePt without the appearance of (101) oriented phase.

Table 6.1: Details of FePt thin film samples with in-plane anisotropy

Name of sample	Thickness (t_{FePt})	Deposition temperature (T_{dep})
S8-TF-A	5 nm	300°C
S8-TF-B	10 nm	300°C
S8-TF-C	20 nm	300°C
S8-TF-D	5 nm	400°C
S8-TF-E	10 nm	400°C
S8-TF-F	20 nm	400°C
S8-TF-G	5 nm	450°C
S8-TF-H	10 nm	450°C
S8-TF-I	20 nm	450°C

The details of the FePt thin films with in-plane magnetization are shown in table 6.1. The acronym TF used in the sample naming denotes the continuous thin film samples. It has been observed that the deposition temperature plays the pivotal role in stabilizing the $L1_0$ ordering. The detailed XRD analysis on similar films are reported in *ref.* [214] which is not a part of this thesis. The hysteresis loops have been measured using a superconducting quantum interference device (SQUID) magnetometer at room temperature. The magnetization reversal along with the domain imaging of the samples have been characterized using the state of art Kerr microscopy.

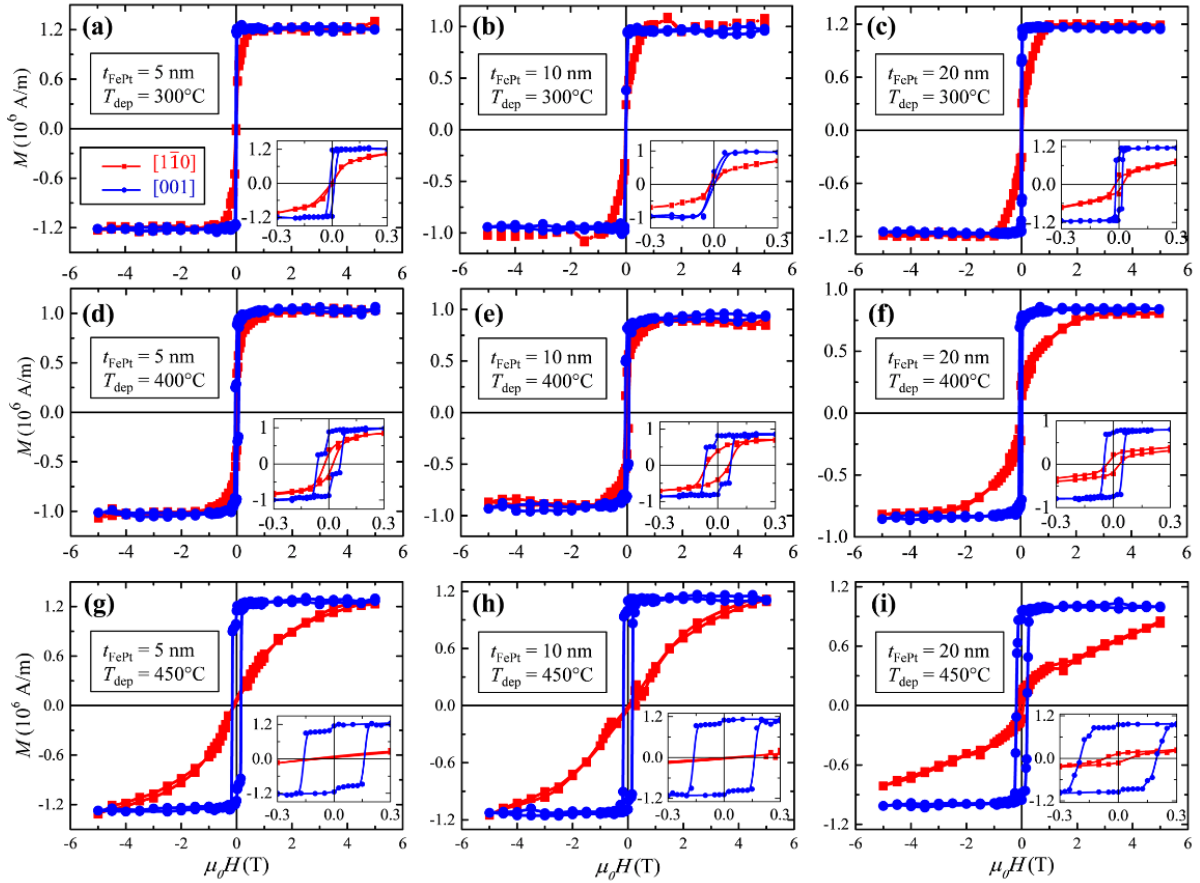


Figure 6.1: Hysteresis loops measured by the SQUID magnetometer for samples S8-TF-A – S8-TF-I shown in (a – i), respectively. The magnetic field has been applied along the MgO [001] and MgO $[1\bar{1}0]$ directions represented by blue circles and red squares, respectively. The inset images in (a – i) show the zoomed-in views of the loops near the reversal.

Fig. 6.1 depicts the hysteresis loops measured along MgO [001] (blue curve) and MgO [1 $\bar{1}$ 0] (red curve) directions for all the samples. From the epitaxial relationship between MgO and FePt, it is evident that the easy magnetization axis should lie along the MgO [001] direction i.e. MgO (110) plane. For all the hysteresis loops shown in fig. 6.1, the MgO [001] and [1 $\bar{1}$ 0] directions correspond to the EA and HA of FePt, respectively. The figure also indicates that high external applied fields are required to saturate magnetization along the [1 $\bar{1}$ 0] direction as both the thickness of the film (t_{FePt}) as well as the deposition temperature (T_{dep}) are increased, suggesting the increase in the magnetic anisotropy energy with increasing t_{FePt} and T_{dep} . A possible reason is the thickness dependence of $L1_0$ ordering for FePt films, in which a thick FePt layer easily promotes the $L1_0$ ordering, resulting in the increase in magnetic anisotropy. Though, increasing the deposition temperature leads to enhancement of anisotropy, T_{dep} has not been increased higher than 450°C because beyond this temperature, FePt (202) superlattice phase starts appearing. With enhancing T_{dep} , the c-axis of FePt phase turns canted from the in-plane direction [214].

Fig. 6.2 (a)–(c) summarize the deposition temperature (T_{dep}) dependence of coercivity (H_C), saturation field (H_S) along the EA, and magnetic anisotropy energy (K_{in}) of the films, respectively, for varying t_{FePt} . As T_{dep} is increased, both H_C and H_S increase monotonously. This result is in contrary with the report by Bublat *et al.* [229], which suggests that both H_C and H_S decrease with increasing deposition temperature. There is not much variation in H_C and H_S when $T_{\text{dep}} = 300^\circ\text{C}$, however they vary significantly when $T_{\text{dep}} = 400^\circ\text{C}$ and 450°C . It should be noted that both H_C and H_S are maximum for the films with $t_{\text{FePt}} = 10$ nm. K_{in} increases significantly when T_{dep} is increased from 300°C to 400°C due to the promotion of $L1_0$ ordering. However, one should note that there is no definite correlation between the tendencies of K_{in} , H_C , and H_S at $T_{\text{dep}} = 400^\circ\text{C}$. H_C and H_S for $t_{\text{FePt}} = 10$ nm are higher than that for $t_{\text{FePt}} = 20$ nm whereas K_{in} for $t_{\text{FePt}} = 10$ nm is lower than $t_{\text{FePt}} = 20$ nm films. The probable reason behind

this can be corroborated to the extrinsic nature of coercive and saturation fields which are not only determined by the intrinsic K_{in} value, but also are affected by structural changes. As described earlier, another crystal orientation of FePt along (101) orientation partially appears when the FePt layer is deposited at high temperature. This indicates that some of crystal grains starts having canting of the EA from the film plane, which can give rise to the enhancement of both H_C and H_S . This also induces a transverse component of magnetization which exists in the films deposited at high temperature. We note that the magnetic anisotropy is highest for sample S8-TF-I ($t_{FePt} = 20$ nm, $T_{dep} = 450^\circ\text{C}$).

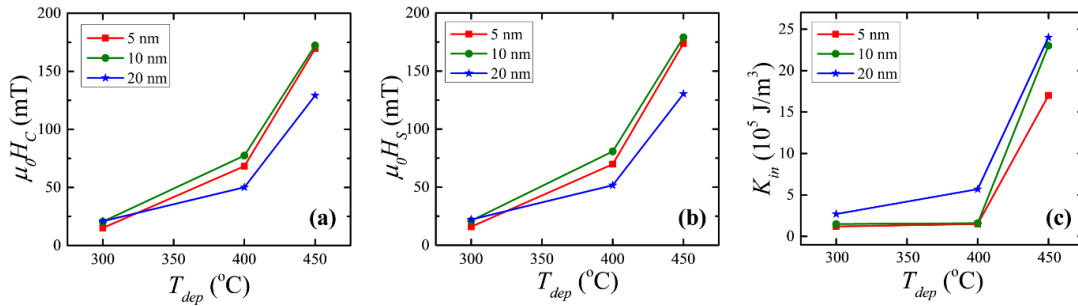


Figure. 6.2: Deposition temperature dependence of (a) coercivity (H_C), (b) saturation field (H_S), (c) magnetic anisotropy energy (K_{in}), for the FePt films with various thicknesses.

Fig. 6.3 (a) shows the hysteresis loop measured along easy axis for sample S8-TF-F ($t_{FePt} = 20$ nm, $T_{dep} = 400^\circ\text{C}$) using longitudinal Kerr microscope. Fig. 6.3 (b – f) are the domain images measured at -100 , 48.86 , 49.30 , 100 , and -50.98 mT, marked by points 1 – 5, respectively, in (a). The square shape of hysteresis loop indicates that the magnetization reversal occurs via DW motion. It can be observed from the hysteresis loop in fig. 6.3 (a) that the sample is negatively saturated at point 1 at $\mu_0 H = -100$ mT. The domains start nucleating from point 2 (fig. 6.3 (c)) at $\mu_0 H = 48.86$ mT. Then, at point 3 ($\mu_0 H = 49.30$ mT), the proportion of domains with black and white contrasts become almost equal and the sample reaches to a state close to zero magnetization. Finally, at $\mu_0 H = 100$ mT (fig. 6.3 (e)), the sample reaches to positive

saturation state. Further, with the reversal of the magnetic field, the sample reaches to almost zero magnetization state in the negative side of the hysteresis loop at $\mu_0 H = -50.98$ mT (fig. 6.3 (f)). From the domain images, we conclude that the magnetization reversal is occurring via 180 degree DW motion. The nucleated domains have walls with sharp edges, which might be due to higher thickness of the film and requirement of lower external magnetic field to saturate the sample [243] or because of the pinning effects.

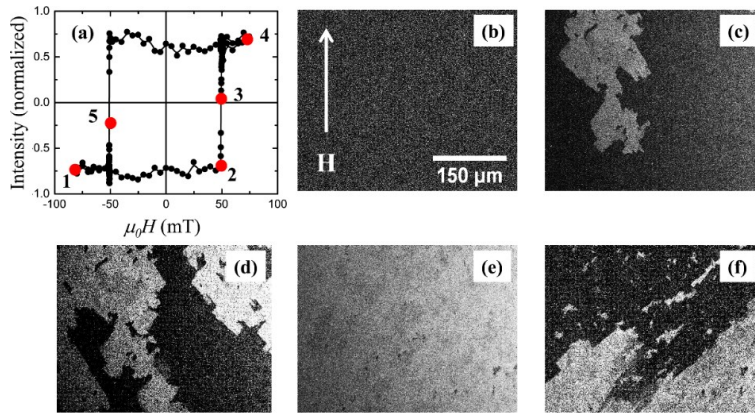


Figure 6.3: (a) Hysteresis loop measured by Kerr microscope in longitudinal mode along EA for sample S8-TF-F ($t_{\text{FePt}} = 20$ nm, $T_{\text{dep}} = 400^\circ\text{C}$). (b – f) show the domain images captured at various positions of the hysteresis loop marked by point 1–5 in (a), respectively.

In order to probe the change in domain structure with varying t_{FePt} and T_{dep} , we have imaged the domains along the EA for all the thin films. Fig. 6.4 depicts the domain images along easy axis (EA) at H_N (a – c) and H_C (d – f) for samples S8-TF-D ($t_{\text{FePt}} = 5$ nm, $T_{\text{dep}} = 400^\circ\text{C}$), S8-TF-E ($t_{\text{FePt}} = 10$ nm, $T_{\text{dep}} = 400^\circ\text{C}$), and S8-TF-F ($t_{\text{FePt}} = 20$ nm, $T_{\text{dep}} = 400^\circ\text{C}$), respectively. Both domain size and shape change significantly as the thickness of the film is varied by keeping the deposition temperature constant. The domains for samples S8-TF-D and S8-TF-E consist of round shaped walls whereas the DWs for sample S8-TF-F are with sharp edges. The occurrence of round shaped domains are expected in samples S8-TF-D and S8-TF-E because of relatively lower thickness and requirement of higher saturation external magnetic field when

compared to sample S8-TF-F [241-243]. Another possible reason to the round shaped domains is the strong pinning mechanisms at lower thicknesses. The round shape of the domains at H_N is not properly visible for sample S8-TF-E in fig. 6.4 (b) because of the use of higher magnification objective lens (20X) for domain imaging. However, imaging with lower magnification objective lens (5X) revealed the nucleation of round domains in S8-TF-E. In strong horizontal fields, these round shaped domains are distorted elliptically [19]. This is often observed for films with out-of-plane anisotropy because of the orientation dependence of domain wall energy [19,21]. However, in the case of such in-plane magnetized samples S8-TF-D and S8-TF-E, the distortion in domain shape may be explained in terms of pinning landscape in the film surface. Further we note that the domain sizes are relatively smaller in sample S8-TF-D in comparison to that in samples S8-TF-E, and S8-TF-F. Hence, we conclude that the domain size increases with the increase in the thickness of the film, which is consistent for all the other samples.

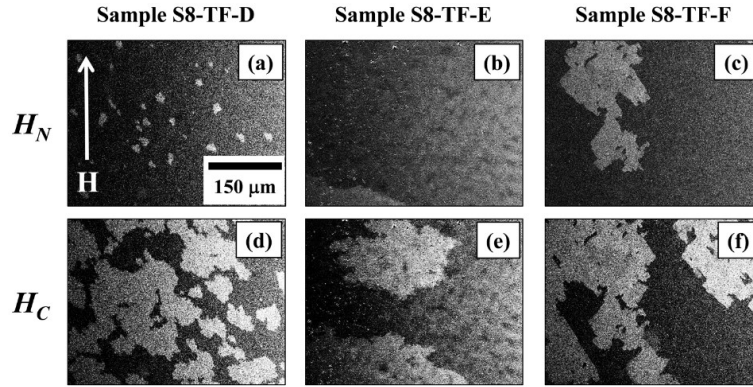


Figure 6.4: Domain images along EA at H_N (a – c) and at H_C (d – f) for samples S8-TF-D – S8-TF-F, respectively.

Fig. 6.5 show the domain images along the EA at H_N (a – c) and at H_C (d – f) for samples S8-TF-C ($t_{\text{FePt}} = 20$ nm, $T_{\text{dep}} = 300^\circ\text{C}$), S8-TF-F ($t_{\text{FePt}} = 20$ nm, $T_{\text{dep}} = 400^\circ\text{C}$), and S8-TF-I ($t_{\text{FePt}} = 20$ nm, $T_{\text{dep}} = 450^\circ\text{C}$), respectively. Here the thickness of the films are kept constant ($t_{\text{FePt}} = 20$ nm) whereas T_{dep} is varied from 300°C to 450°C . We observe that the shape and size of the

domains change significantly with varying T_{dep} . The domains for samples S8-TF-C, S8-TF-F, and S8-TF-I show zigzag patterns. Zigzag walls forms when two domains propagate towards each other and meet head on. These zigzag walls in thin films are charged metastable walls which take such shapes in order to reduce the charge density. It is well understood that a straight wall between two head-on domains will have the strongest charge concentration which decreases by enhancement of the zigzag angle. Charged walls are allowed in thin films because the magnetic stray field can spread into both the space above and below the film. Formation of such walls are forbidden in bulk soft magnetic samples where the stray field is concentrated [19]. The angle between the zigzag walls is characteristic of a specific film whereas the period of the walls depends on different conditions. In the thin films that are used for longitudinal recording, the zigzag walls may be used to separate the information bits [19].

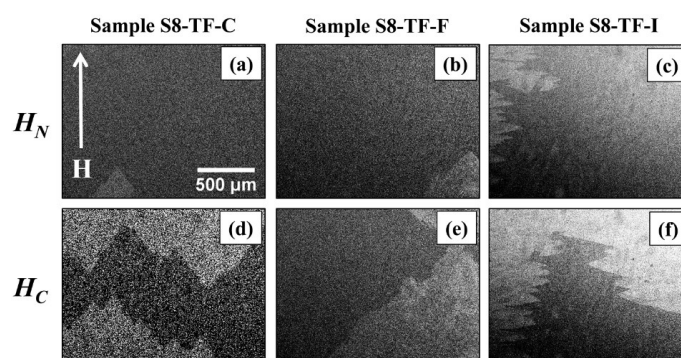


Figure 6.5: Domain images along EA (a – c) at H_N and (d – f) at H_C for samples S8-TF-C, S8-TF-F, and S8-TF-I, respectively.

The boundaries of the zigzag walls become sharper as both the thickness and the deposition temperature are increased. In sample S8-TF-C, the reduction of zigzag period leads to thermodynamically stable state. Domain observation revealed the occurrence of zigzag walls for all the samples (samples S8-TF-G – S8-TF-I) prepared at 450°C. So, the occurrence of zigzag walls can be incorporated with the higher value of magnetic anisotropy energy in such films. We further note that, in sample S8-TF-I, the domains propagate in the transverse direction to the applied magnetic field. From fig. 6.1 (i) it is seen that sample S8-TF-I shows

small remanent magnetization when magnetic field has been applied along the $[1\bar{1}0]$ direction. As mentioned earlier, there may be a presence of transverse component of magnetization (canting of spins away from the easy direction) along with the strong uniaxial anisotropy for films prepared at higher temperature. This may be a possible reason of observing the domains in transverse direction to the applied magnetic field along easy axis.

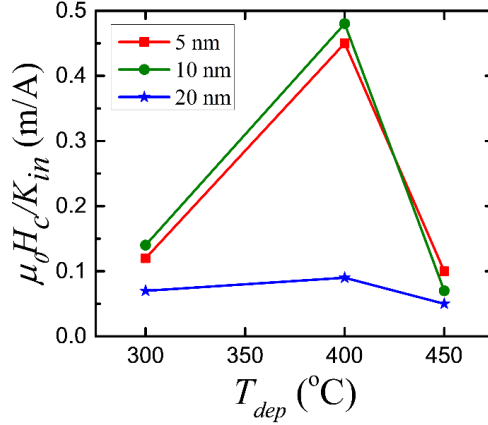


Figure 6.6: Deposition temperature dependence of $\mu_0 H_C / K_{in}$ for all the films prepared with varying t_{FePt} .

The wedge shape amplitude of the zigzag walls are explained by calculating the ratio of H_C and K_{in} . Fig. 6.6 shows the nature of $\mu_0 H_C / K_{in}$ with varying t_{FePt} and, T_{dep} . The amplitude of the zigzag walls increases with the decrease in $\mu_0 H_C / K_{in}$ (fig. 6.6 (a)) value which is in well agreement with the results reported previously [249-253]. The lesser value of $\mu_0 H_C / K_{in}$ ensures higher value of wedge shape amplitude. This amplitude decreases with increase in $\mu_0 H_C / K_{in}$ value and finally loses its wedge shape [254]. It is observed that the zigzag period is reduced in case of samples S8-TF-C, and S8-TF-F which gets diminished in case of samples S8-TF-A, and S8-TF-B forming domains with sharp boundary. There is a transition from domains with sharp boundary to round shaped domains with increase in $\mu_0 H_C / K_{in}$ value ($\sim 0.15 \times 10^{-6}$ m/A). Hence, for samples S8-TF-D and S8-TF-E, domains with round shaped walls are observed as explained in fig. 6.4.

In summary, magnetization reversal has been studied in $L1_0$ ordered FePt thin films with in-

plane anisotropy for variable thickness and deposition temperature. Domain imaging by longitudinal Kerr microscopy revealed observation of round shaped domains for very high value of $\mu_0 H_C / K_{in}$ ($\sim 0.15 \times 10^{-6}$ m/A). Domains with sharp boundary has been observed for films having very high magnetic anisotropy energy. Zigzag domains with large wedge amplitude has been observed in case of films having the $\mu_0 H_C / K_{in}$ value less than 0.1×10^{-6} m/A. The domain size changes significantly with the change in thickness of FePt layer and deposition temperature. The domain size increases with increase in film thickness when the deposition temperature is kept constant. There is presence of a critical thickness of ~ 10 nm where the coercive and saturation field become highest among films with different thicknesses but deposited at a constant temperature.

6.2. Micromagnetic simulations on effect of edge defects on domain patterns in MAL arrays of FePt with PMA using OOMMF:

From the previous works, we have observed slow thermal relaxation in MAL arrays with in-plane anisotropy. However, the speed of relaxation increases for antidot arrays with PMA. In this regard, Dr. S. Bedanta has studied the domain structure and magnetization reversal in MAL arrays of FePt with PMA. Domain imaging using MFM has revealed formation of stripe like domains in such antidot arrays [30].

Table 6.2: List of the simulated antidot samples of FePt with perpendicular anisotropy

Sample Name	Sample class	Sample type	Length of side
S9-SS-TA	Simulation	Triangular antidot	100 nm
S9-SS-SA	Simulation	Square antidot	100 nm
S9-SS-DA	Simulation	Diamond antidot	100 nm

We have performed micromagnetic simulations using OOMMF to elucidate the effect of edge defects on the domain structure in triangular antidot arrays of FePt with PMA. We have further verified the simulation model for other shapes of antidots (square, diamond). Table 6.2 shows the detailed list of simulation samples for FePt with PMA. The acronym SS represents

simulated sample, whereas TA, SA, DA represent triangular, square, and diamond shaped antidot arrays, respectively.

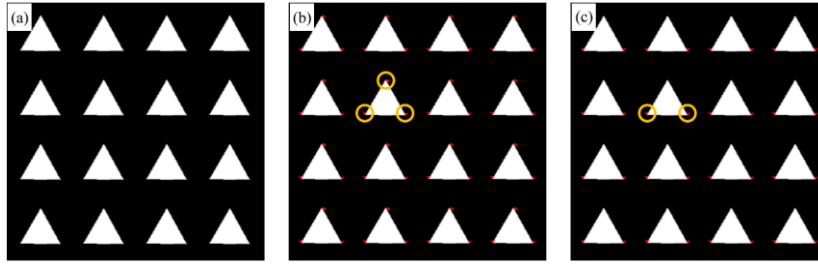


Figure 6.7: The masks used in OOMMF simulation for the triangular antidot sample S9-SS-TA with (a) no defect, (b) defects at each vertices of the triangles, (c) defects at two vertices sharing the base of the triangles. The defects are marked in red color and encircled by yellow circles for a few defects.

The simulations have been performed over an area of $800 \text{ nm} \times 800 \text{ nm}$ by considering 4×4 lattice of the antidots. The materials parameters used for the simulations are the followings: $K_{\text{out}} = 1.5 \times 10^6 \text{ J/m}^3$, $M_S = 1.1 \times 10^6 \text{ A/m}$, $A = 1 \times 10^{-11} \text{ J/m}$. The cell size for the simulations is chosen to be $2 \times 2 \times 2 \text{ nm}^3$. A magnetic damping of 1 has been used to reduce the simulation time since the results do not majorly depend on the damping parameter. We have considered three distinct cases to elucidate on the mechanism of domain formation. In the first case an array of periodic triangular holes have been considered which are defect free. In the second case, we have put magnetic defects with 1% area of the individual holes present at all the three vertices of the triangles. In the third case, the defects are present only at the two vertices of the base of the triangles to aid to nearest neighbor interaction between the holes in the horizontal direction. Fig. 6.7 (a)–(c) show the simulation mask used for the triangular antidot sample S9-SS-TA with no defect, defects at each vertices, and defects at the two vertices sharing the base of the triangles, respectively. The defects are marked in red color and indicated by yellow circles to aid to visualization. The interpretation behind the choice of such sample mask will be explained in the subsequent part. It should be noted that the defects at the edges/vertices of

the holes may appear because of incomplete lift-off, underexposure, improper etching, etc.

Fig. 6.8 (a – l) show the evolution of domains in sample S9-SS-TA under the application of varying magnetic field in the out-of-plane direction. The sample mask used in the simulation is shown in fig. 6.7 (a). It is observed that bubble domain nucleates around the triangular holes. This is expected since the edge of the triangular holes in the antidots act as the nucleation centers for the domains. With enhancement of the magnetic field the bubbles expand in both vertical and horizontal directions before coalescing with each other to complete the reversal. Due to the symmetric arrangement of the holes both domain nucleation and propagation is symmetric. The pinning of domains in between two neighboring antidots is absent in the simulated domain structure.

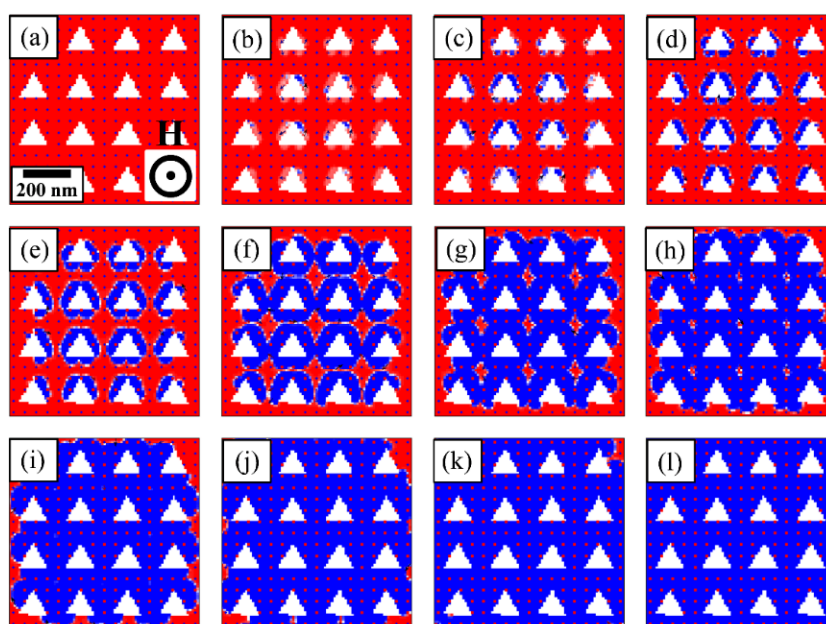


Figure 6.8: (a – l) Evolution of domains in sample S9-SS-TA under application of varying magnetic field. The applied field direction and scale bar is shown in (a). The mask used in this simulation is depicted in fig. 6.7 (a).

It is well established that a magnetic area with less anisotropy in the vicinity of the holes will work as DW trap [255]. Hence, the mask has been modified where the defects are put at each vertices of the triangular holes which may pin the domains in between the successive holes.

Fig. 6.9 (a – l) show the evolution of domains in sample S9-SS-TA under the application of varying magnetic field in the out-of-plane direction. The sample mask used in the simulation is shown in fig. 6.7 (b). The anisotropy of the defect is considered to be $K_{\text{defect}} = 1.0 \times 10^5 \text{ J/m}^3$. It should be noted that the value of K_{defect} is one order lower than that of K_{out} . This ensures nucleation of the domains from the defects (i.e. from the vertices of the triangles).

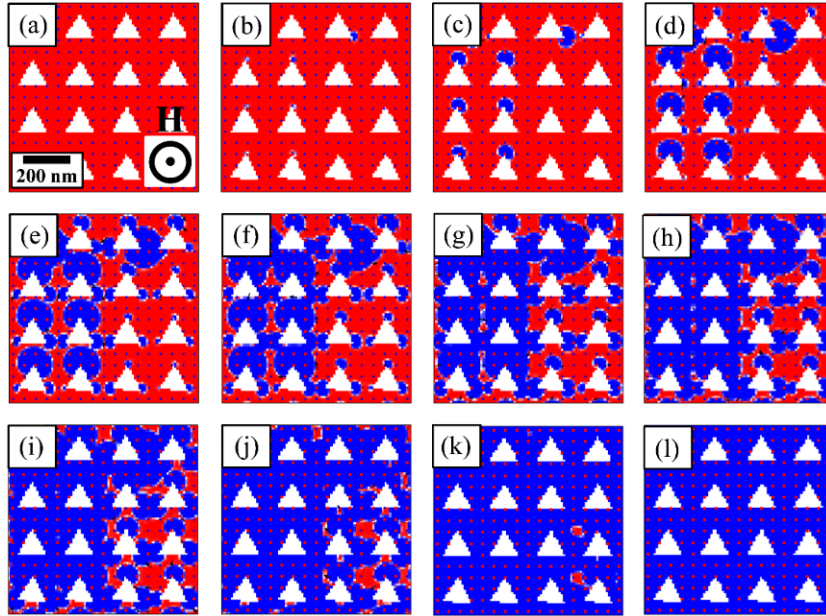


Figure 6.9: (a – l) Evolution of domains in sample S9-SS-TA under application of varying magnetic field. The applied field direction and scale bar is shown in (a). The mask used in this simulation is depicted in fig. 6.7 (b).

Fig. 6.9 (b) and (c) show the nucleation of the bubble domains from the defects. With application of higher reversal fields the walls of the bubble domains propagate sideways. We note that domains with narrow width gets pinned between the successive holes in the horizontal direction (fig. 6.9 (e)). However, the domains maintain its bubble shape along the vertical direction. The defects at the top vertex of the triangles have the nearest neighbor vertex in a greater distance in comparison to the vertices situated at the base of the triangles. Hence, the effect of pinning is less in vertical direction in comparison to that in the horizontal direction. Therefore, for the next sets of simulation, only the defects are considered at the vertices along

the base of the triangular holes as shown in fig. 6.7 (c).

Fig. 6.10 (a – l) show the evolution of domains in sample S9-SS-TA under the application of varying magnetic field in the out-of-plane direction. In this case the defects are positioned at the vertices along the base of the triangular holes as shown in fig. 6.7 (c). Fig. 6.10 (b) and (c) reveal formation of bubble domains from the edge of the triangles similar to the ones observed in fig. 6.9. However, with application of larger reversal fields, the bubbles start propagating and gets pinned between the defects present at the vertices of the triangles. The pinned domains form stripe like domain structure (fig. 6.10 (e – k)). This behavior is similar to the experimentally observed domain structure in triangular antidot arrays of FePt with PMA [30]. Hence, it can be concluded the defects present in the vicinity of the vertices of the triangular holes govern the domain structure in such antidot arrays. However, it should be noted that the experimental part of this work is not a part of this thesis.

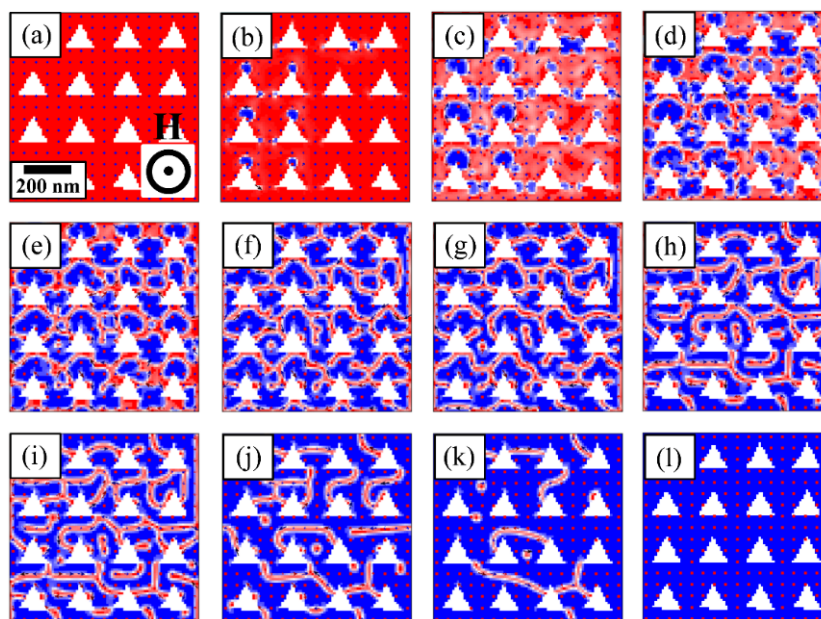


Figure 6.10: (a – l) Evolution of domains in sample S9-SS-TA under application of varying magnetic field. The applied field direction and scale bar is shown in (a). The mask used in this simulation is depicted in fig. 6.7 (c).

In order to check the continuity of the model of the mask, similar micromagnetic simulations

have been performed for other shapes of the antidots (square, and diamond). Fig. 6.11 (a – l) show the evolution of domains in the square antidot sample S9-SS-SA under the application of varying magnetic field in the out-of-plane direction. It should be noted that, unlike triangular antidots, the nearest neighbor distance between the vertices of the successive holes in the square antidots are same along both vertical and longitudinal directions. Hence, the defects are positioned at all the vertices of the square holes in sample S9-SS-SA. Fig. 6.11 (b – d) show nucleation of bubble domains from the vertices of the holes which propagate under the application of reverse magnetic field. The bubbles remain pinned in between the vertices of the successive holes and form stripe like domain structure similar to fig. 6.10. Further, it is observed that the nucleation and propagation of the bubble domains are symmetric in sample S9-SS-SA. This is in contrary to the ones observed in the triangular antidot sample S9-SS-TA in fig. 6.10. The reason behind this can be corroborated to the presence of isotropic square holes in sample S9-SS-SA unlike the anisotropic triangular holes in sample S9-SS-TA.

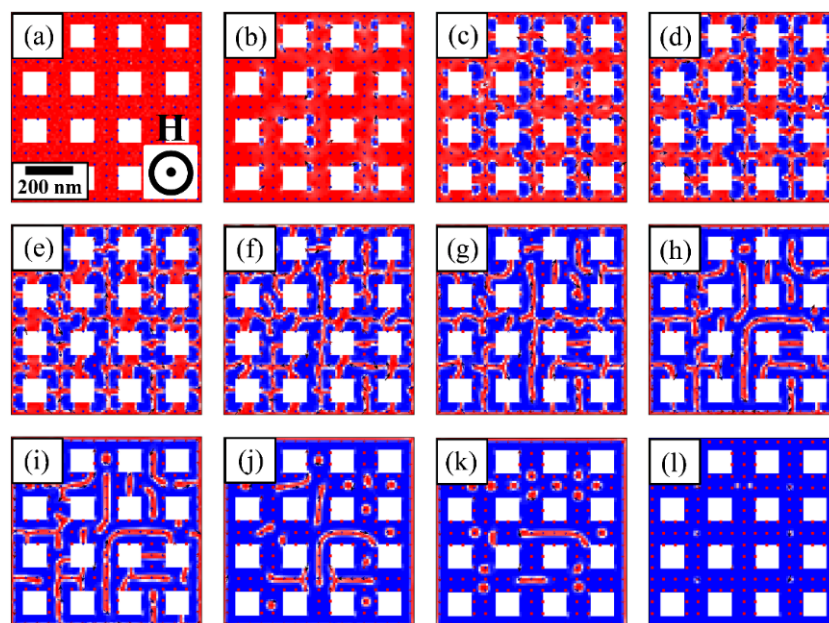


Figure 6.11: (a – l) Evolution of domains in sample S9-SS-SA under application of varying magnetic field. The applied field direction and scale bar is shown in (a). In the sample mask, the defects are present in all four vertices of the square holes.

Fig. 6.12 (a – l) show the evolution of domains in the diamond shaped antidot arrays (sample S9-SS-DA) under the application of varying magnetic field in the out-of-plane direction. Similar to sample S9-SS-SA, the nearest neighbor distance between the vertices of the successive holes in the diamond antidots are same along both vertical and longitudinal directions. Hence, similar to sample S9-SS-SA, the defects are positioned at all the vertices of the diamond shaped holes in sample S9-SS-DA. Fig. 6.12 show nucleation of bubble domains from the vertices of the diamond shaped holes which propagate in both vertical and horizontal direction under the influence of applied magnetic field. The bubble remains pinned in between the defects of the successive holes to form stripe domains similar to samples S9-SS-TA and S9-SS-SA. In contrary to the observation in square antidot sample S9-SS-SA, due to the non-uniform distribution of demagnetizing field in the vicinity of the diamond shaped holes, the bubbles do not propagate in symmetric nature in sample S9-SS-DA.

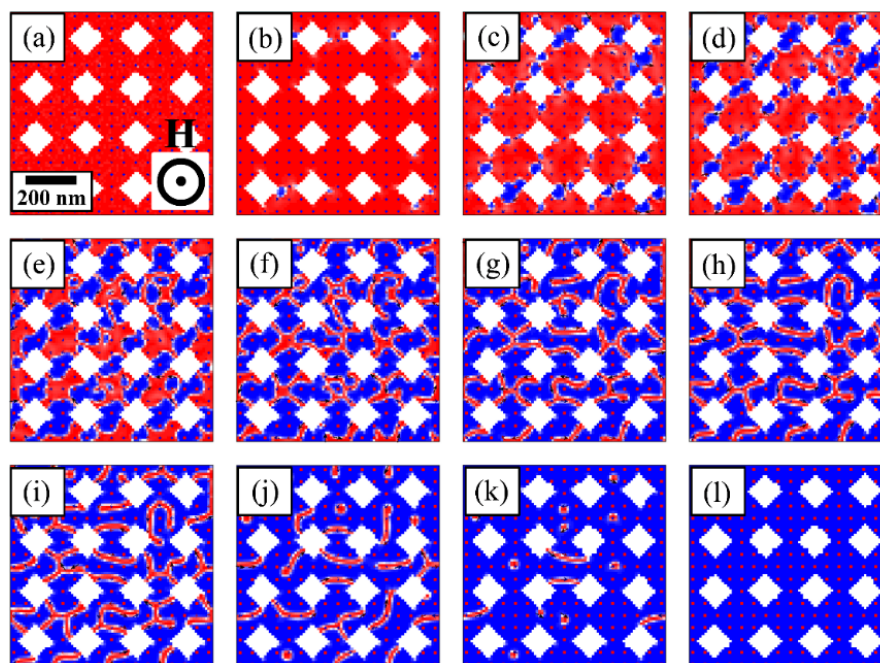


Figure 6.12: (a – l) Evolution of domains in sample S9-SS-DA under application of varying magnetic field. The applied field direction and scale bar is shown in (a). In the sample mask, the defects are present in all four vertices of the diamond shaped holes.

In conclusion, we have shown that triangular antidot array of out-of-plane magnetized FePt show formation of either bubble or stripe domains depending on the presence of edge defects (magnetic region with low anisotropy). In the absence of any defect, the system shows presence of typical bubble domains of perpendicular media with high anisotropy. However, presence of the edge defects pin the domains in between the successive holes and force the domains to propagate in a zigzag path avoiding them. Observation of such domain structure is in well agreement with the experimental observation. The simulations has been extended towards other shapes of antidots (square, and diamond) and verified that the defects play a major role in determining the domain structure in such systems. The possibility of tuning the domain structure in such high anisotropic perpendicular media may have significant future implications in ultra-high density storage technology and spintronics based applications.

CHAPTER 7: Nanocrystalline Ribbons

Tunability of the static and dynamic magnetic properties discussed so far deals with ferromagnetic systems governed by growth induced magnetocrystalline and antidot structure induced shape anisotropy. Nevertheless, there are systems viz. soft magnetic nanocrystalline ribbons where the magnetization behavior can be controlled by combination of magnetocrystalline and magnetoelastic (stress) anisotropy. The response of the DWs in ribbons to the static and alternating applied fields has been discussed in this chapter. These ribbons have important applications in the creation and distribution of efficient electrical power due to their high saturation magnetization and low magnetic core loss [256-261]. There are a very few systems which satisfy these criteria such as: FINEMET (alloy of Fe-Si-B-Nb-Cu), NANOPERM (alloy of Fe-M-B; where M = Zr, Nb), HITPERM (alloy of Fe-Co-M-B; where M = Nb, Zr, Hf) etc. [262-264]. However, such class of materials consist of transition-metal elements. In addition, their magnetic flux density (B_S) is lower in comparison to that of Si-steel [32]. On the contrary, NANOMET (alloy of Fe-Si-B-P-Cu) is a relatively new-type of soft magnetic nanocrystalline alloy with high Fe content (~85%) which provides extremely low coercivity and high B_S [32]. In order to achieve wide NANOMET ribbons for applications, over the years, Co substitution by a small proportion in place of Fe has been established without losing the high value of B_S [32,265,266]. The type of phases (crystalline and amorphous) determine the magnetic properties of such ribbons as high density of α -Fe nanocrystals average out the magnetocrystalline anisotropy [267,268]. Generally, soft magnetic cores are used under the application of AC magnetic field, therefore, understanding of static and dynamic magnetic behavior is important. It is also important for their potential applications in high density magnetic recording, high frequency inductors, microwave filters, transformers, etc. as well as from fundamental research point of view [269-273]. For such applications the understanding of basic magnetic properties such as domain microstructure, DW dynamics, anisotropy etc. are

important. The dynamic behavior of domain walls such as creep, depinning, and slide under external magnetic field in general is well understood [274]. In an oscillating AC field, $H = H_0 e^{ift}$, the strength of finite angular frequency ($f > 0$) introduces additional states of motion [275,276]. By varying the amplitude and frequency of the AC field both DW creep and slide can be activated [277,278]. The nanocrystalline/ amorphous ribbons are quite interesting in this regard since by varying the preparation condition one can tune the crystallinity, internal stress, exchange coupling between the constituent grains, and the anisotropy which in turn modify the dynamic response of the DWs in such systems. With increasing frequency of the AC field and decreasing induced anisotropy of the ribbons, the magnetization process changes from wall displacement to domain nucleation which limits the mean surface wall velocity [279].

In this chapter, we have investigated the static and dynamic response of the DWs of such ribbons where the magnetic switching is governed by different mechanism viz. internal stress in amorphous state, strong exchange coupling having low magnetocrystalline anisotropy, and high anisotropy consisting of strong pinning effect [33]. We show that by varying the annealing temperature of soft magnetic ribbons, it is possible to tune the static and dynamic behavior of the domains [33]. The sample fabrication and structural characterization for the ribbons have been performed via a collaboration with Prof. Parmanand Sharma at Institute of Material Research (IMR), Tohoku University, Japan. The Kerr microscopy imaging under AC and DC magnetic fields has been performed at LNMM, NISER, Bhubaneswar, India.

Table 7.1: Details of prepared nanocrystalline ribbon samples

Sample name	Sample type	Annealing temperature (T_a)
S10A	Not brittle	As-quenched
S10B	Brittle	370°C
S10C	Brittle	420°C
S10D	Brittle	450°C
S10E	Brittle	460°C

Table 7.1 shows the details of the $\text{Fe}_{81.2}\text{Co}_4\text{Si}_{0.5}\text{B}_{9.5}\text{P}_4\text{Cu}_{0.8}$ ribbons prepared by a high frequency induction melting of a mixture of raw materials (Fe, Co, Si, B, P, and Cu). A mixture of high purity metals (99.9% mass pure Fe, Co, and Cu), metalloids (99.9% Si and 99.5% B), pre-melted (99 % Fe_3P and Co_2P) were mixed and melted in high purity argon gas atmosphere at a pressure of 10^{-5} mbar to prepare the alloy ingots. The as prepared alloy ingots were used to synthesize the amorphous ribbons by a single roller melt spinner. Further, the ribbons were annealed under Ar atmosphere from 370°C to 460°C .

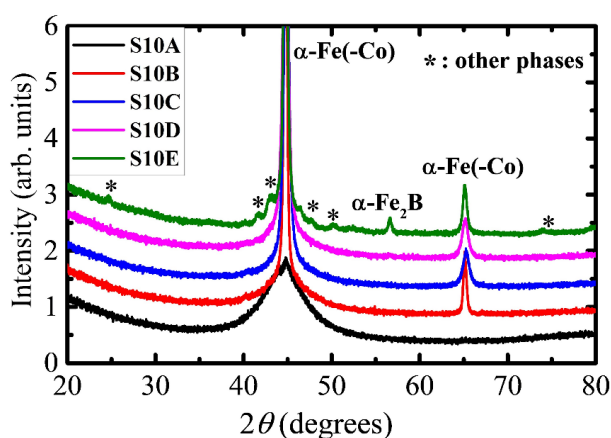


Figure 7.1: XRD patterns of samples S10A–S10E annealed at different temperatures represented by black, red, blue, pink, and green curves, respectively.

Fig. 7.1 shows the XRD patterns for samples S10A–S10E. A typical broad peak for an amorphous material is observed for the as quenched ribbon (sample S10A). With increase in the annealing temperature (T_a) to 370°C , a sharp peak superposed on a broad amorphous peak is observed for S10B. The diffraction peaks corresponding to the $\alpha\text{-Fe(-Co)}$ phase are marked in fig. 7.1. With increase in T_a , the intensity of the peaks increase for samples S10C and S10D. Hence, increase in annealing temperature leads to crystallization of the amorphous structure to the $\alpha\text{-Fe(-Co)}$ phase. However, in addition to the $\alpha\text{-Fe(-Co)}$ phase, other phases (such as $\alpha\text{-Fe}_2\text{B}$, Fe-P) are observed for sample S10E as T_a is enhanced to 460°C . The other phases are marked by '*' in fig. 7.1. TEM measurements on the similar as-quenched and annealed ($T_a =$

425°C) samples have been previously reported in *ref.* [32]. It has been found that amorphous phase was formed in the as-quenched sample. However, homogeneously dispersed α -Fe grains with size 15-20 nm were observed in the annealed sample. Differential scanning calorimetry (DSC) measurements have been performed on similar samples in *ref.* [266]. It was observed that for $T_a \sim 425^\circ\text{C}$ a complete formation of α -Fe(-Co) phase occurred. This behavior remains unaffected for $T_a \leq 450^\circ\text{C}$. Hence, samples S10C ($T_a = 420^\circ\text{C}$) and S10D ($T_a = 450^\circ\text{C}$) lead to formation of crystalline α -Fe(-Co) phase with minimum impurity phases.

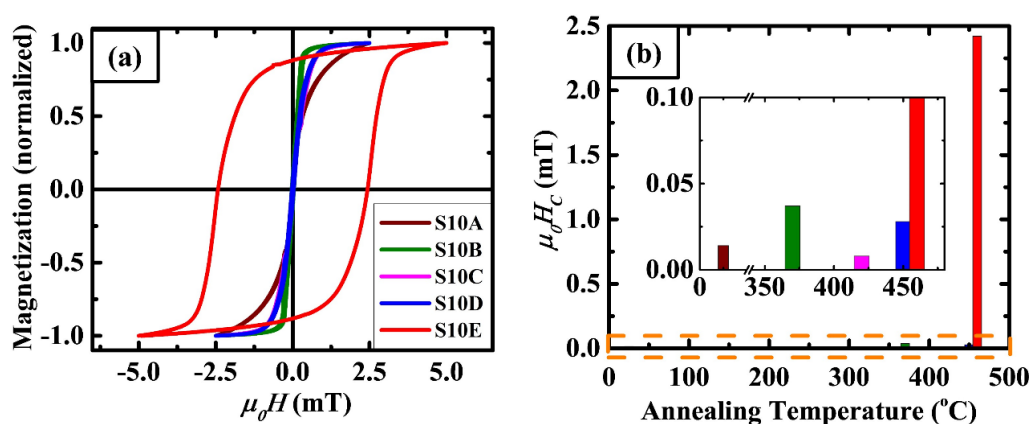


Figure 7.2: (a) Hysteresis loops for samples S10A–S10E, represented by brown, green, pink, blue, and red curves, respectively. (b) H_C vs T_a plot for all the samples extracted from (a). The inset in (b) shows the zoomed-in image of the plot represented by the dotted orange area.

Fig. 7.2 (a) and (b) show the hysteresis loops and the extracted values of H_C , respectively, for all the samples. Sample S10A exhibits S-shaped hysteresis loop with low $\mu_0 H_C \sim 13.82 \mu\text{T}$ ($\sim 11 \text{ A/m}$), which is typical for an amorphous ferromagnetic alloy. Magnetocrystalline anisotropy is absent in S10A but finite H_C results from strong magnetoelastic effects. Sample S10B shows slightly higher $\mu_0 H_C \sim 36.44 \mu\text{T}$ ($\sim 29 \text{ A/m}$) due to inhomogeneous microstructure made from a dilute precipitation of the α -Fe(-Co) grains in an amorphous matrix. Concentration of α -Fe(-Co) grains is significantly high in S10C. This leads to strong

inter-granular exchange coupling which reduces the magnetocrystalline anisotropy of the α -Fe(-Co) grains [266,268] and therefore a small $\mu_0 H_C \sim 7.54 \mu\text{T}$ (6 A/m) is observed. It should be noted that in these ribbons magnetostriction also plays an important role. The coefficient of magnetostriction (λ_S) is much higher for the amorphous alloy ($\sim 30 - 35$ ppm), when compared to Fe (~ -4 ppm) [280]. Therefore, the low H_C of S10C is due to the combined effect of negligible magnetocrystalline and magnetoelastic anisotropies. Compared to S10C, the H_C (~ 22 A/m) increases slightly for S10D and it is due to minor precipitation of high magnetocrystalline anisotropic α -Fe₂B grains. Largest $\mu_0 H_C \sim 2.42$ mT (1931 A/m) is observed in sample S10E due to the precipitation of significant amount of α -Fe₂B grains. It should be noted that in these type of ribbons both compressible and tensile stress can coexist. The origin of the compressive stress is associated to the formation of the higher density crystalline surface on the amorphous bulk [281]. Ok *et al.* discussed the origin of perpendicular anisotropy in amorphous ribbons associated to this compressive stress which aligns the magnetic moments perpendicular to the ribbon plane [282]. On the other hand, the partially crystallized surface layers remain under the tensile stress which align the magnetization parallel to the ribbon plane.

Fig. 7.3 (a – e) show the domain images measured using longitudinal Kerr microscopy for sample S10A under various DC fields ($\mu_0 H_{DC}$) of 15.00, 2.00, 0.00, -2.00, and -15.00 mT, respectively. The domain images reveal the presence of two distinct kinds of patterns: wide domains with 180° walls and the other with fingerprint-like patterns [19,283-286]. It should be noted that in the absence of external magnetic field, the domain arrangement in a ferromagnetic material is governed by the minimization of magnetic Gibbs free energy which is comprised of magnetostatic stray field energy (E_{demag}), anisotropy energy (E_{ani}), and domain wall energy (E_{DW}). If the spontaneous magnetization tends to orient along the ribbon plane (tensile stress), then E_{demag} and E_{ani} become lowest which leads to formation of wide domain structure.

However, when the anisotropy axis is perpendicular to the ribbon plane (compressive stress) a closure domain structure needs to appear to minimize E_s . This closure structure is known as the Landau-Lifshitz domain structure or the fingerprint-like stress domain patterns [285]. Due to high λ_s of amorphous ribbons, stress can induce a strong magnetic anisotropy. It should be noted that the spatial average of total stress in the absence of external forces should be zero. This implies that the domain configuration most likely be inhomogeneous by the formation of two distinct domain patterns. Therefore the domains with 180° walls are observed along the direction of tensile stress governed by the in-plane anisotropy whereas the compressive stress leads to formation of fingerprint-like stress patterns (also associated with the presence of perpendicular magnetic anisotropy) [19]. These stress patterns nucleate early during the magnetization reversal (fig. 7.3(b)) and require higher magnetic field to get saturated (fig. 7.3(e)) in comparison to the domains with 180° walls. This can be understood easily because the rotation of magnetization from easy to hard axis requires larger magnetic field. Thus, the internal stress of the amorphous matrix pins the domains making it hard for them to propagate and hence requires higher field to complete the magnetization reversal. The initial (intrinsic) stress due to quenching in these ribbons usually gets removed by annealing. However, it is difficult to remove the effect of stress in these amorphous ribbons completely and this requires annealing of the ribbons at temperatures close to optimum for nanocrystallization. Previously it has been reported that a peak corresponding to α -Fe starts appearing as the annealing temperature approaches $\sim 350^\circ\text{C}$ [287]. Also, it has been shown that stable microstructure consisting of high density of nano-sized α -Fe grains separated by a thin amorphous layer form in the temperature range of $\sim 420^\circ\text{C}$ to 450°C [32,266]. Fig. 7.3 (f – j) depict the domain structure for sample S10B ($T_a = 370^\circ\text{C}$) at $\mu_0 H_{DC} = 6.00, 1.90, 0.50, -3.10,$ and -6.00 mT, respectively. Due to the low annealing temperature, the crystalline fraction of α -Fe(-Co) is low in this sample. Hence, a combined effect of inhomogeneous stress and low anisotropy results

in formation of disordered fractal domains followed by 180° domain wall motion.

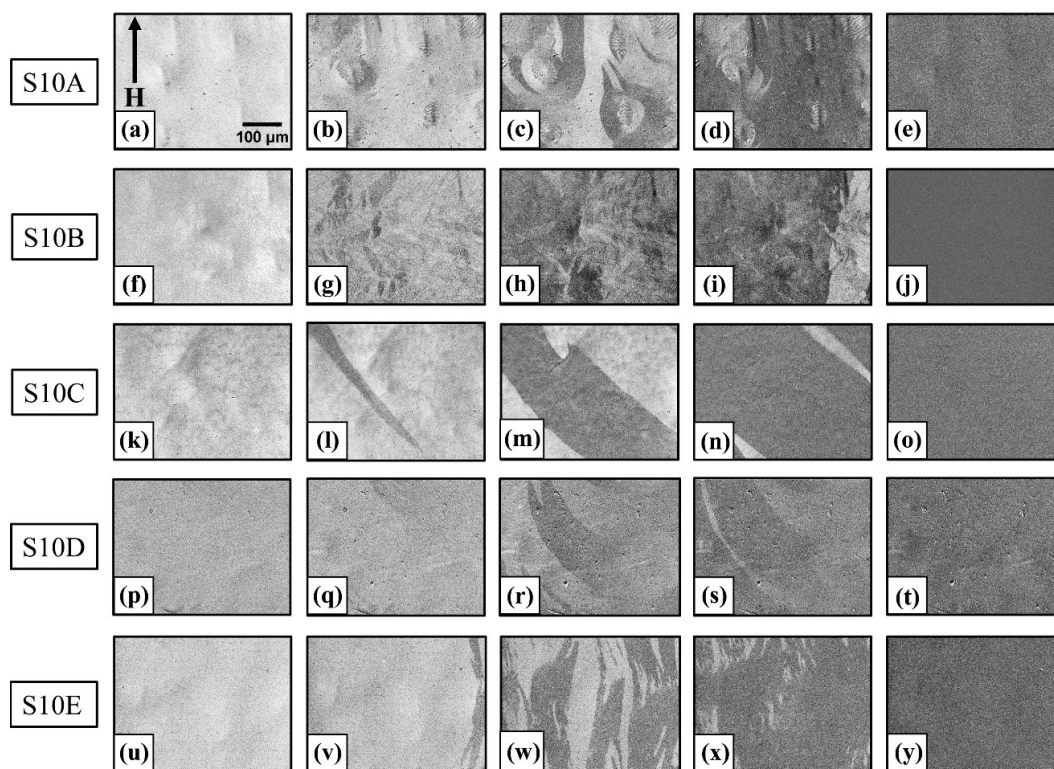


Figure 7.3: Domain images recorded at various magnetic fields corresponding to different points of the hysteresis loops for S10A (a – e), S10B (f – j), S10C (k – o), S10D (p – t), and S10E (u – y), respectively. The scale bar and applied field direction for all the images are same and is shown in (a). See main text for the detailed values of the magnetic field for these images.

Fig. 7.3 (k – o) represent the domain structures for sample S10C at $\mu_0 H_{DC} = 1.50, 0.74, 0.18, -1.13,$ and -1.50 mT, respectively. Annealing at higher temperature ($T_a \geq 400^\circ\text{C}$) leads to crystallization of $\alpha\text{-Fe(-Co)}$ phases which removes the stress from the film surface [32]. High density of $\alpha\text{-Fe(-Co)}$ grains lead to strong exchange interaction which results in a decrease in the magnetocrystalline anisotropy [268]. This further leads to suppression of magnetoelastic anisotropy due to a strong reduction in λ_S . Hence the magnetization reversal occurs via stress and pinning free motion of stripe domain. Sample S10C reveals very low H_C , high B_S , and low core-loss (W) which makes this sample suitable for potential applicability as magnetic core

materials. Fig. 7.3 (p – t) show the domain images for sample S10D at $\mu_0 H_{dc} = 5.00, 2.50, 0, -1.64,$ and -5.00 mT, respectively. Sample S10D contains a minor precipitation of high anisotropic α -Fe₂B grains along with dense α -Fe(-Co) which leads to small enhancement of anisotropy (figure 7.2(a)) and coercivity (figure 7.2(b)). The domains get pinned very weakly by the dilute concentration of Fe₂B grains which results in formation of smaller domains in comparison to that of sample S10C. Fig. 7.3 (u)–(y) show the domain images for sample S10E measured at $\mu_0 H_{DC} = 15.00, -1.13, -4.53, -5.65,$ and -15.00 mT, respectively. The domain size is significantly reduced due to high uniaxial anisotropy. This is because sample S10E contains α -Fe₂B grains with high magnetocrystalline anisotropy (~ 430 kJ/m³, which is almost 10 times higher than that of the α -Fe). This results in significant increase in the anisotropy (fig. 7.2) and pinning in sample S10E.

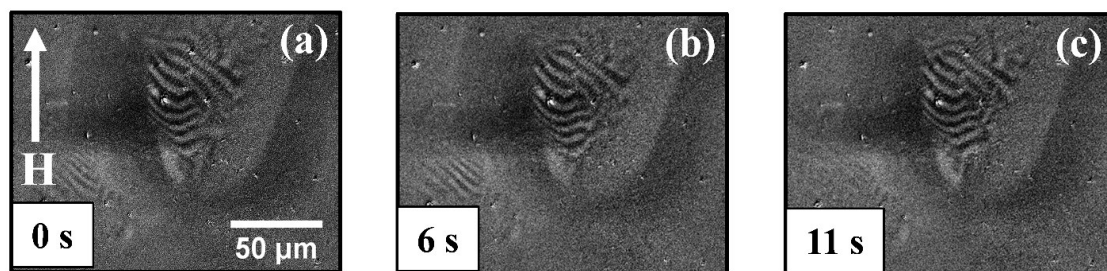


Figure 7.4: (a – c) Domain structure for sample S10A at remanence measured at time (t) = 0, 6, and 11 s after applying an AC field of $\mu_0 H_{AC} = 1$ mT and $f_{AC} = 20$ Hz.

The DW dynamics of the samples has been probed under an AC field $\mu_0 H_{AC} = 1$ mT ($> H_N$) and frequency (f_{AC}) in the range of $1 \leq f \leq 20$ Hz. Fig. 7.4 (a – c) show the temporal evolution of magnetic domains for sample S10A under the application of an AC magnetic field of $\mu_0 H_{AC} = 1$ mT and $f_{AC} = 20$ Hz, measured at time (t) = 0, 6, and 11 s, respectively. For sample S10A, the fingerprint-like ‘stress patterns’ remain stable under the influence of the AC field. The internal inhomogeneous stress of S10A pins the ‘stress patterns’ and keeps them stable even with the application of higher magnetic field (H_{AC}). It has been observed that the DW

behavior does not change significantly when the frequency is varied between 1 to 20 Hz (keeping the same $\mu_0 H_{AC}$). Annealing leads to reduction in magnetoelastic effect due to appearance of α -Fe(-Co) phase in the amorphous matrix. The relatively higher exchange coupling between the scattered α -Fe(-Co) grains result in reduction of the resistive force in sample S10B in comparison to that of S10A. However, the reduced resistive force is still strong enough to keep the domains pinned which leads to back and forth movement of the DWs under the influence of an AC magnetic field. Annealing the ribbons at 420°C leads to further reduction of magnetoelastic and magnetocrystalline anisotropies in S10C. The pinning due to the resistive force also decreases significantly. However, due to the absence of any directional preference (because of low anisotropy), the domains exhibit back and forth motion without any net movement of the DWs. Similar to sample S10A, the nature of DWs remains unaffected with variation in H_{AC} and f_{AC} , in samples S10B, and S10C.

Fig. 7.5 shows the temporal evolution of magnetic domains for sample S10D under the application of an AC field of $\mu_0 H_{AC} = 1$ mT and $f_{AC} = 20$ Hz $t = 0$ to 7.5 s. Domains of two separate contrasts (dark and bright) are marked by yellow and red lines, which demonstrate the motion of two adjacent domains. It can be observed that the domains of both contrasts propagate freely under the applied field. In sample S10D, a dilute proportion of α -Fe₂B grains induce a minor contribution of anisotropy in the system (fig. 7.2). However, the ribbon still remains stress free and soft. Hence the DWs start propagating smoothly with a directional preference (guided by the anisotropy) and are free from any hindering pinning mechanism. This behavior is similar to the DW motion in ‘slide’ regime [274,275]. In sample S10D the behavior of the DWs under the applied AC field has been different for variable frequencies. This is in contrary to the behavior in samples S10A-S10C, where the nature of the DW motion does not change significantly with varying frequency. It is well known that the four modes of DW dynamics such as relaxation, creep, slide and switching can be observed by varying the

frequency of the AC field [278]. Further, it should be noted that for very small frequencies the domains switch between the two oppositely magnetized states. This is what we observe for sample S10D at $f_{AC} = 1$ Hz.

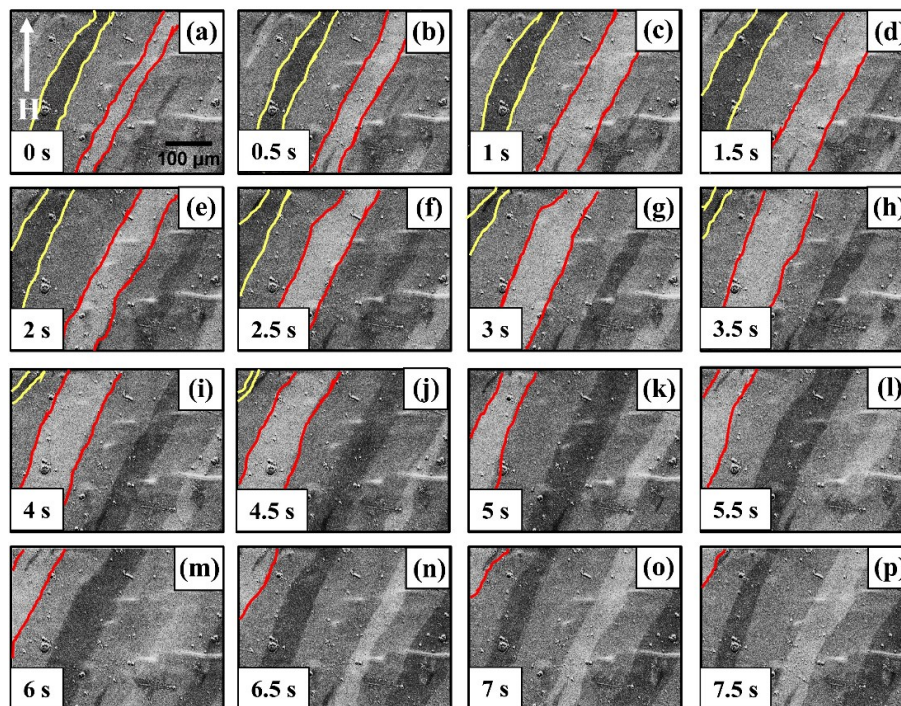


Figure 7.5: (a – p) Domain structure for sample S10D at remanence measured at $t = 0$ to 7.5 s after applying an AC field of $\mu_0 H_{AC} = 1$ mT and $f_{AC} = 20$ Hz.

It is further observed that the DWs are static under the applied ac field in sample S10E ($T_a = 460^\circ\text{C}$). The high anisotropic $\alpha\text{-Fe}_2\text{B}$ and other impurity grains in the sample pin the DWs and hinder their motion. By varying $\mu_0 H_{AC}$ from 0.5 to 5 mT, and f_{AC} from 1 to 20 Hz, no net movement of the DWs was observed. This is consistent with previously reported observation using in-situ Lorentz microscopy (under static field) on magnetic ribbon where the boride precipitates result in less smooth domain wall motion [288].

In this work, we have shown that annealing the $\text{Fe}_{81.2}\text{Co}_4\text{Si}_{0.5}\text{B}_{9.5}\text{P}_4\text{Cu}_{0.8}$ soft magnetic ribbons beyond a temperature ($T_a \sim 400^\circ\text{C}$) crystallizes the alloy with appearance of $\alpha\text{-Fe(-Co)}$ phase. The as-quenched amorphous ribbon shows presence of fingerprint-like ‘stress patterns’ along

with wide domains with 180° walls. Annealing the ribbon at $T_a = 370^\circ\text{C}$ led to formation of disordered fractal domains followed by wide domains with 180° walls. The optimally annealed ribbon at $T_a = 420^\circ\text{C}$ shows low coercive loss and high B_S . Dense packing of $\alpha\text{-Fe(-Co)}$ grains in the ribbons lead to strong exchange interaction and reduction in magnetocrystalline anisotropy which results in occurrence of wide stripe domains. Annealing at higher temperatures ($T_a \sim 460^\circ\text{C}$) revealed appearance of other crystalline phases with high anisotropy along with $\alpha\text{-Fe(-Co)}$ which resulted in elevated coercivity and appearance of smaller domains. The 'stress patterns' remain static even under an AC field of high frequency and amplitude. Annealing the ribbons at $T_a = 450^\circ\text{C}$ leads to reduction in stress with enhancement of exchange coupling and hence the DWs propagate freely under AC field. Annealing at high temperature leads to the appearance of impurity peaks which hinders the free DW propagation. This work clearly reveals that it is possible to tune the domain statics and dynamics in magnetic ribbons by varying the annealing temperature. The study of domain wall dynamics under AC field is helpful in gaining insights for further reduction of energy loss in power transformer and motor cores. It would be desirable to measure the DW velocities in these ribbons which can be achieved by performing experiments under pulsed magnetic fields. Another aspect related to the industrial application of these ribbons is the brittleness which depends on the composition and annealing temperature. Future research in this direction is necessary to reduce the brittleness of magnetic ribbons. MAL arrays of such nanocrystalline ribbons can be studied to explore different static and dynamic magnetic properties by tuning the growth conditions. However, the fabrication of such antidot arrays of ribbons is challenging and hence can be envisaged as a future prospect.

CHAPTER 8: Summary and Outlook

In this thesis we have extensively studied the fabrication and characterization of various MAL arrays. In the 1st chapter we have described the advantage of MAL arrays over dot arrays due to the absence of superparamagnetic limit. The MAL arrays possess various promising applications, however there were several open questions in this field of research. In this context we have fabricated MAL arrays of Co (either with in-plane or out-of-plane magnetization) and Heusler alloy ($\text{Co}_2\text{Fe}_{0.4}\text{Mn}_{0.6}\text{Si}$) by using either photolithography (micro-dimensional) or e-beam lithography (nano-dimensional) employed with sputtering deposition technique. Structural information of the samples have been extracted using RHEED, SEM, AFM, and XRD whereas the magnetic properties of the samples are measured using MOKE, SQUID magnetometry, Kerr, XPEEM microscopy, TR-MOKE, and FMR spectroscopy techniques. For understanding the properties in MAL arrays we have also performed systematic investigation of the parent continuous thin films.

A part of the thesis has been dedicated in understanding the ideal conditions for tuning anisotropy in continuous thin films [11]. We have shown that the domain and anisotropy engineering is possible in the antidot arrays of magnetic thin films with both in-plane and out-of-plane anisotropy. The structure induced shape anisotropy is weak in comparison to the magnetocrystalline one for the micro-dimensional MAL arrays [12,13]. However, the shape anisotropy plays a major role in determining the magnetization switching when the antidot feature size is reduced to nano-dimension [28]. The alignment between both shape and magnetocrystalline anisotropies significantly depends on the antidot architecture. We observe that the size as well as the shape of the domains in the in-plane magnetized antidot arrays strongly depends on the availability of the active magnetic area and distribution of anisotropy in the samples [12,13,28]. On the other hand, the domain structure in the MAL arrays with out-of-plane anisotropy exhibits formation of localized bubbles at the vicinity of the periodic holes

[21]. However, presence of defects at the vertices of the holes pin the domains and modify the structure from bubble to stripe ones which has been shown by micromagnetic simulation for a model FePt MAL arrays [30].

We have further explored the possibility of tuning the thermal relaxation dynamics in the antidot arrays of Co thin films. It has been observed that the speed of relaxation in the MAL arrays is significantly slower than its thin film counterpart [13,16]. This is a drawback for storage applications where rapid reversal of spins is desired for reading and writing information. In order to overcome this limitation, we have further prepared the in-plane magnetized antidot arrays of Co by employing substrate rotation during deposition. We have observed that, although the enhanced exchange coupling due to substrate rotation leads to an increase in the speed of relaxation in the antidot arrays, however the global relaxation still remains slower than that of the parent continuous thin film [12,13,16]. Further to improve this aspect we have studied MAL arrays of Co/Pt films with out-of-plane anisotropy since the Bloch walls propagating in the out-of-plane direction are expected to face less hindrance in the path of propagation. We have achieved faster relaxation in Co/Pt antidots arrays in comparison to its parent continuous thin films [21].

Utilization of MALs as magnonic crystals for the study of SWs demands materials with low Gilbert damping, high saturation magnetization, long SW propagation distance, etc. Investigation of SW spectra in MAL arrays of epitaxial CFMS reveals the formation of additional modes (reducing the frequency gap) in the antidots due to the modification of the demagnetizing field in the vicinity of the holes as well as alignment of the anisotropies present in the system. We have studied the SW modes for various MAL arrays with tuneable shape anisotropy and intrinsic magnetocrystalline anisotropies [28]. The observed tunability of the SW spectra by varying the shape of the antidots opens up new exciting possibilities in fundamental research.

As a future prospect, the feature size of the holes in such antidot arrays can be further reduced for device miniaturization. Suppression of growth induced magnetocrystalline anisotropy and enhancement of shape anisotropy will provide extra degrees of freedom to control the magnetization reversal in these systems by varying the antidot architecture. It will be interesting to know how the magnetization relaxation mechanism is tuned in such systems from both applications and fundamental research point of view. One can also aim to study the dynamics in MAL arrays by applying pulsed magnetic field. Different regimes of DW dynamics viz. relaxation, depinning, creep, slide, Walker-Breakdown, etc. and their evolution with the shape, size, and inter-separation of holes in such MAL arrays are relatively unexplored. Reduction of the feature size to sub-100 nm length scale would lead to high frequency dipole-exchange SW regime with rich prospects for device applications. Further fabrication of MAL arrays can be performed in other systems where the domain size and shape is tuneable. For example in magnetic ribbons which are micron thick, has several promising set of applications and its property can be well controlled by various growth and annealing conditions [33]. It should be also noted that other exotic polygonal shapes for the antidots as well as the lattice symmetry (hexagonal, honeycomb, octagonal, etc.) can be chosen to further tune the shape anisotropy and the internal field distribution to tune the SW spectra and magnetization reversal mechanism.

REFERENCES:

- [1] J. Ferré, *Top. Appl. Phys* **83**, 127 (2002).
- [2] A. O. Adeyeye and N. Singh, *J. Phys. D: Appl. Phys.* **41**, 153001 (2008).
- [3] R. P. Cowburn, A. O. Adeyeye, and J. A. C. Bland, *Appl. Phys. Lett.* **70**, 2309 (1997).
- [4] S. Bedanta and W. Kleemann, *J. Phys. D: Appl. Phys.* **42**, 013001 (2009).
- [5] A. Ünal, S. Valencia, F. Radu, D. Marchenko, K. Merazzo, M. Vázquez, and J. Sánchez-Barriga, *Phys. Rev. Appl.* **5**, 064007 (2016).
- [6] X. K. Hu, S. Sievers, A. Muller, V. Janke, and H. W. Schumacher, *Phys. Rev. B* **84** (2011).
- [7] R. Mandal *et al.*, *ACS Nano* **6**, 3397 (2012).
- [8] D. H. Y. Tse, S. J. Steinmuller, T. Trypiniotis, D. Anderson, G. A. C. Jones, J. A. C. Bland, and C. H. W. Barnes, *Phys. Rev. B* **79** (2009).
- [9] N. Chowdhury and S. Bedanta, *AIP Adv.* **4**, 027104 (2014).
- [10] J. Ben Youssef, N. Vukadinovic, D. Billet, and M. Labrune, *Phys. Rev. B* **69** (2004).
- [11] S. Mallick, S. Mallik, B. B. Singh, N. Chowdhury, R. Gieniusz, A. Maziewski, and S. Bedanta, *J. Phys. D: Appl. Phys.* **51**, 275003 (2018).
- [12] S. Mallick, S. Mallik, and S. Bedanta, *J. Appl. Phys.* **118**, 083904 (2015).
- [13] S. Mallick and S. Bedanta, *J. Magn. Magn. Mater.* **382**, 158 (2015).
- [14] E. Fatuzzo, *Phys. Rev.* **127**, 1999 (1962).
- [15] M. Labrune, S. Andrieu, F. Rio, and P. Bernstein, *J. Magn. Magn. Mater.* **80**, 211 (1989).
- [16] N. Chowdhury, S. Mallick, S. Mallik, and S. Bedanta, *Thin Solid Films* **616**, 328 (2016).
- [17] B. Hillebrands and J. Fassbender, *Nature* **418**, 493 (2002).
- [18] M. Ghidini, G. Zangari, I. L. Prejbeanu, G. Pattanaik, L. D. Buda-Prejbeanu, G. Asti, C. Pernechele, and M. Solzi, *J. Appl. Phys.* **100**, 103911 (2006).
- [19] A. Hubert and R. Schfer, *Magnetic Domains* (Springer-Verlag, 1998).
- [20] M. J. Donahue, OOMMF user's guide, version 1.0, 1999.
- [21] S. Mallick, S. S. Mishra, and S. Bedanta, *Sci. Rep.* **8**, 11648 (2018).
- [22] S. Pan, S. Mondal, T. Seki, K. Takanashi, and A. Barman, *Phys. Rev. B* **94**, 184417 (2016).
- [23] S. Pan, T. Seki, K. Takanashi, and A. Barman, *Phys. Rev. Appl.* **7** (2017).
- [24] I. Galanakis, P. H. Dederichs, and N. Papanikolaou, *Phys. Rev. B* **66**, 174429 (2002).
- [25] V. Kamberský, *Canadian Journal of Physics* **48**, 2906 (1970).
- [26] T. Seki, Y. Sakuraba, H. Arai, M. Ueda, R. Okura, H. Imamura, and K. Takanashi, *Appl. Phys. Lett.* **105**, 092406 (2014).
- [27] D. Kumar, O. Dmytriiev, S. Ponraj, and A. Barman, *J. Phys. D: Appl. Phys.* **45**, 015001 (2012).
- [28] S. Mallick *et al.*, (unpublished).
- [29] O. Ivanov, L. Solina, V. Demshina, and L. Magat, *Met. Metallog* **35**, 81 (1973).
- [30] S. Bedanta, T. Seki, S. Mallick, H. Iwama, T. Shima, and K. Takanashi, (unpublished).
- [31] S. Mallick, S. Bedanta, T. Seki, and K. Takanashi, *J. Appl. Phys.* **116**, 133904 (2014).
- [32] A. D. Setyawan, K. Takenaka, P. Sharma, M. Nishijima, N. Nishiyama, and A. Makino, *J. Appl. Phys.* **117**, 17B715 (2015).
- [33] S. Mallick, P. Sharma, K. Takenaka, A. Makino, and S. Bedanta, *J. Phys. D: Appl. Phys.* **51**, 065007 (2018).
- [34] R. Shull, R. McMichael, L. Swartzendruber, and L. Bennet, (North Holland Publ. Co., Amsterdam, New York, 1992).
- [35] G. C. Hadjipanayis and R. W. Siegel, *Nanophase materials: Synthesis-properties-applications* (Springer Science & Business Media, 2012), Vol. 260.

References

- [36] S. Y. Chou, *Proc. IEEE* **85**, 652 (1997).
- [37] S. Bedanta, PhD Thesis, Universität Duisburg-Essen, Fakultät für Physik (2006).
- [38] D. Weller and A. Moser, *IEEE Trans. Magn.* **35**, 4423 (1999).
- [39] T. Shima, K. Takanashi, Y. K. Takahashi, and K. Hono, *Appl. Phys. Lett.* **81**, 1050 (2002).
- [40] M. Ohtake, S. Ouchi, F. Kirino, and M. Futamoto, *J. Appl. Phys.* **111**, 07A708 (2012).
- [41] S. Haruaki, O. Mikihiko, K. Yuta, N. Hiroshi, and A. Yasuo, *J. J. Appl. Phys.* **52**, 063003 (2013).
- [42] M. J. Van Bael, K. Temst, V. V. Moshchalkov, and Y. Bruynseraede, *Phys. Rev. B* **59**, 14674 (1999).
- [43] P. Vavassori *et al.*, *Phys. Rev. B* **59**, 6337 (1999).
- [44] I. Guedes, N. J. Zaluzec, M. Grimsditch, V. Metlushko, P. Vavassori, B. Ilic, P. Neuzil, and R. Kumar, *Phys. Rev. B* **62**, 11719 (2000).
- [45] C. T. Yu, H. Jiang, L. Shen, P. J. Flanders, and G. J. Mankey, *J. Appl. Phys.* **87**, 6322 (2000).
- [46] I. Guedes, M. Grimsditch, V. Metlushko, P. Vavassori, R. Camley, B. Ilic, P. Neuzil, and R. Kumar, *Phys. Rev. B* **66** (2002).
- [47] P. Vavassori, G. Gubbiotti, G. Zangari, C. T. Yu, H. Yin, H. Jiang, and G. J. Mankey, *J. Appl. Phys.* **91**, 7992 (2002).
- [48] L. J. Heyderman, F. Nolting, and C. Quitmann, *Appl. Phys. Lett.* **83**, 1797 (2003).
- [49] L. J. Heyderman *et al.*, *Phys. Rev. B* **73** (2006).
- [50] C. C. Wang, A. O. Adeyeye, and N. Singh, *Nanotechnology* **17**, 1629 (2006).
- [51] E. Mengotti *et al.*, *J. Appl. Phys.* **103**, 07D509 (2008).
- [52] R. H. Cheng, B. L. Justus, A. Rosenberg, D. N. Mellroy, Z. Holman, D. Zhang, and Y. Kranov, *J. Appl. Phys.* **108**, 086110 (2010).
- [53] N. G. Deshpande, M. S. Seo, X. R. Jin, S. J. Lee, Y. P. Lee, J. Y. Rhee, and K. W. Kim, *Appl. Phys. Lett.* **96**, 122503 (2010).
- [54] E. T. Papaioannou, V. Kapaklis, P. Patoka, M. Giersig, P. Fumagalli, A. Garcia-Martin, E. Ferreira-Vila, and G. Ctistis, *Phys. Rev. B* **81** (2010).
- [55] K. J. Merazzo, D. C. Leitao, E. Jimenez, J. P. Araujo, J. Camarero, R. P. del Real, A. Asenjo, and M. Vazquez, *J. Phys. D: Appl. Phys.* **44**, 505001 (2011).
- [56] R. H. Cheng, A. Rosenberg, D. N. Mellroy, Z. Holman, D. Zhang, and Y. Kranov, *J. Appl. Phys.* **111**, 063902 (2012).
- [57] N. G. Deshpande, M. S. Seo, S. J. Lee, L. Y. Chen, K. W. Kim, J. Y. Rhee, Y. H. Kim, and Y. P. Lee, *J. Appl. Phys.* **111**, 013906 (2012).
- [58] N. G. Deshpande, J. S. Hwang, K. W. Kim, J. Y. Rhee, Y. H. Kim, L. Y. Chen, and Y. P. Lee, *Appl. Phys. Lett.* **100**, 222403 (2012).
- [59] K. J. Merazzo *et al.*, *Phys. Rev. B* **85** (2012).
- [60] M. C. Ambrose and R. L. Stamps, *J. Magn. Magn. Mater.* **344**, 140 (2013).
- [61] J. L. Palma, C. Gallardo, L. Spinu, J. M. Vargas, L. S. Dorneles, J. C. Denardin, and J. Escrig, *J. Magn. Magn. Mater.* **344**, 8 (2013).
- [62] Y. H. Jang and J. H. Cho, *J. Appl. Phys.* **115**, 063903 (2014).
- [63] S. Michea, J. L. Palma, R. Lavin, J. Briones, J. Escrig, J. C. Denardin, and R. L. Rodriguez-Suarez, *J. Phys. D: Appl. Phys.* **47**, 335001 (2014).
- [64] L. A. Rodriguez *et al.*, *Nanotechnology* **25**, 385703 (2014).
- [65] A. Kaidatzis, R. P. del Real, R. Alvaro, J. L. Palma, J. Anguita, D. Niarchos, M. Vazquez, J. Escrig, and J. M. Garcia-Martin, *J. Phys. D: Appl. Phys.* **49**, 175004 (2016).
- [66] F. J. Castano, K. Nielsch, C. A. Ross, J. W. A. Robinson, and R. Krishnan, *Appl. Phys. Lett.* **85**, 2872 (2004).
- [67] D. C. Leitao *et al.*, *J. Phys.: Cond. Matt.* **25**, 066007 (2013).

References

- [68] C. T. Yu, M. J. Pechan, and G. J. Mankey, *Appl. Phys. Lett.* **83**, 3948 (2003).
- [69] C. T. Yu, M. J. Pechan, W. A. Burgei, and G. J. Mankey, *J. Appl. Phys.* **95**, 6648 (2004).
- [70] O. N. Martyanov, V. F. Yudanov, R. N. Lee, S. A. Nepijko, H. J. Elmers, R. Hertel, C. M. Schneider, and G. Schoenhense, *Phys. Rev. B* **75**, 174429 (2007).
- [71] M. H. Yu, L. Malkinski, L. Spinu, W. L. Zhou, and S. Whittenburg, *J. Appl. Phys.* **101**, 09F501 (2007).
- [72] I. Ruiz-Feal *et al.*, *J. Magn. Magn. Mater.* **242-245**, 597 (2002).
- [73] K. R. Pirota, P. Prieto, A. M. J. Neto, J. M. Sanz, M. Knobel, and M. Vazquez, *J. Magn. Magn. Mater.* **320**, E235 (2008).
- [74] F. Garcia-Sanchez, E. Paz, F. Pigazo, O. Chubykalo-Fesenko, F. J. Palomares, J. M. Gonzalez, F. Cebollada, J. Bartolome, and L. M. Garcia, *E. Phys. Lett.* **84**, 67002 (2008).
- [75] C. C. Wang, A. O. Adeyeye, N. Singh, Y. S. Huang, and Y. H. Wu, *Phys. Rev. B* **72**, 174426 (2005).
- [76] S. Klinkhammer, H. Xu, T. Heinzl, U. Gennser, G. Faini, C. Ulysse, and A. Cavanna, *Phys. Rev. B* **77**, 235311 (2008).
- [77] T. J. Meng, J. B. Laloe, S. N. Holmes, A. Husmann, and G. A. C. Jones, *J. Appl. Phys.* **106**, 033901 (2009).
- [78] M. Lange, M. J. Van Bael, V. V. Moshchalkov, and Y. Bruynseraede, *J. Magn. Magn. Mater.* **240**, 595 (2002).
- [79] M. T. Rahman, X. Liu, and A. Morisako, *J. Appl. Phys.* **99**, 08G904 (2006).
- [80] M. T. Rahman, N. N. Shams, Y.-C. Wu, C.-H. Lai, and D. Suess, *Appl. Phys. Lett.* **91**, 132505 (2007).
- [81] M. T. Rahman, N. N. Shams, and C. H. Lai, *Nanotechnology* **19**, 325302 (2008).
- [82] M. T. Rahman, R. K. Dumas, N. Eibagi, N. N. Shams, Y.-C. Wu, K. Liu, and C.-H. Lai, *Appl. Phys. Lett.* **94**, 042507 (2009).
- [83] M. T. Rahman, N. N. Shams, C. H. Lai, J. Fidler, and D. Suess, *Phys. Rev. B* **81** (2010).
- [84] C. Gao, K. Chen, L. Lü, J. Zhao, and P. Chen, *J. Magn. Magn. Mater.* **322**, 3278 (2010).
- [85] D. Tripathy and A. O. Adeyeye, *N. J. Phys.* **13**, 023035 (2011).
- [86] J. Gräfe *et al.*, *Phys. Rev. B* **93** (2016).
- [87] C. Bran, P. Gawronski, I. Lucas, R. P. del Real, P. Strichovanec, A. Asenjo, M. Vazquez, and O. Chubykalo-Fesenko, *J. Phys. D: Appl. Phys.* **50**, 065003 (2017).
- [88] A. V. Chumak, A. A. Serga, and B. Hillebrands, *J. Phys. D: Appl. Phys.* **50**, 244001 (2017).
- [89] V. Kruglyak, S. Demokritov, and D. Grundler, *J. Phys. D: Appl. Phys.* **43**, 264001 (2010).
- [90] A. De, S. Mondal, S. Sahoo, S. Barman, Y. Otani, R. K. Mitra, and A. Barman, *Beilstein J Nanotechnol* **9**, 1123 (2018).
- [91] S. Neusser, H. G. Bauer, G. Duerr, R. Huber, S. Mamica, G. Woltersdorf, M. Krawczyk, C. H. Back, and D. Grundler, *Phys. Rev. B* **84** (2011).
- [92] S. Neusser, B. Botters, and D. Grundler, *Phys. Rev. B* **78** (2008).
- [93] S. Neusser, G. Duerr, H. G. Bauer, S. Tacchi, M. Madami, G. Woltersdorf, G. Gubbiotti, C. H. Back, and D. Grundler, *Phys Rev Lett* **105**, 067208 (2010).
- [94] S. Neusser, G. Duerr, S. Tacchi, M. Madami, M. L. Sokolovskyy, G. Gubbiotti, M. Krawczyk, and D. Grundler, *Phys. Rev. B* **84** (2011).
- [95] S. Neusser and D. Grundler, *Adv. Mater.* **21**, 2927 (2009).
- [96] S. McPhail, C. M. Gurtler, J. M. Shilton, N. J. Curson, and J. A. C. Bland, *Phys. Rev. B* **72**, 094414 (2005).
- [97] H. Ulrichs, B. Lenk, and M. Munzenberg, *Appl. Phys. Lett.* **97**, 092506 (2010).
- [98] S. Tacchi *et al.*, *Phys. Rev. B* **86**, 014417 (2012).
- [99] D. Kumar, P. Sabareesan, W. Wang, H. Fangohr, and A. Barman, *J. Appl. Phys.* **114**,

References

- 023910 (2013).
- [100] R. Mandal, S. Barman, S. Saha, Y. Otani, and A. Barman, *J. Appl. Phys.* **118**, 053910 (2015).
- [101] R. Mandal, P. Laha, K. Das, S. Saha, S. Barman, A. K. Raychaudhuri, and A. Barman, *Appl. Phys. Lett.* **103**, 262410 (2013).
- [102] M. Getzlaff, (2008).
- [103] J. A. Osborn, *Phys. Rev.* **67**, 351 (1945).
- [104] F. Michael, *Rep. Prog. Phys.* **61**, 755 (1998).
- [105] H. Horner and C. M. Varma, *Phys. Rev. Lett.* **20**, 845 (1968).
- [106] D. Sander, *Rep. Prog. Phys.* **62**, 809 (1999).
- [107] B. Cullity, (Addison-Alesley Pub. Co., Reading, 1972).
- [108] A. K. Behera, S. S. Mishra, S. Mallick, B. B. Singh, and S. Bedanta, *J. Phys. D: Appl. Phys.* **51**, 285001 (2018).
- [109] P. Weiss, *Journal de Physique Théorique et Appliquée* **6**, 661 (1907).
- [110] L. Landau and E. Lifshitz, *Phys. Z. Sowjetunion* **8**, 101 (1935).
- [111] K. J. Sixtus and L. Tonks, *Phys. Rev.* **37**, 930 (1931).
- [112] F. Bloch, in *Zur Theorie des Austauschproblems und der Remanenzerscheinung der Ferromagnetika* (Springer, 1932), pp. 295.
- [113] L. Néel, *Adv. Phys.* **4**, 191 (1955).
- [114] R. C. O'handley, *Modern magnetic materials: principles and applications* (Wiley, 2000).
- [115] S. Mallik, N. Chowdhury, and S. Bedanta, *AIP Adv.* **4**, 097118 (2014).
- [116] S. Chikazumi, *Phys. Rev.* **85**, 918 (1952).
- [117] Y. Wang, C. Nelson, A. Melville, B. Winchester, S. Shang, Z.-K. Liu, D. G. Schlom, X. Pan, and L.-Q. Chen, *Phys. Rev. Lett.* **110**, 267601 (2013).
- [118] H. S. Cho, C. Hou, M. Sun, and H. Fujiwara, *J. Appl. Phys.* **85**, 5160 (1999).
- [119] E. Della Torre, *Magnetic hysteresis* (Wiley, 2000).
- [120] Y. Liu, D. J. Sellmyer, and D. Shindo, *Advanced magnetic materials: nanostructural effects* (Springer Science+ Business Media, 2006).
- [121] A. Aharoni, *Phys. Rev.* **119**, 127 (1960).
- [122] L. Néel, *Journal de Physique et le Radium* **12**, 339 (1951).
- [123] F. Stacey, *Aus. J. Phys.* **13**, 599 (1960).
- [124] E. C. Stoner and E. P. Wohlfarth, *Philosophical Transactions of the Royal Society A: Mathematical, Physical and Engineering Sciences* **240**, 599 (1948).
- [125] J. Stöhr and H. C. Siegmann, *Magnetism: from fundamentals to nanoscale dynamics* (Springer Science & Business Media, 2007), Vol. 152.
- [126] T. Gilbert, *Phys. Rev.* **100**, 1243 (1955).
- [127] R. Mandal, PhD Thesis, University of Calcutta (2015).
- [128] A. Kirilyuk, A. V. Kimel, and T. Rasing, *Rev. Mod. Phys.* **82**, 2731 (2010).
- [129] S. Pal, PhD Thesis, University of Calcutta (2014).
- [130] A. Barman and J. Sinha, *Spin Dynamics and Damping in Ferromagnetic Thin Films and Nanostructures* (Springer, 2018).
- [131] M. Van Kampen, C. Jozsa, J. Kohlhepp, P. LeClair, L. Lagae, W. De Jonge, and B. Koopmans, *Phys. Rev. Lett.* **88**, 227201 (2002).
- [132] J. Griffiths, *Nature* **158**, 670 (1946).
- [133] C. Kittel, *Phys. Rev.* **71**, 270 (1947).
- [134] C. Kittel, *Phys. Rev.* **73**, 155 (1948).
- [135] O. Kohmoto, *J. Magn. Magn. Mater.* **262**, 280 (2003).
- [136] S. Saha, PhD Thesis, University of Calcutta (2015).
- [137] F. Keffer, in *Ferromagnetism/Ferromagnetismus* (Springer, 1966), pp. 1.

References

- [138] F. Bloch, *Zeitschrift für Physik* **61**, 206 (1930).
- [139] P. A. Fleury, S. P. S. Porto, L. E. Cheesman, and H. J. Guggenheim, *Phys. Rev. Lett.* **17**, 84 (1966).
- [140] V. Vlaminc and M. Bailleul, *Science* **322**, 410 (2008).
- [141] V. E. Demidov, S. O. Demokritov, D. Birt, B. O’Gorman, M. Tsoi, and X. Li, *Phys. Rev. B* **80**, 014429 (2009).
- [142] D. R. Birt, B. O’Gorman, M. Tsoi, X. Li, V. E. Demidov, and S. O. Demokritov, *Appl. Phys. Lett.* **95**, 122510 (2009).
- [143] C. Kittel, P. McEuen, and P. McEuen, *Introduction to solid state physics* (Wiley New York, 1996), Vol. 8.
- [144] A. G. Gurevich and G. A. Melkov, *Magnetization oscillations and waves* (CRC press, 1996).
- [145] M. Sparks, *Ferromagnetic-relaxation theory* (McGraw-Hill, 1964).
- [146] S. O. Demokritov, B. Hillebrands, and A. N. Slavin, *Phys. Rep.* **348**, 441 (2001).
- [147] C. Herring and C. Kittel, *Phys. Rev.* **81**, 869 (1951).
- [148] R. W. Damon and J. Eshbach, *J. Phys. Chem. Sol.* **19**, 308 (1961).
- [149] Mask Aligner MIDAS, http://www.midas-system.com/board/?board=products_en&category=36&no=60.
- [150] Microresist Technology, <https://www.microresist.de>
- [151] V. R. Manfrinato, PhD Thesis, Massachusetts Institute of Technology (2015).
- [152] P. M. Martin, *Handbook of deposition technologies for films and coatings: science, applications and technology* (William Andrew, 2009).
- [153] D. M. Mattox, *Metal Finishing* **99**, 409 (2001).
- [154] P. Sigmund, *Phys. Rev.* **184**, 383 (1969).
- [155] R. Behrisch, (1981).
- [156] P. J. Kelly and R. D. Arnell, *Vacuum* **56**, 159 (2000).
- [157] S. Swann, *Physics in technology* **19**, 67 (1988).
- [158] D. Depla, S. Mahieu, and J. Greene, in *Handbook of Deposition Technologies for Films and Coatings (Third Edition)* (Elsevier, 2010), pp. 253.
- [159] K. S. Harsha, *Principles of vapor deposition of thin films* (Elsevier, 2005).
- [160] Mantis Deposition System, <https://www.mantisdeposition.com/systems/view/info/qprep-series.html>.
- [161] D. O. Smith, M. S. Cohen, and G. P. Weiss, *J. Appl. Phys.* **31**, 1755 (1960).
- [162] A. Ichimiya, S. Kohmoto, H. Nakahara, and Y. Horio, *Ultramicroscopy* **48**, 425 (1993).
- [163] S. Hasegawa, *Char. Mater* (2012).
- [164] W. H. Bragg and W. L. Bragg, *Proc. R. Soc. Lond. A* **88**, 428 (1913).
- [165] Rigaku XRD, W. H. Bragg, and W. L. Bragg, *Proc. Royal. Soc. A* **88**, 428 (1913).
- [166] SEM <http://trieste.nffa.eu/areas/characterization/sem/>.
- [167] SEM Zeiss Sigma <https://www.zeiss.com/microscopy/int/products/scanning-electron-microscopes/sigma.html>.
- [168] G. Binnig, C. F. Quate, and C. Gerber, *Phys Rev Lett* **56**, 930 (1986).
- [169] AFM CSI, <https://www.csinstruments.eu/nano-observer-afm-microscope/>.
- [170] B. D. Josephson, *Phys. Lett.* **1**, 251 (1962).
- [171] P. W. Anderson and J. M. Rowell, *Phys. Rev. Lett.* **10**, 230 (1963).
- [172] R. C. Jaklevic, J. Lambe, A. H. Silver, and J. E. Mercereau, *Phys. Rev. Lett.* **12**, 159 (1964).
- [173] SQUID Quantum Design, <https://www.qdusa.com/company/index.html>.
- [174] J. Kerr, *The London, Edinburgh, and Dublin Philosophical Magazine and Journal of Science* **3**, 321 (1877).
- [175] M. Faraday, *Philosophical Transactions of the Royal Society of London* **136**, 1 (1846).

References

- [176] R. Schäfer, *Handbook of magnetism and advanced magnetic materials* (2007).
- [177] Kerr Microscope Evico Magnetics, <http://www.evico-magnetics.de/>.
- [178] J. Stohr, Y. Wu, B. D. Hermsmeier, M. G. Samant, G. R. Harp, S. Koranda, D. Dunham, and B. P. Tonner, *Science* **259**, 658 (1993).
- [179] J. Stöhr, *J. Magn. Magn. Mater.* **200**, 470 (1999).
- [180] J. Stöhr, H. Padmore, S. Anders, T. Stammler, and M. Scheinfein, *Surf. Rev. Lett.* **5**, 1297 (1998).
- [181] W. Zhang, University of Twente (2012).
- [182] XPEEM Diamond Light Source, <http://www.diamond.ac.uk/Beamlines/Surfaces-and-Interfaces/106/peem.html>.
- [183] C. P. Poole, *Electron spin resonance: a comprehensive treatise on experimental techniques* (Courier Corporation, 1996).
- [184] J. H. E. Griffiths, *Nature* **158**, 670 (1946).
- [185] FMR Spectrometer NanoOsc, <https://www.qdusa.com/products/nanosc-fmr-spectrometers.html>.
- [186] S. Mallik, S. Mallick, and S. Bedanta, *J. Magn. Magn. Mater.* **428**, 50 (2017).
- [187] H. Sohn and R. H. Victora, *J. Appl. Phys.* **107**, 09B312 (2010).
- [188] R. L. Comstock, *J. Mater. Sci.: Mat. Elec.* **13**, 509 (2002).
- [189] S. Bedanta, T. Eimuller, W. Kleemann, J. Rhensius, F. Stromberg, E. Amaladass, S. Cardoso, and P. P. Freitas, *Phys. Rev. Lett.* **98** (2007).
- [190] Y. Z. Wu, C. Won, and Z. Q. Qiu, *Phys. Rev. B* **65** (2002).
- [191] M. Takahashi and T. Kono, *Journal of the Physical Society of Japan* **15**, 936 (1960).
- [192] Paritosh and D. J. Srolovitz, *J. Appl. Phys.* **91**, 1963 (2002).
- [193] S. van Dijken, G. Di Santo, and B. Poelsema, *Phys. Rev. B* **63** (2001).
- [194] H. Kijima, S. Ohnuma, and H. Masumoto, *IEEE Trans. Magn.* **47**, 3928 (2011).
- [195] G. Herzer, *J. Magn. Magn. Mater.* **112**, 258 (1992).
- [196] H. Giselher, *Physica Scripta* **1993**, 307 (1993).
- [197] H. Ono, M. Ishida, M. Fujinaga, H. Shishido, and H. Inaba, *J. Appl. Phys.* **74**, 5124 (1993).
- [198] O. Idigoras, A. K. Suszka, P. Vavassori, P. Landeros, J. M. Porro, and A. Berger, *Phys. Rev. B* **84** (2011).
- [199] R. Gieniusz, L. T. Baczewski, Z. Kurant, A. Maziewski, and A. Wawro, *J. Magn. Magn. Mater.* **310**, 2198 (2007).
- [200] in *Handbook of Deposition Technologies for Films and Coatings (Third Edition)* (William Andrew Publishing, Boston, 2010), pp. 1.
- [201] K. J. Harte, *J. Appl. Phys.* **39**, 1503 (1968).
- [202] A. Y. Toporov, R. M. Langford, and A. K. Petford-Long, *Appl. Phys. Lett.* **77**, 3063 (2000).
- [203] R. F. Pease and S. Y. Chou, *Proc. IEEE* **96**, 248 (2008).
- [204] J. Vogel *et al.*, *Phys. Rev. B* **72**, 220402 (2005).
- [205] J. L. Maurice, J. Briático, J. Carrey, F. Petroff, L. F. Schelp, and A. Vaurès, *Phil. Mag. A* **79**, 2921 (1999).
- [206] J. Grafe *et al.*, *Nanotechnology* **26**, 225203 (2015).
- [207] R. Bali, M. Kostylev, D. Tripathy, A. O. Adeyeye, and S. Samarin, *Phys. Rev. B* **85** (2012).
- [208] M. J. Donahue and D. G. Porter, 2016).
- [209] N. Nakajima *et al.*, *Phys. Rev. Lett.* **81**, 5229 (1998).
- [210] V. M. Parakkat, K. R. Ganesh, and P. S. Anil Kumar, *AIP Adv.* **6**, 056118 (2016).
- [211] D. Navas, F. Ilievski, and C. A. Ross, *J. Appl. Phys.* **105**, 113921 (2009).
- [212] H. W. Xi, K. Z. Gao, O. Y. Jun, Y. M. Shi, and Y. Z. Yang, *J. Phys.: Cond. Matt.* **20**,

References

295220 (2008).

- [213] A. Adanlété Adjanoh, R. Belhi, J. Vogel, M. Ayadi, and K. Abdelmoula, *J. Magn. Magn. Mater.* **323**, 504 (2011).
- [214] T. Seki, T. Shima, and K. Takanashi, *J. Magn. Magn. Mater.* **272**, 2182 (2004).
- [215] T. Sebastian *et al.*, *Appl. Phys. Lett.* **100**, 112402 (2012).
- [216] T. Kubota, S. Tsunegi, M. Oogane, S. Mizukami, T. Miyazaki, H. Naganuma, and Y. Ando, *Appl. Phys. Lett.* **94**, 122504 (2009).
- [217] Y. Liu, L. R. Shelford, V. V. Kruglyak, R. J. Hicken, Y. Sakuraba, M. Oogane, and Y. Ando, *Phys. Rev. B* **81**, 094402 (2010).
- [218] Y. Sakuraba, M. Ueda, Y. Miura, K. Sato, S. Bosu, K. Saito, M. Shirai, T. J. Konno, and K. Takanashi, *Appl. Phys. Lett.* **101**, 252408 (2012).
- [219] B. Balke, G. H. Fecher, H. C. Kandpal, C. Felser, K. Kobayashi, E. Ikenaga, J.-J. Kim, and S. Ueda, *Phys. Rev. B* **74**, 104405 (2006).
- [220] M. S. Gabor, T. Petrisor, C. Tiusan, M. Hehn, and T. Petrisor, *Phys. Rev. B* **84**, 134413 (2011).
- [221] Y. B. Xu, D. J. Freeland, M. Tselepi, and J. A. C. Bland, *Phys. Rev. B* **62**, 1167 (2000).
- [222] Q. F. Zhan, S. Vandezande, C. Van Haesendonck, and K. Temst, *Appl. Phys. Lett.* **91**, 122510 (2007).
- [223] O. Thomas, Q. Shen, P. Schieffer, N. Tournerie, and B. Lepine, *Phys Rev Lett* **90**, 017205 (2003).
- [224] R. P. Cowburn, S. J. Gray, and J. A. C. Bland, *Phys. Rev. Lett.* **79**, 4018 (1997).
- [225] S. Mallik, S. Mattauch, M. K. Dalai, T. Brückel, and S. Bedanta, *Sci. Rep.* **8**, 5515 (2018).
- [226] S. Mondal, S. Choudhury, S. Barman, Y. Otani, and A. Barman, *RSC Adv.* **6**, 110393 (2016).
- [227] Y. F. Xu, J. S. Chen, and J. P. Wang, *Appl. Phys. Lett.* **80**, 3325 (2002).
- [228] J. U. Thiele, L. Folks, M. F. Toney, and D. K. Weller, *J. Appl. Phys.* **84**, 5686 (1998).
- [229] T. Bublath and D. Goll, *J. Appl. Phys.* **108**, 113910 (2010).
- [230] S. Bedanta, T. Seki, H. Iwama, T. Shima, and K. Takanashi, *Appl. Phys. Lett.* **107**, 152410 (2015).
- [231] T. Shima, T. Moriguchi, S. Mitani, and K. Takanashi, *Appl. Phys. Lett.* **80**, 288 (2002).
- [232] T. Shima, K. Takanashi, Y. K. Takahashi, K. Hono, G. Q. Li, and S. Ishio, *J. Appl. Phys.* **99**, 033516 (2006).
- [233] T. Seki, T. Shima, K. Yakushiji, K. Takanashi, G. Q. Li, and S. Ishio, *J. Appl. Phys.* **100**, 043915 (2006).
- [234] G. Li, H. Saito, S. Ishio, T. Shima, K. Takanashi, and Z. Xiong, *J. Magn. Magn. Mater.* **315**, 126 (2007).
- [235] D. Wang, T. Seki, K. Takanashi, T. Shima, G. Li, H. Saito, and S. Ishio, *J. Appl. Phys.* **105**, 07A702 (2009).
- [236] T. Shima, K. Takanashi, Y. K. Takahashi, K. Hono, G. Q. Li, and S. Ishio, *J. Magn. Magn. Mater.* **266**, 171 (2003).
- [237] T. Suzuki, K. Harada, N. Honda, and K. Ouchi, *J. Magn. Magn. Mater.* **193**, 85 (1999).
- [238] S. Okamoto, N. Kikuchi, O. Kitakami, T. Miyazaki, Y. Shimada, and K. Fukamichi, *Phys. Rev. B* **66**, 024413 (2002).
- [239] F. Casoli, L. Nasi, F. Albertini, S. Fabbrici, C. Bocchi, F. Germini, P. Luches, A. Rota, and S. Valeri, *J. Appl. Phys.* **103**, 043912 (2008).
- [240] X. H. Li, B. T. Liu, W. Li, H. Y. Sun, D. Q. Wu, and X. Y. Zhang, *J. Appl. Phys.* **101**, 093911 (2007).
- [241] G. Bochi, H. J. Hug, D. I. Paul, B. Stiefel, A. Moser, I. I. Parashikov, H. Guntherodt, and R. C. O'Handley, *Phys Rev Lett* **75**, 1839 (1995).

References

- [242] M. Seul and D. Andelman, *Science* **267**, 476 (1995).
- [243] J. A. Cape and G. W. Lehman, *J. Appl. Phys.* **42**, 5732 (1971).
- [244] Z. L. Zhao, J. P. Wang, J. S. Chen, and J. Ding, *Appl. Phys. Lett.* **81**, 3612 (2002).
- [245] R. F. C. Farrow, D. Weller, R. F. Marks, M. F. Toney, D. J. Smith, and M. R. McCartney, *J. Appl. Phys.* **84**, 934 (1998).
- [246] S. Jeong, Y. N. Hsu, D. E. Laughlin, and M. E. McHenry, *IEEE Trans. Magn.* **36**, 2336 (2000).
- [247] T. Maeda, *IEEE Trans. Magn.* **41**, 3331 (2005).
- [248] S. H. Lee and S. H. Eun, *Physica B* **406**, 2646 (2011).
- [249] M. Labrune, S. Hamzaoui, and I. B. Puchalska, *J. Magn. Magn. Mater.* **60**, 243 (1986).
- [250] S. Hamzaoui, M. Labrune, and I. B. Puchalska, *Appl. Phys. Lett.* **45**, 1246 (1984).
- [251] C. Favieres, J. Vergara, and V. Madurga, *J. Phys.: Cond. Matt.* **25**, 066002 (2013).
- [252] Y. Lee, A. R. Koymen, and M. J. Haji-Sheikh, *Appl. Phys. Lett.* **72**, 851 (1998).
- [253] E. J. Hsieh, R. F. Soohoo, C. D. Graham, and J. J. Rhyne, *AIP Conf. Proc.* **5**, 727 (1972).
- [254] I. L. Sanders, R. M. Jones, and A. J. Collins, *J. Phys. D: Appl. Phys.* **10**, 2503 (1977).
- [255] D. Wang, T. Seki, K. Takanashi, and T. Shima, *J. Phys. D: Appl. Phys.* **41**, 195008 (2008).
- [256] R. Hasegawa, *J. Magn. Magn. Mater.* **304**, 187 (2006).
- [257] O. Gutfleisch, M. A. Willard, E. Bruck, C. H. Chen, S. G. Sankar, and J. P. Liu, *Adv Mater* **23**, 821 (2011).
- [258] R. Hasegawa, *J. Magn. Magn. Mater.* **324**, 3555 (2012).
- [259] A. Makino, *IEEE Trans. Magn.* **48**, 1331 (2012).
- [260] Z. Zhang, P. Sharma, and A. Makino, *J. Appl. Phys.* **112**, 103902 (2012).
- [261] Y. Zhang, P. Sharma, and A. Makino, *AIP Adv.* **3**, 062118 (2013).
- [262] Y. Yoshizawa, S. Oguma, and K. Yamauchi, *J. Appl. Phys.* **64**, 6044 (1988).
- [263] A. Makino, T. Hatanai, Y. Naitoh, T. Bitoh, A. Inoue, and T. Masumoto, *IEEE Trans. Magn.* **33**, 3793 (1997).
- [264] M. A. Willard, M. Q. Huang, D. E. Laughlin, M. E. McHenry, J. O. Cross, V. G. Harris, and C. Franchetti, *J. Appl. Phys.* **85**, 4421 (1999).
- [265] A. Urata, H. Matsumoto, S. Yoshida, and A. Makino, *Mater. Sci. For.* **654-656**, 1102 (2010).
- [266] Z. Yan, P. Sharma, and A. Makino, *IEEE Trans. Magn.* **50**, 1 (2014).
- [267] G. Herzer, *IEEE Trans. Magn.* **25**, 3327 (1989).
- [268] G. Herzer, *IEEE Trans. Magn.* **26**, 1397 (1990).
- [269] N. Tsuya, T. Tsukagoshi, K. I. Arai, K. Ogasawara, K. Ohmori, and S. Yasuda, *IEEE Trans. Magn.* **17**, 3111 (1981).
- [270] S. Ikeda, T. Nagae, Y. Shimada, K. H. Kim, and M. Yamaguchi, *J. Appl. Phys.* **99**, 08P507 (2006).
- [271] C. Hamann, R. Mattheis, I. Monch, J. Fassbender, L. Schultz, and J. McCord, *N. J. Phys.* **16**, 023010 (2014).
- [272] D. A. Thompson and J. S. Best, *IBM J. Res. Dev.* **44**, 311 (2000).
- [273] H. Wu, D. S. Gardner, W. Xu, and H. Yu, *IEEE Trans. Magn.* **48**, 4123 (2012).
- [274] W. Kleemann, *Ann. Rev. Mater. Res.* **37**, 415 (2007).
- [275] W. Kleemann, J. Rhensius, O. Petravic, J. Ferre, J. P. Jamet, and H. Bernas, *Phys Rev Lett* **99**, 097203 (2007).
- [276] P. J. Metaxas, J. P. Jamet, A. Mougin, M. Cormier, J. Ferre, V. Baltz, B. Rodmacq, B. Dieny, and R. L. Stamps, *Phys Rev Lett* **99**, 217208 (2007).
- [277] M. Kataja and S. van Dijken, *Rev. Sci. Inst.* **82**, 103901 (2011).
- [278] K. Gross, K. Westerholt, and H. Zabel, *N. J. Phys.* **18**, 033007 (2016).
- [279] S. Flohrer, R. Schafer, J. McCord, S. Roth, L. Schultz, and G. Herzer, *Acta Mater.* **54**,

References

3253 (2006).

[280] M. Kuhnt, M. Marsilius, T. Strache, C. Polak, and G. Herzer, *Scr. Mater.* **130**, 46 (2017).

[281] G. Herzer and H. R. Hilzinger, *J. Magn. Magn. Mater.* **62**, 143 (1986).

[282] H. N. Ok and A. H. Morrish, *Phys. Rev. B* **23**, 2257 (1981).

[283] A. Hubert, *J. Magn. Magn. Mater.* **6**, 38 (1977).

[284] J. D. Livingston and W. G. Morris, *J. Appl. Phys.* **57**, 3555 (1985).

[285] A. Veider, G. Badurek, R. Grössinger, and H. Kronmüller, *J. Magn. Magn. Mater.* **60**, 182 (1986).

[286] H. Kronmüller, M. Fähnle, M. Domann, H. Grimm, R. Grimm, and B. Gröger, *J. Magn. Magn. Mater.* **13**, 53 (1979).

[287] P. Sharma, X. Zhang, Y. Zhang, and A. Makino, *Scr. Mater.* **95**, 3 (2015).

[288] Z. Akase, S. Aizawa, D. Shindo, P. Sharma, and A. Makino, *J. Magn. Magn. Mater.* **375**, 10 (2015).